

# Transient Two-Phase Modelling of Multi-Feed Geothermal Wells

by  
Ryan Tonkin

A thesis submitted in fulfilment of the requirements for the degree of Doctor of  
Philosophy in Engineering Science, the University of Auckland, 2021

# *Abstract*

Geothermal wells play a key role in the development, understanding and utilisation of geothermal resources. It is, therefore, important to have a good understanding of the fluid dynamics and thermodynamic processes that occur within geothermal wells. Numerical simulation provides low-cost insight into the transient behaviour of geothermal wells that is difficult or impossible to measure directly. This research discusses the development of a new transient geothermal wellbore simulator that is capable of modelling the complex flows that occur in geothermal wells.

Transient geothermal wellbore simulators solve equations describing the conservation of mass, momentum and energy. Our review of the literature found that some forms of these governing equations, used in past simulators, did not correctly conserve momentum or energy. However, we found that the impact of these approximations were relatively small for moderate mass flow rates and wellhead pressures. Despite this finding, we implement a three equation model that correctly conserves mass, momentum and energy.

Our numerical formulation of the governing conservation equations is fully-implicit in time. The constitutive model for slip is solved simultaneously with the conservation equations for four primary variables: pressure, temperature (swapped for vapour saturation for two-phase flow), vapour velocity and liquid volume flux.

We developed a set of test cases to ensure that our simulator is capable of modelling the diverse range of flow scenarios that are possible within geothermal wells. These included production and injection, and cases where the wellhead is closed. These cases cover liquid, two-phase and vapour conditions, fast and slow transients, and include examples of counter-flow.

We have developed a simulator that is capable of modelling counter-flow processes in geothermal wells. This project is the first to report results that show counter-flow occurring due to boiling in geothermal wells and is the first to highlight the importance of these processes in geothermal applications. We found that when boiling occurs within a closed well, counter-flow transports heat to the top of the well, which allows a high-temperature, high-saturation two-phase zone to exist alongside cold formation temperatures. This investigation showed that a geothermal wellbore simulator must be able to model counter-flow processes if it is to be used to simulate the shutting in of wells.

We also used our simulator, with an air-water equation of state, to model discharge stimulation methods for non-self-discharging wells. We were able to simulate the successful discharge of a test well with a water level 300 m below the wellhead using air-lifting and air compression.

# *Acknowledgements*

Foremost, I would like to thank my supervisors Prof. Mike O’Sullivan and Dr John O’Sullivan for their time, guidance, commitment, and support throughout the entirety of my research. The countless discussions we had were a continual source of motivation. Special thanks must be extended to Mike, whose prompt feedback always kept me motivated and moving in the right direction.

To the friends I have made at the department throughout the years: Alberto, Antonella, Caroline, Davo, Elvar, James, Ken, Kev, Nico, Nick, Pengliang, Phil, Rishi, Rollie, Tom, Xander and the rest, thank you for all the laughs. To those of you who finished before me, thank you for showing me that it can be done. For those that are yet to finish, good luck. It can be done. Special mention must go to Michael Gravatt, whose jokes never failed to make me grin and whose advice never steered me wrong, and Tony, whose insight into how geothermal systems work in real life was invaluable.

To Joris, Jeremy and Martin, merci beaucoup for the laughs and misadventures.

To my other friends, thank you for the gentle ribbing about remaining a student and reminding me that there is a life outside of study. Special thanks must go to Dana. Your support, kindness and understanding over the past two years have made a world of difference.

Last but not least, I would like to thank my family for their support and understanding. Renee, it has been a pleasure writing my thesis at the same time as you; congratulations on pipping me at the post. To my younger sisters Lauren and Briar, your eccentric personalities never failed to brighten my day. Finally, I wish to thank my Dad for fostering curiosity and a desire to learn, and my Mum for teaching me resilience and encouraging me to “just get it done”.

# Contents

<b>Abstract</b>	<b>i</b>
<b>Acknowledgements</b>	<b>ii</b>
<b>List of Figures</b>	<b>xiii</b>
<b>List of Tables</b>	<b>xix</b>
<b>Symbols</b>	<b>xxi</b>
<b>1 Introduction</b>	<b>1</b>
1.1 Modelling geothermal wellbores . . . . .	3
1.2 Steady-state wellbore modelling . . . . .	5
1.2.1 The early days . . . . .	6
1.2.2 The 1980s and 1990s . . . . .	7
1.2.3 2000 onwards . . . . .	8
1.3 Transient wellbore modelling . . . . .	9
1.4 Motivation and objectives . . . . .	13
1.5 Thesis structure . . . . .	14
<b>2 Conservation equations for two-phase flow in geothermal wellbores</b>	<b>16</b>
2.1 Background . . . . .	17
2.1.1 Multi-phase flow notation . . . . .	17
2.1.2 Modelling single-phase flow . . . . .	25
2.1.3 Modelling multi-phase flow . . . . .	28
2.2 Transient conservation equations . . . . .	32
2.2.1 Alternative conservation of mass equations . . . . .	33
2.2.2 Alternative conservation of momentum equations . . . . .	34
2.2.3 Alternative conservation of energy equations . . . . .	34
2.2.4 Other transient models . . . . .	36
2.3 Steady-state conservation equations . . . . .	37
2.3.1 Conservative models . . . . .	38
2.3.2 Non-conservative models . . . . .	40
2.3.3 Definition of two-phase velocity . . . . .	41
2.4 Conservation equations for homogeneous flow . . . . .	43
2.4.1 Transient homogeneous flow . . . . .	44
2.4.2 Steady-state homogeneous flow . . . . .	45

2.5	Model comparisons . . . . .	45
2.5.1	Approximate momentum flux terms . . . . .	46
2.5.2	Incorrect treatment of area . . . . .	51
2.5.3	Approximate kinetic energy term . . . . .	53
2.6	Summary . . . . .	54
<b>3</b>	<b>Constitutive models for geothermal wellbores</b>	<b>57</b>
3.1	Regimes . . . . .	58
3.1.1	Use of regime-dependent slip models . . . . .	59
3.2	Constitutive models for slip . . . . .	60
3.2.1	Background . . . . .	60
3.2.2	Slip models used in transient wellbore simulators . . . . .	68
3.3	Wellbore friction . . . . .	81
3.3.1	Single-phase flow . . . . .	82
3.3.2	Two-phase flow . . . . .	82
3.4	Wellbore heat transfer . . . . .	86
3.4.1	Analytical model for wellbore heat transfer . . . . .	87
3.5	Source Terms . . . . .	91
3.5.1	Sources of mass . . . . .	92
3.5.2	Sources of momentum . . . . .	94
3.5.3	Sources of energy . . . . .	94
3.6	Properties of pure water . . . . .	95
3.7	Summary . . . . .	95
<b>4</b>	<b>Numerical models for transient geothermal wellbore simulation</b>	<b>97</b>
4.1	Discrete conservation equations . . . . .	98
4.1.1	Conservation of mass . . . . .	98
4.1.2	Conservation of energy . . . . .	100
4.1.3	Conservation of momentum . . . . .	101
4.2	Upstream weighting . . . . .	102
4.2.1	Discrete upstream weighting scheme . . . . .	104
4.2.2	Hybrid upstream weighting scheme . . . . .	106
4.3	Discrete equations for phase slip . . . . .	108
4.3.1	Shi et al.'s (2005) drift-flux model . . . . .	108
4.4	Primary variables . . . . .	111
4.4.1	Primary variable switching . . . . .	111
4.4.2	Persistent primary variables . . . . .	112
4.4.3	Primary variables weighted by mass flow . . . . .	113
4.4.4	Preferred primary variables . . . . .	115
4.5	Boundary conditions . . . . .	120
4.5.1	Production boundary conditions at the wellhead . . . . .	120
4.5.2	Injection boundary conditions at the wellhead . . . . .	123
4.5.3	Closed boundary conditions . . . . .	123
4.6	Solution procedure . . . . .	124
4.6.1	Multi-variate Newton-Raphson method . . . . .	125
4.6.2	Convergence criterion . . . . .	127
4.7	Summary . . . . .	127
<b>5</b>	<b>Testing a transient geothermal wellbore model</b>	<b>129</b>
5.1	Model verification . . . . .	129
5.1.1	Case 1: constant density model . . . . .	130

5.1.2	Case 2: linear density model . . . . .	131
5.1.3	Case 3: Ramey's solution for wellbore heat transport . . . . .	133
5.2	Model validation . . . . .	135
5.2.1	East Mesa 6-1 . . . . .	136
5.2.2	Krafla KJ-11 . . . . .	137
5.2.3	Krafla KJ-22 . . . . .	138
5.2.4	Los Azufres AZ-18 . . . . .	139
5.2.5	Los Humeros H-1 . . . . .	141
5.2.6	Los Humeros H-37 . . . . .	142
5.2.7	WELL-A . . . . .	143
5.2.8	Summary . . . . .	145
5.3	Transient test cases . . . . .	146
5.3.1	Liquid production . . . . .	148
5.3.2	Vapour production . . . . .	160
5.3.3	Injection cases . . . . .	169
5.3.4	Counter-flow cases . . . . .	177
5.4	Summary . . . . .	184
<b>6</b>	<b>Further investigations of the numerical implementation of our transient geothermal wellbore simulator</b>	<b>187</b>
6.1	Primary variable selection . . . . .	187
6.1.1	Velocity formulation . . . . .	188
6.1.2	Volume flux formulation . . . . .	190
6.1.3	Mixed formulation . . . . .	192
6.1.4	Results . . . . .	192
6.1.5	Discussion . . . . .	196
6.2	Calculation of the drift velocity for counter-flow simulations . . . . .	199
6.2.1	Test Case 11: modelling counter-flow below feed-zones . . . . .	200
6.2.2	Test Case 12: heat up of a closed wellbore . . . . .	202
6.2.3	Discussion of solution . . . . .	205
6.3	Improving the numerical performance of our simulator for low mass flow cases . . . . .	206
6.3.1	Calculating the velocity of the non-present phase . . . . .	206
6.3.2	Upstream weighting bias . . . . .	208
6.3.3	Discrete upstream weighting for low mass flow cases . . . . .	210
6.4	Summary . . . . .	211
<b>7</b>	<b>Modelling air-water mixtures</b>	<b>213</b>
7.1	Conservation Equations for air-water mixtures . . . . .	214
7.1.1	Air-water equation of state . . . . .	216
7.2	Numerical implementation . . . . .	220
7.2.1	Discrete conservation equations . . . . .	220
7.2.2	Phase transitions . . . . .	221
7.2.3	Atmospheric boundary conditions . . . . .	223
7.3	Model verification . . . . .	226
7.4	Summary . . . . .	230
<b>8</b>	<b>Wellbore modelling case studies</b>	<b>231</b>
8.1	Counter-flow processes in shut-in wells . . . . .	232
8.1.1	Modelling wellbore heat-up (Test Case 12) . . . . .	232

8.1.2	Modelling wellbore start-up from realistic shut-in conditions . . . .	236
8.1.3	Modelling wellbore shut-in (Test Case 3) . . . . .	240
8.1.4	Discussion . . . . .	242
8.2	Modelling discharge stimulation of geothermal wells . . . . .	244
8.2.1	Initial conditions . . . . .	245
8.2.2	Gas lifting . . . . .	247
8.2.3	Air compression . . . . .	250
8.2.4	Discussion . . . . .	252
8.3	Summary . . . . .	253
<b>9</b>	<b>Conclusions</b>	<b>255</b>
9.1	Model formulation . . . . .	255
9.2	Numerical implementation and testing . . . . .	256
9.3	Wellbore modelling case studies . . . . .	257
9.4	Future work . . . . .	258
9.4.1	Transient wellbore investigations . . . . .	259
9.4.2	Improved modelling of the reservoir . . . . .	260
9.4.3	Improved modelling of transient flow in geothermal wells . . . . .	261
9.5	Achievements . . . . .	262
<b>A</b>	<b>Derivations of the conservation equations</b>	<b>263</b>
A.1	Mixture conservation of mass . . . . .	266
A.1.1	Mass conservation in terms of mixture variables . . . . .	266
A.2	Mixture conservation of momentum . . . . .	267
A.2.1	Momentum conservation in terms of mixture variables . . . . .	269
A.2.2	Steady-state flowing mass fraction form . . . . .	274
A.3	Mixture conservation of energy equation . . . . .	276
A.3.1	Gravity as a body force . . . . .	277
A.3.2	Garcia-Valladares et al. (2006) energy equation . . . . .	279
A.3.3	Thermal energy equation . . . . .	283
<b>B</b>	<b>Derivation of analytical heat transfer term</b>	<b>288</b>
<b>C</b>	<b>Additional test cases</b>	<b>290</b>
C.1	Test Case 13: vapour down-flow into a two-phase block . . . . .	290
C.2	Test Case 14: liquid down-flow into a two-phase block . . . . .	294
C.3	Test Case 15: liquid down-flow from a two-phase block . . . . .	297
<b>D</b>	<b>Viscosity of an air-water vapour mixture</b>	<b>301</b>
	<b>Bibliography</b>	<b>304</b>

# List of Figures

1.1	An illustration of the structure of a geothermal wellbore. . . . .	2
2.1	Coordinate system used in this work. The origin, $z = 0$ , is a reference elevation e.g., sea level. . . . .	27
2.2	Comparison of pressure profiles for Test Case 6 simulated using the (i) exact, (ii) no momentum flux and (iii) approximate model given in (2.76). . . . .	47
2.3	Comparison of output curves for Test Case 6 generated using the (i) exact, (ii) no momentum flux and (iii) approximate model given in (2.76). . . . .	48
2.4	Comparison of pressure profiles for Test Case 4 simulated using the (i) exact, (ii) no momentum flux and (iii) approximate model given in (2.76). . . . .	50
2.5	Comparison of output curves for Test Case 4 generated using the (i) exact, (ii) no momentum flux and (iii) approximate model given in (2.76). . . . .	50
2.6	Comparison of pressure profiles for Test Case 4 simulated using the (i) exact, (ii) no momentum flux and (iii) incorrect treatment of area change. . . . .	52
2.7	Comparison of output curves for Test Case 4 generated using the (i) exact, (ii) no momentum flux and (iii) incorrect treatment of area change. . . . .	52
2.8	Comparison of vapour mass fractions for a 1000m well with a diameter of 0.2 m producing 2000 kJ/kg fluid at 55 kg/s for three cases: (i) exact, (ii) approximate and (iii) no kinetic energy. . . . .	54
3.1	Regimes for upwards flow in vertical pipes. . . . .	59
3.2	Orkiszewski's regime boundaries for $T = 250$ °C and $d = 0.2$ m. . . . .	72
3.3	Saturation vs. flowing mass fraction for various mass flux values calculated using GWELL's slip model as described by McGuinness (2015) (without smoothing). All mass flow rates were run using $T = 250$ °C and $d = 0.2$ m. . . . .	72
3.4	Discontinuities in predicted vapour saturation due to a small change in mass flux calculated using $T = 250$ °C and $d = 0.2$ m when using Rouhani I. . . . .	74
3.5	Discontinuities in phase velocities calculated using $T = 250$ °C, $x_{fv} = 0.1$ and $d = 0.2$ m when using Rouhani I. . . . .	74
3.6	Comparison of Rouhani I, Rouhani II and Rouhani III for $F_m = 250$ kg/s/m <sup>2</sup> , $T = 250$ °C and $d = 0.2$ m. . . . .	76
3.7	Multiplier that modifies $u_d$ for flow in deviated wells. . . . .	79
3.8	Slip model by Shi et al. (2005), using the method described in 3.2.2.4, run for varying mass fluxes using $T = 250$ °C and $d = 0.2$ m. . . . .	80
3.9	Vapour and drift velocities in a stagnant liquid ( $u_l = 0$ ) for $T = 250$ °C. This represents the minimum vapour velocity to prevent down-flow. . . . .	81
3.10	Comparison of constitutive models for friction for the case where $P = 5$ bara, $F_m = 500$ kg/s/m <sup>2</sup> , $d = 0.1$ m and $\epsilon = 1.0 \times 10^{-5}$ m. . . . .	85
3.11	A) Diagrammatic representation of a generic wellbore modified from Willhite (1967) and B) the simplified wellbore structure used in this work. . . . .	88



3.12	Comparison of Ramey (1962) and Chiu and Thakur (1991) A) transient time functions, and B) wellbore heat loss for $k_{res} = 2.4$ W/m, $k_{cem} = 1.4$ W/m, $T_{wb} = 300$ °C, $T_{res} = 200$ °C, $r_{wb} = 0.1$ m and $r_{cem} = 0.15$ m. . . .	90
3.13	Grant's relative permeability curves calculated using $S_{lr} = 0.5$ and $S_{sr} = 0.1$ . This is the default model used in this work. . . . .	94
4.1	Wellbore discretisation scheme showing the indexing convention. . . . .	99
4.2	The discrete momentum conservation equation is centred on the interface $i + 1/2$ between blocks $i$ and $i + 1$ . The effective momentum control volume is shown by the dashed lines. . . . .	101
4.3	Non-physical oscillations in the simulated vapour saturation caused by using central differencing when simulating Test Case 3. . . . .	103
4.4	The momentum flux differences in the momentum equation are upwinded depending on the direction of flow of each phase. . . . .	105
4.5	Variable switching for A) phase transitions from liquid to two-phase conditions and B) phase transitions from two-phase to vapour conditions. . .	119
4.6	Diagrammatic representation of production, injection and shut-in boundary conditions. . . . .	120
5.1	Comparison of numerical and analytical solutions for liquid flow for verification Case 1. Plot A) compares the numerical and analytical pressures and B) plots the normalised pressure residuals. . . . .	130
5.2	Comparison of numerical and analytical solutions for vapour flow for verification Case 1. Plot A) compares the numerical and analytical pressures and B) plots the normalised pressure residuals. . . . .	131
5.3	Comparison of numerical and analytical solutions for liquid flow for verification Case 2. Plot A) compares the numerical and analytical solutions for pressure vs. drilled depth and B) plots the normalised residuals for the drilled depth. . . . .	132
5.4	Comparison of numerical and analytical solutions for vapour flow for verification Case 2. Plot A) compares the numerical and analytical solutions for pressure vs. drilled depth and B) plots the normalised residuals for the drilled depth. . . . .	132
5.5	Comparison of numerical and analytical solutions for liquid flow for verification Case 3. Plot A) compares the numerical and analytical temperatures and B) plots the normalised temperature residuals. . . . .	134
5.6	Comparison of numerical and analytical solutions for liquid flow for verification Case 3. Plot A) compares the numerical and analytical temperatures and B) plots the normalised temperature residuals. . . . .	134
5.7	Comparison of simulated pressure and temperature profiles with measured data for well EM 6-1. . . . .	136
5.8	Comparison of simulated pressure and temperature profiles with measured data for well KJ-11. . . . .	137
5.9	Comparison of simulated pressure and temperature profiles with measured data for well KJ-22. . . . .	139
5.10	Comparison of simulated pressure and temperature profiles with measured data for well AZ-18. . . . .	140
5.11	Comparison of simulated pressure and temperature profiles with measured data for well H-1. . . . .	142
5.12	Comparison of simulated pressure and temperature profiles with measured data for well H-37. . . . .	143

5.13	A) The well track showing the deviation. B) The wellbore radius, with the cement radius shown in grey. Feed-zone locations are shown in red. . .	144
5.14	Comparison of simulated pressure and temperature profiles with measured data for Well-A. . . . .	145
5.15	The possible phase state and flow direction combinations for liquid and two-phase up-flow, showing A) pure liquid up-flow, B) up-flow from a liquid block into a two-phase block, C) two-phase up-flow into a liquid block and D) two-phase up-flow. . . . .	148
5.16	Initial conditions for Test Case 1 showing A) pressure and B) temperature. Plot C) shows the wellbore structure with the cement radius shown in grey.	150
5.17	Plots of A) pressure B) temperature C) total mass flow rate and D) vapour saturation for Test Case 1, which show the two-phase region slowly progressing down the well. . . . .	150
5.18	Initial conditions for A) pressure and B) temperature for Test Case 2. Plot C) shows the feed locations and the wellbore structure, in which the cement radius is shown in grey. . . . .	152
5.19	Plots of A) pressure B) temperature C) total mass flow rate and D) vapour saturation at various times, which show the rapid flashing process that occurs in Test Case 2. . . . .	153
5.20	Initial conditions for A) pressure and B) vapour saturation for Test Case 3. Plot C) shows the feed locations and the wellbore structure, in which cement radius is shown in grey. . . . .	154
5.21	Initial conditions for A) phase velocities and B) phase mass flow rates for Test Case 3. Plot C) shows the feed locations and the wellbore structure, in which the cement radius is shown in grey. . . . .	155
5.22	Plots of A) pressure, B) static vapour mass fraction and vapour saturation and C) the mass flow rates of each phase one hour after shut-in for Test Case 3. . . . .	155
5.23	Initial conditions for A) pressure and B) temperature for Test Case 4. Plot C) shows the feed locations and the wellbore structure, in which the cement radius is shown in grey. . . . .	157
5.24	Initial conditions for A) phase velocities and B) phase mass flows rates for Test Case 4. Plot C) shows the feed locations and the wellbore structure, in which the cement radius is shown in grey. . . . .	157
5.25	Simulated profiles for A) pressure, B) temperature, C) mass flow and D) vapour saturation during Test Case 4. . . . .	158
5.26	The possible phase state and flow direction combinations for vapour up-flow, showing A) pure vapour up-flow, B) up-flow from a vapour block into a two-phase block and C) two-phase up-flow into a vapour block. . .	160
5.27	A comparison of A) pressure and B) temperature within the well for the vapour inflow conditions and the two-phase inflow conditions for Test Case 5. . . . .	162
5.28	A comparison of A) vapour saturation and B) phase mass flow rates within the well for the vapour inflow conditions and the two-phase inflow conditions for Test Case 5. . . . .	162
5.29	A comparison of A) pressure and B) temperature within the well for the two-phase inflow conditions, vapour inflow condition and transitioning between the two states, for Test Case 6. . . . .	164

5.30	A comparison of A) vapour saturation and B) phase mass flow rates within the well for the two-phase inflow conditions, vapour inflow condition and transitioning between the two states, for Test Case 6. . . . .	165
5.31	A comparison of A) pressure and B) temperature within the well for the vapour inflow conditions and the two-phase inflow conditions for Test Case 7. . . . .	166
5.32	A comparison of A) vapour saturation and B) phase mass flow rates within the well for the vapour inflow conditions and the two-phase inflow conditions for Test Case 7. . . . .	166
5.33	A comparison of A) pressure and B) temperature within the well for the vapour inflow conditions and the two-phase inflow conditions for Test Case 8. . . . .	168
5.34	A comparison of A) vapour saturation and B) phase mass flow rates within the well for the vapour inflow conditions and the two-phase inflow conditions for Test Case 8. . . . .	169
5.35	The possible phase state and flow direction combinations for vapour up-flow, showing A) liquid down-flow B) two-phase down-flow into a liquid block, C) two-phase down-flow, D) liquid down-flow into a two-phase block, E) vapour down-flow, F) vapour down-flow into a two-phase block and G) two-phase down-flow into a vapour block. . . . .	170
5.36	Initial conditions for Test Case 9 showing A) pressure and B) temperature. The wellbore radius and feed location are shown in plot C). . . . .	172
5.37	Results showing A) pressure, B) temperature, C) total mass flow and D) vapour saturation for Test Case 9. . . . .	173
5.38	Initial conditions for Test Case 10 showing A) pressure and B) temperature. The wellbore radius and feed location are shown in plot C). . . . .	175
5.39	Results for Test Case 10 showing A) pressure, B) temperature, C) total mass flow rate and D) static mass fraction at various times. . . . .	176
5.40	The phase and flow direction combinations that are possible for counter-flow. Plot A) shows vapour up-flow from a two-phase block and liquid down-flow from a liquid block, B) shows up-flow and down-flow between two-phase blocks, and C) shows vapour up-flow from a vapour block and liquid down-flow from a two-phase block. . . . .	177
5.41	Initial conditions for A) pressure and B) temperature for Test Case 11. The wellbore structure and feed locations are shown in C). . . . .	179
5.42	Initial conditions for A) phase velocity and B) phase mass flow rate for Test Case 11. The wellbore structure and feed locations are shown in C). . . . .	179
5.43	Steady-state results showing A) pressure and B) temperature for Test Case 11. . . . .	180
5.44	Steady-state profiles of A) vapour saturation and B) phase mass flow rates for Test Case 11. . . . .	180
5.45	Steady-state profiles of A) vapour saturation and B) phase mass flow showing counter-flow occurring below the feed-zone for Test Case 11. . . . .	181
5.46	A comparison of A) liquid mass flow rate, B) vapour mass flow rate and C) vapour saturation for Test Case 11 using different formation temperature profiles. . . . .	182
5.47	Initial conditions for A) pressure and B) temperature for Test Case 12. . . . .	184
5.48	A) Pressure, B) static vapour mass fraction and saturation, and C) mass flow for Test Case 12 after after 30 days of heating up. . . . .	184

6.1	Comparisons of the total number of A) time steps, B) linear solves and C) EOS errors for Test Cases 1 – 4 for the velocity, volume flux and mixed formulations. Plot D) compares the time stepping for Test Case 1. . . . .	194
6.2	Comparisons of the total number of A) time steps, B) linear solves and C) EOS errors for Test Cases 5 – 8 for the velocity, volume flux and mixed formulations. Plot D) compares the time stepping for Test Case 7. . . . .	195
6.3	Comparisons of vapour saturation profiles for simulations using the average interface saturation and the upstream vapour saturation to calculate the drift velocity. Plot A) shows the entire well, while B) shows the subsection of the well where the erroneous saturation value occurs. The feed interval is highlighted in red. . . . .	201
6.4	A) A diagrammatic representation of the flow scenario occurring for Test Case 11. B) The drift velocity calculated using the saturation from blocks $i$ and $i + 1$ and the average saturation at $i + 1/2$ . . . . .	201
6.5	A) A diagrammatic representation of the flow scenario occurring for Test Case 12. B) The drift velocity calculated using the saturation from blocks $M - 1$ and $M$ and the average saturation at $M - 1/2$ . . . . .	204
6.6	A) an illustration of the upstream-weighting bias. Here the dashed arrow indicates the assumed flow direction of a non present phase. B) Non-physical vapour saturation profile that results from the upstream weighting bias. . . . .	209
7.1	Variable switching for A) phase transitions from liquid to two-phase conditions and B) phase transitions from two-phase to vapour conditions for the air-water EOS. . . . .	222
7.2	Diagrammatic representation of the atmospheric boundary conditions discussed in Sections 7.2.3.1 and 7.2.3.2. . . . .	223
7.3	Comparison of simulation results with the semi-analytical solution defined by Pan, Webb and Oldenburg (2011). . . . .	228
7.4	Comparison of the steady-state vapour saturation for Test Case 3 with no air and 0.1% air. . . . .	229
8.1	Wellbore conditions for Test Case 12 for A) pressure, B) temperature and C) vapour saturation after 2 days of injection and after 30 days of being shut-in. . . . .	233
8.2	Plots of the liquid, vapour, and total mass flow A) 21 hours, B) 28 hours, C) 3 days and 22 hours and D) 30 days after shut-in for Test Case 12. These plots show that counter-flow occurs within the well as it heats up. The corresponding wellbore saturation is shown diagrammatically to the right of each mass flow plot. . . . .	234
8.3	Plots of A) pressure, B) wellbore and formation temperature, and C) vapour and air mass fractions vs. elevation for the wellbore described in Section 8.1.2 after 30 days of heat-up. . . . .	237
8.4	Plots of A) total mass flow rate within the well, showing inter-zonal flow. B) Mass flow rates for the liquid and vapour phases between 0 and -600 mRL, showing counter-flow exists in the wellbore described in Section 8.1.2 after 30 days of heat-up. . . . .	237
8.5	Profiles of A) pressure, B) temperature, C) total mass flow and D) vapour saturation as the well described in Section 8.1.2 is opened to flow. . . . .	239
8.6	Wellbore profiles of A) pressure B) temperature C) total mass flow and D) vapour saturation at different times after 60 days of production. . . . .	241

8.7	Wellbore profiles of A) liquid mass flow and B) vapour mass flow at different times after 60 days of production. . . . .	242
8.8	Initial conditions for A) pressure, B) temperature and C) vapour saturation and air mass fraction for a well with a water level below the wellhead.	246
8.9	Conditions after 30 minutes of air-lifting at 0.01 kg/s for A) pressure, B) liquid and vapour mass flow rates and C) vapour saturation, $S_v$ , static vapour mass fraction, $x_{sv}$ , and static air mass fraction, $x_s^a$ for the well described in Section 8.2.1. . . . .	248
8.10	Results of successful air-lifting with an air mass flow rate of 0.05 kg/s showing A) pressure, B) temperature, C) total mass flow and D) vapour saturation at various times for the well described in Section 8.2.1. . . . .	249
8.11	A) pressure, B) temperature and C) vapour saturation and mass fraction profiles before and after air compression (0.05 kg/s injected for five hours) for the well described in Section 8.2.1. . . . .	251
8.12	Results of discharge stimulation with a compressed pressure of 27 bara showing A) pressure, B) temperature, C) total mass flow and D) vapour saturation at various times after opening the well described in Section 8.2.1.	251
C.1	Flow scenario showing water vapour flowing down into a two-phase block.	291
C.2	Initial conditions for Test Case 13 showing A) pressure and B) temperature. The wellbore radius and feed location are shown in plot C). . . . .	292
C.3	Plots of A) pressure B) temperature C) total mass flow rate and D) static vapour mass fraction at various times for Test Case 13. . . . .	293
C.4	Flow scenario showing liquid water flowing down into a two-phase block. .	294
C.5	Initial conditions for Test Case 14 showing A) pressure and B) temperature. The wellbore radius and feed location are shown in plot C). . . . .	295
C.6	Plots of A) pressure B) temperature C) total mass flow rate and D) static vapour mass fraction at various times for Test Case 14. . . . .	295
C.7	Flow scenario showing liquid down-flow from a two-phase block into a liquid block. . . . .	297
C.8	Initial conditions for A) pressure and B) vapour saturation for Test Case 15. Plot C) shows the feed locations and the wellbore structure. . . . .	298
C.9	Initial conditions for A) phase velocities and B) phase mass flow rates for Test Case 15. Plot C) shows the feed locations and the wellbore structure.	298
C.10	Plots of A) pressure B) temperature C) total mass flow rate and D) vapour saturation at various times for Test Case 15. . . . .	300

# List of Tables

2.1	Feed properties for Test Case 6 presented in Figures 2.2 and 2.3. . . . .	47
3.1	Orkiszewski (1967) regime boundaries and GWELL’s drift velocity equations as described by McGuinness (2015). . . . .	71
3.2	Values of $B_s$ for a smooth pipe given by Chisholm (1973). . . . .	85
3.3	Reservoir representation in past transient geothermal wellbore simulators. . . . .	92
4.1	Primary variable switching for two-phase flow of pure water. . . . .	112
4.2	Persistent primary variables for two-phase flow of pure water. . . . .	113
4.3	Possible values of flowing vapour mass fraction, $x_{fv}$ , for flow scenarios that are possible during two-phase flow. . . . .	115
4.4	Combinations of primary variables tested in this work. . . . .	116
4.5	Primary variable values to determine the current phase-state of the fluid. . . . .	116
4.6	Pressure, temperature and saturation conditions during phase transitions. Transitions from single-phase to two-phase conditions are identified using the pressure. Transitions from two-phase to single-phase conditions are identified using the vapour saturation. . . . .	118
5.1	KJ-11 Feed parameters estimated by Bjornsson (1987). . . . .	137
5.2	Simulation parameters for well KJ-22. . . . .	139
5.3	Feed-zone parameters and locations for KJ-22. . . . .	139
5.4	Simulation parameters for well AZ-18. . . . .	140
5.5	Simulation parameters for well H-1. . . . .	141
5.6	Simulation parameters for well H-37. . . . .	142
5.7	Estimated feed-zone properties and locations for WELL-A. . . . .	144
5.8	Summary of MRSS and MNRSS values for the validation problems. . . . .	145
5.9	Summary of the transient processes that are modelled in test cases discussed in Section 5.3. . . . .	147
5.10	Reservoir and wellbore parameters required for analytical heat flux calculations. . . . .	147
5.11	Simulation and wellbore parameters for Test Case 1. . . . .	149
5.12	Feed-zone properties and locations for Test Case 1. . . . .	151
5.13	Simulation and wellbore parameters for Test Case 2. . . . .	152
5.14	Feed-zone properties and locations for Test Case 2. . . . .	152
5.15	Simulation and wellbore parameters for Test Case 4. . . . .	156
5.16	Feed-zone properties and locations for Test Case 4. . . . .	157
5.17	Simulation and wellbore parameters for Test Case 5. . . . .	161
5.18	Feed-zone properties and locations for Test Case 5. . . . .	161
5.19	Simulation and wellbore parameters for Test Case 6. . . . .	163
5.20	Feed-zone properties and locations for Test Case 6. . . . .	163
5.21	Simulation and wellbore parameters for Test Case 7. . . . .	165

5.22	Feed-zone properties and locations for Test Case 7. . . . .	166
5.23	Simulation and wellbore parameters for Test Case 8. . . . .	168
5.24	Feed-zone properties and locations for Test Case 8. . . . .	168
5.25	Simulation and wellbore parameters for Test Case 9. . . . .	171
5.26	Mass flow and flowing enthalpy boundary conditions prescribed at the wellhead for Test Case 9. . . . .	171
5.27	Feed-zone properties and locations for Test Case 9. . . . .	171
5.28	Feed-zone properties and locations for Test Case 10. . . . .	174
5.29	Simulation and wellbore parameters for Test Case 10. . . . .	174
5.30	Mass flow and flowing enthalpy boundary conditions prescribed at the wellhead for Test Case 10. . . . .	174
5.31	Simulation and wellbore parameters for Test Case 11. . . . .	178
5.32	Feed properties and locations for Test Case 11. The deep feed-zone is slowly "turned off" over a period of 87.5 days. . . . .	178
5.33	Simulation and wellbore parameters for Test Case 12. . . . .	183
5.34	Feed-zone properties and locations for Test Case 12. . . . .	183
6.1	Combinations of primary variables tested in this work. . . . .	188
6.2	Results of Test Cases 1 – 4 for the velocity, volume flux and mixed formu- lations. . . . .	194
6.3	Results of Test Cases 5 – 8 for the velocity, volume flux and mixed formu- lations. The * indicates that the simulation was stopped prior to completion. . . . .	194
7.1	Primary variable values used to determine the current phase-state of the fluid. . . . .	216
7.2	Coefficients for calculating the enthalpy of air (Irvine and Liley, 1984). . . . .	219
7.3	Pressure, temperature and saturation primary variables during phase tran- sitions. . . . .	220
7.4	Parameters and location of the atmospheric feed. . . . .	225
7.5	Simulation and wellbore parameters for air-water verification simulation. . . . .	228
8.1	Wellbore and simulation parameters for the case described in Section 8.1.2, which simulates opening a realistic well to flow. . . . .	236
8.2	Feed-zone properties for the case described in Section 8.1.2, which simu- lates opening a realistic well to flow. . . . .	236
8.3	Reservoir and atmospheric feed for the discharge stimulation simulations in Sections 8.2.2 and 8.2.3. . . . .	245
8.4	Wellbore and simulation parameters for the discharge stimulation simula- tions in Sections 8.2.2 and 8.2.3. . . . .	245
C.1	Simulation and wellbore parameters for Test Case 13. . . . .	291
C.2	Feed-zone properties and locations for Test Case 13. . . . .	291
C.3	Mass flow and flowing enthalpy boundary conditions prescribed at the wellhead for Test Case 14. . . . .	294
C.4	Simulation and wellbore parameters for Test Case 14. . . . .	296
C.5	Feed-zone properties and locations for Test Case 14. . . . .	296
C.6	Simulation and wellbore parameters for Test Case 15. . . . .	297
C.7	Feed-zone properties and locations for Test Case 15. . . . .	297
D.1	Constants used in the calculation of the viscosity of a mixture of air and water vapour. . . . .	303

# Symbols

symbol	name	unit
$A$	wellbore cross-sectional area	$\text{m}^2$
$A_\beta$	cross-sectional area of phase $\beta$	$\text{m}^2$
$A_{int}$	interface area per unit volume	$1/\text{m}$
$C$	circumference	$\text{m}$
$C_A$	hold up coefficient	-
$C_0$	drift-flux shape parameter	-
$c_p$	specific heat capacity	$\text{J/kg/K}$
$c_{res}$	specific heat capacity of the formation	$\text{J/kg/K}$
$d$	wellbore diameter	$\text{m}$
$E$	energy per unit volume	$\text{J/m}^3$
$E_\beta$	phase energy per unit volume	$\text{J/m}^3$
$e$	specific internal energy	$\text{J/kg}$
$e_\beta$	specific internal energy of phase $\beta$	$\text{J/kg}$
$e_{T\beta}$	total specific internal energy of phase $\beta$	$\text{J/kg}$
$F_m$	total mass flux	$\text{kg/m}^2/\text{s}$
$F_{m\beta}$	mass flux of phase $\beta$	$\text{kg/m}^2/\text{s}$
$F_V$	total volume flux	$\text{m/s}$
$F_{V\beta}$	volume flux of phase $\beta$	$\text{m/s}$
$f$	friction factor	-
$f_{tp}$	two-phase friction factor	-
$g$	gravitational acceleration	$\text{m/s}^2$
$H$	enthalpy per unit volume	$\text{J/m}^3$
$h$	specific enthalpy	$\text{J/kg}$
$h_{sol}^a$	heat of solution	$\text{J/kg}$



$h_\beta$	specific enthalpy of phase $\beta$	J/kg
$h_{mix}$	static specific mixture enthalpy	J/kg
$h_{fmix}$	flowing specific mixture enthalpy	J/kg
$h_{T\beta}$	total specific enthalpy of phase $\beta$	J/kg
<b>J</b>	Jacobian matrix	-
$K_u$	Kutateladze number	-
$k$	permeability	m <sup>2</sup>
$k_h$	Henry's constant	Pa
$k_{res}$	thermal conductivity of the formation	W/m/K
$k_{r\beta}$	relative permeability of phase $\beta$	-
$L_B$	bubble-slug regime boundary	-
$L_s$	slug-transitional regime boundary	-
$L_m$	transitional-mist regime boundary	-
$M$	mass	kg
$M_\beta$	mass of phase $\beta$	kg
$M^\kappa$	mass of component $\kappa$	kg
$M_\beta^\kappa$	mass of component $\kappa$ in phase $\beta$	kg
$MW^\kappa$	molecular weight of component $\kappa$	g/mol
$m_\beta^\kappa$	mole fraction of component $\kappa$ in phase $\beta$	-
$N_b$	Bond number	-
$P$	pressure	Pa
$P^\kappa$	partial pressure of component $\kappa$	Pa
$P_\beta$	pressure of phase $\beta$	Pa
PI	productivity index	m <sup>3</sup>
$Q_m$	total mass flow rate	kg/s
$Q_{m\beta}$	mass flow rate of phase $\beta$	kg/s
$Q_V$	total volume flow rate	m <sup>3</sup> /s
$Q_{V\beta}$	volume flow rate of phase $\beta$	m <sup>3</sup> /s
$Q_{heat}$	formation heat flow rate	W
$q_{ener}$	energy source term	W/m <sup>3</sup>
$\hat{q}_{ener}$	total energy source term	W/m <sup>3</sup>
$q_{heat}$	formation heat flow rate per unit volume	W/m <sup>3</sup>
$q_{mass}$	mass source term	kg/s/m <sup>3</sup>

$q_{mass}^{\kappa}$	mass source term for component $\kappa$	kg/s/m <sup>3</sup>
$q_{mom}$	momentum source term	kg/s <sup>2</sup> /m <sup>2</sup>
$\mathbf{R}$	vector of residuals	-
$Re$	Reynolds number	-
$r$	wellbore radius	m
$S$	velocity ratio (slip ratio)	-
$S_{\beta}$	saturation of phase $\beta$	-
$s$	distance along wellbore	m
$T$	temperature	°C
$T_{\beta}$	temperature of phase $\beta$	°C
$T_f$	formation temperature	°C
$U$	overall heat transfer coefficient	W/m <sup>2</sup> /K
$U_{\beta}$	upstream weighting parameter for phase $\beta$	-
$u_{\beta}$	velocity of phase $\beta$	m/s
$u_c$	characteristic velocity	m/s
$u_d$	drift velocity	m/s
$u_{mix}$	mixture velocity	m/s
$u_r$	relative velocity	m/s
$u_{svf}$	vapour superficial flooding velocity	m/s
$u_{vD}$	dimensionless vapour velocity	-
$u_{uni}$	uniform velocity	m/s
$V$	volume	m <sup>3</sup>
$V_{\beta}$	volume of phase $\beta$	m <sup>3</sup>
$X_{tol}$	tolerance used in upwinding procedure	-
$\mathbf{x}$	vector of primary variables	-
$x_{s\beta}$	static mass fraction of phase $\beta$	-
$x_{f\beta}$	flowing mass fraction of phase $\beta$	-
$x_{\beta}^{\kappa}$	static mass fraction of component $\kappa$ in phase $\beta$	-
$x_f^{\kappa}$	flowing mass fraction of component $\kappa$	-
$x_s^{\kappa}$	static mass fraction of component $\kappa$	-
$z$	elevation	mRL

Greek letters	name	unit
$\alpha$	productivity parameter	kg/s/Pa
$\alpha_t$	thermal diffusivity of the formation	m <sup>2</sup> /s
$\beta$	volumetric gas flow ratio	-
$\Gamma$	interface mass source term	kg/m <sup>2</sup> /s
$\Gamma^2$	Chisholm physical property parameter	-
$\gamma$	momentum flux slip term	kg/m/s <sup>2</sup>
$\epsilon$	absolute roughness	m
$\theta$	angle of well from vertical	°
$\lambda$	velocity relaxation coefficient	kg/m <sup>3</sup> /s
$\mu$	pressure relaxation coefficient	s m/kg
$\mu_\beta$	dynamic viscosity of phase $\beta$	Pa s
$\rho_\beta$	density of phase $\beta$	kg/m <sup>3</sup>
$\rho_\beta^\kappa$	density of component $\kappa$ in phase $\beta$	kg/m <sup>3</sup>
$\rho_{mix}$	mixture density	kg/m <sup>3</sup>
$\rho_{mix}^*$	profile adjusted mixture density	kg/m <sup>3</sup>
$\sigma_{vl}$	vapour/liquid interface tension	kg/s <sup>2</sup>
$\tau$	wellbore friction term	kg/m/s <sup>2</sup>
$\tau_{LO}$	liquid only friction term	kg/m/s <sup>2</sup>
$\Phi^2$	two-phase multiplier	-



# Chapter 1

## Introduction

Geothermal energy is the thermal energy contained in the Earth's crust, mantle and core that originates from the formation of the planet and the decay of radiogenic isotopes, in particular uranium, thorium and potassium (Gando et al., 2011). Some areas, mainly at plate boundaries, have unusually high temperatures near the Earth's surface, resulting in features such as fumaroles, hot springs and geysers. Geothermal resources such as these have been used for cultural purposes and mineral extraction for more than 2000 years (Grant and Bixley, 2011). However, it was not until the early 1900s that power generation from deeper geothermal resources began at Larderello, Italy.

Conventional geothermal resources are exploited by drilling wells, which are usually kilometres deep, to access the high-temperature fluid contained within a reservoir. The flow of hot geothermal fluid up the well transports heat to the surface, where steam, or in some cases a secondary fluid, can be used to generate electricity by driving turbines in much the same way as in traditional thermal power stations. This method of utilising geothermal resources relies on high permeability in the reservoir, typically in the form of fractured rock or geological structures such as faults. Directional drilling allows geothermal wells to deviate from vertical to target specific geological structures with high-temperature and permeability (Zarrouk and McLean, 2019). High permeability in the reservoir allows hot geothermal fluid to flow towards the well at a rate high enough for commercial electricity production. This flow is caused by the difference in pressure between the aquifer and the well.

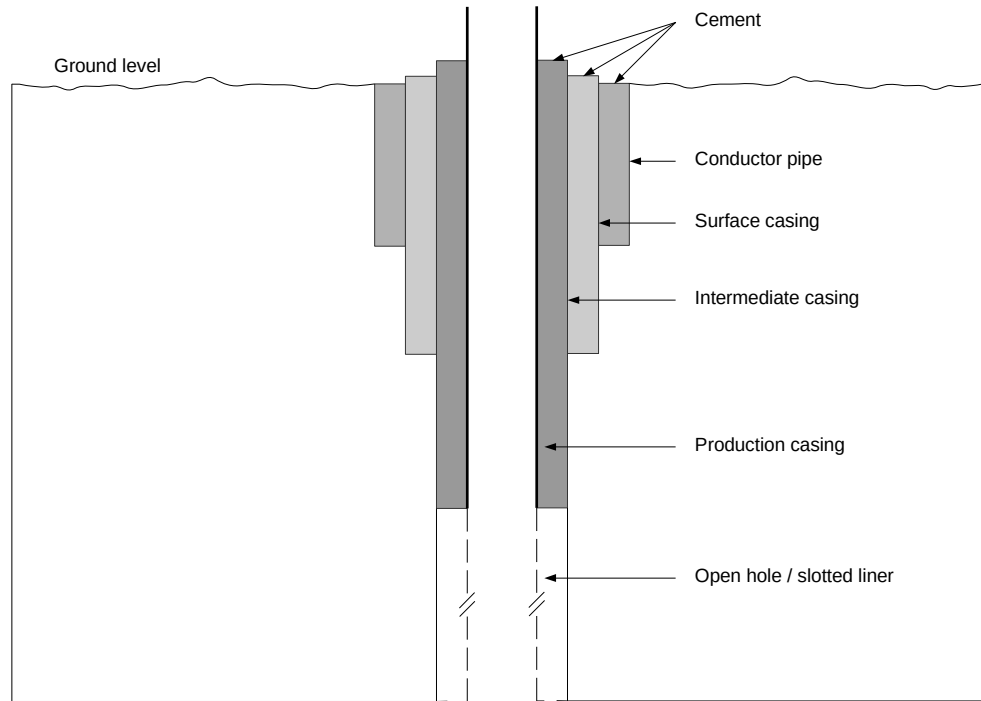


FIGURE 1.1: An illustration of the structure of a geothermal wellbore.

Geothermal wells are also used to re-inject the separated liquid water back into the reservoir. Re-injection was initially carried out as a safe and environmentally friendly way of disposing of geothermal waste water (Axelsson, 2012). The additional recharge caused by re-injection has the added benefit of maintaining reservoir pressure, which helps prevent production decline and maintain surface expressions of cultural significance.

An illustration of a typical geothermal wellbore is shown in Figure 1.1. The top section of a well is characterised by concentric casings that provide structural stability during drilling and general operations, anchorage and support for the wellhead, prevent unintended flow between shallow aquifers and the deep reservoir, and protect the well against corrosion, fracturing and general breakdown (Hole, 2008).

Geothermal fluid flows through the innermost casing, called the production casing. The diameter of the production casing can range from 7 inches (17.78 cm) in small wells to 13  $\frac{3}{8}$  inches (33.97 cm) in large diameter wells (Zarrouk and McLean, 2019). Below this, a slotted liner is typically installed to provide stability while still allowing fluid to enter the well from the reservoir. The internal diameter of a slotted liner can range from 4  $\frac{1}{2}$  inches (11.4 cm) to 9  $\frac{5}{8}$  inches (24.45 cm). In shallow, low-temperature wells, the production section is sometimes left "open", i.e., without a slotted liner.

The final design of a well (e.g., casing design, diameter, depth and direction) is influenced by the wellbore requirements (e.g., desired mass flow and budgetary constraints), reservoir conditions (e.g., enthalpy, permeability and geological features) and surface requirements (e.g., the proximity to surface facilities, topography and consent requirements).

Geothermal wells play a key role in the development, understanding and utilisation of geothermal resources (Grant and Bixley, 2011; Zarrouk and McLean, 2019). It is, therefore, important to have a good understanding of the fluid dynamics and thermodynamic processes that occur within geothermal wells. However, it is often not possible to directly measure important parameters as the harsh operating conditions in geothermal wellbores prevent measuring equipment from being installed. Therefore, numerical simulation is a useful option for providing insight into the complex processes that occur within geothermal wells. It offers a low-cost method for understanding wellbore behaviour to aid decision making. This thesis discusses the development of a new transient geothermal wellbore simulator that is capable of modelling the many complex processes that occur within geothermal wells.

## 1.1 Modelling geothermal wellbores

As explained above, in conventional geothermal systems, wells are conduits for flow between the reservoir and surface facilities. For high-temperature systems, flow in geothermal wells is typically two-phase, i.e., it is a mixture of liquid water and vapour. Two-phase flow is a special case of multi-phase flow, which refers to situations in which any combination of several phases (liquids, gases and solids) or immiscible fluids are flowing simultaneously (Yadigaroglu and Hewitt, 2018). Multi-phase flow is complex due to the interaction of the phases as they flow and is characterised by rapid changes in thermodynamic properties. The interaction of the phases differs significantly depending on the saturation and flow rate of the two-phase fluid. Typically, this behaviour has been modelled by broadly categorising similar types of flow using flow regimes that describe the topological structure assumed by the phases (Chisholm, 1983; Ishii and Hibiki, 2011; Yadigaroglu and Hewitt, 2018). In many cases, the phases are not homogeneously

mixed and can flow at different rates (a phenomenon called phase slip). Phase slip affects the transport of mass, momentum and energy and can result in scenarios such as counter-flow, where the phases flow in opposite directions.

Multi-phase flow in geothermal wells is complicated further by multiple factors. Firstly, the physical structure of the well presents modelling challenges. As discussed above, geothermal wells are typically kilometres long, deviated and have a wide diameter. This means the conditions within a geothermal well fall outside the conditions normally investigated in the wider multi-phase flow literature on topics such as nuclear engineering and refrigeration (Vijayan et al., 2000; Godbole et al., 2011).

Secondly, geothermal fluid is not pure water. Instead, it is a mixture of water, dissolved salts (e.g., sodium chloride, calcium carbonate and silica) and non-condensable gases (e.g.,  $\text{H}_2\text{S}$ ,  $\text{CO}_2$  and air). These additional components affect the thermodynamic properties of the geothermal fluid. Additionally, dissolved salts may deposit within the well, changing the physical structure of the well with time.

Finally, the behaviour of a geothermal wellbore, at times, can depend strongly on the behaviour of the reservoir, a system that is very complex in its own right. The pressure, temperature, saturation and permeability of an aquifer are often not known. These parameters have a significant effect on the properties of the fluid flowing into the well. Additionally, in many cases, a reservoir will have multiple permeable aquifers at varying depths. In this case, a well may have more than one feed-zone. We call this a multi-feed well. In some multi-feed wells, there are considerable differences between the conditions in each feed. This results in rapid changes in the properties of the fluid and the flow dynamics within the well. Additionally, the presence of multiple feeds can cause complex transient processes such as well cycling and inter-zonal flow.

Geothermal wellbore simulators are useful for gaining insight into some of the complexities discussed above. These simulators use numerical methods to solve the equations governing the conservation of mass, momentum and energy, which describe how a multi-phase fluid flows within a pipe. Additional relationships are required to model processes such as phase slip (the relative motion of the phases), wall friction, formation heat transfer, and sources of fluid from the reservoir. These are called constitutive models.



In the literature, there are two types of simulators, namely, steady-state and transient simulators. Steady-state simulators, which make up the majority of the literature, assume that wellbore flow does not change with time. These investigations are reviewed in Section 1.2 below. Transient simulators are able to model how the conditions within a well change with time. By comparison, relatively few transient geothermal wellbore simulators have been developed. In fact, we found only four simulators that were capable of modelling general transient flow in geothermal wells. These simulators, and the other less general investigations, are summarised in Section 1.3.

Our review found that the literature on geothermal wellbore modelling lacked clarity. Specifically, past investigations (both transient and steady-state) used many different mathematical formulations of the conservation of mass, momentum and energy equations. It was difficult to differentiate between formulations that correctly conserve these quantities and formulations that do not. Therefore, we completed an in-depth review of the governing equations for two-phase flow in geothermal wells, which is presented in Chapter 2.

## 1.2 Steady-state wellbore modelling

Steady-state investigations make up the vast majority of the geothermal wellbore modelling literature. These investigations assume wellbore conditions do not change with time and are, therefore, not central to the discussion of transient wellbore modelling. Therefore, an exhaustive review of all of them is beyond the requirements of this thesis. Instead, we first outline some of the typical applications of steady-state geothermal wellbore simulators. We then present a timeline summarising the key models and important advances in steady-state geothermal wellbore modelling.

Steady-state simulators have been used to gain a better understanding of the behaviour of wells over a wide range of operating conditions. Topics of interest include the response of a well to changes in wellhead pressure, the maximum possible flow rate and the fraction of steam produced at the wellhead (Bodvarsson and Benson, 1984; Marquez et al., 2015). Also, steady-state simulators have often been used to develop productivity curves (also called deliverability or output curves) showing plots of mass flow rate against

wellhead pressure, for example, see Gould (1974), Nathenson (1974), Sanyal et al. (1979), Bjornsson (1987), Hadgu (1989) and Alvarez and Cinco (2011). Most recently, Battistelli et al. (2020) simulated output curves for super-critical flow in the IDDP-1 well in Krafla, Iceland.

Steady-state wellbore simulators have also been used to assess how changes in wellbore design, such as pipe diameter (Freeston and Gunn, 1993; King et al., 1995) or changes in reservoir conditions (Itoi et al., 1988; Battistelli et al., 1992) affect the productivity of a well.

Early investigations suggested that the presence of multiple feeds has a significant impact on production from geothermal wells (Bjornsson and Bodvarsson, 1987; Freeston and Hadgu, 1987). Many steady-state simulators are capable of modelling multiple feeds, with mass inflow at each feed set at a fixed value or calculated using a productivity relationship. Simulators with multi-feed capability have also been used for designing remedial work, for example, by investigating the impact of plugging a cold feed (Molina et al., 1998; Hastriansyah et al., 2015; Gunawan et al., 2015).

Early investigations by Barelli et al. (1982) indicated that dissolved salts and non-condensable gases can impact geothermal wellbore flow and several simulators, for example, Gunn (1992), McGuinness (2015), Franz (2015) and Battistelli et al. (2020), account for these components. The impact of scaling caused by chemicals such as calcite has been assessed by simulation (Goyal et al., 1980; Chierici et al., 1981; Parlaktuna, 1985; Takahashi, 1988; Battistelli et al., 1990; Satman et al., 1999; Zolfagharroshan and Khomehchi, 2020; Khasani et al., 2021).

### 1.2.1 The early days

An early numerical model capable of simulating two-phase flow with slip between the phases was presented by Gould (1974). This study investigated the ability of common oil and gas slip models to match geothermal well data from the Wairakei and Broadlands (now called Ohaaki) geothermal fields. Elliot (1975) and Dittman (1977) developed very similar models to Gould (1974) but used different equations of state for brine and allowed for a variable casing diameter.

### 1.2.2 The 1980s and 1990s

The early 1980s saw improvements in modelling with the inclusion of additional components. Bilicki et al. (1981) modelled the presence of salts and Barelli et al. (1982) presented the first model to account for the presence of both dissolved salts and non-condensable gasses.

Bjornsson (1987) developed a simulator (HOLA) that was able to model flow in wellbores with multiple feed-zones. The momentum conservation equation used in HOLA did not account correctly for the effects of variable diameter on momentum transport (McGuinness, 2015). Despite this error, HOLA was able to match downhole profiles very well (Bjornsson and Bodvarsson, 1987) and quickly became an industry-standard simulator that provided a basis for further development. Aunzo et al. (1991) extended HOLA to account for non-condensable gases (NCGs) and dissolved salts. These extended simulators were named GWELL and GWNACL, respectively. More recently, Kato et al. (2015) adapted GWELL's slip correlations to investigate highly deviated wells, and Bhat et al. (2005) and Ayala (2010) coupled GWELL to the TOUGH2 reservoir simulator.

Hadgu (1989) developed three wellbore simulators: WFSA for multi-feed wells with dissolved salts, WFSB for single feed wells with high NCG content and STMFLW to handle wells in vapour-dominated fields (see also Hadgu and Freeston (1990)). Gunn (1992) combined all three into the single commercial simulator, WELLSIM. WELLSIM has become an industry-standard simulator and is being continually updated. It now offers a variety of slip correlations and well design options. As was the case with GWELL, WELLSIM did not account correctly for changes in wellbore area on momentum transport and approximated the kinetic energy term, which is discussed further in Section 2.3. Despite these issues, WELLSIM produces good matches to field data and is used extensively in the geothermal industry (for example, see King et al. (1995), Molina et al. (1998), Armenta et al. (2015), Hastriansyah et al. (2015) and Gunawan et al. (2015)) and has been used for coupled reservoir-wellbore simulations (Murray and Gunn, 1993).

### 1.2.3 2000 onwards

In 2012, Gudmundsdottir developed a simulator called FLOWELL. FLOWELL was coupled with TOUGH2 and integrated within the iTOUGH inverse modelling package (Finsterle, 2011; Gudmundsdottir et al., 2013a; Gudmundsdottir and Jonsson, 2015).

In 2015, McGuinness made extensive modifications to GWELL to develop SIMGWELL for EDC (Energy Development Corporation), which was reported on by Marquez et al. (2015). McGuinness ensured that the momentum conservation equation accounted correctly for changes in the area of the well. Additional slip correlations were included, and discontinuities in regime dependent slip models, such as those given by Orkiszewski (1967) and Hadgu (1989) (used in WELLSIM), were smoothed to improve the numerical performance of the simulator. SIMGWELL was further modified by McGuinness (2015) to produce SWELFLO, which is still under active development.

Franz (2015) developed a new simulator named Paiwera as an in-house tool for Mighty River Power in New Zealand (now Mercury Energy). This work noted that, in some cases, existing wellbore simulators could suffer from poor or failed convergence. This behaviour presents difficulties when trying to model coupled wellbore-reservoir systems. The work of Franz (2015) focused on developing a more robust wellbore simulator that could, in some cases, determine why a wellbore simulation failed and suggest methods for managing the problem appropriately. A similar model (with additional functionality) has been included in the Volsung reservoir modelling package (Franz and Clearwater, 2021).

More recently, Battistelli et al. (2020) simulated output curves for the super-critical IDDP-1 well in the Krafla geothermal field, Iceland. The steady-state simulator used, named PROFILI, extends the work of Barelli et al. (1982) that is discussed above in Section 1.2.1. It appears to be the only steady-state simulator capable of modelling super-critical flow in geothermal wells.

Our literature review for steady-state geothermal wellbore modelling indicated that the correct form of the conservation equations to use in steady-state simulations was not clear. Therefore, we have included the literature on steady-state modelling in our review of the governing conservation equations in Chapter 2.

### 1.3 Transient wellbore modelling

An overview of the few transient wellbore simulators presented in the geothermal literature is given below. The conservation equations used in these investigations are discussed in detail in Section 2.

Miller (1979) developed the first numerical simulator capable of modelling transient two-phase flow in a geothermal wellbore. It assumed homogeneous conditions, i.e. the velocities of the two phases, liquid and vapour, were equal. Miller (1980*b*) extended this model to account for phase slip (the tendency for the liquid and vapour to flow at different velocities), naming it WELLBORE. WELLBORE was used to investigate the effect of wellbore storage on transient well tests by coupling it to a simple reservoir model (Miller, 1980*a*; Miller et al., 1982).

More recently, Khasani et al. (2017) used WELLBORE to investigate how different methods of opening and closing the wellhead affect the time taken to reach the stable conditions that are required for measurements taken during production testing. For a generic well, they found that reducing the flow rate at the wellhead (i.e., partially closing the well) resulted in faster stabilisation times than increasing the flow rate (opening the well). They also found that step changes in the wellhead mass flow rate resulted in a longer pressure transient within the wellbore than that obtained with slower wellhead operations.

Lu et al. (2006) developed a simplified transient model to study geysering effects in a gassy, low-temperature geothermal well. They were able to reproduce measurements taken from a geysering well at Te Aroha, New Zealand. In this case, the geysering was caused by the exsolution of CO<sub>2</sub> gas from the liquid as it flows up the well. However, their assumptions of isothermal conditions and the use of a steady-state momentum conservation equation make this model unsuitable for general transient geothermal wellbore studies.

García-Valladares et al. (2006) presented a transient geothermal wellbore simulator named GEOWELLS. Their work presented comparisons between simulation results and steady-state pressure and temperature data from wells in the Los Humeros and Los Azufres

fields in Mexico. They investigated how uncertainty in boundary conditions (pressure, temperature and enthalpy) and the constitutive model for slip can affect the results of wellbore simulation. They found simulation results were very sensitive to uncertainty in the slip model and suggested more accurate correlations should be developed specifically for geothermal applications.

Later on, GEOWELLS was used in conjunction with machine learning techniques to develop and test a new correlation for phase slip (Alvarez Del Castillo et al., 2012). This new slip correlation was shown to outperform existing models by Duns and Ros (1963) and Dix (1971). However, the complete set of equations by Duns and Ros (1963) were not used. Although GEOWELLS is a transient simulator, there have been no publications demonstrating its transient capabilities.

Pan, Oldenburg, Wu and Pruess (2011) developed T2WELL, which is the only commercially available transient geothermal wellbore simulator. T2WELL extends the TOUGH2 reservoir simulator by including a wellbore subdomain within the existing reservoir grid (Pan and Oldenburg, 2012, 2014). It is designed for coupled wellbore-reservoir simulations but can also be used as a stand-alone wellbore simulator (Vasini et al., 2018). Initial investigations with T2WELL studied the sequestration of CO<sub>2</sub> in a depleted (low-pressure) gas reservoir using the ECO2N equation of state (Pan, Oldenburg, Pruess and Wu, 2011). Later studies investigated the use of CO<sub>2</sub> as an alternative working fluid for the extraction of geothermal energy using the ECO2H equation of state (Pan et al., 2015).

Vasini et al. (2018) used T2WELL, together with the EWASG equation of state, to model the transient production testing of high enthalpy wells that discharge a mixture of H<sub>2</sub>O-CO<sub>2</sub>-NaCl. Production data were matched to transient coupled reservoir-wellbore simulations for a well with two feed-zones. The authors showed that transient coupled simulations could be used to improve the interpretation of measurements taken during production testing but suggested that inverse modelling would be required to improve the match of the model results to the data.

T2WELL has also been used with EOS1 (Pruess et al., 2012) to model the flow of pure water. Rutqvist et al. (2018) coupled T2WELL-EOS1 with the FLAC3D geomechanical

simulator to model the mechanical stresses that occur in a well as it starts to flow. They found that the rapid increase in temperature that occurs during start-up can cause cement failure in shallow regions of the well. Rutqvist et al. (2020) continued this work, studying the mechanical stresses caused by variable production from geothermal wells. They found ramping production up slowly and never fully shutting the well reduces the mechanical stress experienced by the wellbore. More recently, Doran et al. (2021) used T2WELL-EOS1 to model the flow of pure water in an unconventional closed-loop heat exchanger. Their work investigated how factors such as mass flow rate and wellbore design affected energy recovery from the system (i.e., the energy flow rate at the wellhead).

T2WELL has also been used to model two-phase flows in oil and gas wells. Pan et al. (2018) used T2WELL to assess why a "top kill", where liquid was injected at the wellhead to prevent flow from a well, failed to control the blowout that occurred at the Aliso Canyon Underground Gas Storage Facility. Their simulations of the well and surrounding formation, which included complex transient flow processes and fluid exchange between the well and the annulus, found that additional periods of injection after the main kill attempt are likely to have been effective in preventing the gas leakage from re-occurring.

Finally, recent investigations by Battistelli et al. (2020) used T2WELL and the EOS2H equation of state, which accounts for high-temperature mixtures of water and  $\text{CO}_2$ , to simulate transient flow in a wellbore producing from a super-critical reservoir. Wellbore and reservoir characteristics were based on those of the IDDP-1 well at Krafla, Iceland.

Itoi et al. (2014) investigated the oscillation in wellhead conditions that occur in some multi-feed wellbores. They used an in-house transient wellbore model that assumed homogeneous phase velocities, meaning the effects of phase slip were not modelled. Oscillations in wellbore production were induced using a cyclic wellhead pressure boundary condition. This work was extended by Yamamura et al. (2017) who induced oscillations in mass flow within the well while maintaining a constant wellhead pressure. Their test

case featured a deep hot feed and a shallow cooler feed. They found that the magnitude and duration of the cycling process were affected by the difference in temperature between the shallow and deep feed-zones.

Akbar et al. (2016) presented a transient geothermal wellbore model implemented using the COMSOL finite element package. Their work investigated the sensitivity of wellbore flow to well diameter, wellbore roughness and slip relationships. Slip relationships were shown to significantly impact wellbore simulation results, while increases in diameter influence wellbore flow only up until a certain diameter. The effects of surface roughness were negligible for their sample problem. Akbar et al. (2016) presented a simulation approximating airlifting in a geothermal well to demonstrate the transient capability of their simulator. Airlifting is a method of stimulating a non-self-discharging well to flow. During this process, air is injected into the well below the water level. The aim is to displace the liquid water above the injection depth, reducing pressure at the feed-zone, allowing hot geothermal fluid to be produced. However, their simulation did not explicitly represent the water level or the injection of air. Instead, the entire well was initialised using an approximate air-water mixture with a modified density and specific heat capacity.

Of the simulators discussed above, only those by Miller (1980*b*) (WELLBORE), García-Valladares et al. (2006) (GEOWELLS), Pan, Oldenburg, Wu and Pruess (2011) (T2WELL) and Akbar et al. (2016) can be considered to be general two-phase geothermal wellbore simulators. However, the simulators by Miller (1980*b*), García-Valladares et al. (2006) and Akbar et al. (2016) do not appear to be able to model wells with more than one feed-zone.

We concluded from the literature for transient geothermal wellbore modelling that:

- Different formulations of the governing conservation equations for two-phase flow in wells have been used. It is unclear whether all of the models are equivalent or whether some models are approximate.
- A variety of different constitutive models (describing phase slip, wall friction and heat transfer) have been used. The best choice of each constitutive model is not clear.



- The role of counter-flow, where vapour flows up while liquid flows down, in geothermal wells has not been discussed or demonstrated in the context of wellbore modelling. We think that this process may be important in geothermal wells with low mass flow rates.
- Airlifting, a method of stimulating non-self-discharging geothermal wells by injecting air below the water level of a well, has been approximated by Akbar et al. (2016). However, simulations that model the water level and air injection during this process have not been presented.
- Air compression, a method of stimulating non-self-discharging wells by injecting air at the wellhead, has not been modelled using a transient geothermal wellbore simulator.

## 1.4 Motivation and objectives

Based on the literature review presented above, the main objective of our research is to develop a new transient geothermal wellbore simulator capable of modelling the diverse range of flow scenarios that can occur in multi-feed geothermal wells. This includes cases such as:

- rapid flashing during the opening of a well to flow,
- rapidly shutting in a flowing well,
- realistic initial conditions for wells with water levels below the wellhead,
- discharge stimulation methods, and
- counter-flow due to boiling in geothermal wells.

However, we found that the correct form of the governing equations to use in our simulator was not clear. Therefore, the first objective of our research was to complete a detailed review of the governing equations used in both steady-state and transient geothermal wellbore simulators. The review aimed to determine whether models correctly conserve key quantities. It investigated the impact that different modelling assumptions make on

simulation results, and determined the best form of the governing equations to use in our simulator.

Our review indicated that the role of counter-flow processes in geothermal wells had not been discussed in the literature. We knew that these processes are important in geothermal wells with low mass flow, for example, when two-phase conditions exist within a closed well. Therefore, an objective of this research is to investigate the role of counter-flow processes in geothermal wells. It was also unclear whether the combination of governing equations, constitutive models and the numerical method used by each model was suitable for modelling counter-flow. This is one of the motivations for developing our own simulator.

As discussed above, Akbar et al. (2016) presented transient simulations that approximated the airlifting of a geothermal well. We decided that simulations of stimulation methods could be improved by explicitly representing air. Specifically, we think that simulations of discharge stimulation should begin from conditions that accurately reflect the water level within the well. Therefore, we developed an air-water equation of state for our transient geothermal wellbore simulator and investigated the stimulation of non-self-discharging geothermal wells using airlifting and air compression.

## 1.5 Thesis structure

Chapter 2 presents the governing conservation equations selected for our transient geothermal wellbore simulator. These are compared to other conservation equations presented in the literature. The differences between the various formulations are discussed, and inconsistencies in some of the existing formulations are highlighted.

Chapter 3 discusses the constitutive equations required for model closure. Possible modelling options for phase slip, wall friction, heat transfer to the formation and reservoir sources are reviewed. The constitutive models selected for our simulator are discussed in detail.

Chapter 4 outlines the discrete formulation of the equations presented in Chapters 2 and 3. This includes discussions of the solution procedure and the selection of appropriate primary variables and boundary conditions.

Chapter 5 discusses the testing of our transient geothermal wellbore simulator. First, we present simple analytical solutions used to validate the implementation of the numerical model in code. Then, comparisons between measured pressure and temperature profiles are used to verify that the simulator is capable of representing production in geothermal wells. Finally, Chapter 5 describes a set of transient test cases that were developed to ensure our simulator can model the wide variety of flow scenarios that are possible in geothermal wells. These test cases were also used throughout the development of the simulator and are referenced during discussions in other chapters.

Many challenges were faced while developing the numerical method used in this simulator. Chapter 6 presents some of the interesting numerical investigations completed during this work and discusses how modelling decisions influence the results and numerical performance of our simulator.

Non-condensable gases can have a significant impact on the results of wellbore simulation. Specifically, air is required to represent wells with water levels below the wellhead and to model some methods of discharge stimulation. We discuss the extension of our simulator to the modelling of air-water mixtures in Chapter 7.

Chapter 8 discusses applications of our transient geothermal wellbore simulator. The first half of Chapter 8 is dedicated to discussing the role of counter-flow in shut-in geothermal wells. Following this, we discuss simulating discharge stimulation of geothermal wells using airlifting and air compression.

Lastly, the conclusions drawn from this work are presented in Chapter 9. Recommendations for future work are also discussed.

## Chapter 2

# Conservation equations for two-phase flow in geothermal wellbores

Initially, we found the existing geothermal wellbore modelling literature confusing. The main cause of confusion was that previous wellbore simulators used various versions of the governing equations to represent mass, momentum, and energy conservation. This lack of consistency in describing the behaviour of flow in a geothermal well makes it unclear whether some models correctly conserve key quantities and presents difficulties when comparing models. It also made it difficult to determine the best form of governing conservation equations to implement in this work. Given this problem, the first objective of this study was to review the conservation equations used in past geothermal wellbore models and determine the appropriate form of the conservation equations to use in our new simulator. This chapter presents our investigation into the governing conservation equations used in geothermal wellbore modelling.

First, we present the background information required for this discussion. This includes a summary of the key notation and variables used in this thesis and information on single-phase and two-phase modelling. Section 2.2 presents the governing conservation equations for the three-equation model for two-phase flow that is used in this work.

The other transient conservation equations presented in the geothermal literature are then compared to these equations. Section 2.3 then reviews the steady-state conservation equations presented in the geothermal literature while Section 2.4 presents the homogeneous conservation equations used in the past and discusses their applicability to multi-phase simulation. Some of the models used in past investigations use approximate momentum and energy conservation equations. The impact of these approximations on some test case simulations is discussed in Section 2.5.

## 2.1 Background

### 2.1.1 Multi-phase flow notation

There is no universally accepted notation for multi-phase flow in a geothermal well. The notation adopted for this thesis is a combination of what is commonly used in the geothermal wellbore and reservoir modelling literature. This section defines the fundamental quantities used in two-phase flow analysis and follows the more comprehensive works of Chisholm (1983), Ishii and Hibiki (2011) and Yadigaroglu and Hewitt (2018).

#### 2.1.1.1 Area averaging

The one-dimensional, area-averaged conservation equations are derived by integrating three-dimensional conservation equations over the cross-sectional area of the pipe. In general, the cross-sectional average of a variable  $f$  is defined as:

$$\langle f \rangle_A \equiv \frac{1}{A} \int_A f(x, y, z, t) dA. \quad (2.1)$$

Here,  $x$ ,  $y$  and  $z$  are Cartesian coordinates,  $t$  is time and  $A$  is the cross sectional area of the pipe.

The derivation of the area averaged conservation equations requires the product of variables to be averaged over the cross-sectional area of the pipe. In general, the average of the products does not equal the product of the averages, i.e. for any variables  $f = \langle f \rangle_A + f'$  and  $g = \langle g \rangle_A + g'$  (Berry et al., 2014):

$$\langle fg \rangle_A = \langle f \rangle_A \langle g \rangle_A + \langle f'g' \rangle_A. \quad (2.2)$$

However, Berry et al. (2014) notes that the covariance terms that result from the averaging process are usually assumed to be negligible, i.e.  $\langle f'g' \rangle_A = 0$  and  $\langle fg \rangle_A = \langle f \rangle_A \langle g \rangle_A$ . We make the same approximation when developing our transient geothermal wellbore simulator and make use of the notational simplification  $\langle f \rangle \Rightarrow f$  in the remainder of this thesis.

### 2.1.1.2 Saturation

In two-phase wellbore analysis, it is assumed that a control volume of a wellbore,  $V$ , is occupied by the liquid and vapour phases, with volumes  $V_l$  and  $V_v$ , respectively, meaning,

$$V = V_l + V_v. \quad (2.3)$$

In (2.3) and henceforth, the subscripts  $l$  and  $v$  are used to denote the liquid and vapour phases, respectively. The average volumetric fraction, or saturation, of a phase in a wellbore element of length,  $\Delta s$ , is given by,

$$S_l = \frac{V_l}{V} = \frac{A_l \Delta s}{A \Delta s} = \frac{A_l}{A}, \quad (2.4)$$

and

$$S_v = \frac{V_v}{V} = \frac{A_v \Delta s}{A \Delta s} = \frac{A_v}{A}. \quad (2.5)$$

By definition:

$$S_l + S_v = 1. \quad (2.6)$$

Two-phase fluid models are commonly presented in terms of  $S_v$  alone, with  $S_l$  eliminated by rearranging (2.6) and substituting it into the governing conservation equations. The volume fraction of vapour,  $S_v$ , is also referred to as the *vapour saturation* or the *void fraction*. The volume fraction of liquid,  $S_l$ , is also referred to as the *liquid saturation*, *liquid holdup* or simply *holdup*. Alternative symbols for  $S_v$  and  $S_l$  have often been used. For example,  $\alpha$  is commonly used instead of  $S_v$ , especially when  $S_l$  is not explicitly used in the governing equations.

### 2.1.1.3 Volume and mass flows

The total volume flow rate,  $Q_V$ , is the sum of the volume flow rates of the two phases and therefore:

$$Q_V = Q_{Vl} + Q_{Vv}. \quad (2.7)$$

The volume flow rates of the phases can be expressed in terms of the phase velocities as follows:

$$Q_{Vl} = u_l A_l = u_l S_l A, \quad (2.8)$$

and

$$Q_{Vv} = u_v A_v = u_v S_v A. \quad (2.9)$$

Here,  $u_\beta$  and  $A_\beta$  are the cross-sectional area of phase  $\beta$ . The total volumetric flux,  $F_V$ , is the total volume flow rate per unit area of the well. It is found by dividing the total volume flow rate,  $Q_V$ , by the cross-sectional area,  $A$ , to get:

$$F_V = \frac{Q_V}{A} = \frac{Q_{Vl}}{A} + \frac{Q_{Vv}}{A} = F_{Vl} + F_{Vv}. \quad (2.10)$$

The total volume flux is an important parameter in two-phase flow analysis. It is also referred to as the *velocity of the centre of volume*, the *superficial velocity* or the *homogeneous velocity* (Chisholm, 1983). Often the symbol  $j$  has been used for total or mixture volume flux instead of  $F_V$ .

The phase volume fluxes in (2.10) can be expressed in terms of the product of velocity and saturation by dividing (2.8) and (2.9) by area,  $A$ , to get:

$$F_{Vl} = \frac{Q_{Vl}}{A} = u_l S_l, \quad (2.11)$$

and

$$F_{Vv} = \frac{Q_{Vv}}{A} = u_v S_v. \quad (2.12)$$

These volumetric fluxes,  $F_{Vl}$  and  $F_{Vv}$ , are commonly referred to as the *superficial phase velocities*.

The total mass flow rate of a two-phase fluid is the sum of the mass flow rates of each phase:

$$Q_m = Q_{ml} + Q_{mv}, \quad (2.13)$$

where the liquid and vapour mass flow rates are defined as:

$$Q_{ml} = Q_{Vl}\rho_l = \rho_l u_l A_l = A\rho_l u_l S_l, \quad (2.14)$$

and

$$Q_{mv} = Q_{Vv}\rho_v = \rho_v u_v A_v = A\rho_v u_v S_v. \quad (2.15)$$

Here,  $\rho_l$  and  $\rho_v$  are the densities of the phases.

Dividing  $Q_m$  by the total cross-sectional area of the wellbore gives the total mass flux,  $F_m$ :

$$F_m = \frac{Q_m}{A} = \frac{Q_{ml}}{A} + \frac{Q_{mv}}{A} = F_{ml} + F_{mv}. \quad (2.16)$$

From (2.14) and (2.15), the separate components of liquid and vapour mass flux are given by:

$$F_{ml} = \frac{Q_{ml}}{A} = F_{Vl}\rho_l = \rho_l u_l S_l, \quad (2.17)$$

and

$$F_{mv} = \frac{Q_{mv}}{A} = F_{Vv}\rho_v = \rho_v u_v S_v. \quad (2.18)$$

The mass fluxes given in (2.16)—(2.18) are sometimes referred to as *mass velocities* (Chisholm, 1983).

#### 2.1.1.4 Mass fractions

Mass fractions are fundamental to the analysis of two-phase flow as, in general, we deal with mass averaged variables. There are two definitions of mass fractions that are used in two-phase flow analysis. These are the static and flowing mass fractions, which are defined and compared below.

The static mass fractions,  $x_{sv}$  and  $x_{sl}$ , are also referred to as *static qualities*. They are defined as the ratio of the mass (in place) of a phase to the total mass of the



mixture:

$$x_{sl} = \frac{\rho_l A_l}{\rho_l A_l + \rho_v A_v} = \frac{\rho_l S_l}{\rho_l S_l + \rho_v S_v} = \frac{\rho_l S_l}{\rho_{mix}}, \quad (2.19)$$

and

$$x_{sv} = \frac{\rho_v A_v}{\rho_l A_l + \rho_v A_v} = \frac{\rho_v S_v}{\rho_l S_l + \rho_v S_v} = \frac{\rho_v S_v}{\rho_{mix}}. \quad (2.20)$$

Here, the mixture density,  $\rho_{mix}$ , is the average density of the two-phase fluid, which is given by:

$$\rho_{mix} = \rho_l S_l + \rho_v S_v. \quad (2.21)$$

It follows simply, by definition, or by adding (2.19) and (2.20) that:

$$x_{sl} + x_{sv} = 1. \quad (2.22)$$

The static mass fractions are useful for defining mass averaged quantities. For example, the mixture velocity, which is the average velocity of the centre of mass of a two-phase fluid, is defined as:

$$u_{mix} = \frac{F_m}{\rho_{mix}} = \frac{\rho_l u_l S_l + \rho_v u_v S_v}{\rho_{mix}} = x_{sv} u_v + x_{sl} u_l. \quad (2.23)$$

The total mass flux can be represented using mixture properties by rearranging (2.23) to get:

$$F_m = \rho_{mix} u_{mix}. \quad (2.24)$$

The flowing mass fractions, which are used extensively in the analysis of two-phase pipe flow, are defined as the ratio of the mass flow of a phase to the total mass flow of the mixture:

$$x_{fl} = \frac{Q_{ml}}{Q_m} = \frac{F_{ml}}{F_m} = \frac{\rho_l F_{Vl}}{F_m} = \frac{\rho_l u_l S_l}{\rho_{mix} u_{mix}}, \quad (2.25)$$

and

$$x_{fv} = \frac{Q_{mv}}{Q_m} = \frac{F_{mv}}{F_m} = \frac{\rho_v F_{Vv}}{F_m} = \frac{\rho_v u_v S_v}{\rho_{mix} u_{mix}}. \quad (2.26)$$

Again, by definition or by adding (2.25) and (2.26):

$$x_{fv} + x_{fl} = 1. \quad (2.27)$$

The flowing mass fraction of steam is often referred to as *dryness fraction*, *flowing quality* or typically just *quality*.

We note that the mass and volume flow rates (or fluxes) of each phase can be calculated easily from the flowing mass fractions, densities and total mass flow by rearranging (2.25) and (2.26). We can relate the total volume and total mass fluxes using the flowing mass fractions by substituting (2.26) and (2.25) into (2.10) to get:

$$F_V = F_m \left( \frac{x_{fv}}{\rho_v} + \frac{x_{fl}}{\rho_l} \right), \quad (2.28)$$

which is a useful relationship when manipulating two-phase flow equations.

While the static and flowing mass fractions appear similar, they are not, in general, the same. This is demonstrated by considering:

$$\frac{x_{fv}}{x_{sv}} = \frac{\rho_v u_v S_v}{\rho_{mix} u_{mix}} \bigg/ \frac{\rho_v S_v}{\rho_{mix}} = \frac{u_v}{u_{mix}}. \quad (2.29)$$

It is clear from (2.29) that the flowing and static vapour mass fractions are only equivalent when  $u_v = u_{mix}$ . A similar argument shows that the flowing and static liquid mass fractions are only equal when  $u_l = u_{mix}$ . It, therefore, follows that the flowing and static mass fractions are only equal when  $u_v = u_l$ , a situation referred to as homogeneous flow.

One source of confusion in the literature is that the term *quality* is often not clearly defined. Yadigaroglu and Hewitt (2018) note that general two-phase flow equations are typically specified in terms of static variables, and quality refers to the static mass fraction of vapour. However, Thome (2006) and Yadigaroglu and Hewitt (2018) point out that quality almost always refers to the flowing mass fraction of vapour in the context of multi-phase pipe flow. This is because flowing quantities (e.g.,  $x_{fv}$  and  $h_{fmix}$ ) are easy to work with as their definitions allow the flow rates of both phases to be calculated

easily and because they are more convenient to measure than their static counterparts (e.g.,  $x_{sv}$  and  $h_{mix}$ ).

For example, in a geothermal context, two-phase flow conditions can be measured at the wellhead using a total flow calorimeter (Grant and Bixley, 2011). Here, two-phase flow from the well is discharged for a short time into the calorimeter, which contains cold water. The mass flow rate and flowing enthalpy of the two-phase fluid are estimated by measuring the change in volume and temperature of the liquid within the calorimeter over the test period (Grant and Bixley, 2011). Another common measurement technique is the James lip pressure method, which is used to estimate the flowing enthalpy and total mass flow rate of a well. Grant and Bixley (2011) note that this method is the most versatile and economical option for measuring flow in high productivity wells. This empirical relationship correlates the lip pressure (pressure measured at the end of the well when discharging to atmospheric conditions) to the liquid mass flow rate (e.g., measured using a weir box) and flowing enthalpy of the production fluid. Grant and Bixley (2011) and Zarrouk and McLean (2019) give further information on two-phase flow measurement techniques for geothermal wells.

The different definitions of quality make it difficult to interpret some formulations of the conservation equations. We try to clarify this issue by highlighting whether static or flowing variables are used in each of the models presented in Sections 2.2 and 2.3.

#### 2.1.1.5 Energy content

The energy content of the fluid in the wellbore can be described in several ways. The thermal energy of each phase, per unit volume of the wellbore, is:

$$E_l = \rho_l S_l e_l, \quad (2.30)$$

and

$$E_v = \rho_v S_v e_v. \quad (2.31)$$

Here,  $e_v$  and  $e_l$  are the specific internal energy of each phase. The specific enthalpy of each phase is defined in terms of internal energy by:

$$h_l = e_l + \frac{P}{\rho_l}, \quad (2.32)$$

and

$$h_v = e_v + \frac{P}{\rho_v}. \quad (2.33)$$

Here,  $P$  is the pressure in the wellbore. Given these definitions, the enthalpies of each phase per unit volume of the wellbore are given by:

$$H_l = \rho_l S_l h_l, \quad (2.34)$$

and

$$H_v = \rho_v S_v h_v. \quad (2.35)$$

The average specific enthalpy of a two-phase fluid is commonly used in discussing the conservation of energy for fluid flow within a pipe. However, as was the case with the mass fractions, there are both static and flowing definitions of the average specific enthalpy. The static specific mixture enthalpy,  $h_{mix}$ , is the total enthalpy of the fluid (the sum of (2.34) and (2.35)) divided by the average two-phase density, i.e.:

$$h_{mix} = \frac{H_l + H_v}{\rho_{mix}} = \frac{\rho_l S_l h_l + \rho_v S_v h_v}{\rho_{mix}} = x_{sl} h_l + x_{sv} h_v, \quad (2.36)$$

whereas the flowing specific mixture enthalpy,  $h_{fmix}$ , is the total energy flow rate divided by the total mass flow rate of the two-phase fluid:

$$h_{fmix} = \frac{A(H_v u_v + H_l u_l)}{Q_m} = \frac{F_{mv}}{F_m} h_v + \frac{F_{ml}}{F_m} h_l = x_{fl} h_l + x_{fv} h_v. \quad (2.37)$$

From (2.36) and (2.37), it follows that the static and flowing mixture specific enthalpies are only equal when  $x_{f\beta} = x_{s\beta}$ . As discussed in Section 2.1.1.4, this only occurs when the phase velocities are equal (i.e., for homogeneous flow conditions).

Combining (2.37) and (2.26) and rearranging for  $x_{fv}$  allows the flowing vapour mass

fraction to be calculated from the flowing enthalpy. This is useful, for example, when  $h_{f_{mix}}$  is measured at the wellhead (discussed briefly in Section 2.1.1.4) or if it is used as a primary variable.

Finally, some authors, for example García-Valladares et al. (2006) and Yadigaroglu and Hewitt (2018), have introduced the total specific enthalpy of each phase  $h_{Tl}$  and  $h_{Tv}$ , defined as the sum of the specific enthalpy, specific kinetic energy and specific potential energy of each phase:

$$h_{Tl} = h_l + \frac{u_l^2}{2} + gz, \quad (2.38)$$

and

$$h_{Tv} = h_v + \frac{u_v^2}{2} + gz. \quad (2.39)$$

Similarly, the total specific internal energy of each phase, used by Berry et al. (2014), is:

$$e_{Tl} = e_l + \frac{u_l^2}{2} + gz, \quad (2.40)$$

and

$$e_{Tv} = e_v + \frac{u_v^2}{2} + gz. \quad (2.41)$$

Here,  $g$  is gravitational acceleration, which is equal to  $9.81 \text{ m/s}^2$ .

### 2.1.2 Modelling single-phase flow

The derivation of the single-phase governing equations for conservation of mass, momentum and energy has been covered in depth by many authors. For example, Anderson (1995) provides a good introduction to the derivation of general single-phase conservation equations in three dimensions. One-dimensional conservation equations suitable for flow in pipes are derived by integrating the three-dimensional equations over the cross-sectional area of the wellbore. This one-dimensional averaging is covered in detail by authors such as Ishii and Hibiki (2011), Berry et al. (2014) and Yadigaroglu and Hewitt (2018).

One-dimensional conservation equations describing the flow of a single-phase fluid in a pipe with a variable cross-sectional area are given in (2.42)–(2.44) below. These equations are consistent with the two-phase conservation equations presented in Section 2.2. They

can be derived by substituting  $S_v = 0$  and  $S_l = 1$  (for liquid conditions) or  $S_v = 1$  and  $S_l = 0$  (for vapour conditions) into the two-phase conservation equations given in (2.53), (2.54) and (2.55).

The conservation of mass in a 1D pipe is governed by the equation:

$$\frac{\partial \rho}{\partial t} + \frac{1}{A} \frac{\partial}{\partial s} [A \rho u] - q_{mass} = 0 \quad (2.42)$$

Here,  $\rho$  is the fluid density,  $u$  is the fluid velocity,  $A$  is the cross-sectional area of the well and  $q_{mass}$  represents sources of mass. Equation (2.42) is similar to those given by Miller (1979) and Yadigaroglu and Hewitt (2018), although neither of these authors include the source term, and Yadigaroglu and Hewitt (2018) makes the substitution  $F_m = \rho u$ .

The equation governing conservation of momentum, derived from Newton's second law, is:

$$\frac{\partial}{\partial t} [\rho u] + \frac{1}{A} \frac{\partial}{\partial s} [A \rho u^2] + \frac{\partial P}{\partial s} + \rho g \frac{dz}{ds} + \frac{2}{r} \tau - q_{mom} = 0 \quad (2.43)$$

Here,  $P$  is the pressure,  $z$  is the elevation,  $s$  is the distance along the wellbore,  $g$  is gravitational acceleration (equal to  $9.81 \text{ m/s}^2$ ) and  $q_{mom}$  is the momentum source term. The slope  $dz/ds$  describes the deviation of the well from vertical. The coordinate system used in this work is shown in Figure 2.1. Some authors have used different coordinate systems or  $g = -9.81 \text{ m/s}^2$  and, therefore, have the opposite sign for the gravitational components in (2.43) and (2.44). A momentum equation similar to (2.43) is given by Yadigaroglu and Hewitt (2018), although they make the substitution  $F_m = \rho u$  and do not include the source term.

The shear stress,  $\tau$ , models the loss of momentum due to wall friction. In single-phase pipe flow, this term is usually modelled using the empirical Darcy-Weisbach equation (e.g., see Brown (2018) or Berry et al. (2014)). In two-phase analysis, there are two predominant methods, namely multiplier methods and mixture methods. These models for two-phase wellbore friction are discussed further in Section 3.3.

The conservation of energy equation below is a statement of the first law of thermodynamics. The single-phase version of the energy conservation equation given by Pan,

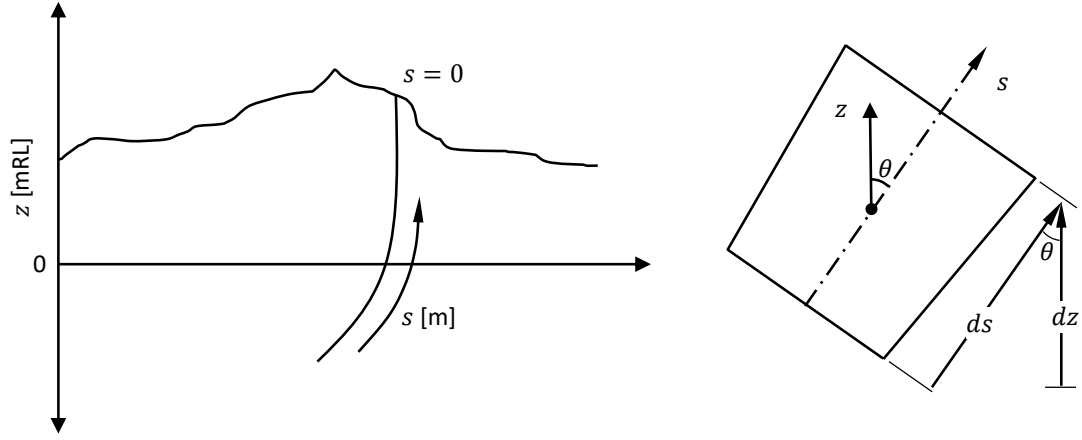


FIGURE 2.1: Coordinate system used in this work. The origin,  $z = 0$ , is a reference elevation e.g., sea level.

Oldenburg, Wu and Pruess (2011), when axial heat conduction is assumed to be negligible, is:

$$\frac{\partial}{\partial t} \left[ \rho \left( e + \frac{u^2}{2} \right) \right] + \frac{1}{A} \frac{\partial}{\partial s} \left[ A \rho u \left( h + \frac{u^2}{2} \right) \right] + \rho u g \frac{dz}{ds} + q_{heat} - q_{ener} = 0. \quad (2.44)$$

Here,  $e$  is the specific internal energy,  $h$  is the specific enthalpy and  $q_{ener}$  is the energy source term. Heat transfer between the well and the surrounding formation is modelled by  $q_{heat}$ . Here,  $q_{heat}$  is positive for heat transfer from the well to the reservoir. Most geothermal wellbore simulators approximate this term analytically, for example, see Hasan and Kabir (2010), Gunn (1992) (WELLSIM) or McGuinness (2015) (SWELFLO). However, formation heat transfer can also be modelled numerically by coupling the wellbore to a radial heat transfer equation (Miller, 1980b; García-Valladares et al., 2006) or a 3D numerical reservoir model (Pan, Oldenburg, Wu and Pruess, 2011). Wellbore heat transfer is discussed further in Section 3.4.

Sources of mass, momentum and energy are given by  $q_{mass}$ ,  $q_{mom}$  and  $q_{ener}$ . Here, the sign convention used is that these terms are positive for flow from the reservoir to the well. Source terms are typically modelled using productivity relationships, which relate the mass flow rate of a feed to the difference in pressure between the well and feed zone (McGuinness, 2014). Some investigations couple wellbore models with radial flow equations (Miller et al., 1982), or to a 3D numerical reservoir simulator, for example, Pan, Oldenburg, Wu and Pruess (2011), to represent flow to and from the reservoir. For

our simulator, we use productivity relationships to model reservoir source terms. We discuss this further in Section 3.5.

Single-phase flow plays an important role in some geothermal processes, such as producing pure steam or re-injecting liquid water. However, in general for high-temperature geothermal systems, both phases exist within the wellbore and, therefore, a geothermal wellbore simulator capable of modelling both single-phase and multi-phase flow is required. We discuss two-phase modelling in the following section.

### 2.1.3 Modelling multi-phase flow

Unlike single-phase fluid flow, there are many alternative models for two-phase flow of varying complexity. Examples include homogeneous, mixture, drift-flux, and two-fluid formulations. Each formulation has differences in the number of unknowns, number of conservation equations and choice of constitutive equations (of which there are many alternatives), and each varies in complexity.

Below we present the two-fluid, two-pressure model, which is considered state-of-the-art for general two-phase analysis (Berry et al., 2014). We then discuss the simplification of this model to the three-equation mixture model that is commonly used for modelling flow in geothermal wells and is used in our simulator. A derivation of our three-equation mixture model from the two-fluid, two-pressure model is given in Appendix A.

The two-fluid, two-pressure model uses seven equations to model two-phase pipe flow. This includes individual mass, momentum and energy conservation equations for each phase and an additional equation specifying the evolution of vapour saturation. Berry et al. (2014) first derived equations governing two-phase flow in a three-dimensional field using ensemble averaging. The one-dimensional, area-averaged equations were derived by integrating over the cross-sectional area of the pipe. As noted in Section 2.1.1.1 above, this derivation requires the product of variables to be averaged over the cross-sectional area. In these cases, Berry et al. (2014) makes the approximation that  $\langle fg \rangle_A = \langle f \rangle_A \langle g \rangle_A$ .

Using the notation defined in Section 2.1.1, Berry et al.'s (2014) mass, momentum and energy balance equations, as well as the saturation evolution equation, can be written



for the liquid phase as:

$$\frac{\partial S_l \rho_l A}{\partial t} + \frac{\partial S_l \rho_l u_l A}{\partial s} = -\Gamma A_{int} A, \quad (2.45)$$

$$\begin{aligned} \frac{\partial S_l \rho_l u_l A}{\partial t} + \frac{\partial S_l A (\rho_l u_l^2 + P_l)}{\partial s} = \\ P_{int} A \frac{\partial S_l}{\partial s} + P_l S_l \frac{\partial A}{\partial s} + A \lambda (u_v - u_l) \\ - \Gamma A_{int} u_{int} A - F_{wall,l} - F_{f,v} + S_l \rho_l A \mathbf{g} \cdot \hat{\mathbf{n}}_{axis}, \end{aligned} \quad (2.46)$$

$$\begin{aligned} \frac{\partial S_l \rho_l e_{Tl} A}{\partial t} + \frac{\partial S_l u_l A (\rho_l e_{Tl} + P_l)}{\partial s} = \\ P_{int} u_{int} A \frac{\partial S_l}{\partial s} - \bar{P}_{int} A \mu (P_l - P_v) + \bar{u}_{int} A \lambda (u_v - u_l) \\ + \Gamma A_{int} \left( \frac{P_{int}}{\rho_{int}} - h_{Tl,int} \right) A + Q_{int,l} + Q_{wall,l}, \end{aligned} \quad (2.47)$$

and

$$\frac{\partial S_l A}{\partial t} + u_{int} A \frac{\partial S_l}{\partial s} = A \mu (P_l - P_v) - \frac{\Gamma A_{int} A}{\rho_{int}}. \quad (2.48)$$

Similarly, the conservation equations for the vapour phase are written as:

$$\frac{\partial S_v \rho_v A}{\partial t} + \frac{\partial S_v \rho_v u_v A}{\partial s} = \Gamma A_{int} A, \quad (2.49)$$

$$\begin{aligned} \frac{\partial S_v \rho_v u_v A}{\partial t} + \frac{\partial S_v A (\rho_v u_v^2 + P_v)}{\partial s} = \\ P_{int} A \frac{\partial S_v}{\partial s} + P_v S_v \frac{\partial A}{\partial s} + A \lambda (u_l - u_v) \\ + \Gamma A_{int} u_{int} A - F_{wall,v} - F_{f,l} + S_v \rho_v A \mathbf{g} \cdot \hat{\mathbf{n}}_{axis}, \end{aligned} \quad (2.50)$$

$$\begin{aligned} \frac{\partial S_v \rho_v e_{Tv} A}{\partial t} + \frac{\partial S_v u_v A (\rho_v e_{Tv} + P_v)}{\partial s} = \\ P_{int} u_{int} A \frac{\partial S_v}{\partial s} - \bar{P}_{int} A \mu (P_v - P_l) + \bar{u}_{int} A \lambda (u_l - u_v) \\ - \Gamma A_{int} \left( \frac{P_{int}}{\rho_{int}} - h_{Tv,int} \right) A + Q_{int,v} + Q_{wall,v}, \end{aligned} \quad (2.51)$$

and

$$\frac{\partial S_v A}{\partial t} + u_{int} A \frac{\partial S_v}{\partial s} = A \mu (P_v - P_l) + \frac{\Gamma A_{int} A}{\rho_{int}}. \quad (2.52)$$

For two-phase flow, the saturation of one phase is always known from the relationship  $S_l + S_v = 1$ . Therefore, either (2.48) or (2.52) is not required (typically (2.48) is discarded) reducing the total number of equations to seven.

In Equations (2.45)–(2.52),  $A_{int}$  is the interfacial surface area per unit volume of the two-phase mixture and  $\Gamma$  is the net mass transfer per unit interfacial area from the liquid to the vapour phase. The interface pressure and average interface pressure are  $P_{int}$  and  $\bar{P}_{int}$ , respectively. Similarly,  $u_{int}$  and  $\bar{u}_{int}$  are the interface velocity and average interface velocity. The total phase enthalpy at the interface is given by  $h_{T\beta,int}$ . Frictional forces are modelled by  $F_{wall,\beta}$ , which is the friction force from the wall acting on phase  $\beta$ , and  $F_{f,\beta^*}$ , which is the friction force acting on phase  $\beta$  by phase  $\beta^*$ . Finally,  $Q_{int,\beta}$  and  $Q_{wall,\beta}$  represent the heat transfer to phase  $\beta$  from the interface and wall, respectively. The pressure and velocity relaxation coefficients are given by  $\mu$  and  $\lambda$ , respectively. These parameters describe how the two-phase system approaches thermodynamic equilibrium (Berry et al., 2014). The term  $\mathbf{g} \cdot \hat{\mathbf{n}}_{axis}$  is the component of gravity in the axial direction, which is equal to  $-g \, dz/ds$  in our notation. The remaining parameters are defined in Section 2.1.1 above.

Constitutive equations which describe the rate of mass, momentum and energy transfer between the liquid and vapour phases are required to complete the seven-equation model presented above (Ishii and Hibiki, 2011; Berry et al., 2014). Additionally, interface variables and balance equations (referred to as jump conditions by Ishii and Hibiki (2011)) are required to ensure mass, momentum and energy are conserved across the interface between phases.

The seven-equation model can be simplified by assuming that the pressures of each phase are equal. Berry et al. (2014) note that, in many practical applications, the pressures of each phase are very similar. This assumption eliminates one independent variable and serves as a replacement for the vapour saturation equation given in (2.52). This six-equation model is often referred to as the two-fluid model or classical two-fluid model. Detailed discussions of this model are given by Kocamustafaogullari (1971), Ishii and

Hibiki (2011) and Berry et al. (2014). The six-equation model has been implemented in nuclear reactor simulators, as discussed, for example, by Liles (1979) and Geffraye et al. (2011).

The two-fluid model may be simplified to a five-equation drift-flux model with two mass conservation equations, one mixture momentum equation and two energy equations, by introducing a constitutive equation for slip (Kim and Roy, 1981; Webb and Rowe, 1986). This provides a relationship between the flow of each phase and saturation, thus allowing one independent variable to be eliminated.

The four-equation drift-flux model, with two mass conservation equations, one momentum equation and one energy equation, is derived from the five-equation drift-flux model by also assuming the phases are at the same temperature (Zou et al., 2015). This assumption is generally appropriate for flow in geothermal wellbores due to small radial temperature gradients and the well-mixed, highly advective nature of the fluid flow. This model is discussed at length in other works, for example, see (Kocamustafaogullari, 1971; Webb and Rowe, 1986; Ishii and Hibiki, 2011; Zou et al., 2015; Lee et al., 2019).

Finally, the three-equation model that is used in this work is obtained from the four-equation drift-flux model above by assuming the fluid is at saturation conditions. This implies that mass transfer between the phases occurs instantaneously and that temperature is no longer an independent variable (*i.e.*,  $T = T_{sat}(P)$ ) meaning a single mixture mass equation may be used in place of the two individual phase mass equations for the two phases.

We expect the impact of non-equilibrium processes on geothermal wellbore simulation to be relatively small compared to the effect of uncertainty in key parameters such as the reservoir/source characteristics, formation temperatures, wellhead conditions and wellbore geometry (e.g., scale accumulation or damage). Therefore, the three-equation model was deemed to be the appropriate conservation model to use in our transient geothermal wellbore simulator. However, Boure and Delhaye (1982) note that it is not always clear when and where non-equilibrium processes will be influential. In fact, a recent study by Pereira and Fowler (2020) indicated that non-equilibrium dynamics influence the point at which gas exsolves from the liquid phase in oil and gas wells. As this process is similar

to flashing in geothermal wells, their work suggests that non-equilibrium fluid dynamics may be influential in geothermal wellbore simulation. Therefore, a geothermal wellbore simulator capable of modelling non-equilibrium flows may be a worthwhile improvement on the standard three-equation model.

Below we discuss the three-equation model and compare it to other models presented in the geothermal wellbore modelling literature.

## 2.2 Transient conservation equations

Equations (2.53), (2.54) and (2.55) describe the conservation of mass, momentum and energy within a geothermal wellbore with a variable cross-sectional area. This mathematical model describes the behaviour of the fluid as a mixture rather than accounting for each phase individually and assumes:

- 1-D flow – variables are averaged across the well cross-section,
- same pressure in the liquid and vapour phases,
- negligible axial heat conduction,
- local thermodynamic equilibrium between the phases (both phases are at the same temperature, which is equal to the saturation temperature), and
- there is a relationship between the velocities of liquid and gas (slip relationship).

The conservation of mass for a two-phase fluid is modelled by (Yadigaroglu and Hewitt, 2018):

$$\frac{\partial}{\partial t} [\rho_l S_l + \rho_v S_v] + \frac{1}{A} \frac{\partial}{\partial s} [A \rho_l S_l u_l + A \rho_v S_v u_v] - q_{mass} = 0. \quad (2.53)$$

Here,  $S_\beta$  is the phase saturation,  $u_\beta$  is the phase velocity and  $\rho_\beta$  is the phase density. External sources of mass are modelled using  $q_{mass}$ , which is defined in Section 3.5.

The conservation of momentum is modelled by (Yadigaroglu and Hewitt, 2018):

$$\begin{aligned} \frac{\partial}{\partial t} [\rho_l S_l u_l + \rho_v S_v u_v] + \frac{1}{A} \frac{\partial}{\partial s} [A \rho_l S_l u_l^2 + A \rho_v S_v u_v^2] \\ + \frac{\partial P}{\partial s} + \frac{2}{r} \tau + (\rho_l S_l + \rho_v S_v) g \frac{\partial z}{\partial s} - q_{mom} = 0. \end{aligned} \quad (2.54)$$

Here,  $P$  is wellbore pressure,  $g$  is gravitational acceleration and  $\tau$  is wellbore wall friction, which is defined in Section 3.3. The external source or sink of momentum is given by  $q_{mom}$ , which is defined in Section 3.5.

The conservation of energy equation for the flow of a two-phase mixture in a geothermal well is given below in terms of the thermal energy and kinetic energy of each phase, with the energy flux given in terms of enthalpy (Pan, Oldenburg, Wu and Pruess, 2011):

$$\begin{aligned} \frac{\partial}{\partial t} \left[ \rho_l S_l \left( e_l + \frac{u_l^2}{2} \right) + \rho_v S_v \left( e_v + \frac{u_v^2}{2} \right) \right] \\ + \frac{1}{A} \frac{\partial}{\partial s} \left[ A \rho_l S_l u_l \left( h_l + \frac{u_l^2}{2} \right) + A \rho_v S_v u_v \left( h_v + \frac{u_v^2}{2} \right) \right] \\ + (\rho_l S_l u_l + \rho_v S_v u_v) g \frac{\partial z}{\partial s} + q_{heat} - q_{ener} = 0 \quad (2.55) \end{aligned}$$

Here,  $q_{heat}$  is the heat flux between the wellbore and the formation due to conduction, which is defined in Section 3.4, and the energy source term  $q_{ener}$  is used to model flow between the well and the reservoir. We define this term in Section 3.5. Pan, Oldenburg, Wu and Pruess (2011) included an axial heat conduction term in their version of (2.55). We assume this to be negligible and it is not included.

### 2.2.1 Alternative conservation of mass equations

The conservation of mass equation can also be written in terms of mixture quantities (Miller, 1980*b*; Akbar et al., 2016; García-Valladares et al., 2006; Yadigaroglu and Hewitt, 2018):

$$\frac{\partial}{\partial t} [\rho_{mix}] + \frac{1}{A} \frac{\partial}{\partial s} [A \rho_{mix} u_{mix}] - q_{mass} = 0. \quad (2.56)$$

This mixture form of the mass equation is exact and is equivalent to (2.53). It is derived by substituting the definitions of mixture density,  $\rho_{mix}$ , given in (2.21) and velocity,  $u_{mix}$ , given in (2.23) into (2.53).

The four previous, general transient geothermal wellbore simulators have used either (2.53) (Pan, Oldenburg, Wu and Pruess, 2011) or (2.56) (Miller, 1980*b*; Akbar et al., 2016; García-Valladares et al., 2006) to represent conservation of mass.

### 2.2.2 Alternative conservation of momentum equations

García-Valladares et al. (2006) and Miller (1980b) used the momentum conservation equation given in (2.54). However, the other two general geothermal wellbore simulators, by Pan, Oldenburg, Wu and Pruess (2011) and Akbar et al. (2016), use a momentum equation formulated in terms of mixture variables:

$$\begin{aligned} \frac{\partial}{\partial t} [\rho_{mix} u_{mix}] + \frac{1}{A} \frac{\partial}{\partial s} [A \rho_{mix} u_{mix}^2 + \gamma] \\ + \frac{\partial P}{\partial s} + \frac{2}{r} \tau + (\rho_l S_l + \rho_v S_v) g \frac{\partial z}{\partial s} - q_{mom} = 0, \end{aligned} \quad (2.57)$$

where the transport of momentum due to phase slip is denoted by  $\gamma$ , which is defined by:

$$\gamma = \left( \frac{S_v}{1 - S_v} \right) \left( \frac{\rho_l \rho_v \rho_{mix}}{\rho_{mix}^*} \right) [(C_0 - 1) u_{mix} + u_d]^2. \quad (2.58)$$

Equation (2.57) makes use of the drift-flux constitutive model for slip. This model, discussed at length in Section 3.2.1.4, describes the relative motion of each phase using two empirical parameters, the drift velocity,  $u_d$ , and the profile parameter,  $C_0$ . In (2.58),  $\rho_{mix}^*$  is the profile adjusted mixture density defined in (3.14). The derivation of (2.57), starting from (2.54), is given in Appendix A.2.1.1.

Equation (2.57) is mathematically equivalent to (2.54) but is less general as it requires that the drift-flux constitutive model is used to describe slip.

### 2.2.3 Alternative conservation of energy equations

Some authors, for example García-Valladares et al. (2006), Berry et al. (2014) and Yadi-garoglu and Hewitt (2018) have introduced the total specific enthalpy of each phase  $h_{Tl}$  and  $h_{Tv}$ . These are defined in (2.38) and (2.39) as the sum of the specific enthalpy, specific kinetic energy and specific potential energy of each phase. In this case (2.55) can be combined with the mass equation (2.53) to give the energy equation in terms of total enthalpy:

$$\begin{aligned} \frac{\partial}{\partial t} [\rho_l S_l h_{Tl} + \rho_v S_v h_{Tv} - P] \\ + \frac{1}{A} \frac{\partial}{\partial s} [A \rho_l S_l u_l h_{Tl} + A \rho_v S_v u_v h_{Tv}] + q_{heat} - \hat{q}_{ener} = 0 \end{aligned} \quad (2.59)$$

Equation (2.59) is equivalent to (2.55), which is shown in Appendix A.3.1.

García-Valladares et al. (2006) presented the following, highly rearranged version of (2.59) in discrete, non-conservative form. A continuous version of their equation is given below:

$$(h_{Tv} - h_{Tl}) \frac{\partial}{\partial t} [\rho_v S_v] + \rho_v S_v \frac{\partial h_{Tv}}{\partial t} + \rho_l S_l \frac{\partial h_{Tl}}{\partial t} - \frac{\partial P}{\partial t} + \frac{Q_m}{A} \frac{\partial h_{Tl}}{\partial s} + \frac{1}{A} \frac{\partial}{\partial s} [Q_{mv} (h_{Tv} - h_{Tl})] + q_{heat} = 0. \quad (2.60)$$

Apart from the omission of the external source term no approximations were made in the derivation of (2.60) from (2.55). The derivation of this equation from their discrete model is provided in Appendix A.3.2.

Some forms of the energy conservation equation used in previous transient geothermal wellbore simulators are approximations of (2.55). For example, Miller (1980a) gave an energy equation in terms of thermal energy, for a constant area well, equivalent to:

$$\frac{\partial}{\partial t} [\rho_l S_l e_l + \rho_v S_v e_v] + \frac{\partial}{\partial s} [\rho_l S_l u_l h_l + \rho_v S_v u_v h_v] - (S_l u_l + S_v u_v) \frac{\partial P}{\partial s} + q_{heat} = 0. \quad (2.61)$$

Equation (2.61) is derived by subtracting rearranged forms of the mass and momentum conservation equations for each phase from (2.55). This manipulation, given in Appendix A.3.3, results in a net transport term related to the difference in phase velocities and a term representing energy dissipation due to friction, both of which are not included in (2.61). In a geothermal wellbore, these terms are likely to be small when compared to changes in total enthalpy and the net transfer of heat between the well and the reservoir, meaning the impact of their omission on the results of geothermal wellbore simulations is likely to be small.

Akbar et al. (2016) used the following approximate energy conservation equation using mixture quantities for flow in vertical wells with constant area:

$$\begin{aligned} \frac{\partial}{\partial t} \left[ \rho_{mix} \left( h_{f_{mix}} + \frac{u_{mix}^2}{2} - P \right) \right] \\ + \frac{\partial}{\partial s} \left[ \rho_{mix} u_{mix} \left( h_{f_{mix}} + \frac{u_{mix}^2}{2} \right) \right] + \rho_{mix} u_{mix} g + q_{heat} = 0 \quad (2.62) \end{aligned}$$

This is essentially the same as the single-phase energy equation, (2.44), with the subscript ‘mix’ added to all quantities. Akbar et al. (2016) did not define the mixture enthalpy explicitly, however, from their definition and use of flowing mass fraction ( $X$  in their notation), it can be deduced that they used the flowing mixture enthalpy given by (2.37). As a result, the total fluid enthalpy term in the time derivative,  $\rho_{mix} h_{f_{mix}}$ , is incorrect and thus (2.62) does not correctly conserve energy. Expanding this term gives  $(\rho_l S_l u_l h_l + \rho_v S_v u_v h_v)/u_{mix}$ , which is erroneously weighted by velocity. The static specific mixture enthalpy defined in (2.36) should be used instead of the flowing enthalpy within the time derivative in (2.62) to conserve energy correctly.

Additionally, in (2.62), the kinetic energy of the fluid is modelled using the mixture velocity. The approximation made in modelling kinetic energy in this way are likely to be small (see Section 2.5 below for further discussion).

#### 2.2.4 Other transient models

Two other transient geothermal wellbore models have been developed but were targeted at either the drilling process or geysering in a well rather than general wellbore behaviour and therefore have not been included in the discussion presented in Section 2.2.1 above.

The first of these, developed by Tian and Finger (2000), was used to model drilling processes. The governing equations were for three-phase fluid flow including drilling fragments, nitrogen gas or air, and various drilling fluids. The simulator has a complex mathematical formulation with seven conservation equations. Three mass conservation equations were used, one for each individual phase. Two momentum equations were used, a mixture equation for the liquid and vapour phases and an extra equation for the solid cuttings. Tian and Finger (2000) solved two mixture energy equations, one for



flow in the drill string and the other for flow in the annulus between the drill string and formation. None of the mixture equations included the effects of slip between the liquid and gas phases on momentum and energy transport.

The second simulator, developed by Lu et al. (2006), investigated geysering in a gassy, low-temperature geothermal well. It implemented individual mass conservation equations for each phase but assumed isothermal conditions and therefore did not solve an energy conservation equation. A mixture momentum equation was used but both the momentum accumulation (first term in (2.57)) and momentum flux (second term in (2.57)) were assumed to be zero. In this case, the pressure gradient is a function of gravity and frictional forces only. These assumptions are violated in cases where significant fluid acceleration occurs, such as when opening a well to flow or rapidly shutting in a flowing well.

## 2.3 Steady-state conservation equations

Most previous geothermal wellbore investigations have assumed steady-state conditions, meaning that the time derivatives in the governing conservation equations were discarded. A review of the literature revealed many different steady-state formulations have been used. In some cases, it was unclear whether the different equations were equivalent and if they all correctly conserved key quantities.

This section reviews the conservation equations used in the literature on steady-state geothermal wellbore modelling. The discussion is presented below in three general sections: conservative formulations, non-conservative formulations and mixture velocity formulations. Here, the conservative formulation, discussed in Section 2.3.1, refers to the Eulerian form of the governing equations. Section 2.3.2 discusses non-conservative formulations of the governing equations presented in the literature. Both forms of the partial differential equations are mathematically equivalent; however, when discretised using finite difference methods the non-conservative formulation is not guaranteed to globally conserve flow quantities, whereas a finite volume discretisation of the conservative form of the governing equations will globally conserve flow quantities. This section

reviews conservative and non-conservative models in the literature and identifies whether or not assumptions were made in their derivation.

The discussion presented in this section focuses primarily on the formulation of the momentum and energy equations as, under steady-state conditions, the mass flow is known from the boundary conditions.

### 2.3.1 Conservative models

For steady-state conditions, the time derivatives in the transient conservation equations, (2.53), (2.54) and (2.55), are discarded and the equations simplify to:

$$\frac{1}{A} \frac{d}{ds} [A\rho_l S_l u_l + A\rho_v S_v u_v] - q_{mass} = 0 \quad (2.63)$$

$$\frac{1}{A} \frac{d}{ds} [A\rho_l S_l u_l^2 + A\rho_v S_v u_v^2] + \frac{dP}{ds} + \frac{2}{r} \tau + (\rho_l S_l + \rho_v S_v) g \frac{dz}{ds} - q_{mom} = 0 \quad (2.64)$$

$$\begin{aligned} \frac{1}{A} \frac{d}{ds} \left[ A\rho_l S_l u_l \left( h_l + \frac{u_l^2}{2} \right) + A\rho_v S_v u_v \left( h_v + \frac{u_v^2}{2} \right) \right] \\ + (\rho_l S_l u_l + \rho_v S_v u_v) g \frac{dz}{ds} + q_{heat} - q_{ener} = 0 \end{aligned} \quad (2.65)$$

Conservation equations similar to (2.63) - (2.65) have been presented by several authors, for example Dittman (1977), Barelli et al. (1982) and Tachimori (1982). However, it is more common to present the equations in non-conservative form, which is discussed in Section 2.3.2 below.

The governing equations used by Gudmundsdottir (2012) in FloWell are a quasi-linear form of (2.63) - (2.65), written in terms of the derivatives of flux terms with respect to the primary variables.

The wellbore simulator HOLA, developed by Bjornsson (1987), was the first to account for multiple feed-zones. The derivative codes, GWELL and GWNACL (Aunzo et al., 1991), extended HOLA to include CO<sub>2</sub> and salt, respectively. Bjornsson (1987) gave the governing equations in conservative form, formulating them in terms of flowing mass fractions:

$$\frac{d}{ds} [F_m(x_{fv}u_v + x_{fl}u_l)] + \frac{dP}{ds} + (\rho_v S_v + \rho_l S_l) g \frac{dz}{ds} + \frac{2}{r} \tau = 0 \quad (2.66)$$

$$\frac{1}{A} \frac{d}{ds} \left[ Q_m \left( x_{fv} \left( h_v + \frac{1}{2} u_v^2 + gz \right) + x_{fl} \left( h_l + \frac{1}{2} u_l^2 + gz \right) \right) \right] + q_{heat} = 0 \quad (2.67)$$

Equation (2.66) correctly conserves momentum, and is equivalent to (2.64), when the wellbore area is constant. However, momentum is not correctly conserved in sections of the well with a change in diameter. This is shown in Appendix A.2.2. This problem was also noted by McGuinness (2013) who showed that using (2.66) results in a pressure drop approximately twice as large as the correct momentum flux term (first term in (2.64)) across a wellbore block with a change in diameter. We discuss this issue further in Section 2.5 below.

The energy equation (2.67), formulated in terms of total enthalpy, correctly accounts for changes in wellbore area, is exact, and is equivalent to (2.65). Equation (2.67) can be derived by substituting the definitions of flowing mass fraction, given in (2.26) and (2.25), into (2.67). Term 2 in (2.65) is obtained by separating the gravity component in the first term of (2.67) and noting that total mass flow,  $Q_m$ , and the gravitational acceleration,  $g$ , do not change with respect to  $s$ .

The governing equations for steady flow can be written in terms of mixture variables, which can be obtained by dropping the time derivatives from the mass (2.56) and momentum (2.57) equations. Goyal et al. (1980) gave the mixture form of the equations, presented below in (2.68) - (2.70), in terms of the relative velocity,  $u_r$ , defined in (3.22). However, it is more common to use non-conservative versions of the governing equations when using mixture variables. These are discussed in Section 2.3.2.

$$\frac{1}{A} \frac{d}{ds} [A (\rho_{mix} u_{mix})] - q_{mass} = 0, \quad (2.68)$$

$$\begin{aligned} \frac{1}{A} \frac{d}{ds} [A \rho_{mix} u_{mix}^2] + \frac{1}{A} \frac{d}{ds} \left[ \frac{A S_v (1 - S_v) \rho_v \rho_l u_r^2}{\rho_{mix}} \right] \\ + \frac{dP}{ds} + \frac{2}{r} \tau + \rho_{mix} g \frac{dz}{ds} - q_{mom} = 0, \end{aligned} \quad (2.69)$$

$$\begin{aligned} \frac{1}{A} \frac{d}{ds} [A \rho_{mix} u_{mix} e_{mix}] + \frac{1}{A} \frac{d}{ds} \left[ \frac{AS_v (1 - S_v) \rho_v \rho_l (e_v - e_l) u_r}{\rho_{mix}} \right] \\ + \frac{P}{A} \frac{d}{ds} [A u_{mix}] + \frac{P}{A} \frac{d}{ds} \left[ \frac{AS_v (1 - S_v) (\rho_l - \rho_v) u_r}{\rho_{mix}} \right] + q_{heat} - q_e = 0. \end{aligned} \quad (2.70)$$

Equation (2.69) is equivalent to (2.64) and its derivation requires no approximations. However, (2.70) does not follow exactly from (2.65), rather it is the steady version of the thermal energy equation (2.61) given by Miller (1980*b*). Terms 2 and 4 model the effects of slip in terms of  $u_r$  and are equivalent to the energy flux (term 2) in (2.61). However, as was the case with (2.61), Equation (2.70) is approximate. This is because the manipulation required to eliminate kinetic energy from (2.65) results in a term representing energy dissipation due to friction and a net energy transport term that were not included in (2.70). The impact of this simplification is likely to be small.

Chadha et al. (1993) also uses a mixture form of the governing equations but omit changes in momentum and energy caused by the relative motion of the phases. In this case, the momentum and thermal energy equations can be simplified and are essentially the same as single-phase equations with the subscript ‘mix’ added to all quantities:

$$\frac{1}{A} \frac{d}{ds} [A \rho_{mix} u_{mix}^2] + \frac{dP}{ds} + \frac{2}{r} \tau + \rho_{mix} g \frac{dz}{ds} - q_{mom} = 0, \quad (2.71)$$

$$\frac{1}{A} \frac{d}{ds} [A \rho_{mix} u_{mix} h_{mix}] - u_{mix} \frac{dP}{ds} + q_{heat} - q_{ener} = 0. \quad (2.72)$$

These equations still allow phases to flow at different velocities; however, the simplifications mean that changes in momentum and energy due to the relative motion of steam and water are not included, and therefore mass and energy are not correctly conserved.

### 2.3.2 Non-conservative models

The majority of steady-state wellbore simulators have used a non-conservative form of the conservation equations. Non-conservative formulations can be derived by manipulating the conservative models presented in Section 2.3.1 above.

Non-conservative momentum and energy equation are commonly formulated in terms of the flowing mass fractions. They follow directly, with no approximation, from the exact equations (2.64) and (2.65) using the definitions of flowing mass fractions in (2.26) and

(2.25):

$$\frac{Q_m}{A} \frac{d}{ds} [x_{fl} u_l + x_{fv} u_v] + \frac{dP}{ds} + \frac{2}{r} \tau + \rho_{mix} g \frac{dz}{ds} = 0, \quad (2.73)$$

$$\frac{Q_m}{A} \frac{d}{ds} \left[ x_{fl} \left( h_l + \frac{u_l^2}{2} \right) + x_{fv} \left( h_v + \frac{u_v^2}{2} \right) \right] + F_m g \frac{dz}{ds} + q_{heat} = 0. \quad (2.74)$$

These equations have been used in the wellbore simulators SWELFLO (McGuinness, 2015) and SIMGWELL (Marquez et al., 2015). Equation (2.74) was also used by Elliot (1975), Dittman (1977), Michaelides (1980) and Bilicki et al. (1981).

Formulating the governing equations in terms of  $x_{fv}$  is useful for modelling steady-state flow when either the flowing mass fraction or flowing enthalpy is used as a primary variable. Also, it is convenient when a slip equation is defined in terms of  $x_{fv}$ , such as in (3.2) or (3.19). However, formulating the conservation equations in this way presents difficulties when modelling counter-flow processes or shut-in wells. This problem is discussed further in Section 4.4.

For wells with constant area, the flux term in the momentum equation (2.73) can be written in terms of  $x_{fv}$  alone by substituting the definition of velocity in terms of flowing mass fraction (i.e., (2.25) rearranged):

$$F_m^2 \frac{d}{ds} \left[ \frac{x_{fl}^2}{S_l \rho_l} + \frac{x_{fv}^2}{S_v \rho_v} \right] + \frac{dP}{ds} + \frac{2}{r} \tau + \rho_{mix} g \frac{dz}{ds} = 0. \quad (2.75)$$

Equation (2.75) has been implemented in several simulators (Michaelides, 1980; Bilicki et al., 1981; Parlaktuna, 1985), and in the commercial simulator WELLSIM (Hadgu, 1989; Gunn, 1992). Equation (2.75) correctly conserves momentum, and is equivalent to (2.73), when the wellbore area is constant. However, momentum is not correctly conserved in sections of the well with changing diameter (the same problem noted above for equation (2.66)).

### 2.3.3 Definition of two-phase velocity

Simplified non-conservative forms of the momentum and energy conservation equations in terms of an average two-phase velocity have been used in geothermal wellbore simulators and are discussed below.

### 2.3.3.1 Momentum conservation

Several investigators have used the following approximate non-conservative momentum equation:

$$\rho_{mix}u \frac{du}{ds} + \frac{dP}{ds} + \frac{2}{r}\tau + \rho_{mix}g \frac{dz}{ds} = 0. \quad (2.76)$$

The definition of the average two-phase velocity,  $u$ , varies between investigators. Several authors (Chierici et al., 1981; Hasan and Kabir, 2010; Franz, 2015; Franz and Clearwater, 2021) formulate (2.76) using the volume weighted, total volume flux ( $u = F_V = S_v u_v + S_l u_l$ ). In this case, (2.76) does not follow from (2.64) and, therefore, does not correctly conserve momentum when slip between phases is allowed. Equation (2.76) is only equivalent to (2.64) under homogeneous flow conditions.

Cinar et al. (2006) and Cinar and Onur (2015) also formulate (2.76) using volume flux, however, they subsequently assume that momentum flux (term 1 in (2.76)) is negligible and discard it.

Early models developed by Gould (1974), Farouq Ali (1981), and Ortiz-Ramirez (1983) are all based on (2.76), however, they replace the momentum flux term with an empirical approximation originally derived by Poettman and Carpenter (1952) and popularised by Orkiszewski (1967).

### 2.3.3.2 Energy conservation

Some authors, for example Gould (1974), Ortiz-Ramirez (1983), Farouq Ali (1981), Parlaktuna (1985), Hadgu (1989) and Gunn (1992), used the following mixture form of the non-conservative energy conservation equation:

$$F_m \frac{d}{ds} \left[ h_{f,mix} + \frac{u^2}{2} + zg \right] + q_{heat} = 0, \quad (2.77)$$

where the flowing mixture enthalpy  $h_{f,mix}$  is as defined in (2.37). Here the flowing mixture enthalpy is as defined in (2.37) and, as with (2.76), the definition of the average velocity,  $u$ , used to calculate the kinetic energy varies between investigators. Farouq Ali (1981), Parlaktuna (1985), Hadgu (1989) and Gunn (1992) use the mass averaged

velocity ( $u = u_{mix}$ ) while Gould (1974) and Ortiz-Ramirez (1983) use volume flux ( $u = F_V = S_v u_v + S_l u_l$ ).

Equation (2.77) correctly conserves thermal energy and gravitational potential energy (first and third component of term 1), however, the kinetic energy term,  $u^2/2$  does not follow exactly from (2.74) as  $F_m u^2/2 \neq (\rho_l S_l u_l^3 + \rho_v S_v u_v^3)/2$ .

An alternative non-conservative form of (2.77) is given below in (2.78). It was used by Chierici et al. (1981), Hasan and Kabir (2010), Franz (2015) and Franz and Clearwater (2021) who all used volume flux as the average velocity. It can be derived by separating the individual components in term 1 of (2.77), differentiating the kinetic energy term and dividing the whole equation by the total mass flux,  $F_m$ :

$$\frac{dh_{f_{mix}}}{ds} + u \frac{du}{ds} + g \frac{dz}{ds} + \frac{q_{heat}}{F_m} = 0 \quad (2.78)$$

Equation (2.78) correctly conserves thermal energy (term 1) and potential energy (term 3) but, as with (2.77), the kinetic energy term (term 2) is approximate.

## 2.4 Conservation equations for homogeneous flow

Homogeneous models, sometimes called homogeneous equilibrium models (HEM), use a simplified formulation that assumes the liquid and vapour phases are in local thermodynamic equilibrium and are flowing at the same average velocity. In general, this is equivalent to treating the flow as a pseudo-single-phase fluid, with properties averaged over the two phases.

Homogeneous models are considered to be reasonably accurate for flows with high vapour saturation (known as mist flow) where the entrained liquid droplets are travelling at approximately the same velocity as the vapour phase or for wells with very high mass flow rates (Thome, 2006). However, they do not allow for the significant slip that occurs during processes such as flashing and are incapable of modelling counter-flow where the liquid and vapour phases flow in opposite directions.

### 2.4.1 Transient homogeneous flow

The conservation equations for homogeneous fluid flow, given below in (2.79)–(2.81), are derived by substituting  $u_v = u_l = u$  into (2.68), (2.57) and (2.55) and are very similar to the single-phase equations (2.42)–(2.44) given in Section 2.1.2.

$$\frac{\partial}{\partial t} [\rho_{mix}] + \frac{1}{A} \frac{\partial}{\partial s} [A \rho_{mix} u] - q_{mass} = 0, \quad (2.79)$$

$$\frac{\partial}{\partial t} [\rho_{mix} u] + \frac{1}{A} \frac{\partial}{\partial s} [A \rho_{mix} u^2] + \frac{\partial P}{\partial s} + \frac{2}{r} \tau + \rho_{mix} g \frac{\partial z}{\partial s} - q_{mom} = 0, \quad (2.80)$$

and

$$\begin{aligned} \frac{\partial}{\partial t} \left[ \rho_{mix} \left( e_{mix} + \frac{u^2}{2} \right) \right] + \frac{\partial}{\partial s} \left[ \rho_{mix} u \left( h_{mix} + \frac{u^2}{2} \right) \right] \\ + \rho_{mix} u g + q_{heat} - q_{ener} = 0. \end{aligned} \quad (2.81)$$

Two transient wellbore simulators that use homogeneous flow models have been developed. The first of these, developed by Miller (1979), was based on the conservative form of the mixture equations for mass conservation (2.79) and momentum conservation (2.80). It used an approximate conservative, mixture, thermal energy equation - the same as (2.61) after substituting  $u_v = u_l = u$ . Miller (1979) used  $P, e_{mix}$  as mass and energy primary variables and  $F_m$  as the momentum primary variable. The simulator was applied to investigating the effect of wellbore storage on geothermal well tests (Miller, 1980a). Itoi et al. (2013; 2014) modified Miller's (1979) simulator to account for two feed-zones and investigated well cycling.

The second simulator, developed by Yamamura et al. (2016), was based on a homogeneous flow model that is equivalent to (2.79)–(2.81). They used the following non-conservative momentum equation:

$$\rho_{mix} \frac{\partial u}{\partial t} + \rho_{mix} u \frac{\partial u}{\partial s} + \frac{\partial P}{\partial s} + \frac{2}{r} \tau + \rho_{mix} g \frac{\partial z}{\partial s} = 0 \quad (2.82)$$

Equation (2.82) is derived by expanding the derivatives in (2.80) and subtracting a manipulated form of the mass conservation equation (2.79). It is exact and equivalent to (2.80) when  $q_{mom} = u \times q_{mass}$  or if  $q_{mom}$  is assumed to be negligible.



Their energy equation, given in (2.83), is formulated in terms of total homogeneous mixture enthalpy,  $h_{Tmix} = h_{mix} + u^2/2 + gz$ . It follows from (2.59) after substituting  $u_v = u_l = u$  and is equivalent to (2.81):

$$\frac{\partial}{\partial t} [\rho_{mix} h_{Tmix} - P] + \frac{1}{A} \frac{\partial}{\partial s} [Au \rho_{mix} h_{Tmix}] + q_{heat} - q_h = 0 \quad (2.83)$$

Equations (2.82) and (2.83) were solved with the homogeneous mass equation (2.79) using  $P, u$  and  $h_{Tmix}$  as primary variables.

### 2.4.2 Steady-state homogeneous flow

Non-conservative equations have been used in homogeneous steady-state investigations. The steady form of (2.80) used by Nandanwar and Anderson (2014) is:

$$\rho_{mix} u \frac{du}{ds} + \frac{dP}{ds} + \frac{2}{r} \tau + \rho_{mix} g \frac{dz}{ds} = 0. \quad (2.84)$$

Equation (2.84) has also been formulated in terms of mass flux and specific volume by Itoi et al. (1988), Sánchez-Upton (1995, 2000) and Tokita and Itoi (2004). This form is derived by substituting  $u = F_m / \rho_{mix}$  and the definition of specific volume ( $\nu = 1 / \rho_{mix}$ ) into (2.84) and removing  $F_m$  from the spatial derivative.

The momentum equation (2.84) is typically solved together with the steady-state form of the energy equation given by (2.83) (García et al., 1999, 2002; Garcia-Gutierrez et al., 2002) or (2.81) (Sánchez-Upton, 1995, 2000). Itoi et al. (1988) and Tokita and Itoi (2004) solved the specific volume form of (2.84) while replacing the energy equation by the assumption of constant enthalpy up the wellbore.

A formulation of the homogeneous steady-state momentum equation by Nathenson (1974) assumed negligible acceleration effects. In this case, the first term of (2.84) is set equal to zero.

## 2.5 Model comparisons

Sections 2.2 and 2.3 demonstrate that there are differences in the mathematical models used in various geothermal wellbore simulators. Commonly used approximations

include:

- Approximate momentum flux terms ((2.71) and (2.76))
- Incorrect treatment of changes in area in the momentum flux term ((2.66) and (2.75))
- Approximating the kinetic energy using average parameters ((2.77) and (2.78))

We ran numerical simulations, using the simulator described in this thesis, for a range of flow scenarios to investigate the impact of the most common approximations on wellbore modelling results.

### 2.5.1 Approximate momentum flux terms

The flux term in the momentum equation models the effect of acceleration on momentum conservation within the well. Equation (2.71) ignores the effect of slip on momentum flux, while (2.76) approximates this term using the average volume flux.

Results for three steady-state models were compared:

- (i) Exact: (2.64) with correct momentum flux
- (ii) No momentum flux: (2.64) but with momentum flux (term (1)) deleted
- (iii) Approximate: (2.76) with approximate momentum flux using  $u = F_V$

These different formulations of the momentum conservation equation were investigated using our transient geothermal wellbore simulator (run to steady-state). In all cases, the momentum conservation equation was solved implicitly together with the mass (2.63) and energy (2.65) conservation equations. Other than the variation in the momentum flux term, all modelling parameters were the same. Test Cases 4 and 6, described later on in Sections 5.3.1.4 and 5.3.2.2, are used as examples.

Test Case 6 models two-phase flow in a shallow 200 m well. It was originally developed to test transitions between two-phase and vapour conditions. It was chosen as an example for the model comparisons because the addition of high enthalpy fluid causes the wellbore flow to accelerate. Therefore, this case was expected to demonstrate the differences between results obtained with the different momentum flux terms.

TABLE 2.1: Feed properties for Test Case 6 presented in Figures 2.2 and 2.3.

Name	Elev. [mRL]	$P$ [bara]	$T$ [°C]	$S_v$ [-]	$Q_m$ [kg/s]	$h_f$ [kJ/kg]	PI [m <sup>3</sup> ]
Feed 1	-180 to -200	20	212.37	0	10.58	908.5	1E-12
Feed 2	-50 to -60	20	300	1	0.645	3025	1E-12

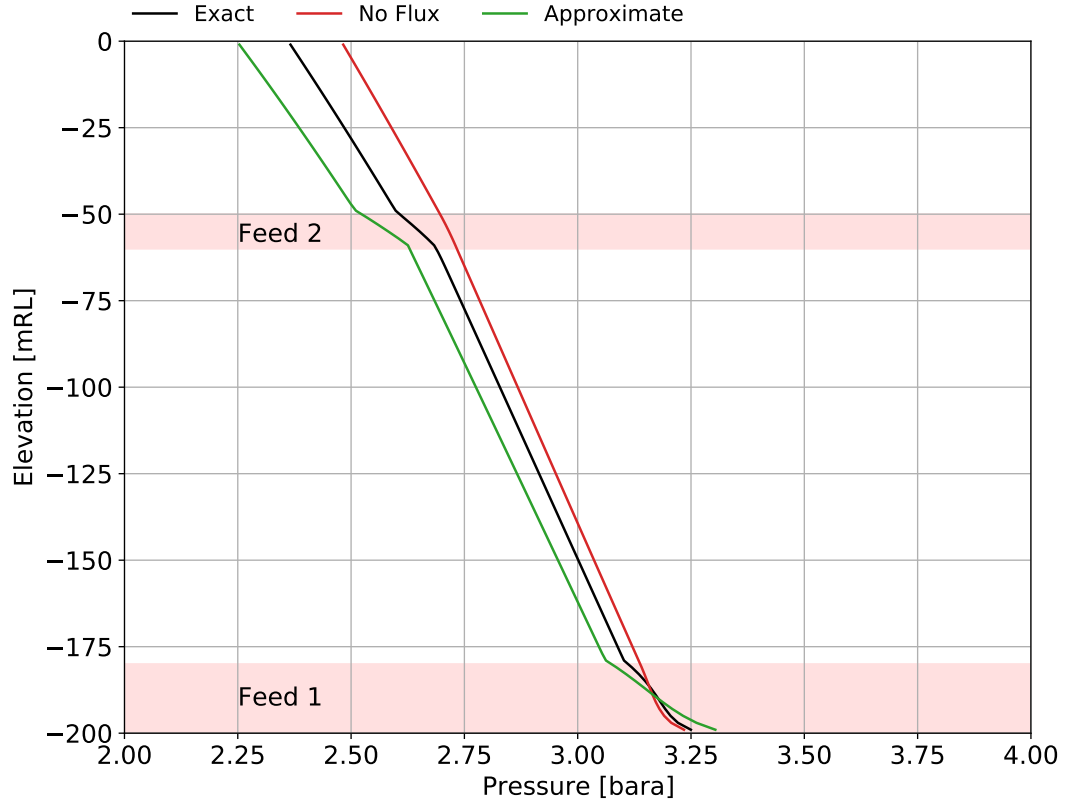


FIGURE 2.2: Comparison of pressure profiles for Test Case 6 simulated using the (i) exact, (ii) no momentum flux and (iii) approximate model given in (2.76).

The well is fed by a high enthalpy shallow vapour feed and a deeper, low enthalpy, liquid feed. Test Case 6 has a mass flow of 12 kg/s and a flowing wellhead enthalpy of approximately 1030 kJ/kg. The feed properties are given in Table 2.1 while the remaining model parameters are given in Section 5.3.2.2.

Figure 2.2 compares the wellbore pressures simulated using the three different momentum equations. The difference in pressure between the three models is evident, although the absolute difference is small. The wellhead pressure simulated using the approximate momentum flux term in (2.76) is 2.24 bara, approximately 5.5% lower than 2.37 bara simulated with the exact model. Thus, the wellhead pressure is approximately 5% higher when momentum flux is not modelled.

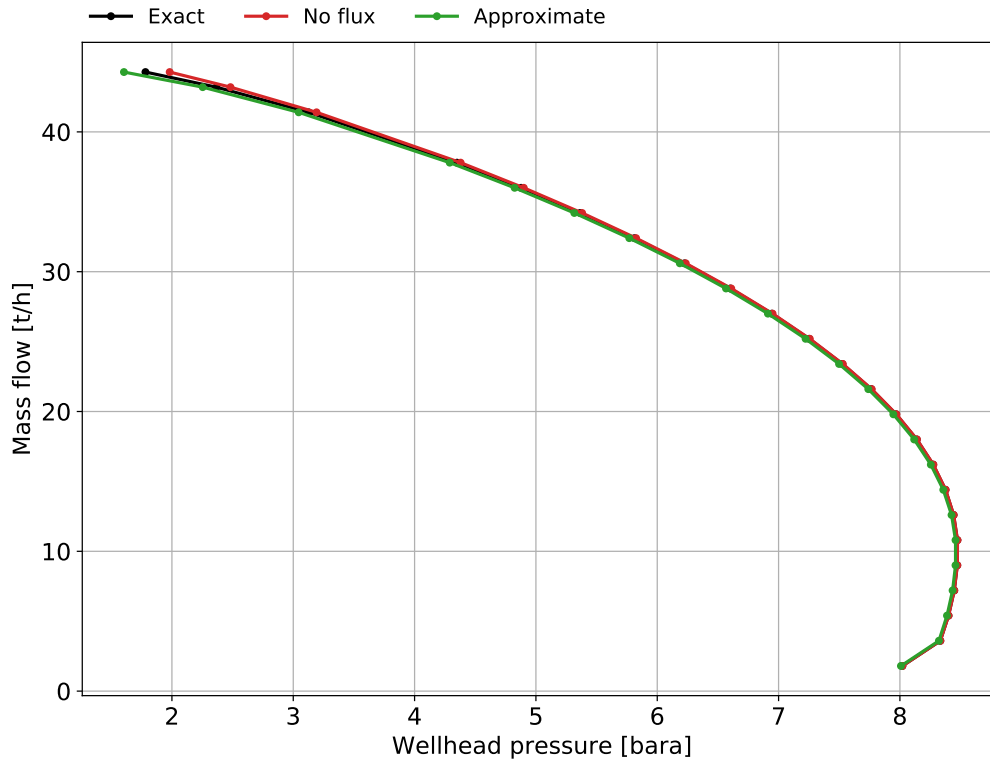


FIGURE 2.3: Comparison of output curves for Test Case 6 generated using the (i) exact, (ii) no momentum flux and (iii) approximate model given in (2.76).

The differences shown in Figure 2.2 are primarily due to the increase in mass flow rate that occurs when fluid is added to the well over the production intervals, which are highlighted in red in Figure 2.2. The approximate momentum flux term calculates larger pressure drops due to acceleration than the exact model. By comparison, there is no change in the pressure gradient due to the addition of fluid when the momentum flux term is not included.

Output curves for Test Case 6 are compared in Figure 2.3 to show the impact of the different momentum flux terms. There is very little difference between the output curves generated using the three models for this test case.

Test Case 4 is another multi-feed production case but with a higher total mass flow and more realistic feed-zone parameters than Test Case 6. The feed-zone and simulation parameters for this test case are given in Section 5.3.1.4. Figure 2.4 compares the simulated pressures in the top 800 m of the well for the exact, approximate, and no momentum flux models for a wellhead mass flow rate of 31.25 kg/s. In this case, the effect of fluid acceleration on pressure drop is most obvious in the top 200 m of the well, where the

pressure gradient begins to increase. Again, the approximate momentum flux used in (2.76) over-estimates the pressure loss due to fluid acceleration. The final wellhead pressure is 1.8 bara, 43% lower than for the exact model at 3.15 bara. The wellhead pressure is 4.25 bara when momentum flux is not included, a 35% increase compared to the exact model.

Figure 2.4 shows that the differences between the approximate and exact models do not become significant until the effects of acceleration start to become influential in the top 200 m of the well. By comparison, when momentum flux is not modelled, differences in pressure are evident above -750 mRL. These differences at depth are caused by a change in the wellbore area, which occurs at -750 mRL. The rapid change in pressure gradient at this depth, which is evident in the exact and approximate momentum flux models, is caused by this change in cross-sectional area. The no momentum flux approximation does not model the change in momentum that occurs due to this change in area.

Figure 2.5 compares the output curves for Test Case 4. While the differences between models are more noticeable than for Test Case 6, there is still relatively little difference between the approximate models and the exact model until high flow rates are used. At these high flow rates, acceleration effects start to become influential, and differences in the wellhead pressure for a given flow rate are seen.

These test cases show that, in general and as expected, the error caused by ignoring momentum flux completely is larger than that caused by using the approximate form given in (2.76). Under standard operating conditions, i.e., relatively high wellhead pressures and moderate mass flow rates, the differences between results appear to be relatively small. However, significant differences in calculated pressure profiles are possible when large fluid acceleration occurs, mainly at high flow rates. In these cases, the approximate volume flux formulation of (2.76) will over-estimate the pressure loss due to acceleration.

The results of Test Case 4 show that an exact representation of the derivative of momentum flux such as those given in (2.64), (2.69) or (2.73) should be used in a geothermal wellbore model. However, the errors introduced by not doing so are likely to be small for moderate flow rates and slowly varying flows.

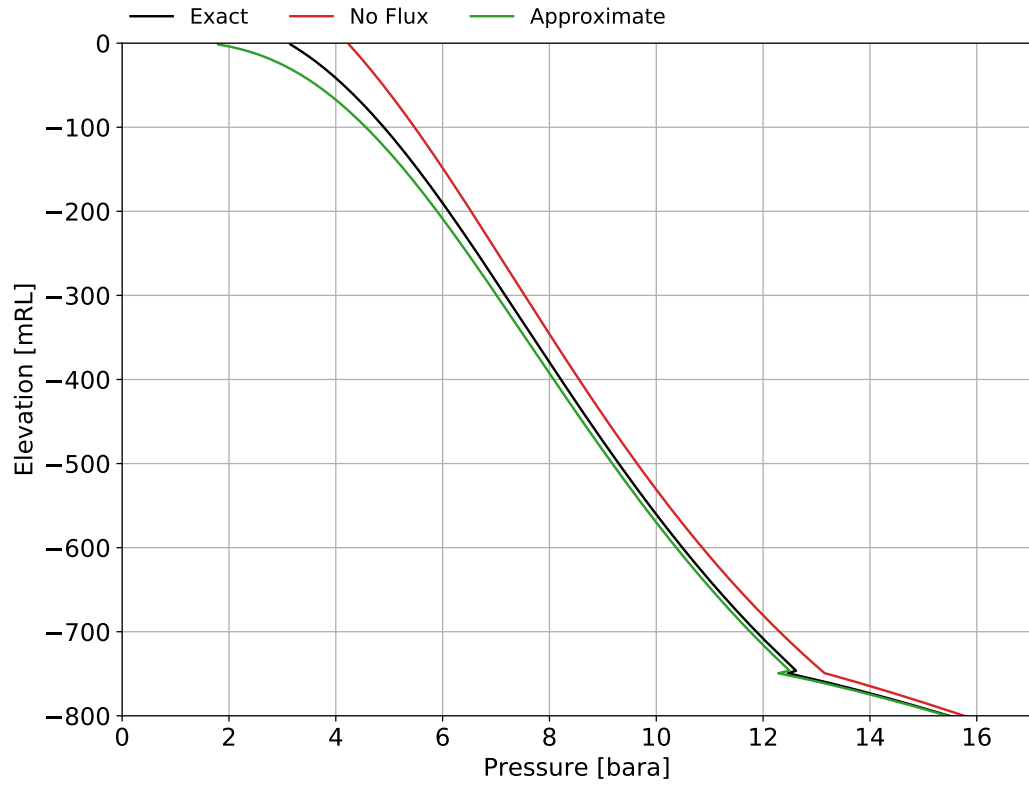


FIGURE 2.4: Comparison of pressure profiles for Test Case 4 simulated using the (i) exact, (ii) no momentum flux and (iii) approximate model given in (2.76).

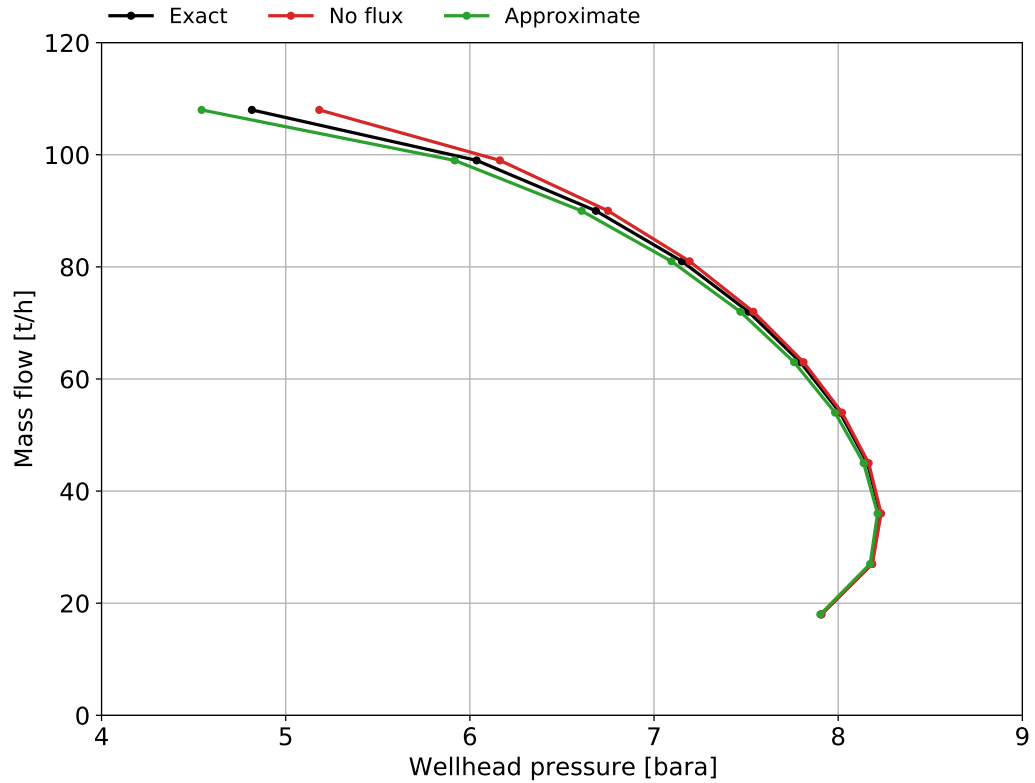


FIGURE 2.5: Comparison of output curves for Test Case 4 generated using the (i) exact, (ii) no momentum flux and (iii) approximate model given in (2.76).

### 2.5.2 Incorrect treatment of area

As noted above, equations (2.66) and (2.75) do not correctly conserve momentum over changes in wellbore diameter despite being used in the well known simulators GWELL and WELLSIM. McGuinness (2013) first noticed this inconsistency when modernising GWELL and corrected it for use in SWELFLO. McGuinness (2013) estimated that the incorrect momentum flux term resulted in a pressure drop twice the size of the correct result and further noted that, while noticeable, the incorrect treatment of changes in the wellbore cross-sectional area in the momentum flux term had little impact on the output curves for a sample well.

Test Case 4 is used to show the impact of incorrectly conserving momentum across changes in the wellbore area. The results in Figure 2.6 show that the increase in pressure across the area change, located at -750 mRL, is much larger with the incorrect momentum term than with the exact model. This results in an offset in the pressure profile and a wellhead pressure of 3.75 bara, 18% larger than the exact model.

The output curve generated using the incorrect treatment of area change is compared to the exact and no flux curves in Figure 2.7. Again, differences are relatively small for moderate mass flow rates and relatively high wellhead pressures. In fact, for this test case, the effect of incorrectly accounting for changes in area is smaller than the errors introduced by using the approximate models discussed above.

Test Case 4 confirms the findings of McGuinness (2013) that, while noticeable, the impact of incorrectly accounting for area change in the momentum conservation equation is likely to be small when modelling geothermal wellbores. This gives confidence in past results from simulators such as GWELL and WELLSIM. However, given that there is no clear advantage to approximating momentum conservation over changes in wellbore area, we suggest that correctly formulated momentum conservation equations, for example, (2.64) (2.69) or (2.73), should always be used in geothermal wellbore simulators.

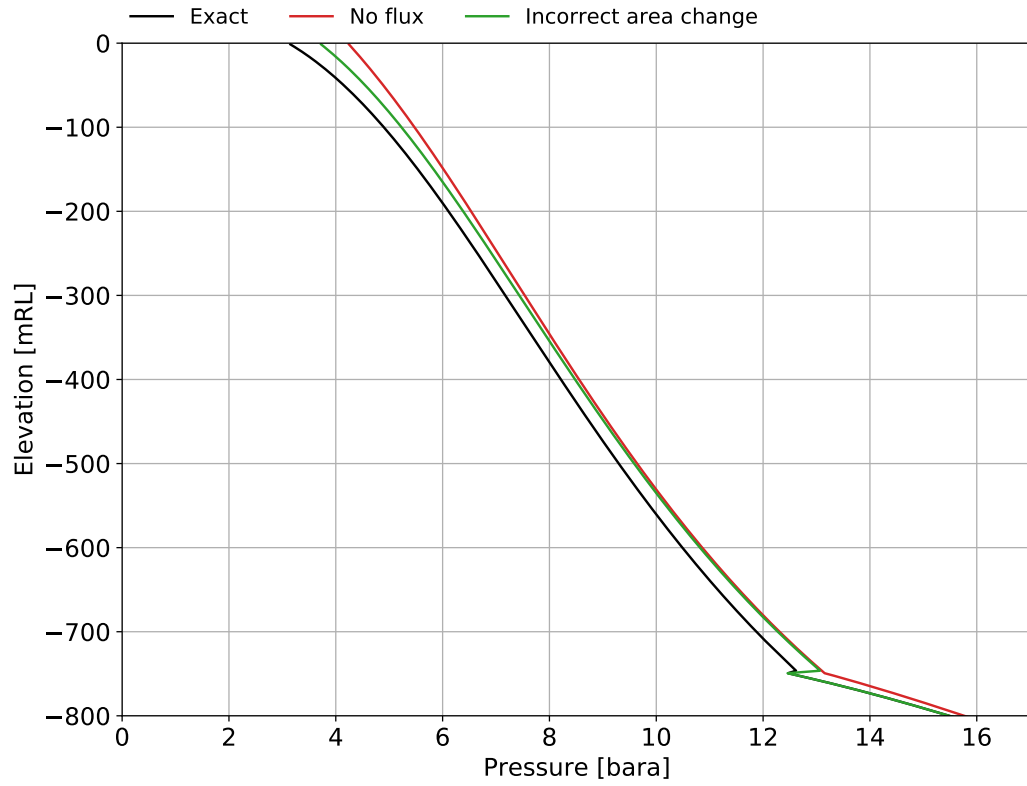


FIGURE 2.6: Comparison of pressure profiles for Test Case 4 simulated using the (i) exact, (ii) no momentum flux and (iii) incorrect treatment of area change.

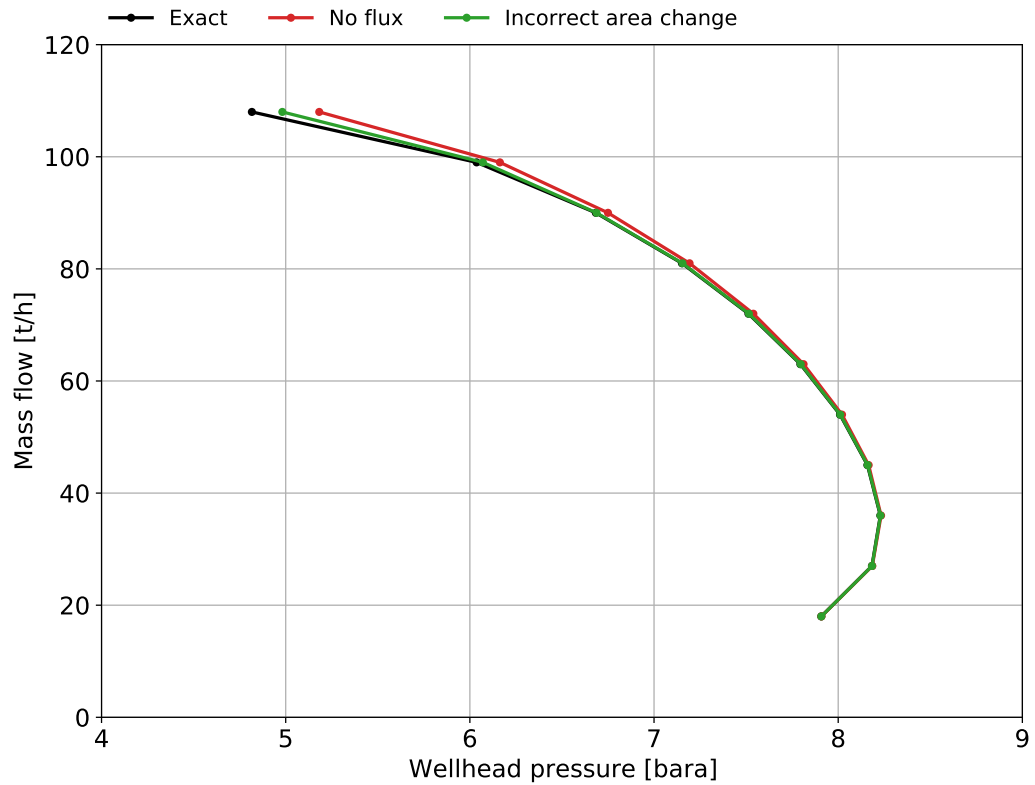


FIGURE 2.7: Comparison of output curves for Test Case 4 generated using the (i) exact, (ii) no momentum flux and (iii) incorrect treatment of area change.



### 2.5.3 Approximate kinetic energy term

Equations (2.77) and (2.78) approximate the kinetic energy of the fluid using an average velocity, either the saturation weighted volume flux or mass weighted mixture velocity. Simulations of a simple single feed well were run for a range of inflow conditions to investigate the impact of these approximations. Simulations were run for mass flows between 10 and 100 kg/s and for fluid enthalpies between 400 and 2800 kJ/kg. A wellhead pressure of 4 bara was used for all cases and heat flux to or from the formation was ignored. The well had a length of 1000 m and a diameter of 0.2 m.

Differences in results are most evident in the mass fractions simulated for cases with high mass flow and high enthalpy (both of which cause high fluid velocities). Figure 2.8 provides an example of the differences in vapour mass fraction for the case in which 2000 kJ/kg fluid is injected at 55 kg/s. Figure 2.8 shows almost no difference between results obtained using the approximate and exact representations of kinetic energy. When kinetic energy is ignored completely, the wellhead vapour mass fraction is 0.662, only 2.8% larger than for the exact model. This causes a small increase of approximately 2.5% in the estimated steam flow at the wellhead. Similar results were obtained for other test cases.

Additionally, the effect of approximate kinetic energy terms on transient problems was investigated using the set of test cases described in Section 5.3. These problems include a range of inflow conditions and fast and slow transient processes. Almost no differences were observed between results obtained using the approximate and exact representations of kinetic energy in all cases. Given these results, it appears that the approximate representation of kinetic energy is not an important issue in geothermal wellbore modelling.

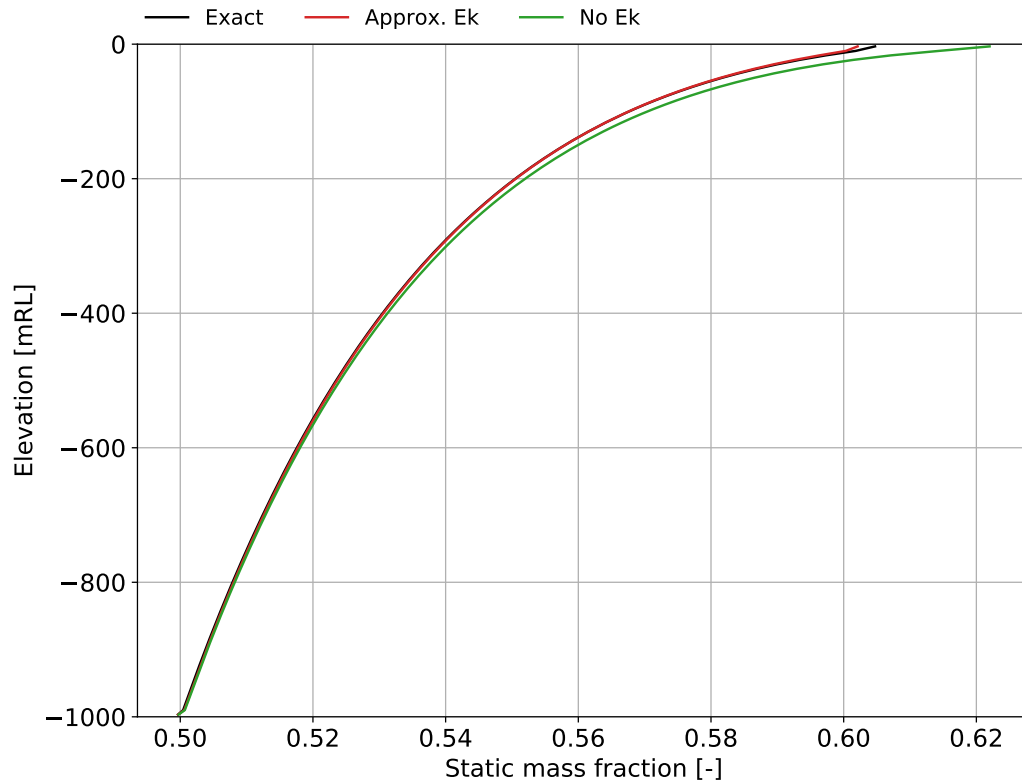


FIGURE 2.8: Comparison of vapour mass fractions for a 1000m well with a diameter of 0.2 m producing 2000 kJ/kg fluid at 55 kg/s for three cases: (i) exact, (ii) approximate and (iii) no kinetic energy.

## 2.6 Summary

This chapter reviewed the conservation equations presented in the geothermal wellbore modelling literature and highlighted some of the complications associated with modelling multi-phase fluid in geothermal wellbores. The past literature shows that many variations of multi-phase models have been used, however, there is limited information about how each model was derived, what assumptions were made in their derivation and how they relate to other models presented in the literature.

To clarify these problems, conservation models from the geothermal wellbore modelling literature were compared to a physically accurate form of the mass, momentum and energy conservation equations given in (2.53), (2.54) and (2.55). This comparison indicated that governing conservation equations can be formulated in terms of mixture variables without making additional assumptions (e.g., see (2.56) and (2.57)). However, we found

that some formulations of the momentum equation commonly used in steady-state models did not correctly conserve momentum flux (e.g., see (2.71) and (2.76)). Additionally, some simulators do not correctly conserve momentum across changes in wellbore area (see (2.66) and (2.75)).

Models using common approximate momentum flux terms were compared to the physically accurate model using Test Cases 4 and 6. These cases indicated that the approximation of momentum flux terms does affect the results of wellbore simulations. Specifically, differences in wellhead pressure can be observed for cases with higher flow rates. However, these test cases also showed that the impact of incorrectly conserving momentum is relatively small for moderate mass flows and relatively high wellhead pressures.

It was also found that some models use approximate representations of kinetic energy, using average variables (e.g., see (2.77) and (2.78)). However, we found that this approximation made little difference to the results of our test case simulations. Despite this result, we have retained the correct kinetic energy terms in our model.

After reviewing the two-phase conservation models used in the geothermal literature, we decided to implement the "full" three-equation model. These equations are repeated here for clarity:

$$\frac{\partial}{\partial t} [\rho_l S_l + \rho_v S_v] + \frac{1}{A} \frac{\partial}{\partial s} [A \rho_l S_l u_l + A \rho_v S_v u_v] - q_{mass} = 0 \quad (2.85)$$

$$\begin{aligned} \frac{\partial}{\partial t} [\rho_l S_l u_l + \rho_v S_v u_v] + \frac{1}{A} \frac{\partial}{\partial s} [A \rho_l S_l u_l^2 + A \rho_v S_v u_v^2] \\ + \frac{\partial P}{\partial s} + \frac{2}{r} \tau + (\rho_l S_l + \rho_v S_v) g \frac{\partial z}{\partial s} - q_{mom} = 0 \end{aligned} \quad (2.86)$$

$$\begin{aligned} \frac{\partial}{\partial t} \left[ \rho_l S_l \left( h_l + \frac{u_l^2}{2} \right) + \rho_v S_v \left( h_v + \frac{u_v^2}{2} \right) - P \right] \\ + \frac{1}{A} \frac{\partial}{\partial s} \left[ A \rho_l S_l u_l \left( h_l + \frac{u_l^2}{2} \right) + A \rho_v S_v u_v \left( h_v + \frac{u_v^2}{2} \right) \right] \\ + (\rho_l S_l u_l + \rho_v S_v u_v) g \frac{\partial z}{\partial s} + q_{heat} - q_{ener} = 0 \end{aligned} \quad (2.87)$$

This decision was made because they correctly conserve mass, momentum and energy and are the most general form of the three-equation model of those that we reviewed. While alternative (or approximate) representations may have benefits in some cases, e.g., when using the directional solution procedures used in steady-state modelling, we do not think use of approximate conservation equations is justified or necessary in the development of a new transient wellbore simulator.

In order to solve the conservation equations discussed in this chapter, additional equations are required to describe phase slip, wall friction, conductive heat exchange with the formation, and sources of mass, momentum and energy from feed-zones. These equations, known as constitutive models, are discussed in the following chapter.

## Chapter 3

# Constitutive models for geothermal wellbores

The conservation laws, presented in Chapter 2, have more unknowns than the number of equations meaning supplementary constitutive equations are required. In geothermal wellbore modelling, constitutive models account for the effects of relative velocity or slip between the phases, wall friction, heat transfer to and from the surrounding formation, and sources of mass, momentum and energy. The specific choice of constitutive models influences the ability of a simulator to match wellbore data and affects how transient processes evolve with time (Akbar et al., 2016).

This chapter discusses the constitutive models used in our transient wellbore simulator. For each constitutive model, we briefly review the common methods used in the past and justify our selection. The most influential constitutive model, describing phase slip, is discussed in Section 3.2. Shorter discussions on wall friction, heat transfer and source terms are given in Sections 3.3, 3.4 and 3.5, respectively.

Other auxiliary equations are required to define the thermodynamic properties of water in terms of our chosen primary variables. These equations are not reproduced in this work but are summarised in Section 3.6.

### 3.1 Regimes

A wide range of flow conditions are possible within a geothermal wellbore, making it challenging to develop a constitutive model that is accurate for all flow conditions. Of all the required constitutive models, the slip relationship is the most dependent on the flow conditions within the well. Modellers have traditionally separated wellbore flow into different regions, referred to as flow regimes, to tackle this issue. Different constitutive models are then used to represent slip (and sometimes wall friction) depending on the flow regime.

The following four categories, ordered in terms of increasing steam fraction, are commonly used to identify two-phase flow regimes for upwards flow in vertical geothermal wells. Figure 3.1 shows these flow regimes, namely: bubbly, slug, transitional, and annular/mist. Each is discussed below.

**Bubbly flow** is characterised by discrete vapour bubbles dispersed throughout a continuous liquid phase. The bubbles may be non-uniformly distributed throughout the pipe and exhibit a complex motion, coalescing with other bubbles then breaking apart. The volume fraction of vapour is low in this regime but depends on the flow rate. At high flow rates where turbulent fluctuations break up larger bubbles, bubbly flow can persist at higher volume fractions of vapour. Some authors, for example Hasan and Kabir (2010) and Taitel et al. (1980) refer to this latter case as **dispersed bubbly flow**.

**Slug flow**, also referred to as **plug flow**, is characterised by bullet-shaped volumes of vapour, called Taylor bubbles, separated by "slugs" of liquid. This type of flow occurs as smaller vapour bubbles coalesce to form a large bubble, similar in size to the diameter of the pipe. A thin film of liquid surrounds the Taylor bubble, and the liquid slug often contains dispersed small bubbles.

**Transitional flow (churn flow)** occurs when an increase in mass flow and/or enthalpy causes the breakdown of Taylor bubbles into a chaotic and turbulent state in which the phases tend to oscillate or churn. Transitional flow spans a large range of vapour flow rates. At high vapour flow rates, it resembles degenerate annular flow and may be sub-categorised as **semi-annular flow**. In transitional flow, the velocity of the liquid film

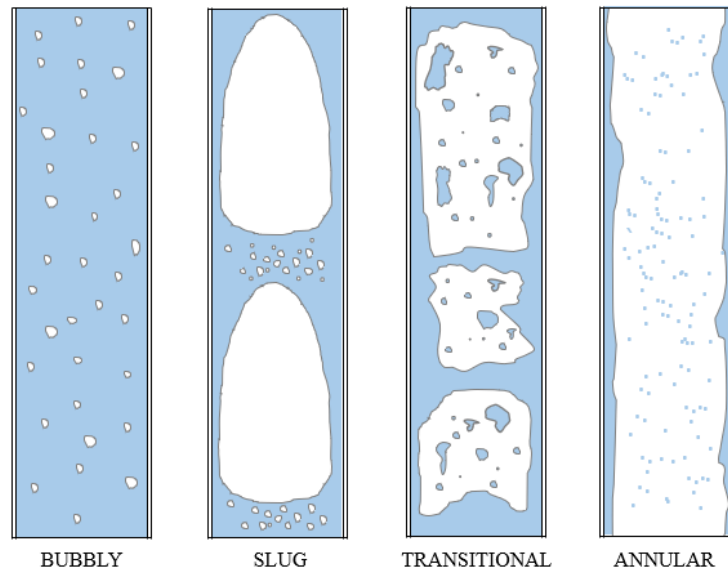


FIGURE 3.1: Regimes for upwards flow in vertical pipes.

can change direction and flow in the opposite direction to the vapour. Alternative names for the transitional flow regime include **froth flow** or **intermittent flow**.

**Annular flow** occurs when a high vapour fraction eliminates liquid slugs resulting in a flow with a continuous vapour core surrounded by a thin liquid film. Liquid drops can be entrained in the vapour phase leading to the alternate name of mist flow. Some authors classify **mist flow** as a separate regime that occurs when there is not enough liquid to sustain a significant film of liquid on the wall (Gunn, 1992).

### 3.1.1 Use of regime-dependent slip models

Regime-dependent slip models have two components: firstly there are equations that define the boundaries between the slip regimes, and secondly there are equations defining slip in each regime. Various regime-dependent slip models have been used in previous steady-state geothermal wellbore models. For example, Duns and Ros (1963), Orkiszewski (1967) and Hadgu (1989) gave regime-dependent slip models that are still in use today. However, these models commonly have discontinuous transitions between the equations used to describe slip in each regime. Orkiszewski's slip model, which is discussed in Section 3.2.2.2 below, suffers from this problem. McGuinness (2015) noted that

discontinuities such as these cause poor convergence and non-physical results in steady-state modelling. McGuinness (2015) smoothed the discontinuities in slip for regime-dependent models given by Duns and Ros (1963), Orkiszewski (1967) and Hadgu (1989) to improve the numerical performance of the steady-state simulator SWELFLO.

Discontinuities in constitutive relationships are expected to cause poor numerical performance in transient simulations. As a result, the regime-dependent models with discrete regime transitions, which are commonplace in the steady-state literature, have been avoided in this work. Thus, a key consideration when choosing the constitutive models for our transient simulator was their ability to vary smoothly as conditions change within the well.

## 3.2 Constitutive models for slip

### 3.2.1 Background

In general, the liquid and vapour phases will flow at different velocities. This behaviour is typically referred to as *phase slip* or simply *slip*. The three-equation model used in our simulator requires the addition of a constitutive model to describe phase slip. This section gives an overview of the formulation of the most common slip models, namely: the velocity ratio, void fraction, hold-up coefficient, drift-flux and relative velocity models. These models use empirical parameters derived from historical wellbore data or laboratory-scale testing to describe phase slip. The specific choice of empirical relationship can influence simulation results significantly, as is shown by García-Valladares et al. (2006), Gudmundsdottir et al. (2013b), Hasan and Kabir (2010), and Akbar et al. (2016). These works indicate that the choice of slip model is one of the most influential factors affecting the ability of a simulator to match wellbore data.

Despite their importance to geothermal wellbore simulation, there is still no single slip model that adequately matches wellbore data in all cases. As a result, most commercial simulators, for example, WELLSIM (Gunn, 1992), SWELFLO (McGuinness, 2015) and GUDRUN (Franz and Clearwater, 2021), provide a list of slip correlations that the user can try to obtain the best match to data for a given well. Common choices



of slip models for steady-state simulators include those by Duns and Ros (1963), Orkiszewski (1967), Hagedorn and Brown (1965), Hadgu (1989) (available in WELLSIM) and Aunzo et al. (1991) (a modified version of Orkiszewski's model used initially in HOLA/GWELL).

Franz and Clearwater (2021) note that several factors limit the performance of these slip models, including:

- their applicability to limited ranges for parameters such as pressure, enthalpy, pipe deviation and diameter,
- the presence of discontinuities in their formulations, which are non-physical and cause poor numerical performance, and
- uncertainty about their formulation due to a lack of clarity in the original publications, which makes validation and verification of their implementation difficult.

Over 100 different slip relationships have been presented in the wider two-phase modelling literature (Ribeiro et al., 2020). Several reviews have investigated the predictive accuracy of different subsets of these slip models (Diener and Friedel, 1998; Vijayan et al., 2000; Woldesemayat and Ghajar, 2007; Godbole et al., 2011; Bhagwat and Ghajar, 2012; Ribeiro et al., 2020). However, these works do not cover the empirical models typically used in geothermal modelling. The data sets used for these comparative studies typically contain thousands of data points from pipe flow experiments presented in the literature. These data sets can include results from horizontal, deviated and vertical pipe flow experiments conducted for various different mass flow rates, pressures and mass fractions. However, the pipe diameter used in these experiments is typically less than 10 cm. This is significantly smaller than the production casing used in geothermal wells, which can range from 7 inches (17.78 cm) for small wells to 13 <sup>3</sup>/<sub>8</sub> inches (33.97 cm) in large diameter wells (Zarrouk and McLean, 2019). Therefore, the correlations suggested in these comparative studies will not necessarily perform well in geothermal applications.

As with the geothermal wellbore modelling literature, there is no consensus on "the best" empirical slip model as each review finds a different model best fits their data. However, a drift-flux correlation by Rouhani and Axelsson (1970), which is referred to as Rouhani

II in this work and is discussed in Section 3.2.2.3 below, has placed within the top three correlations for upwards flow in vertical and inclined pipes in several reviews (Diener and Friedel, 1998; Woldesemayat and Ghajar, 2007; Godbole et al., 2011; Bhagwat and Ghajar, 2012).

Given the issues with the slip models currently used in geothermal wellbore simulators, we believe that they should be systematically reviewed in a similar fashion to the general review papers discussed above. Such a review should assess the ability of each model to reproduce data from flow in vertical and deviated pipes with wide diameters. Additionally, comparisons of the predictive ability of each correlation on geothermal wellbore data should be aimed at determining under what conditions (e.g., wellhead mass flow rate and enthalpy) each correlation performs well. This type of study would hopefully improve the ‘trial and error’ method currently used when simulating geothermal wells.

The review of slip correlations for geothermal applications proposed above is beyond the scope of this thesis. Instead, the remainder of this section provides background on the mathematical formulation of the different models that have been used to describe slip. Following this, Section 3.2.2 outlines the features that we require from an empirical slip model. We then review the empirical models by Rouhani and Axelsson (1970), Orkiszewski (1967) and Shi et al. (2005), which have all been used in other transient geothermal wellbore simulators, and assess whether or not they meet our requirements.

### 3.2.1.1 Velocity ratio model

The velocity ratio (also called the slip ratio),  $S$ , is defined as:

$$S \equiv \frac{u_v}{u_l} = \frac{\rho_l}{\rho_v} \frac{x_{fv}}{1 - x_{fv}} \frac{1 - S_v}{S_v}. \quad (3.1)$$

Here, rearranged versions of (2.26) and (2.25), making  $u_v$  and  $u_l$  the subjects, were used to derive the relationship between velocity ratio, vapour saturation and flowing mass fraction. Solving (3.1) for the vapour saturation gives:

$$S_v = \frac{x_{fv}}{x_{fv} + \frac{\rho_v}{\rho_l}(1 - x_{fv})S} = \frac{1}{1 + S \frac{\rho_v}{\rho_l} \frac{1 - x_{fv}}{x_{fv}}}. \quad (3.2)$$

Many past studies have used empirical correlations for  $S$ , ranging from simple density ratios, for example Chisholm (1973) and Zivi (1964), to complex non-linear functions, for example the correlation by Premoli et al. (1970).

From (2.25), (2.26) and (3.2), the phase velocities in terms of the slip ratio and flowing mass fractions are:

$$u_v = \frac{F_m x_{fv}}{\rho_v S_v} = F_m \left( \frac{x_{fv}}{\rho_v} + S \frac{x_{fl}}{\rho_l} \right), \quad (3.3)$$

and

$$u_l = \frac{F_m x_{fl}}{\rho_l S_l} = \frac{F_m}{S} \left( \frac{x_{fv}}{\rho_v} + S \frac{x_{fl}}{\rho_l} \right). \quad (3.4)$$

Equations (3.2) – (3.4) are important relationships when  $x_{fv}$  is used as a primary variable, which is a common choice in geothermal wellbore modelling.

### 3.2.1.2 Void fraction (vapour saturation) model

Some correlations define the void fraction (or vapour saturation) in terms of other parameters. For example, Butterworth (1975) noted that a number of independently developed correlations (e.g., Lockhart and Martinelli (1949); Baroczy (1966); Harrison (1975); Chen (1986)) share a similar form to (3.2), but without including the slip ratio, namely:

$$S_v = \frac{1}{1 + a \left( \frac{1-x_{fv}}{x_{fv}} \right)^b \left( \frac{\rho_v}{\rho_l} \right)^c \left( \frac{\mu_l}{\mu_v} \right)^d}, \quad (3.5)$$

where  $a$ ,  $b$ ,  $c$  and  $d$  are calculated by fitting (3.5) to experimental data. Some void fraction correlations have a more complex form than (3.5), e.g., Smith (1969) and Dispenza (1987).

### 3.2.1.3 Hold-up coefficient

In this case vapour saturation is given in terms of a hold-up coefficient  $C_A$  (named after Armand (1945) who was an early user of this formula):

$$S_v = C_A \beta. \quad (3.6)$$

Here  $\beta$  is the volumetric gas flow ratio (also called the homogeneous vapour saturation) given by:

$$\beta = \frac{F_{Vv}}{F_{Vv} + F_{Vl}} = \frac{1}{1 + \left( \frac{1-x_{fv}}{x_{fv}} \right) \left( \frac{\rho_v}{\rho_l} \right)}. \quad (3.7)$$

The definition of  $\beta$  in terms of the flowing mass fraction, given in (3.7), is derived by substituting (2.26) and (2.28) into the volume flux ratio, also given in (3.7).

Armand (1945) gave complicated, regime-dependent formulae for  $C_A$ . McGuinness (2015) recommended the following simpler version and adopted it for the simulator SWELFLO:

$$C_A = \frac{1}{\beta + \frac{1-\beta}{\sqrt{1-\beta(1-\rho_v/\rho_l)}}}, \quad (3.8)$$

where  $\beta$  is given by (3.7).

Garg et al. (2004) provided the following formula (rewritten in our notation) for flowing mass fraction in terms of static mass fraction which, using (2.20), can be shown to be equivalent to (3.6) and (3.7):

$$x_{fv} = \frac{x_{sv}}{(1-x_{sv})C_A + x_{sv}(1-\rho_l(1-C_A)/\rho_v)}. \quad (3.9)$$

Garg et al. (2004) gave plots of  $C_A$  as a function of a nondimensional variable  $Z$  that is a product of powers of the Reynolds number, Froude number, flowing liquid volume fraction and liquid saturation.

### 3.2.1.4 Drift-flux model

The drift-flux model was first presented by Zuber and Findlay (1965) and relates the phase velocities to the average volume flux of the fluid using two empirical parameters: the distribution coefficient,  $C_0$ , and the drift velocity,  $u_d$ . In this model the vapour velocity is given by:

$$u_v = C_0 F_V + u_d, \quad (3.10)$$

and the liquid velocity is given by:

$$u_l = \left( \frac{1-S_v C_0}{1-S_v} \right) F_V - \left( \frac{S_v}{1-S_v} \right) u_d. \quad (3.11)$$

Here,  $F_V$  is the total volume flux. The distribution coefficient,  $C_0$ , models the combined effect of variations in saturation and velocity across the wellbore. For example, the vapour phase will tend to congregate in the centre of a pipe due to viscous wall effects. The average drift velocity,  $u_d$ , describes the tendency of the vapour phase to travel faster than the fluid mixture, for example, due to buoyancy effects (Shi et al., 2005). The parameters  $C_0$  and  $u_d$  are calculated using empirical models.

The steady-state geothermal wellbore simulator developed by Hasan and Kabir (2010) uses a regime dependent drift-flux model. Although, instead of solving (3.10) for the vapour velocity, they substitute (2.12) into (3.10) and rearrange for vapour saturation to get:

$$S_v = \frac{F_{Vv}}{C_0 F_V + u_d}. \quad (3.12)$$

Some authors (e.g., Pan, Oldenburg, Wu and Pruess (2011) and Akbar et al. (2016)) formulate the drift-flux model in terms of the mixture velocity (or mass flux). To do this, it is useful to define the relationship between mass flux and volume flux in terms of  $C_0$  and  $u_d$ . Substituting (3.10) and (3.11) into (2.23) and rearranging for volume flux gives:

$$F_V = \frac{\rho_{mix}}{\rho_{mix}^*} u_{mix} + \frac{S_v(\rho_l - \rho_v)}{\rho_{mix}^*} u_d, \quad (3.13)$$

where the profile adjusted density of the fluid mixture,  $\rho_{mix}^*$ , is defined by Pan, Oldenburg, Wu and Pruess (2011) as:

$$\rho_{mix}^* = S_v C_0 \rho_v + (1 - S_v C_0) \rho_l. \quad (3.14)$$

Substituting (3.13) back into (3.10) and (3.11) gives the phase velocities in terms of the mixture velocity (or mass flux using (2.24)):

$$u_v = \left( C_0 \frac{\rho_{mix}}{\rho_{mix}^*} \right) u_{mix} + \left( \frac{\rho_l}{\rho_{mix}^*} \right) u_d, \quad (3.15)$$

and

$$u_l = \left( \frac{(1 - S_v C_0) \rho_{mix}}{(1 - S_v) \rho_{mix}^*} \right) u_{mix} - \left( \frac{\rho_v S_v}{(1 - S_v) \rho_{mix}^*} \right) u_d. \quad (3.16)$$

Pan, Oldenburg, Wu and Pruess (2011) implemented the empirical drift-flux model given by Shi et al. (2005), presented in Section 3.2.2.4, using (3.15) and (3.16).

Some authors use a simplified drift-flux model with  $C_0 = 1$ . In this case, (3.10) and (3.11) simplify to:

$$u_v = F_V + u_d, \quad (3.17)$$

and

$$u_l = F_V - \frac{S_v}{1 - S_v} u_d. \quad (3.18)$$

The best example of this simplified drift-flux model in a geothermal context is the regime dependent slip model used by Bjornsson (1987) and Aunzo et al. (1991), which is based on regime transitions given by Orkiszewski (1967). These correlations, presented in Section 3.2.2.2 below, were also presented by McGuinness (2015) as the modified Orkiszewski correlation.

Orkiszewski's (1967) original slip model has been used in several geothermal wellbore simulators, for example, Upadhyay et al. (1977), Chierici et al. (1981), Ortiz-Ramirez (1983), Chadha et al. (1993). Most notably, Orkiszewski's correlation set (or the modified version from GWELL) is included as an option in WELLSIM (Gunn, 1992), SWELFLO (McGuinness, 2015) and REGIN (Franz and Clearwater, 2021), all of which are commercially available steady-state simulators.

Equations (3.10)-(3.18) are useful for calculating the phase velocities when the saturation and total volume flow (or total mass flow) are known. However, as discussed in Section 2.1.1.4, the flowing mass fraction is often known (from wellhead measurements or as a primary variable), and the fluid saturation must be determined. To do this, (2.26) and (2.28) are substituted into (3.12), which after rearranging gives:

$$S_v = \frac{x_{fv}}{C_0 \left( x_{fv} + \frac{\rho_v}{\rho_l} (1 - x_{fv}) \right) + \frac{A \rho_v u_d}{Q_m}}. \quad (3.19)$$

Geothermal wellbore simulators developed by García-Valladares et al. (2006), Gudmundsdottir (2012) and Akbar et al. (2016) implement drift-flux models by Rouhani

and Axelsson (1970) using (3.19). Rouhani and Axelsson's (1970) correlations are discussed further in Section 3.2.2.3. Akbar et al. (2016) also implement the drift-flux model given by Shi et al. (2005) in this way.

We note the similarity between the equations for calculating  $S_v$  from  $x_{fv}$  given in (3.2) and (3.19) for the slip ratio and drift-flux models. A relationship between these two slip models can be derived by substituting (2.28) and (3.3) into (3.10) and rearranging to get:

$$S = C_0 + (C_0 - 1) \frac{\rho_l}{\rho_v} \left( \frac{x_{fv}}{1 - x_{fv}} \right) + \frac{\rho_l}{F_m(1 - x_{fv})} u_d. \quad (3.20)$$

For the case where  $C_0 = 1$ , (3.20) simplifies to:

$$S = 1 + \frac{\rho_l}{F_m(1 - x_{fv})} u_d = 1 + \frac{u_d}{F_{vl}}. \quad (3.21)$$

### 3.2.1.5 Relative velocity model

Some authors, for example Miller (1980b), model slip using the relative velocity which is defined as the difference between the average velocity of each phase:

$$u_r = u_v - u_l. \quad (3.22)$$

Miller (1980b) and Goyal et al. (1980) used empirical, regime dependent correlations for evaluating  $u_r$  in terms of other quantities, based on a modified version of the flow regimes and slip correlations compiled by Duns and Ros (1963) and modified by Orkiszewski (1967).

To compare (3.22) with the drift-flux model, (3.11) can be rearranged to give:

$$u_l = \frac{1 - C_0 S_v}{C_0(1 - S_v)} u_v - \frac{1}{C_0(1 - S_v)} u_d. \quad (3.23)$$

In the case where  $C_0 \approx 1$  (an approximation made in models used by Bjornsson (1987), Aunzo et al. (1991) and Pan, Oldenburg, Wu and Pruess (2011), for example) then a comparison of (3.22) and (3.23) gives:

$$u_d \approx (1 - S_v) u_r, \quad (3.24)$$

which highlights the difference between  $u_d$  and  $u_r$ .

Finally, to calculate the vapour saturation using  $u_r$ , we substitute (2.11) and (2.12) into (2.10). After rearranging, this results in a quadratic in  $S_v$ , which when solved gives:

$$S_v = 0.5 \left[ 1 + \frac{F_V}{u_r} - \left( \left( 1 + \frac{F_V}{u_r} \right)^2 - 4 \frac{F_{Vv}}{u_r} \right)^{1/2} \right]. \quad (3.25)$$

Orkiszewski's (1967) original regime-dependent slip model used (3.25) to calculate  $S_v$ , using  $u_r = 0.24$  m/s for the bubble regime.

Equation (3.25) allows the saturation to be calculated from the flowing mass fraction,  $x_{fv}$ , by first calculating the vapour and total volume fluxes using (2.26) and (2.28), respectively.

### 3.2.2 Slip models used in transient wellbore simulators

One of the main goals of this thesis is to model transient counter-flow processes in geothermal wells. Given this objective, we required a slip model that:

- accurately represents flow in large diameter, deviated pipes,
- has a smooth and differentiable form suitable for transient simulation, and
- is able to model counter-flow.

The best choice of slip model for our work, given these requirements, was not obvious. In this section, we review the empirical models used in past transient geothermal wellbore simulators. Our review does not cover the slip models used in steady-state geothermal wellbore simulators (other than a modified version of Orkiszewski's (1967) correlation by Aunzo et al. (1991)) due to their applicability to limited data ranges, the presence of discontinuities in their formulations, and uncertainty about their exact formulation.

From our review, we determined that the drift-flux correlation given by Shi et al. (2005) best fulfilled our requirements and was, therefore, selected for use in our simulator. We briefly discuss some of the other slip models considered and the reasons for our choice in the following sections.



### 3.2.2.1 Homogeneous slip model

The homogeneous slip model assumes the two phases are flowing at the same average velocity. The homogeneous slip model is considered to be reasonably accurate for flows with high vapour saturation (known as mist flow) where the entrained liquid droplets are travelling at approximately the same velocity as the vapour phase or for wells with high mass flow rates (Thome, 2006).

The homogeneous slip model simply states:

$$u_v = u_l. \quad (3.26)$$

Homogeneous flow can be considered as a special case of any of the different slip models presented above, for example,  $S = 1$  when using the slip ratio definition,  $C_0 = 1$  and  $u_d = 0$  when using the drift-flux model or  $C_A = 1$  when using a hold-up coefficient. However, the relative velocity model gives the simplest, and most intuitive, description of homogeneous conditions:

$$u_r = u_v - u_l = 0. \quad (3.27)$$

The homogeneous model is the simplest description of slip and was the first description of slip implemented in our simulator. It was used in the development and testing of the numerical implementation discussed in the following chapter. However, the homogeneous model cannot accurately represent general wellbore flow and, by definition, cannot model counter-flow. It, therefore, does not meet the requirements for our transient simulator.

### 3.2.2.2 Orkiszewski's regime dependent slip model (WELLBORE/GWELL)

The first transient geothermal wellbore simulator, named WELLBORE, was developed by Miller (1980b) and implemented a modified form of Orkiszewski's (1967) regime-dependent slip model. However, the way these equations are implemented is not clear in Miller's (1980b) original report. Specifically, it is not clear whether Miller (1980b) incorrectly used velocities rather than volume fluxes when implementing Orkiszewski's regime boundaries. Additionally, the equation describing the slip within the bubbly

regime appears to be a drift-flux equation (originally given by Zuber and Findlay (1965)) rather than an equation for relative velocity.

Given these issues with WELLBORE's documentation, we have presented here the drift-flux model originally used in GWELL (Bjornsson, 1987; Aunzo et al., 1991). However, we make use of the dimensional correction in (3.29) made by McGuinness (2015). This model is expected to be similar to Miller's intended implementation and is defined in Table 3.1.

This slip model separates flow into the bubbly, slug, transitional and mist regimes. A different equation for slip is solved for each regime. These are summarised in Table 3.1. The regime boundaries in this slip model are defined by Orkiszewski (1967) using the empirical parameters  $L_B$ ,  $L_s$  and  $L_m$ , which are defined below.

The bubbly-slug boundary is defined as:

$$L_B = \beta, \quad (3.28)$$

where:

$$L_B = \max(1.071 - 0.7275F_V^2/d, 0.13). \quad (3.29)$$

Here,  $d$  is the pipe diameter and the vapour volume flux ratio (homogeneous vapour saturation) is:

$$\beta = \frac{F_{Vv}}{F_V}. \quad (3.30)$$

Equation (3.28) means that bubbly flow occurs when  $\beta < L_B$  and slug flow occurs when  $\beta \geq L_B$ .

Similarly, the slug-transitional regime boundary is defined as:

$$u_{vD} = L_s, \quad (3.31)$$

where:

$$L_s = 50 + 36u_{vD} \frac{F_{Vl}}{F_{Vv}}, \quad (3.32)$$

and the dimensionless vapour velocity was defined by Orkiszewski (1967) as:

$$u_{vD} = F_{Vv} \left( \frac{\rho_l}{g\sigma_{vl}} \right)^{0.25}. \quad (3.33)$$

Here,  $\sigma_{vl}$  is the surface tension between the vapour and liquid phases.

Finally, the transitional-mist regime boundary is defined as:

$$u_{vD} = L_m, \quad (3.34)$$

where:

$$L_m = 75 + 84 \left( u_{vD} \frac{F_{Vl}}{F_{Vv}} \right)^{0.75} \quad (3.35)$$

The limits of each regime, which are defined by the equations above, are summarised in Table 3.1 below.

To plot the boundaries between each regime, (3.28) – (3.35) are solved for  $x_{fv}$  at various mass flow rates using a fixed temperature (or pressure) and pipe diameter. Brent's method is used as these equations are non-linear. Figure 3.2 plots the regime boundaries for a well with a diameter of 0.2 m at 250 °C (for total mass flow rates below 350 kg/s). Plots such as Figure 3.2 are commonly referred to as flow maps.

Figure 3.3 plots vapour saturation (predicted using the slip model) vs. flowing vapour mass fraction for Orkiszewski's (1967) model. Plots such as this are useful for comparing

TABLE 3.1: Orkiszewski (1967) regime boundaries and GWELL's drift velocity equations as described by McGuinness (2015).

Flow Regime	Regime limits	Drift velocity [m/s]
Bubbly	$\beta < L_B$	$1.53 \left( \frac{\sigma_{vl}g(\rho_l - \rho_v)}{\rho_l^2} \right)^{0.25}$
Slug	$\beta \geq L_B; u_{vD} < L_s$	$0.35 \sqrt{gd(1 - \frac{\rho_v}{\rho_l})}$
Transitional	$L_s \leq u_{vD} \leq L_m$	$0.35 \sqrt{gd(1 - \frac{\rho_v}{\rho_l})} \left( \frac{L_m - u_{vD}}{L_m - L_s} \right)$
Mist	$u_{vD} > L_m$	0

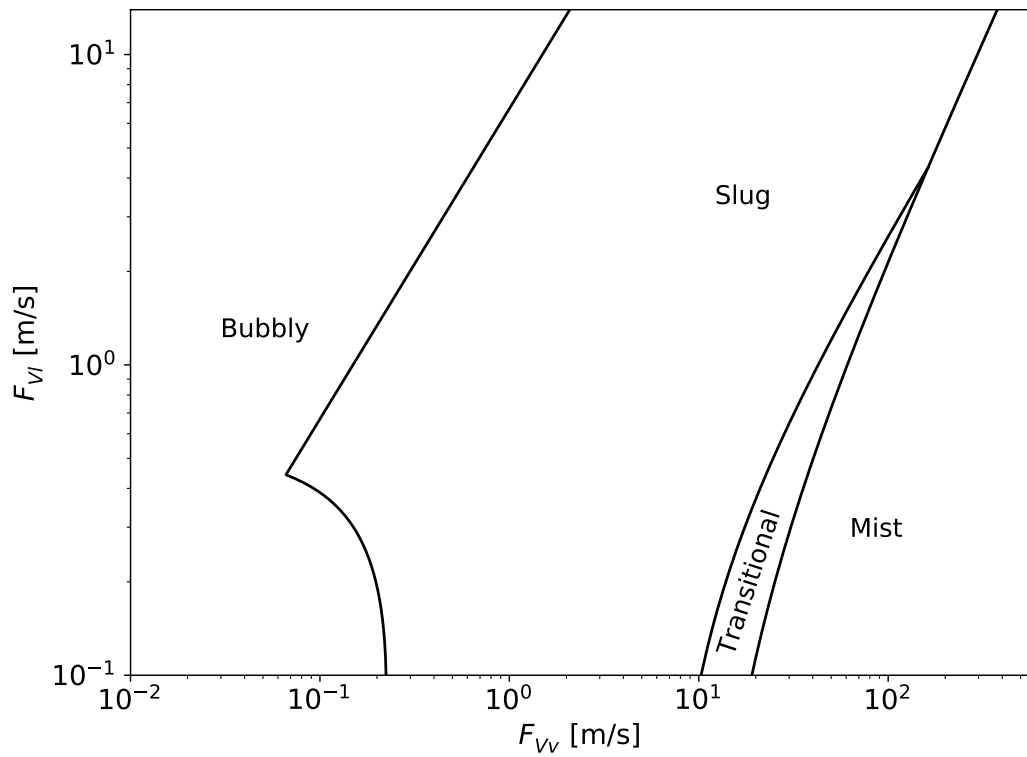


FIGURE 3.2: Orkiszewski's regime boundaries for  $T = 250\text{ }^{\circ}\text{C}$  and  $d = 0.2\text{ m}$ .

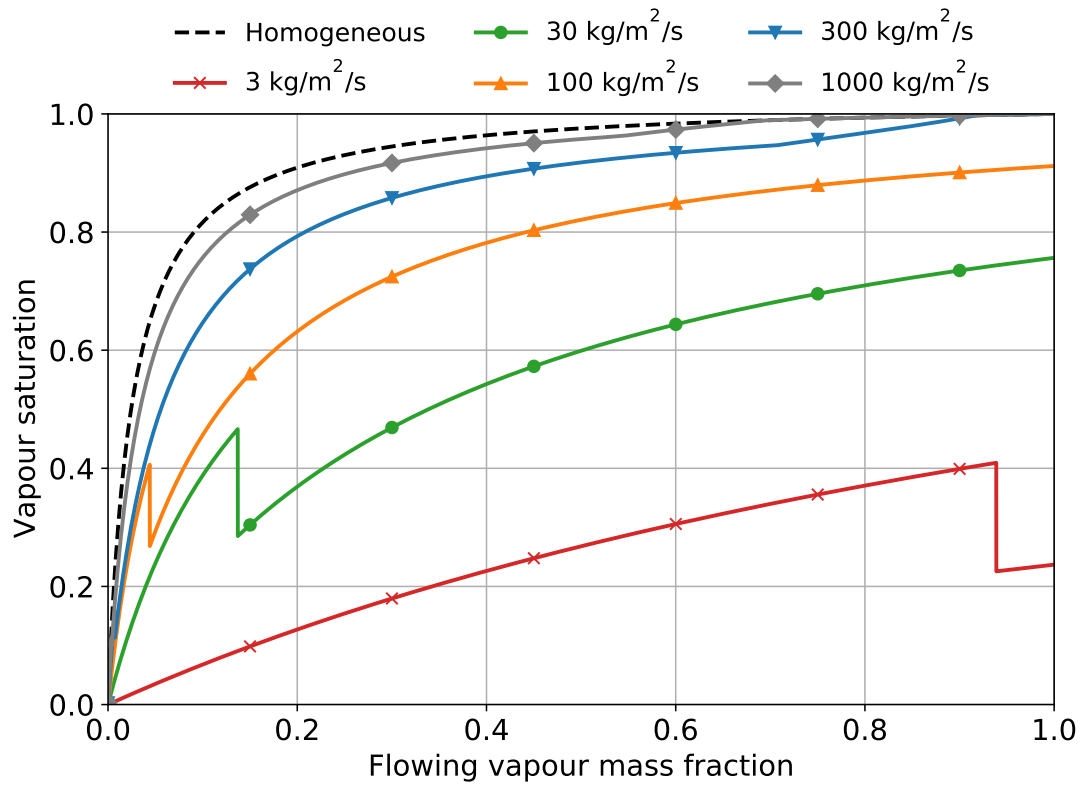


FIGURE 3.3: Saturation vs. flowing mass fraction for various mass flux values calculated using GWELL's slip model as described by McGuinness (2015) (without smoothing).

All mass flow rates were run using  $T = 250\text{ }^{\circ}\text{C}$  and  $d = 0.2\text{ m}$ .

different slip models. Figure 3.3 shows that this drift-flux model approaches homogeneous conditions as the total mass flow increases. The discontinuous transition between the bubbly and slug regime is shown clearly by the profiles for the 3 - 100 kg/m<sup>2</sup>/s cases.

A version of Orkiszewski's model is included in all of the simulators currently used in industry, for example, WELLSIM, SWELFLO and GUDRUN. However, it is not appropriate for use in our simulator for two reasons. Firstly, the discontinuity between the bubble and slug regimes will cause numerical difficulties in transient simulations (although, we do note that the version of this correlation by McGuinness (2015) has smooth regime transitions). Secondly, this model cannot be used in counter-flow simulations (McGuinness, 2015).

### 3.2.2.3 Rouhani and Axelsson (1970) drift-flux model

Empirical correlations by Rouhani and Axelsson (1970) were used in transient geothermal simulators developed by García-Valladares et al. (2006) and Akbar et al. (2016). However, there is uncertainty in the literature as to the correct form of this relationship. The original work by Rouhani and Axelsson (1970) gives the following formulae for the distribution parameter and drift velocity:

$$C_0 = \begin{cases} 1.54 & F_m < 200 \\ 1.12 & F_m \geq 200 \end{cases}, \quad (3.36)$$

and

$$u_d = 1.18 \left[ \frac{g\sigma_{vl}(\rho_l - \rho_v)}{\rho_l^2} \right]^{1/4}. \quad (3.37)$$

Here,  $\sigma_{vl}$  is the surface tension between the vapour and liquid phases. We refer to this correlation as Rouhani I.

The discontinuity in  $C_0$  causes the step change in the plot of saturation vs. flowing mass fraction shown in Figure 3.4 as the mass flux increases past 200 kg/m<sup>2</sup>/s. These discontinuities are also evident in the phase velocities, which are calculated using (3.10) and (3.11), that are shown in Figure 3.5. Discontinuities such as these will cause difficulties in modelling even the simplest wellbore start-up processes.

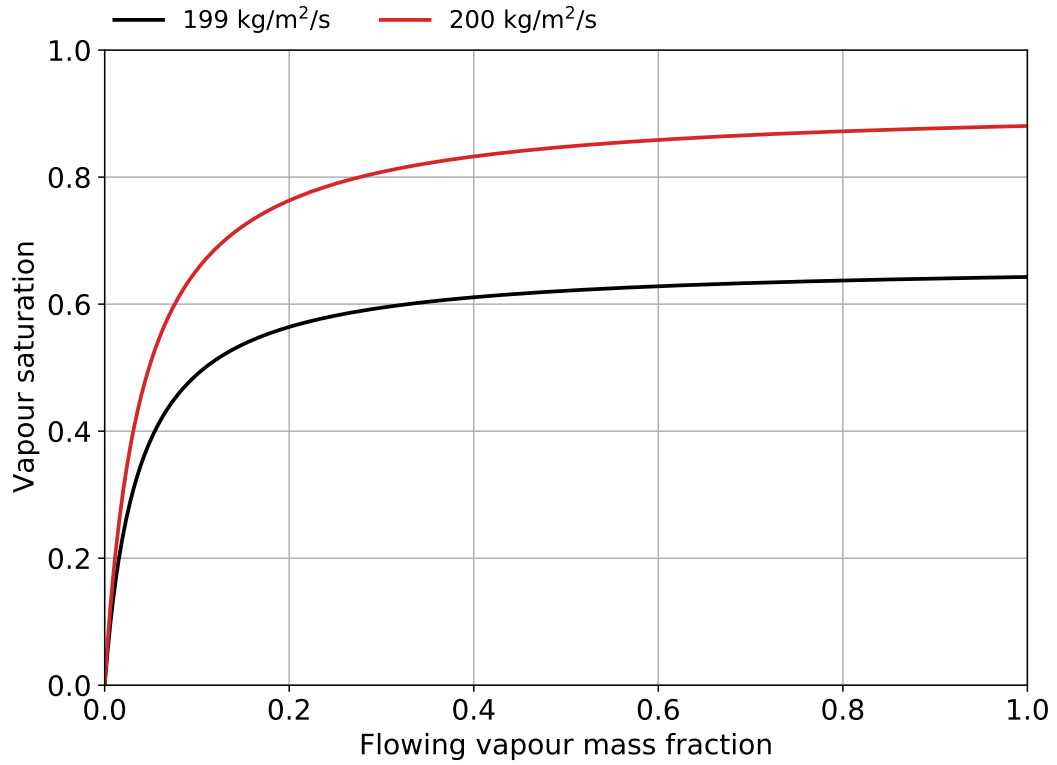


FIGURE 3.4: Discontinuities in predicted vapour saturation due to a small change in mass flux calculated using  $T = 250\text{ }^{\circ}\text{C}$  and  $d = 0.2\text{ m}$  when using Rouhani I.

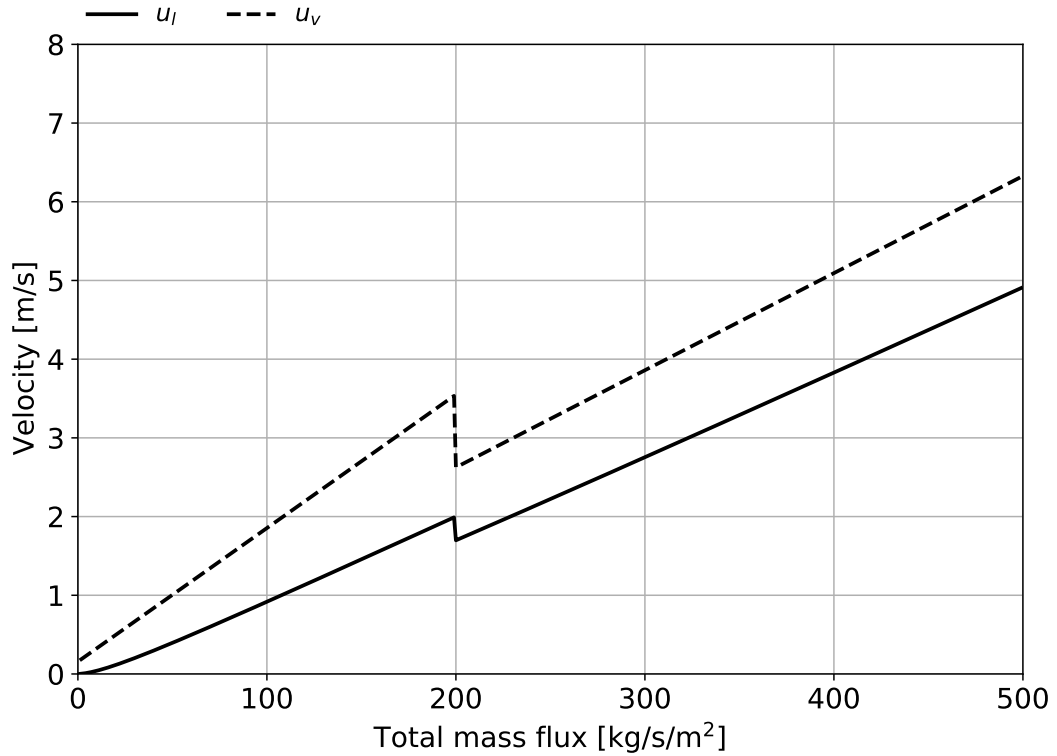


FIGURE 3.5: Discontinuities in phase velocities calculated using  $T = 250\text{ }^{\circ}\text{C}$ ,  $x_{fv} = 0.1$  and  $d = 0.2\text{ m}$  when using Rouhani I.

García-Valladares et al. (2006) and Gudmundsdottir (2012) also attribute a drift-flux relationship to Rouhani and Axelsson (1970). However, their formulae differ from those given in this original work. García-Valladares et al. (2006) and Gudmundsdottir (2012) give:

$$C_0 = 1 + 0.12(1 - x_{fv}), \quad (3.38)$$

and

$$u_d = 1.18(1 - x_{fv}) \left[ \frac{g\sigma_{vl}(\rho_l - \rho_v)}{\rho_l^2} \right]^{1/4}, \quad (3.39)$$

which we call Rouhani II. The main difference between Rouhani I and Rouhani II is that the formulae in Rouhani II are weighted by  $(1 - x_{fv})$ . This weighting drives  $C_0 \rightarrow 1$  and  $u_d \rightarrow 0$ , i.e. towards homogeneous conditions, as the flowing vapour mass fraction,  $x_{fv}$ , increases.

The basis of these drift-flux formulae is even more confused as Akbar et al. (2016) attribute two drift-flux models to Rouhani and Axelsson (1970): the first is the same as (3.36) and (3.37) whereas the second uses (3.39) for  $u_d$  and the following formula for  $C_0$ :

$$C_0 = \begin{cases} 1 + 0.2(1 - x_{fv}) & S_v < 0.1 \\ 1 + 0.2(1 - x_{fv}) \left( \frac{gd\rho_l^2}{F_m^2} \right)^{1/4} & S_v \geq 0.1 \end{cases}, \quad (3.40)$$

where  $d$  is the internal diameter of the well and  $g$  is the gravitational constant. We refer to this correlation as Rouhani III.

Figure 3.6 compares plots of saturation vs. mass fraction for the three versions of Rouhani and Axelsson (1970) for a mass flux of 250 kg/m<sup>2</sup>/s and shows significant differences in the vapour saturation predicted by each model. Of the three models, Rouhani II is the only one that performs relatively well over a wide range of co-current flow conditions according to several extensive reviews of slip models (Diener and Friedel, 1998; Woldesemayat and Ghajar, 2007; Godbole et al., 2011; Bhagwat and Ghajar, 2012). This makes Rouhani II the best candidate of the three for modelling the flow in production wells, however, its formulation presented difficulties when modelling counter-flow or cases where the flow direction changes. This is because the Rouhani II and III formulae are functions of  $x_{fv}$ . The flowing vapour mass fraction is defined as  $x_{fv} = Q_{mv}/Q_m$  making  $x_{fv}$  and therefore  $C_0$  and  $u_d$ , undefined when total mass flow,  $Q_m$ , is zero.

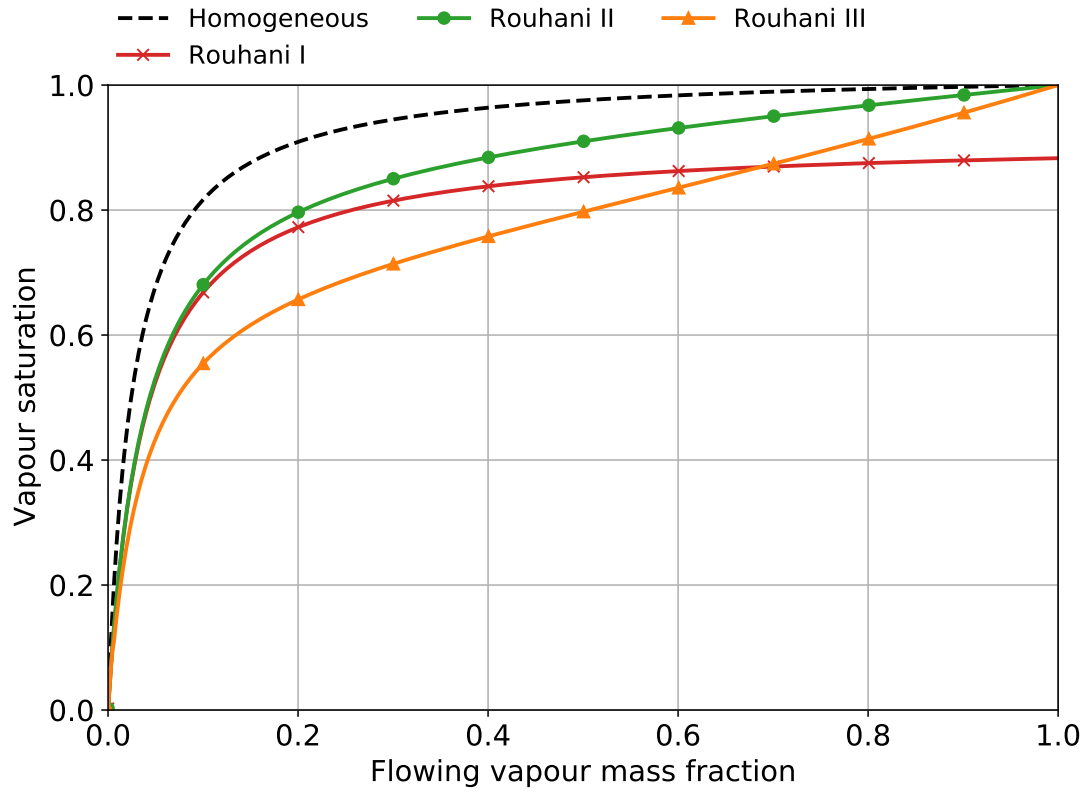


FIGURE 3.6: Comparison of Rouhani I, Rouhani II and Rouhani III for  $F_m = 250$  kg/s/m<sup>2</sup>,  $T = 250$  °C and  $d = 0.2$  m.

Given the discontinuities in Rouhani I and the flowing mass fraction weighting in Rouhani II and III, we decided that none of the Rouhani correlations were appropriate for our simulator.

#### 3.2.2.4 Shi et al. (2005) drift-flux model

Shi et al. (2005) presented functions for  $C_0$  and  $u_d$  that change smoothly as conditions change within the well. Their empirical relationships were optimised for use in wide-diameter (15 cm), deviated pipes using experimental data from Oddie et al. (2003). This makes their model well suited for geothermal applications. Pan, Oldenburg, Wu and Pruess (2011) modified Shi et al.'s (2005) original formulation for application in their simulator T2WELL.

Shi et al.'s (2005) model is based on two flow regimes, each using a different equation for  $u_d$ . The bubbly regime, as described above, applies to low vapour saturation cases. The second flow regime, called the film-flooding regime, applies to higher saturation values.



This model avoids discontinuities between slip models by using linear interpolation, based on the vapour saturation, to transition between the two regimes. The saturation range over which this transition occurs was chosen to best reproduce the experimental data from Oddie et al. (2003). Pan, Oldenburg, Wu and Pruess (2011) replaced this linear transition with the smooth function given in (3.43) below to ensure the drift velocity and its derivatives were continuous over the entire range of vapour saturation.

The Shi et al. (2005) drift-flux model is used in our wellbore simulator. It was chosen because of its optimisation for wide-diameter, deviated wells, as well as its smooth functional form. Additionally, the dependence of this relationship on saturation (rather than flowing mass fraction) makes it suitable for modelling counter-flow, a process of interest in this work. We make use of some of the modifications made by Pan, Oldenburg, Wu and Pruess (2011), these are noted below.

In this model, the drift velocity is a function of vapour saturation,  $S_v$ , the phase densities,  $\rho_v$  and  $\rho_l$ , the characteristic velocity,  $u_c$ , the Kutateladze number  $K_u$ , the shape parameter  $C_0$ , and inclination function,  $m(\theta)$ :

$$u_d = m(\theta) \frac{(1 - S_v C_0) K(S_v, K_u, C_0)}{S_v C_0 \sqrt{\rho_v / \rho_l} + 1 - S_v C_0} u_c. \quad (3.41)$$

Despite its complex form, (3.41) is an explicit function of pressure, saturation, and volume flux. Although, as we discuss below, (3.41) is a function of pressure and saturation only in our implementation.

In (3.41) the characteristic velocity,  $u_c$ , is given by Harmathy (1960) as:

$$u_c = \left( \frac{\sigma_{vl} g (\rho_l - \rho_v)}{\rho_l^2} \right)^{1/4}, \quad (3.42)$$

where,  $\sigma_{vl}$  is the surface tension between the vapour and liquid phases.

The function  $K(S_v, K_u, C_0)$  is used to transition between the bubble rise and the film

flooding regimes. As mentioned above, Pan, Oldenburg, Wu and Pruess (2011) replaced the original linear interpolation with the following smooth and differentiable function:

$$K(S_v, K_u, C_0) = \begin{cases} 1.53 & S_v \leq a_1 \\ 1.53 + \frac{C_0 K_u - 1.53}{2} \left[ 1 - \cos \left( \pi \frac{S_v - a_1}{a_2 - a_1} \right) \right] & a_1 < S_v < a_2 \\ C_0 K_u & S_v \geq a_2 \end{cases} \quad (3.43)$$

Here,  $a_1$  and  $a_2$  are the vapour saturations at which the regime transition starts and ends. Shi et al. (2005) found their optimal values to be  $a_1 = 0.06$  and  $a_2 = 0.21$ .

In (3.43),  $K_u$  is the Kutateladze number, calculated following Pan, Oldenburg, Wu and Pruess (2011) as:

$$K_u = \left[ \frac{C_{ku}}{\sqrt{N_b}} \left( \sqrt{1 + \frac{N_b}{C_{ku}^2 C_w}} - 1 \right) \right]^{1/2}, \quad (3.44)$$

where  $C_w$  is a wall friction factor that Richter (1981) approximated as 0.008. Pan, Oldenburg, Wu and Pruess (2011) set  $C_{ku} = 142$  (rather than 75 as was done by Richter (1981)) to improve the fit of  $K_u$  to data.

The Bond number,  $N_b$ , in (3.44) is defined as:

$$N_b = d^2 \left( \frac{g(\rho_l - \rho_v)}{\sigma_{vl}} \right), \quad (3.45)$$

where  $d$  is the wellbore diameter.

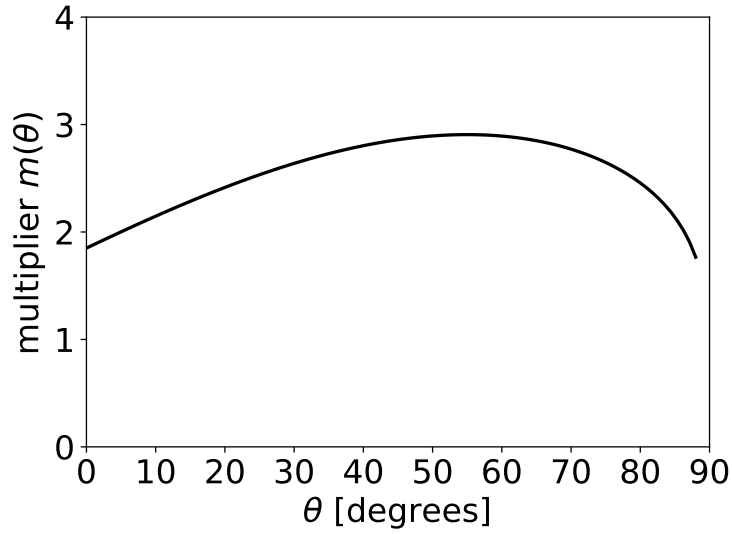
The drift velocity is modified for flow in deviated wells (up to  $88^\circ$  from vertical) using  $m(\theta)$ , defined as:

$$m(\theta) = 1.85(\cos \theta)^{0.21}(1 + \sin \theta)^{0.95}. \quad (3.46)$$

Figure 3.7 plots  $m(\theta)$  against the pipe deviation from vertical. Note that  $m(\theta) = 1.85$  for flow in vertical pipes.

The profile parameter,  $C_0$ , used in (3.41) and (3.43) is calculated as described in Shi et al. (2005), i.e.:

$$C_0 = \frac{C_{max}}{1 + (C_{max} - 1)\eta^2}. \quad (3.47)$$

FIGURE 3.7: Multiplier that modifies  $u_d$  for flow in deviated wells.

Here,  $\eta$  is:

$$\eta = \frac{\beta - B}{1 - B} \quad \text{for } 0 \leq \beta \leq 1, \quad (3.48)$$

where  $B$  is the threshold parameter where  $C_0$  starts to drop below  $C_{max}$  calculated as (Pan, Oldenburg, Wu and Pruess, 2011):

$$B = \frac{2}{C_{max}} - 1.0667, \quad (3.49)$$

and  $\beta$  is calculated from Shi et al. (2005) as:

$$\beta = \max \left( S_v, A_0 \frac{S_v |F_V|}{u_{sfg}} \right). \quad (3.50)$$

Here, the vapour superficial ‘flooding’ velocity,  $u_{svf}$  is calculated as:

$$u_{svf} = K_u \left( \frac{\rho_l}{\rho_g} \right)^{1/2} u_c, \quad (3.51)$$

and  $A_0$  is a constant that controls how quickly  $C_0$  tends to one with increases in saturation. In T2WELL, Pan, Oldenburg, Wu and Pruess (2011) provide the option of choosing either  $C_{max} = 1$  or  $C_{max} = 1.2$  in (3.47). However, the optimised model by Shi

et al. (2005), which is used in this work, sets  $C_{max} = 1$ . In this case (3.47) gives:

$$C_0 = \frac{1}{1 + (1 - 1)\eta^2} = 1. \quad (3.52)$$

Clearly,  $C_0 = 1$  regardless of any of the other tunable parameters in (3.48)–(3.51). As  $\beta$  (given in (3.50)) is the only parameter that depends on volume flux in our implementation,  $u_d$  can be calculated explicitly knowing only pressure and saturation of the fluid as (3.41) simplifies to:

$$u_d = m(\theta) \frac{(1 - S_v) K(S_v, K_u)}{S_v \sqrt{\rho_v / \rho_l} + 1 - S_v} u_c. \quad (3.53)$$

Figure 3.8 shows profiles of saturation vs. flowing mass fraction for varying mass fluxes. The smooth nature of the equation is evident. Crucially, the solution procedure described above does not require the flowing mass fraction and does not involve any division by total mass flux, meaning that  $C_0$  and  $u_d$  are well defined for counter-flow cases.

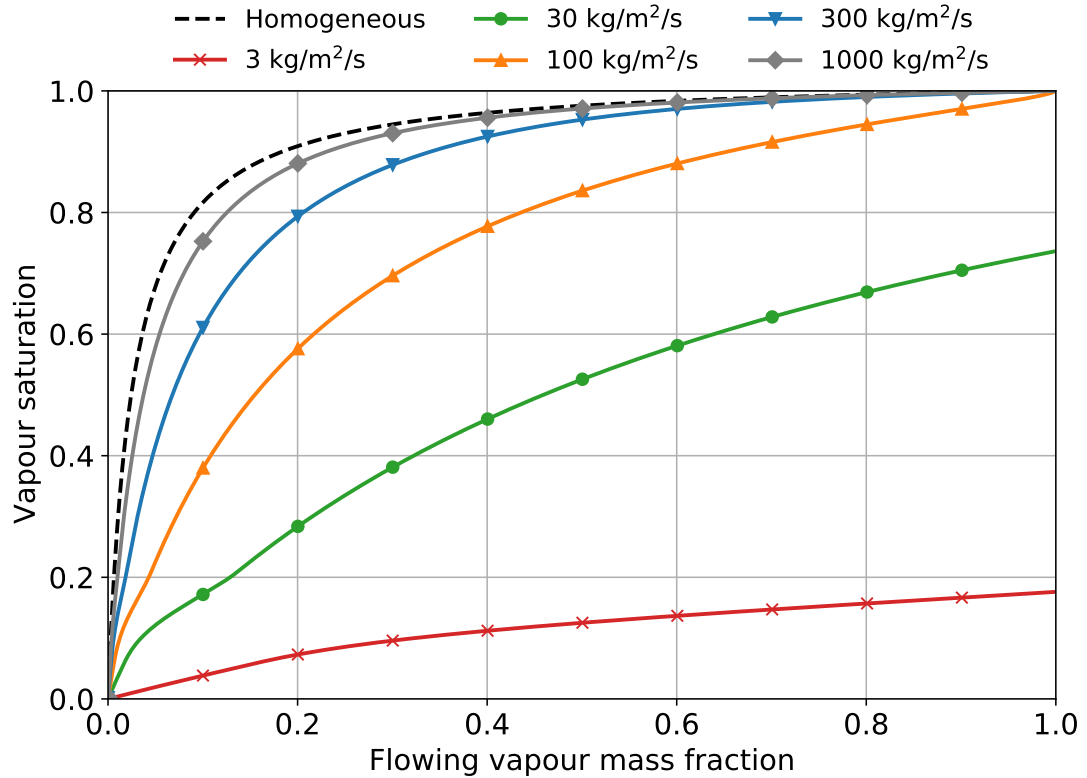


FIGURE 3.8: Slip model by Shi et al. (2005), using the method described in 3.2.2.4, run for varying mass fluxes using  $T = 250$  °C and  $d = 0.2$  m.

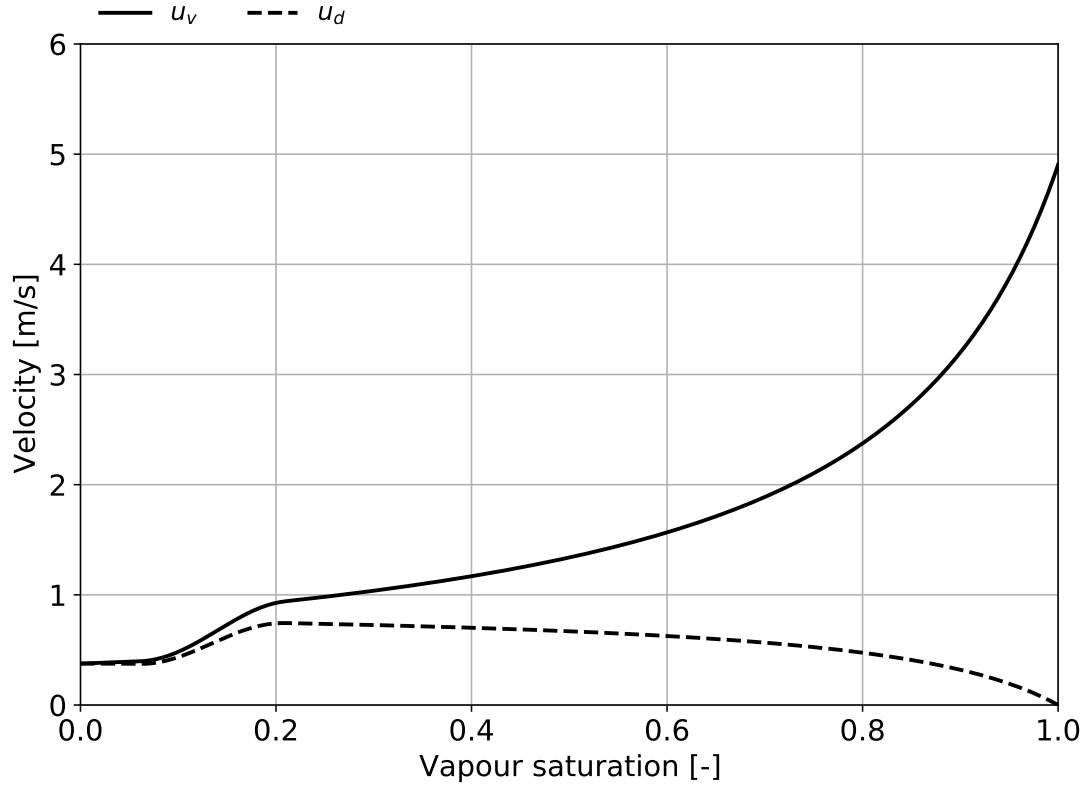


FIGURE 3.9: Vapour and drift velocities in a stagnant liquid ( $u_l = 0$ ) for  $T = 250$  °C. This represents the minimum vapour velocity to prevent down-flow.

Figure 3.9 plots the upper limit of the counter-flow regime as defined by Shi et al.'s (2005) drift-flux model. This is the minimum vapour velocity required to prevent liquid down-flow. This velocity is calculated by substituting  $u_l = 0$  into (3.10) and rearranging for  $u_v$ .

### 3.3 Wellbore friction

A constitutive equation is required to describe the frictional effects of the pipe wall on flow within the well. These frictional forces appear in the conservation of momentum equation (2.54) and are represented by the symbol  $\tau$ . Modelling frictional effects for single-phase pipe flow is well understood, as outlined in Section 3.3.1. For two-phase flow, there are two predominant methods used in the literature, which are discussed and compared in Section 3.3.2.

### 3.3.1 Single-phase flow

The frictional loss for single-phase flow in pipes is well understood. For single-phase flow, the contribution of wall friction to the pressure gradient is given by:

$$\frac{2}{r}\tau_{sp} = \frac{f}{4r}\rho u|u|. \quad (3.54)$$

Here,  $f$  is the Darcy friction factor. For laminar flow ( $Re < 2400$ ),  $f$  is given by:

$$f = \frac{64}{Re}, \quad (3.55)$$

where  $Re$  is the Reynolds number, defined as

$$Re = \frac{\rho u d}{\mu}. \quad (3.56)$$

Here,  $\mu$  is the dynamic viscosity of the single-phase fluid and  $d$  is the internal diameter of the wellbore.

For turbulent flow ( $Re \geq 2400$ ) the Colebrook-White equation (Colebrook, 1939),

$$\frac{1}{\sqrt{f}} = -2 \log_{10} \left( \frac{\epsilon}{3.7d} + \frac{2.51}{Re\sqrt{f}} \right), \quad (3.57)$$

is solved implicitly for  $f$ . In (3.57),  $\epsilon$  is the absolute roughness of the wellbore material.

Many approximations of the Colebrook-White equation exist, Moody's equation,

$$f = 0.0055 \left[ 1 + \left( 2 \times 10^4 \frac{\epsilon}{d} + \frac{10^6}{Re} \right)^{1/3} \right], \quad (3.58)$$

is also provided as a more computationally efficient option in our simulator.

### 3.3.2 Two-phase flow

Unlike the classical single-phase theory, the correct method for calculating the effects of friction under two-phase conditions is not clear. Two methods used in past geothermal simulators are discussed and compared below.

### 3.3.2.1 Average mixture variables

A simple method for calculating the two-phase pressure drop uses (3.54) with two-phase parameters, such that:

$$\frac{2}{r}\tau_{tp} = \frac{f_{tp}}{4r}\rho_{mix}u_{mix}|u_{mix}|. \quad (3.59)$$

Here,  $u_{mix}$  is the mass weighted average velocity, defined in (2.23). The two-phase friction factor,  $f_{tp}$ , is calculated from (3.57) or (3.58) using the following two-phase Reynolds number:

$$Re_{tp} = \frac{F_m d}{S_l \mu_l + S_v \mu_v}. \quad (3.60)$$

The same method was used in transient geothermal wellbore models developed by Pan, Oldenburg, Wu and Pruess (2011) and Akbar et al. (2016). Steady-state models by Hasan and Kabir (2010) and Franz and Clearwater (2021) use the volume flux rather than the mixture velocity in (3.59).

This friction model has the advantageous property that when  $S_v = 0$  or  $S_v = 1$ :

$$\tau_{tp} = \tau_{sp}$$

$$Re_{tp} = Re_{sp}$$

$$f_{tp} = f_{sp}$$

which means (3.59) is continuous across transitions to and from single-phase conditions. This continuity property makes physical sense and is favourable from a numerical perspective.

### 3.3.2.2 Multiplier methods

The other model that is commonly used in geothermal wellbore simulators to represent wall friction makes use of a *two-phase multiplier*,  $\Phi^2$ . First introduced by Lockhart and Martinelli (1949), multiplier methods correlate the two-phase frictional pressure gradient to a reference friction term using  $\Phi^2$ :

$$\frac{2}{r}\tau_{tp} = \Phi^2 \frac{2}{r}\tau_{ref}. \quad (3.61)$$

The definition of the reference friction term,  $\tau_{ref}$ , differs depending on the investigator. Some authors, for example Orkiszewski (1967) and Hadgu (1989), calculate  $\tau$  differently depending on the flow regime, while García-Valladares et al. (2006) uses average two-phase variables (the same as (3.59)). However, it seems most common to use the *liquid only* friction term, defined as (Chisholm, 1983; Yadigaroglu and Hewitt, 2018):

$$\frac{2}{r}\tau_{ref} = \frac{2}{r}\tau_{LO} = \frac{f_{LO}}{4r} \frac{F_m^2}{\rho_l}. \quad (3.62)$$

Here, the liquid only friction factor,  $f_{LO}$ , is calculated using (3.57) where  $Re_{LO} = F_m d / \mu_l$ . This method is used in the transient simulator WELLBORE (Miller, 1980b) and in steady simulators by Goyal et al. (1980), Parlaktuna (1985), Aunzo et al. (1991) (GWELL), McGuinness (2015) (SWELFLO) and Gudmundsdottir and Jonsson (2015) (FLOWELL), for example.

Several empirical correlations are available for  $\Phi^2$ . Geothermal simulators have used correlations by Chisholm (1973) (Miller, 1980b; Aunzo et al., 1991; McGuinness, 2015), Beattie (1973) (García-Valladares et al., 2006; Gudmundsdottir and Jonsson, 2015) and Friedel (1979) (Gudmundsdottir and Jonsson, 2015), for example.

### 3.3.2.3 Comparison of methods

The mixture method, outlined in Section 3.3.2.1, is compared here to the multiplier method by Chisholm (1973). Chisholm's correlations for  $\Phi^2$  was used in geothermal applications by Miller (1980b), Goyal et al. (1980), Parlaktuna (1985), Aunzo et al. (1991) and McGuinness (2015).

Chisholm's multiplier uses  $\tau_{LO}$ , defined in (3.62), as the reference friction term and the two-phase multiplier,  $\Phi^2$ , is calculated as:

$$\phi^2 = 1 + (\Gamma^2 - 1)[B_R x_{fv}(1 - x_{fv}) + x_{fv}^2], \quad (3.63)$$

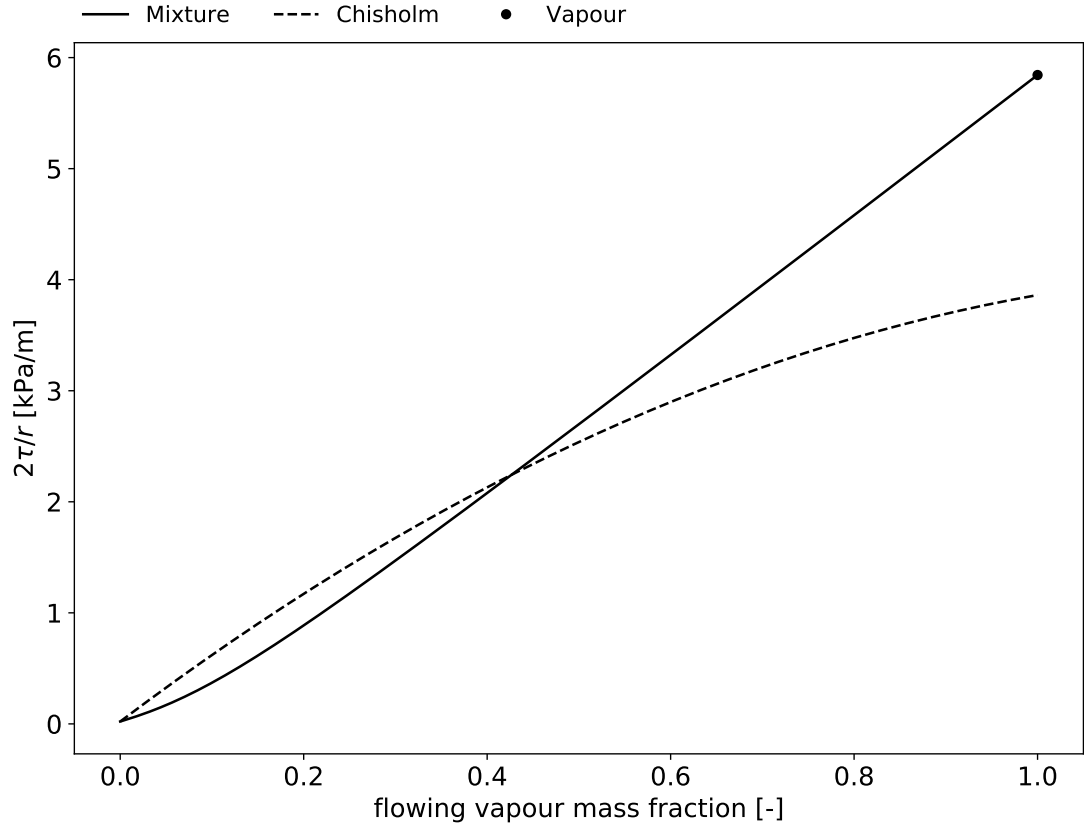
where  $\Gamma^2$  is:

$$\Gamma^2 = \left( \frac{\mu_v}{\mu_l} \right)^{0.25} \frac{\rho_l}{\rho_v}. \quad (3.64)$$



TABLE 3.2: Values of  $B_s$  for a smooth pipe given by Chisholm (1973).

$\Gamma$	$F_m$	$B_s$
$\leq 9.5$	$< 500$	4.8
	$500 \leq F_m \leq 1900$	$2400/F_m$
	$\geq 1900$	$55/\sqrt{F_m}$
$9.5 < \Gamma < 28$	$\leq 600$	$520/(\Gamma\sqrt{F_m})$
	$> 600$	$21/\Gamma$
$\geq 28$		$15000/(\Gamma^2\sqrt{F_m})$

FIGURE 3.10: Comparison of constitutive models for friction for the case where  $P = 5$  bara,  $F_m = 500$  kg/s/m<sup>2</sup>,  $d = 0.1$  m and  $\epsilon = 1.0 \times 10^{-5}$  m.

McGuinness (2015) modified  $B_R$  to account for the effects of rough pipes:

$$B_R = 0.5B_s \left( 1 + \left( \frac{\mu_v}{\mu_l} \right)^2 + 10^{-300\epsilon/r} \right). \quad (3.65)$$

Here,  $B_s$  is the term originally given by Chisholm (1973) for smooth pipes. It is defined in Table 3.2 as a function of  $\Gamma$  and  $F_m$ .

Figure 3.10 compares the frictional pressure drops calculated using the two models for

the case where  $P = 5$  bara,  $F_m = 500$  kg/s/m<sup>2</sup>,  $d = 0.1$  m and  $\epsilon = 1.0 \times 10^{-5}$  m. The mixture friction model is not an explicit function of flowing mass fraction. Therefore, in order to compare the two friction models, Shi et al.'s (2005) slip model was used to calculate the vapour saturation implicitly from the flowing mass fraction.

Figure 3.10 shows significant differences between the two models for two-phase friction, especially when the flowing mass fraction is larger than 0.6. It is clear from Figure 3.10 that Chisholm's model for friction is not continuous when transitioning between the frictional pressure gradient calculated for two-phase and that for pure vapour, which is shown by the black dot. This is expected to cause numerical difficulties when simulating transitions between these regions for transient cases. Additionally, the mixture model avoids the issues discussed above in relation to the slip models associated with the flowing mass fraction for low mass flows. Given these issues, we have chosen to model frictional effects using the mixture model described in Section 3.3.2.1.

### 3.4 Wellbore heat transfer

Heat is exchanged between the formation and wellbore fluid as it flows within the well. The rate of heat transfer changes with time due to local changes in the formation temperature caused by the fluid flowing in the well. Simulators developed by García-Valladares et al. (2006) and Miller (1980*b*) model reservoir heat transfer numerically using finite difference approximations. Akbar et al. (2016) ignore reservoir transients and only models heat flux through the wellbore structure. Pan, Oldenburg, Wu and Pruess (2011) provide both numerical and analytical options in their simulator T2WELL.

Numerical modelling of the heat transfer in the formation provides the most accurate representation of the heat transfer between the well and formation. It involves using discrete heat transport equations (e.g., transient radial heat conduction (Miller, 1980*b*) or flow in porous media (Pan, Oldenburg, Wu and Pruess, 2011)) to model how the formation temperatures change with time in response to the simulated wellbore flow. These methods require coupling between the numerical models that describe the well and formation.

In our simulator, we have chosen to represent formation heat transfer analytically. The method presented below is simpler to implement and less expensive computationally when compared to representing heat flow in the formation numerically. Analytical models approximate the decrease in heat transfer between the well and formation that occurs after a period of constant production. This representation of formation heat transfer is obviously an approximation for transient scenarios. However, as mass flow within the well increases, the reservoir heat transfer term becomes relatively small compared to the energy flux within the well. As a result, reservoir heat transfer has little influence on well behaviour for cases with moderate flow rates.

Unfortunately, the same cannot be said when mass flow is low. Examples of such flows considered in this work include modelling the development of vapour caps in hot geothermal wells (Section 8.1.1) and modelling discharge stimulation (Section 8.2). Cases such as these may benefit from the more accurate representation of heat transfer that is gained by representing heat flow in the reservoir numerically.

### 3.4.1 Analytical model for wellbore heat transfer

In our simulator, wellbore heat transfer is modelled analytically using (Horne and Shinohara, 1979; Hasan and Kabir, 2010):

$$q_{heat} = \frac{1}{A} \frac{dQ_{heat}}{ds} = \frac{2}{r} \frac{k_{res} U (T_{wb} - T_{res})}{k_{res} + rUf(t)}. \quad (3.66)$$

Here  $q_{heat}$  is heat flow per unit volume and  $dQ_{heat}/ds$  is the heat flow per unit length of the well. In (3.66),  $T_{wb}$  is the wellbore fluid temperature and  $U$  is the over-all heat transfer coefficient which describes the thermal resistance of the structure of the wellbore. The reservoir is described by its thermal conductivity,  $k_{res}$ , its temperature,  $T_{res}$ , and the time function,  $f(t)$ , which approximates the transient processes in the formation. Equation (3.66) is derived by considering the heat flux through the structure of the wellbore, given in (3.67), and the heat flux in the reservoir, given in (3.70). These components are discussed below.

The heat flow per unit length through the wellbore structure, which for the purpose of this work includes everything other than the formation, is proportional to the difference

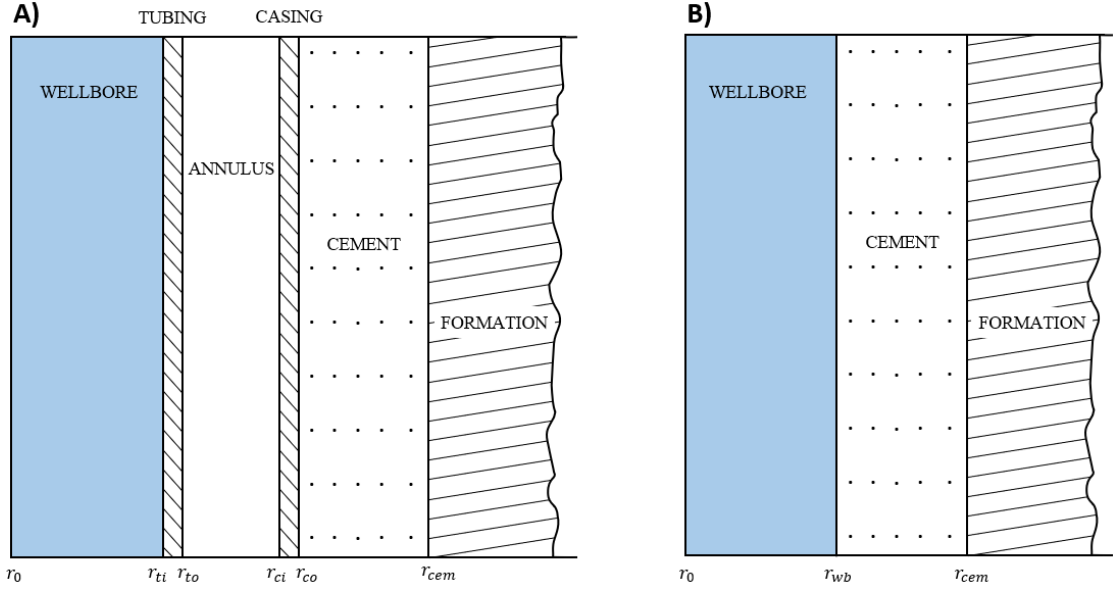


FIGURE 3.11: A) Diagrammatic representation of a generic wellbore modified from Willhite (1967) and B) the simplified wellbore structure used in this work.

between the temperature of the fluid in the well and the temperature at the cement-formation interface (Ramey, 1962; Willhite, 1967):

$$\frac{dQ_{heat}}{ds} = 2\pi r_{wb} U (T_{wb} - T_{cem}). \quad (3.67)$$

Here,  $r_{wb}$  and  $T_{wb}$  are the radius and temperature of the wellbore.  $T_{cem}$  is the temperature of the cement-formation interface (at  $r_{cem}$ ) as shown in Figure 3.11.

The over-all heat transfer coefficient,  $U$ , represents the net thermal conductivity of everything between the wellbore and the reservoir. Willhite (1967) provides a derivation of  $U$  for the generic wellbore given in Figure 3.11 A):

$$\frac{1}{U} = \frac{r_{to}}{r_{ti} h_{wb}} + \frac{1}{h_c + h_r} + \frac{r_{to}}{k_t} \ln \left( \frac{r_{to}}{r_{ti}} \right) + \frac{r_{to}}{k_{cas}} \ln \left( \frac{r_{co}}{r_{ci}} \right) + \frac{r_{to}}{k_{cem}} \ln \left( \frac{r_{cem}}{r_{co}} \right) \quad (3.68)$$

Here,  $h_{wb}$  is the convective heat transfer coefficient between the fluid and the tubing, and  $h_c$  and  $h_r$  are the convective and radiative heat transfer coefficients in the annulus. The annulus is a void between the production string and the casing commonly used in the oil and gas industry for well monitoring, control and intervention. The  $k$  terms are the thermal conductivity of the tubing (t), casing (cas) and cement (cem). The inner and outer radius of each of these components is shown in Figure 3.11 A).

A simplified approach, shown in Figure 3.11 B), has been used in our simulator. The convective heat transfer coefficient,  $h_{wb}$ , and the thermal conductivity of the tubing and casing,  $k_t$  and  $k_{cas}$ , are all relatively large. This means terms 1, 3 and 4 in (3.68), are all negligible. Additionally, most geothermal wellbores do not have an annulus and, therefore, term 2 in (3.68) can be discarded. Therefore, we approximate the total thermal resistance of the wellbore as the thermal resistance of the cement:

$$U = \frac{k_{cem}}{r_{wb} \ln \frac{r_{cem}}{r_{wb}}}. \quad (3.69)$$

Here,  $r_{wb}$  refers to the radius of the production string and  $r_{cem}$  refers to radius of the cement-formation interface. Both  $r_{wb}$  and  $r_{cem}$  can vary with depth. This simplified approach was also used by Vasini et al. (2018) in their work with T2WELL.

Heat transfer within the reservoir is a transient process. As fluid is produced from the reservoir the temperature in the formation surrounding the wellbore will tend towards the temperature of the wellbore fluid. This decreases the rate of heat transfer between the wellbore and formation. Ramey (1962) proposed that this effect could be approximated as:

$$\frac{dQ_{heat}}{ds} = \frac{2\pi k_{res}(T_{cem} - T_{res})}{f(t)} \quad (3.70)$$

Here,  $k_{res}$  and  $T_{res}$  are the thermal conductivity and temperature of the formation. The time function,  $f(t)$ , approximates the transient nature of wellbore-formation heat exchange, increasing with time to decrease the rate of heat loss.

Ramey (1962) proposed using the time function:

$$f(t) = -\ln \frac{r_{cem}}{2\sqrt{\alpha_t t}} - 0.29, \quad (3.71)$$

where the thermal diffusivity of the formation is  $\alpha_t = k_{res}/(\rho_{res}c_{res})$ . Here,  $c_{res}$ ,  $k_{res}$  and  $\rho_{res}$  are the heat capacity, thermal conductivity and density of the formation. The value of Ramey's time function, calculated using (3.71), is given for the first 100 days in Figure 3.12 A). However, it is not suitable for use in transient wellbore simulation as it is inaccurate for short time periods. Figure 3.12 A) indicates that Ramey's time function

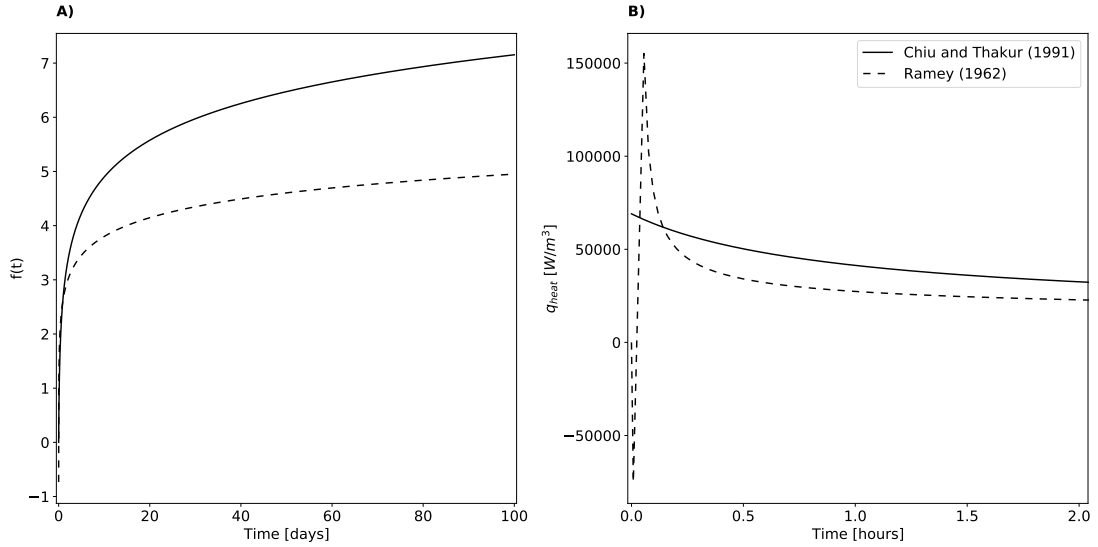


FIGURE 3.12: Comparison of Ramey (1962) and Chiu and Thakur (1991) A) transient time functions, and B) wellbore heat loss for  $k_{res} = 2.4$  W/m,  $k_{cem} = 1.4$  W/m,  $T_{wb} = 300$  °C,  $T_{res} = 200$  °C,  $r_{wb} = 0.1$  m and  $r_{cem} = 0.15$  m.

is negative during early time periods resulting in a discontinuity in  $q_{heat}$  shown in Figure 3.12 B).

Instead, the time function given by Chiu and Thakur (1991) is used in our simulator:

$$f(t) = 0.982 \ln \left( 1 + 1.81 \frac{\alpha_t t}{r_{cem}^2} \right). \quad (3.72)$$

Vasini et al. (2018) implemented this time function in T2WELL and showed that it matched numerical simulations for radial heat conduction quite well. Importantly, this time function does not cause a discontinuity in the heat flow term for early time periods, as shown in 3.12 B).

The equation for total heat transfer, given in (3.66) above, is derived in Appendix B by substituting (3.67) for  $T_{cem}$  in (3.70) and rearranging the result.

### 3.5 Source Terms

Modelling production (or injection) requires the specification of inflow (or outflow) conditions. For the simplest cases, inflow (or outflow) may be specified using the boundary conditions (e.g., total mass flow, pressure and enthalpy) as was done in transient investigations by García-Valladares et al. (2006) and Akbar et al. (2016). However, this limits the simulator to modelling a single feed at the bottom of the well.

Instead, it is better to represent feed-zones using source terms in the governing conservation equations as this allows multiple sources at different locations within the well. This was done by Yamamura et al. (2017) who approximated reservoir behaviour using productivity relationships in their homogeneous simulator. This method calculates the mass flow of a feed from the difference in pressure between the well and reservoir. It allows the mass contribution from each feed to change in response to changing conditions in the well (e.g., due to flashing or a change in wellhead pressure) and allows the feed-zone to accept fluid, i.e., for fluid to flow out of the well into the reservoir. However, feed-zone properties (e.g., pressure and enthalpy) do not change due to production. Instead, their change must be specified by the user. This is known as one-way coupling, i.e. the feeds affect the wellbore flow, but the wellbore flow does not affect the feed properties.

Other investigations of transient flow have coupled the wellbore simulator to a numerical reservoir model. This provides a more realistic but more complex representation of the feed-zone. Specifically, it allows the feed properties to change in response to the behaviour of the well, for example, changes in pressure, temperature and saturation after extended periods of production or injection.

Miller (1980a) and Miller et al. (1982) used a simple radial model to describe the reservoir. Pan, Oldenburg, Wu and Pruess (2011) developed the most advanced coupling procedure combining TOUGH2 and T2WELL. A well sub-domain was prescribed within a TOUGH2 reservoir model within which the wellbore conservation equations were solved. Mass and energy conservation equations were solved implicitly, however, the momentum flux in the well was lagged in time.

TABLE 3.3: Reservoir representation in past transient geothermal wellbore simulators.

Author	Reservoir model	Wellbore model	Coupling method
Miller (1980a)	Radial single-phase	Homogeneous	Semi-implicit
Miller et al. (1982)	Radial reservoir	WELLBORE	Semi-implicit
Pan, Oldenburg, Wu and Pruess (2011)	TOUGH2	T2WELL	Semi-implicit
García-Valladares et al. (2006)	Boundary conditions	Two-phase slip	-
Akbar et al. (2016)	Boundary conditions	Two-phase slip	-
Yamamura et al. (2017)	Darcy flow	Homogeneous	One-way

For our simulator, we approximate the reservoir using a simple deliverability model based on Darcy flow. While this approximation is somewhat restrictive (as feed parameters do not change due to interaction with the wellbore), it avoids the complexity of fully coupled procedures while still allowing many interesting scenarios to be modelled. The models used to describe sources of mass, momentum and energy are discussed below.

### 3.5.1 Sources of mass

The total mass source is the sum of the liquid and vapour components,

$$q_{mass} = q_{mv} + q_{ml}, \quad (3.73)$$

where  $q_{mass}$  is positive for flow from the reservoir into the well.

The reservoir mass source for each fluid phase,  $q_{m\beta}$ , is calculated using a deliverability equation based on two-phase Darcy flow:

$$q_{m\beta} = \frac{1}{A} \left( \frac{k_{r\beta} \rho_{\beta}}{\mu_{\beta}} \right) \left( \frac{PI}{h} \right) (P_{res} - P_{wb}). \quad (3.74)$$

Here,  $k_{r\beta}$  and  $\mu_{\beta}$  are the relative permeability and kinematic viscosity of each phase,  $P_{res}$  is the reservoir pressure,  $A$  is the cross-sectional area of the well and  $h$  is the length of the production interval.

For steady radial flow with skin effects, the productivity index, PI, is (Pruess et al., 2012):

$$PI = \frac{2\pi kh}{\ln(r_{res}/r) + s - 1/2}, \quad (3.75)$$



where  $k$  is the permeability of the feed,  $r_{res}$  is the radius of the reservoir,  $r$  is the radius of the well and  $s$  is the skin factor. However, in our model, we specify the PI as an input rather than calculating it from (3.75).

Relative permeability curves modify Darcy's law for multi-phase flow. They represent the fact that when multiple phases flow in a porous media, the flow in a given phase may be inhibited by the presence of the other phase. Grant's relative permeability curves (Grant, 1977; Croucher, 2020) are used in all simulations discussed in this thesis, however, others including linear, Pickens, Corey and Van Genuchten curves have also been provided as options in our simulator. The formulae for Grant's curves are provided below, while the other relative permeability curves are defined elsewhere (Croucher, 2020).

Grant's curves are defined as a function of  $S_*$ :

$$S_* = \frac{S_l - S_{lr}}{1 - S_{lr} - S_{sr}}, \quad (3.76)$$

where  $S_l$  is the liquid saturation, and  $S_{lr}$  and  $S_{sr}$  are constants prescribed by the modeller. In this work  $S_{lr} = 0.5$  and  $S_{sr} = 0.1$  have been used.

The relative permeability of the liquid phase,  $k_{rl}$ , is:

$$k_{rl} = \begin{cases} 1 & S_v < S_{sr} \\ S_*^4 & S_{sr} \leq S_v \leq 1 - S_{lr} \\ 0 & S_v > 1 - S_{lr} \end{cases}, \quad (3.77)$$

and the vapour relative permeability is defined as  $k_{rv} = 1 - k_{rl}$ . Figure 3.13 gives Grant's curves calculated using  $S_{lr} = 0.5$  and  $S_{sr} = 0.1$ .

Combining (3.73) and (3.74), the total mass input can be written in terms of a lumped parameter,  $\alpha$ :

$$q_{mass} = \frac{\alpha}{Ah} (P_{res} - P_{wb}). \quad (3.78)$$

Alternatively,  $q_{mass}$  can be set at a fixed value.

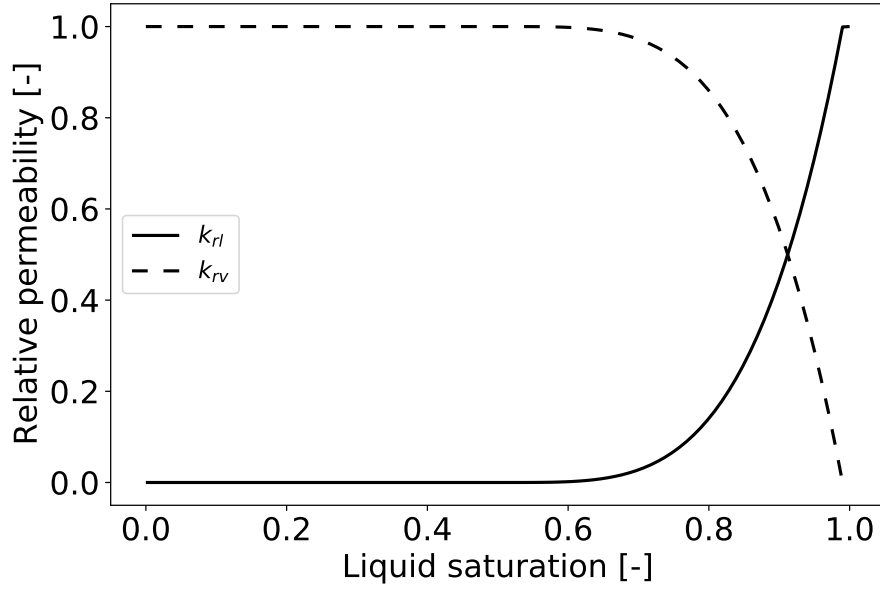


FIGURE 3.13: Grant's relative permeability curves calculated using  $S_{lr} = 0.5$  and  $S_{sr} = 0.1$ . This is the default model used in this work.

### 3.5.2 Sources of momentum

We assume that fluid from a feed enters the well perpendicular to the direction of flow as was done by Bendiksen et al. (1991) and Shirdel and Sepehrnoori (2012). This means that the in-flowing fluid does not add any momentum to the well and must be accelerated upon entry. As a result, the momentum source from feeds,  $q_{mom}$ , is zero.

It is noted here that modelling the reservoir source as a flux across the bottom boundary implicitly provides a source of momentum. This is because the fluid is flowing upon entry into the well and, therefore, has momentum.

### 3.5.3 Sources of energy

The source of energy from a feed is

$$q_{ener} = q_{mass} h_{feed}, \quad (3.79)$$

where  $h_{feed}$  is the flowing enthalpy of the feed calculated using the relative permeabilities:

$$h_{feed} = \frac{\frac{h_v k_{rv}}{\mu_v} + \frac{h_l k_{rl}}{\mu_l}}{\frac{k_{rv}}{\mu_v} + \frac{k_{rl}}{\mu_l}}. \quad (3.80)$$

Alternatively, the flowing enthalpy is prescribed as an input when the lumped parameter model (3.78) is used.

### 3.6 Properties of pure water

Additional equations are required to define the thermodynamic properties of the water. In this work, we use the IAPWS-IF97 correlations (Dittmann, 2000). The density and enthalpy of each phase are calculated from these equations as functions of pressure and temperature. Additionally, when two-phase conditions exist, the pressure and temperature are related by the saturation condition. This means in the two-phase region, the density and enthalpy of each phase are functions of pressure (or temperature) alone.

The viscosity of each phase is calculated from the IAPWS-08 correlations (Huber et al., 2009) as a function of temperature and the phase density. Additionally, the surface tension between the liquid and vapour phases,  $\sigma_{vl}$ , is required to calculate the drift velocity. The surface tension is calculated as described in the IAPWS (2014) release as a function of temperature.

### 3.7 Summary

The selection of constitutive models plays an important role in the ability of a geothermal wellbore simulator to represent real-world scenarios. This chapter reviews the literature on the constitutive models used in geothermal wellbore modelling. Based on this review, we selected constitutive models describing phase slip, friction, heat transfer, and reservoir source terms for use in our model.

The constitutive models selected for our simulator are:

**Slip:** The drift-flux model by Shi et al. (2005), with modifications made by Pan, Oldenburg, Wu and Pruess (2011), is used in our simulator and is outlined in Section 3.2.2.4. This slip model was developed for flow in large diameter deviated pipes and varies smoothly as a function of vapour saturation. Finally, this model avoids division

by total mass flow, making it suitable for modelling complex scenarios such as counter-flow. All of these factors make the drift-flux model by Shi et al. (2005) a good choice for our transient wellbore simulator.

**Friction:** The model used for friction is given in (3.59). It is essentially the same as the classic Moody formula for wall friction in single-phase pipe flow, however, it uses averaged two-phase variables in place of single-phase variables. This model is continuous across phase boundaries. It is the same formulation as is used in T2WELL (Pan, Oldenburg, Wu and Pruess, 2011).

**Heat transfer:** The heat transfer between the wellbore and reservoir is modelled analytically using (3.66). This equation approximates the heat transfer based on the difference between the wellbore and the formation temperatures. The effect of the wellbore structure is approximated as the thermal resistance of the cement, and the transient behaviour of the reservoir is approximated using the time function given in (3.72).

**Source terms:** Feed-zones are modelled as sources of mass, momentum and energy, as outlined in Section 3.5. Reservoir behaviour is approximated using a simple deliverability model based on Darcy flow. This model assumes that sources of mass and energy are proportional to the difference between the feed-zone and wellbore pressures. This allows the mass and energy contribution from each feed to change in response to changing conditions in the well. However, feed-zone properties (e.g., pressure and enthalpy) do not change due to production or injection. Finally, we assumed that fluid entering and exiting the well does so perpendicular to the well, and therefore, the momentum source is zero.

## Chapter 4

# Numerical models for transient geothermal wellbore simulation

The conservation of mass, momentum and energy equations discussed in Chapter 2 are strongly coupled, highly non-linear and cannot be solved analytically. This chapter discusses how to obtain a numerical solution of these equations.

First, discrete conservation equations, which approximate the continuous PDEs over a subsection of the well, are given in Section 4.1. The solution of the discrete equations requires upstream weighting for numerical stability (Degrez, 2009). Two methods, a discrete and a hybrid upstream weighting scheme, were implemented in this work and are discussed in Section 4.2.

Additionally, we solve a fourth equation, the constitutive model describing phase slip, at the same time as the conservation equations. The numerical implementation of Shi et al.'s (2005) drift-flux model is discussed in Section 4.3.

The discretisation of the governing equations (including slip), with implicit time differencing, results in a system of non-linear algebraic equations. This set of equations is solved for primary variables, which describe the thermodynamic state of the well. Section 4.4 introduces the concept of primary variables and discusses the options used in past geothermal wellbore simulators. The primary variables used in our simulator are then discussed in Section 4.4.4.

Boundary conditions are required to constrain the generalised flow equations to a specific case. Production, injection and no-flow boundary conditions are discussed in Section 4.5. Finally, with the addition of boundary conditions, the system of discrete equations can be solved. We use the multi-variate Newton-Raphson method. This numerical method is presented in Section 4.6.

## 4.1 Discrete conservation equations

Discretisation involves formulating the continuous conservation equations, given in (2.53), (2.54) and (2.55), in a discrete form suitable for numerical computation. These discrete equations approximate the continuous PDEs over a subsection of the well.

To discretise the conservation equations, we define the wellbore variables at discrete points in space and time. We define scalar wellbore properties, for example, pressure, temperature and saturation, at the centre of each wellbore element. Flowing variables, for example, phase velocities, mass fluxes and volume fluxes are defined on the interface between elements as shown in Figure 4.1. A fully implicit discretisation in time is used, meaning all equations are expressed in terms of the unknown thermodynamic parameters at the current time  $t^{n+1}$ .

The conservation equations, and the drift-flux model for slip, are solved for  $[P]_i^{n+1}$ ,  $[T]_i^{n+1}$  (single-phase) or  $[S_v]_i^{n+1}$  (two-phase),  $[u_v]_{i+1/2}^{n+1}$  and  $[F_{Vl}]_{i+1/2}^{n+1}$  as primary thermodynamic variables using the Newton-Raphson method. This choice of primary variables is discussed further in Section 4.4.

### 4.1.1 Conservation of mass

The discrete mass conservation equation, given in residual form (formulated so the residual should equal zero), is:

$$[R_{mass}]_{4i+2}^{n+1} = \frac{1}{\Delta t} \left( [S_v \rho_v + S_l \rho_l]_i^{n+1} - [S_v \rho_v + S_l \rho_l]_i^n \right) + \frac{1}{[V]_i} \left( [AF_{mv} + AF_{ml}]_{i+1/2}^{n+1} - [AF_{mv} + AF_{ml}]_{i-1/2}^{n+1} \right) - [q_{mass}]_i^{n+1} = 0 \quad (4.1)$$

Here, the superscripts  $n + 1$  and  $n$  indicate the current and previous time steps, respectively. The subscript  $i$  is the spatial index of an element centre. The subscript  $i + 1/2$  is the index of the interface between elements  $i$  and  $i + 1$ . In (4.1),  $[R_{mass}]_{4i+2}^{n+1}$  is the mass residual, which is the imbalance in the discrete mass conservation equation. This is a measure of how close the left hand side of (4.1) is to equalling zero. Here, the subscript  $4i + 2$  is the index of the residual in the array of residuals (for example, see (4.53)) used when solving the discrete conservation equations.

In (4.1),  $\Delta t = t^{n+1} - t^n$  is the time step and the volume of a wellbore block is  $[V]_i$ , defined as:

$$[V]_i = A_i \Delta s_i, \quad (4.2)$$

where  $A_i$  is the average cross sectional area and  $\Delta s_i$  is the axial length of block  $i$ .

The mass flux of a phase on an interface is defined as

$$[F_{m\beta}]_{i+1/2}^{n+1} = [\rho_\beta S_\beta]_{i+1/2}^{n+1} [u_\beta]_{i+1/2}^{n+1}, \quad (4.3)$$

Here, interface saturation and density,  $[S_\beta]_{i+1/2}^{n+1}$  and  $[\rho_\beta]_{i+1/2}^{n+1}$ , are weighted according to the direction of the flow. This is called *upstream weighting* or *upwinding* and is required

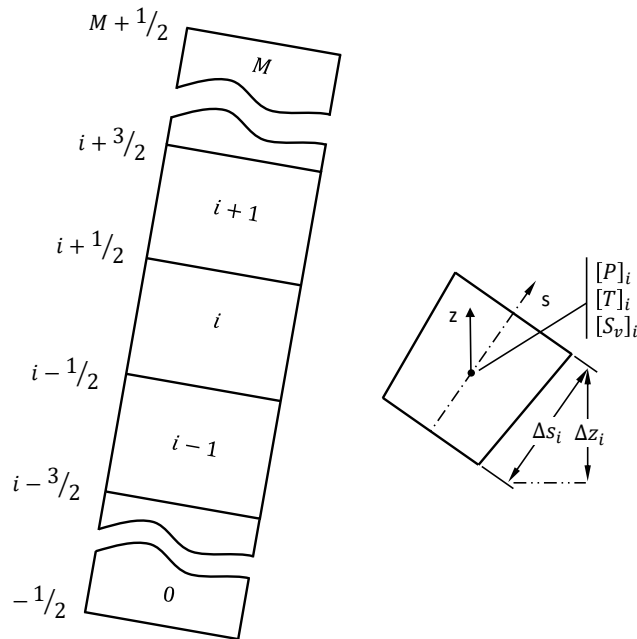


FIGURE 4.1: Wellbore discretisation scheme showing the indexing convention.

for numerical stability. The calculation of these upwinded variables is discussed in Section 4.2 below.

In (4.3), the vapour velocity  $[u_v]_{i+1/2}^{n+1}$  is calculated as a primary variable. The liquid velocity is calculated as a secondary variable from the liquid volume flux:

$$[u_l]_{i+1/2}^{n+1} = \begin{cases} [F_{Vl}]_{i+1/2}^{n+1}/[S_l]_{i+1/2}^{n+1} & , [S_l]_{i+1/2}^{n+1} \neq 0 \\ 0 & , [S_l]_{i+1/2}^{n+1} = 0 \end{cases}. \quad (4.4)$$

Here, we set the liquid velocity to equal zero when the upstream weighted saturation equals zero to avoid division by zero.

#### 4.1.2 Conservation of energy

The discrete energy conservation equation, given in residual form, is:

$$\begin{aligned} [R_{ener}]_{4i+3}^{n+1} = & \frac{[S_v \rho_v H_v + S_l \rho_l H_l - P]_i^{n+1} - [S_v \rho_v H_v + S_l \rho_l H_l - P]_i^n}{\Delta t} \\ & + \frac{1}{[V]_i} \left( [AF_{mv} H_v + AF_{ml} H_l]_{i+1/2}^{n+1} - [AF_{mv} H_v + AF_{ml} H_l]_{i-1/2}^{n+1} \right) \\ & + [q_{heat}]_i^{n+1} + [F_{mv} + F_{ml}]_i^{n+1} g \frac{\Delta z_i}{\Delta s_i} - [q_{ener}]_i^{n+1} = 0. \end{aligned} \quad (4.5)$$

Here,  $H_\beta$  is the sum of the specific enthalpy and specific kinetic energy of each phase,

$$[H_\beta]_i^{n+1} = [h_\beta]_i^{n+1} + [E_{K\beta}]_i^{n+1}, \quad (4.6)$$

where  $[E_{K\beta}]_i^{n+1}$  is the average specific kinetic energy of a phase. It is calculated as the average of the specific kinetic energy on the surrounding interfaces,

$$[E_{K\beta}]_i^{n+1} = \frac{1}{2} \left( \frac{1}{2} [u_\beta^2]_{i+1/2}^{n+1} + \frac{1}{2} [u_\beta^2]_{i-1/2}^{n+1} \right). \quad (4.7)$$

In (4.5), the specific enthalpy of a phase on an interface,  $[H_\beta]_{i+1/2}^{n+1}$ , is upstream weighted as defined in Section 4.2.

In (4.5), the block centred mass flux, which is used in the term for the power exerted by gravity, is defined as:

$$[F_{m\beta}]_i^{n+1} = [\rho_\beta S_\beta]_i^{n+1} [u_\beta]_i^{n+1}, \quad (4.8)$$



where, the average velocity at  $i$  is the average of the interface velocities:

$$[u_\beta]_i^{n+1} = \frac{1}{2} \left( [u_\beta]_{i+1/2}^{n+1} + [u_\beta]_{i-1/2}^{n+1} \right). \quad (4.9)$$

Here, the vapour velocity at  $i + 1/2$  is calculated as a primary variable and the liquid velocity is calculated using (4.4).

#### 4.1.3 Conservation of momentum

The discrete momentum equation is centred on the block interface at  $i + 1/2$ . The momentum control element is shown by the dashed lines in Figure 4.2. The discrete momentum equation, cast in residual form, is:

$$\begin{aligned} [R_{mom}]_{4i+4}^{n+1} = & \frac{[F_{mv} + F_{ml}]_{i+1/2}^{n+1} - [F_{mv} + F_{ml}]_{i+1/2}^n}{\Delta t} + \frac{[F_v^{mom}]_{i+1/2}^{n+1} + [F_l^{mom}]_{i+1/2}^{n+1}}{[V]_{i+1/2}} \\ & + \frac{P_{i+1}^{n+1} - P_i^{n+1}}{\Delta s_{i+1/2}} + \left[ \frac{2}{r} \tau \right]_{i+1/2}^{n+1} + [\rho_{mix}^{ave}]_{i+1/2}^{n+1} g \frac{\Delta z_{i+1/2}}{\Delta s_{i+1/2}} - [q_{mom}]_{i+1/2}^{n+1} = 0 \end{aligned} \quad (4.10)$$

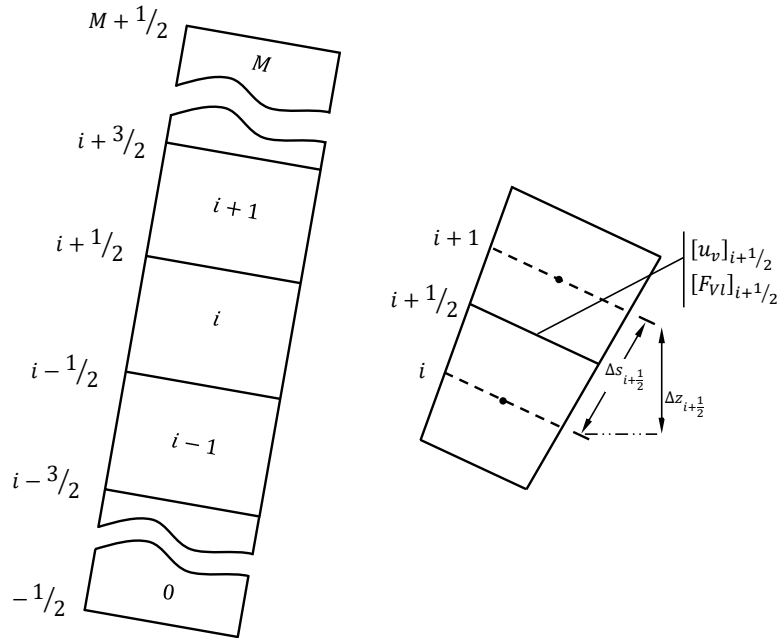


FIGURE 4.2: The discrete momentum conservation equation is centred on the interface  $i + 1/2$  between blocks  $i$  and  $i + 1$ . The effective momentum control volume is shown by the dashed lines.

Here,  $[F_v^{mom}]_{i+1/2}^{n+1}$  and  $[F_l^{mom}]_{i+1/2}^{n+1}$  are the upstream weighted momentum flux differences for the vapour and liquid phases, respectively. These depend on the direction in which a phase is flowing and are defined in Section 4.2 below.

The constitutive model for friction is formulated numerically as:

$$\left[ \frac{2}{r} \tau \right]_{i+1/2}^{n+1} = \frac{[f]_{i+1/2}^{n+1}}{4[r]_{i+1/2}} \frac{[F_m]_{i+1/2}^{n+1} |[F_m]_{i+1/2}^{n+1}|}{[\rho_v S_v]_{i+1/2}^{n+1} + [\rho_l S_l]_{i+1/2}^{n+1}} \quad (4.11)$$

where  $[\rho_\beta S_\beta]_{i+1/2}^{n+1}$  are the upstream weighted saturations and densities, and the total mass flux on the interface is:

$$[F_m]_{i+1/2}^{n+1} = [F_{mv}]_{i+1/2}^{n+1} + [F_{ml}]_{i+1/2}^{n+1} \quad (4.12)$$

The gravity term in (4.10) uses the average mixture density on the interface,

$$[\rho_{mix}^{ave}]_{i+1/2}^{n+1} = \frac{1}{2} \left( [\rho_v S_v + \rho_l S_l]_i^{n+1} + [\rho_v S_v + \rho_l S_l]_{i+1}^{n+1} \right), \quad (4.13)$$

Equation (4.13) is used instead of the upwinded saturations and densities as, in simulations with low mass flow, the liquid velocity can flip between positive and negative values after each Newton iteration. This causes the upwinded densities and saturations to change with each Newton step, resulting in slow and sometimes failed convergence.

Finally, in (4.10), the effective interface volume,  $[V]_{i+1/2}$ , is the average of the volumes of the surrounding elements:

$$[V]_{i+1/2} = \frac{1}{2} ([V]_{i+1} + [V]_i) \quad (4.14)$$

## 4.2 Upstream weighting

Advective processes typically dominate transient wellbore simulations. For these problems, a central difference discretisation may lead to oscillatory solutions that become increasingly non-physical as advective processes become more dominant (Degrez, 2009).

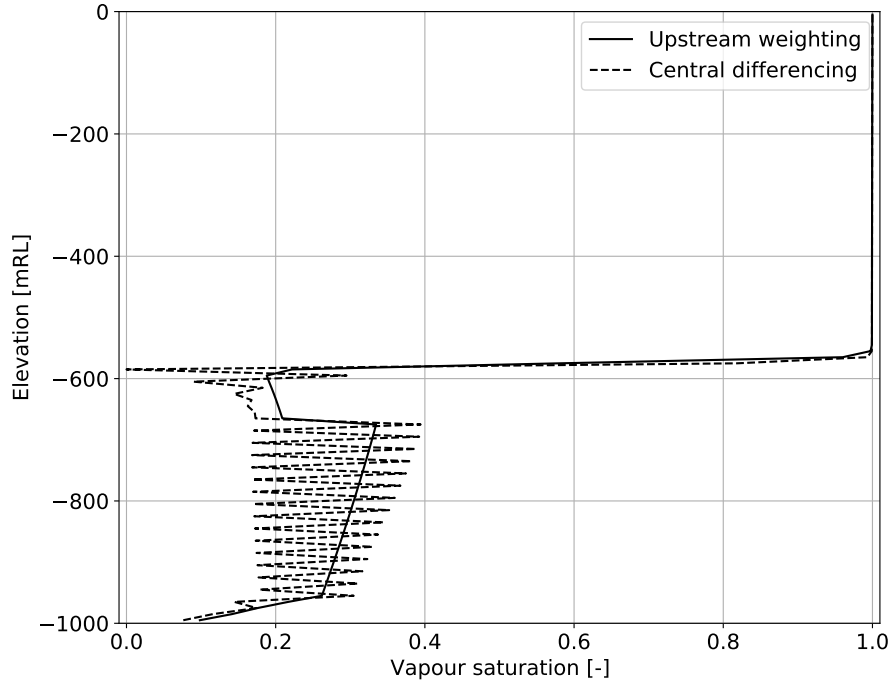


FIGURE 4.3: Non-physical oscillations in the simulated vapour saturation caused by using central differencing when simulating Test Case 3.

Figure 4.3 gives an example of oscillations caused by using a central differencing scheme for Test Case 3, which is described in Section 5.3.1.3. This simulation models the rapid shut-in of a flowing well and involves rapid changes in pressure, saturation and mass flow within the well. Figure 4.3 shows the erroneous oscillations in the vapour saturation that occur 22 minutes and 15 seconds after shut-in when a central differencing scheme is used.

Oscillations, such as those shown in Figure 4.3, can be prevented by using *upstream weighting*, also known simply as *upwinding*. Here, the discrete flux derivatives for the mass, momentum and energy equations are calculated using upstream points. In other words, when a phase is flowing up the well, unknowns on the interface between two blocks are taken from the block below. For down-flow, the interface values are taken from the block above. Our numerical method uses upwinded density, saturation and enthalpy on the interface. Additionally, the entire momentum flux derivative is upwinded depending on the direction of flow. The numerical stability of methods using upstream weighting comes at the cost of increased numerical diffusion.

Two methods of upstream weighting, which we call the discrete and hybrid methods, were implemented in this work and are discussed below.

#### 4.2.1 Discrete upstream weighting scheme

Discrete upstream weighting is the simplest form of upwinding and was the first method implemented in our simulator. Discrete upwinding weights interface variables according to the direction of the flow. When the direction of flow changes, there is a change in the upwinding direction, which results in a change in the value of the upwinded variable.

For this method, the interface saturation, density and enthalpy for phase  $\beta$  are calculated using:

$$[S_\beta]_{i+1/2}^{n+1} = \begin{cases} [S_\beta]_i^{n+1}, & [X_\beta]_{i+1/2}^{n+1} > 0 \\ [S_\beta]_{i+1}^{n+1}, & [X_\beta]_{i+1/2}^{n+1} < 0 \end{cases} \quad (4.15)$$

$$[\rho_\beta]_{i+1/2}^{n+1} = \begin{cases} [\rho_\beta]_i^{n+1}, & [X_\beta]_{i+1/2}^{n+1} > 0 \\ [\rho_\beta]_{i+1}^{n+1}, & [X_\beta]_{i+1/2}^{n+1} < 0 \end{cases} \quad (4.16)$$

$$[H_\beta]_{i+1/2}^{n+1} = \begin{cases} [H_\beta]_i^{n+1}, & [X_\beta]_{i+1/2}^{n+1} > 0 \\ [H_\beta]_{i+1}^{n+1}, & [X_\beta]_{i+1/2}^{n+1} < 0 \end{cases} \quad (4.17)$$

Here,  $[X_\beta]_{i+1/2}^{n+1}$  refers to the flowing primary variable of each phase. This is  $[u_v]_{i+1/2}^{n+1}$  and  $[F_{Vl}]_{i+1/2}^{n+1}$  for the vapour and liquid phases, respectively.

The upstream weighted momentum flux differences are:

$$[F_\beta^{mom}]_{i+1/2}^{n+1} = \begin{cases} [AS_\beta \rho_\beta u_\beta^2]_{i+1/2}^{n+1} - [AS_\beta \rho_\beta u_\beta^2]_{i-1/2}^{n+1}, & [X_\beta]_{i+1/2}^{n+1} > 0 \\ [AS_\beta \rho_\beta u_\beta^2]_{i+3/2}^{n+1} - [AS_\beta \rho_\beta u_\beta^2]_{i+1/2}^{n+1}, & [X_\beta]_{i+1/2}^{n+1} < 0 \end{cases} \quad (4.18)$$

Figure 4.4 shows how the momentum flux differences given in (4.18) are taken for different flow scenarios that can occur in a well. For co-current up-flow, the momentum flux difference at  $i + 1/2$  for each phase is taken between quantities at the interfaces  $i + 1/2$  and  $i - 1/2$ , while for down-flow, the difference is taken between quantities at the interfaces  $i + 3/2$  and  $i + 1/2$ . For counter flow cases, where vapour flows up and liquid flows down,

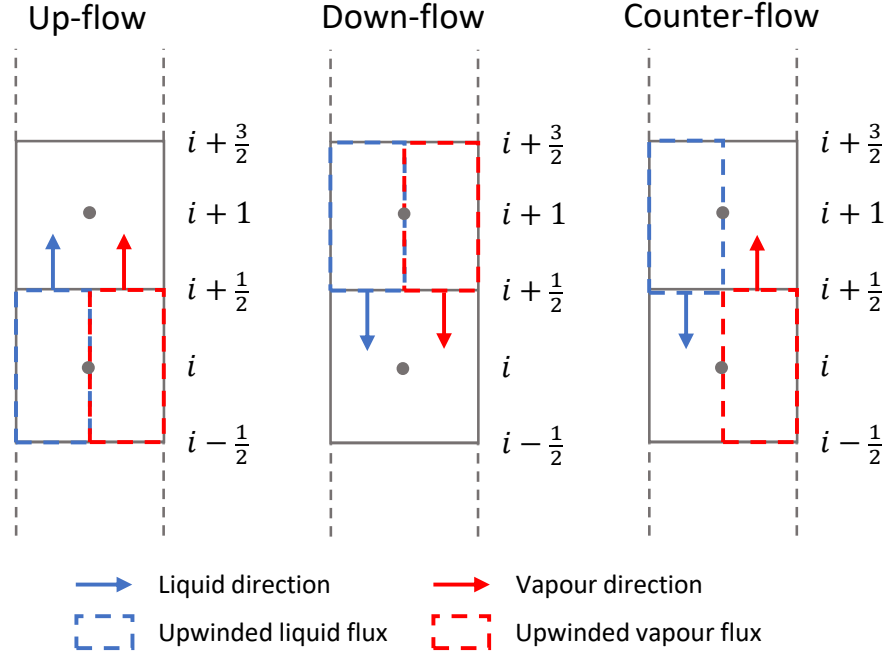


FIGURE 4.4: The momentum flux differences in the momentum equation are upwinded depending on the direction of flow of each phase.

the differences are taken based on the direction of the flow of the phase as is shown in Figure 4.4.

Equations (4.15)–(4.18) do not specify an upwinding direction when  $[X_\beta]_{i+1/2}^{n+1} = 0$ . An upwinding direction, which we call the *upwinding bias*, must be assumed for this case. We use the average of the phase velocities (or volume fluxes) from the adjacent interfaces to calculate the upwinding direction. If this is also zero, then positive upwinding (i.e. flow up the well) is assumed.

The transition between upwinding directions can cause convergence issues when the mass flow of a phase is small. In these cases, the upwinding direction of a phase can change with successive Newton iterations, which causes the value of upwinded variables to change. As a result, the residuals do not converge to a suitable tolerance, and the time step must be dropped. We found that discrete upwinding could result in poor numerical performance for low mass flow cases. These issues, and how we improved the numerical performance of our simulator for these cases, are discussed further in Section 6.3.

### 4.2.2 Hybrid upstream weighting scheme

Hybrid upstream weighting attempts to provide a solution to some of the issues associated with discrete upwinding. Hybrid upwinding methods transition smoothly between upwinding directions to avoid sudden changes in upstream weighted terms.

The interface values for saturation, density and enthalpy using hybrid upwinding are:

$$[\rho_\beta]_{i+1/2}^{n+1} = \frac{1 + [U_\beta]_{i+1/2}^{n+1}}{2} [\rho_\beta]_i^{n+1} + \frac{1 - [U_\beta]_{i+1/2}^{n+1}}{2} [\rho_\beta]_{i+1}^{n+1}, \quad (4.19)$$

$$[S_\beta]_{i+1/2}^{n+1} = \frac{1 + [U_\beta]_{i+1/2}^{n+1}}{2} [S_\beta]_i^{n+1} + \frac{1 - [U_\beta]_{i+1/2}^{n+1}}{2} [S_\beta]_{i+1}^{n+1}, \quad (4.20)$$

and

$$[H_\beta]_{i+1/2}^{n+1} = \frac{1 + [U_\beta]_{i+1/2}^{n+1}}{2} [H_\beta]_i^{n+1} + \frac{1 - [U_\beta]_{i+1/2}^{n+1}}{2} [H_\beta]_{i+1}^{n+1}. \quad (4.21)$$

Here, the upwinding parameter  $[U_\beta]_{i+1/2}^{n+1}$  is used to transition between upwinding directions. It varies smoothly between -1 for downwards flow and +1 for upwards flow. We vary  $[U_\beta]_{i+1/2}^{n+1}$  depending on the value of the primary variable  $[X_\beta]_{i+1/2}^{n+1}$  using a modified version of the smooth function given by Pan, Oldenburg, Wu and Pruess (2011):

$$[U_\beta]_{i+1/2}^{n+1} = \begin{cases} -1 & [X_\beta]_{i+1/2}^{n+1} \leq -X_{tol} \\ -\cos\left(\pi \frac{[X_\beta]_{i+1/2}^{n+1} + X_{tol}}{2X_{tol}}\right) & -X_{tol} \leq [X_\beta]_{i+1/2}^{n+1} \leq X_{tol} \\ 1 & [X_\beta]_{i+1/2}^{n+1} \geq X_{tol} \end{cases} \quad (4.22)$$

Here,  $X_{tol}$  defines the range over which  $[U_\beta]_{i+1/2}^{n+1}$  transitions between upwinding directions. When  $[X_\beta]_{i+1/2}^{n+1} = 0$ , the interface variable is calculated as the average of the values in the adjacent blocks. This results in a central difference approximation of the flux derivatives in the mass and energy equations. The hybrid weighting of the momentum flux difference is handled slightly differently. First, we define the upwinded differences for up-flow and down-flow for each phase:

$$[F_\beta^{up}]_{i+1/2}^{n+1} = [A\rho_\beta S_\beta u_\beta^2]_{i+1/2}^{n+1} - [A\rho_\beta S_\beta u_\beta^2]_{i-1/2}^{n+1}, \quad (4.23)$$

and

$$[F_\beta^{down}]_{i+1/2}^{n+1} = [A\rho_\beta S_\beta u_\beta^2]_{i+3/2}^{n+1} - [A\rho_\beta S_\beta u_\beta^2]_{i+1/2}^{n+1}. \quad (4.24)$$

Equations (4.23) and (4.24) are the same as the discrete upstream momentum flux differences given in (4.18).

The upwinding parameter,  $[U_\beta]_{i+1/2}^{n+1}$ , which is defined in (4.22), is used to smoothly transition between (4.23) for up-flow and (4.24) for down-flow using:

$$[F_\beta^{mom}]_{i+1/2}^{n+1} = \frac{1 + [U_\beta]_{i+1/2}^{n+1}}{2} [F_\beta^{up}]_{i+1/2}^{n+1} + \frac{1 - [U_\beta]_{i+1/2}^{n+1}}{2} [F_\beta^{down}]_{i+1/2}^{n+1}. \quad (4.25)$$

Evaluating the momentum flux difference (combining (4.25) with term 2 in (4.10)) when  $[U_\beta]_{i+1/2}^{n+1} = 0$  (i.e., when the velocity or volume flux of a phase is zero), we get:

$$\frac{1}{[V]_{i+1/2}} \left( \frac{1}{2} [F_v^{up}]_{i+1/2}^{n+1} + \frac{1}{2} [F_v^{down}]_{i+1/2}^{n+1} \right) = \frac{1}{[A]_{i+1/2}} \frac{[A\rho_v S_v u_v^2]_{i+3/2}^{n+1} - [A\rho_v S_v u_v^2]_{i-1/2}^{n+1}}{2\Delta s}. \quad (4.26)$$

Equation (4.26) is the central difference approximation of the momentum flux derivative ( $f'(s) = (f(s + \Delta s) - f(s - \Delta s))/2\Delta s$ ), which assumes that the interfaces  $i + 3/2$  and  $i - 1/2$  are equal distances from  $i + 1/2$ . Therefore, our hybrid upstream weighting method requires a constant grid size, i.e.,  $\Delta s = \text{constant}$ .

One of the difficulties with hybrid upstream weighting is selecting an appropriate value for  $X_{tol}$  (the value of the range over which the transition between upwinding direction occurs). Conditions based on the Peclet number, which describes the relative importance of advective and diffusive processes, have been suggested (Spalding, 1972). However, as noted above, our method uses the value of the flowing primary variables ( $[u_v]_{i+1/2}^{n+1}$  and  $[F_{Vl}]_{i+1/2}^{n+1}$ ) to transition between upwinding directions over a manually set transition range. We found  $X_{tol} = 1E - 6$  worked well on a range of problems and is, therefore, used as the default tolerance.

### 4.3 Discrete equations for phase slip

In this work, the constitutive equation describing phase slip is solved implicitly at the same time as the conservation equations. This is advantageous because it provides implicit knowledge of the flow direction for both phases. This allows both phases to be upwinded independently without using the flowing mass fraction as a primary variable (discussed further in Section (4.4) below) and without lagging any variables in time.

Additionally, it allows different slip models, which may be formulated in terms of different variables, to be implemented in the same way. For example, the drift-flux model by Shi et al. (2005) (discussed in Section 3.2.2.4) is a function of vapour saturation and pressure. By comparison, the Rouhani II model (discussed in Section 3.2.2.3) is a function of the flowing mass fraction and pressure.

We found the formulation of the drift-flux model to have a significant effect on the ability of the simulator to model counter-flow. The method described below was found to provide good numerical performance for all of our test cases and was developed during the numerical investigations presented later on in Chapter 6.

#### 4.3.1 Shi et al.'s (2005) drift-flux model

We implement the drift-flux model by solving the vapour velocity equation given in (3.10) and the conservation equations simultaneously. This equation is formulated numerically as:

$$[R_{slip}]_{4i+5}^{n+1} = [u_v]_{i+1/2}^{n+1} - [C_0]_{i+1/2}^{n+1} ([S_v u_v]_{i+1/2}^{n+1} + [F_{VI}]_{i+1/2}^{n+1}) - [u_d]_{i+1/2}^{n+1} = 0 \quad (4.27)$$

In (4.27),  $[C_0]_{i+1/2}^{n+1}$  and  $[u_d]_{i+1/2}^{n+1}$  are defined using the empirical model by Shi et al. (2005). As noted in Section 3.2.2.4, the optimised parameters suggested by Shi et al. (2005) mean that:

$$[C_0]_{i+1/2}^{n+1} = 1 \quad (4.28)$$

for all cases. We have made this simplification in the following discussion of the calculation of the drift velocity.



We found that the numerical implementation of  $u_d$  impacted the ability of our simulator to model counter-flow. Specifically, the handling of vapour saturation in this calculation proved to be important. A detailed discussion of how this method was developed is given in Section 6.2.

To calculate the drift velocity we first calculate  $[u_d^N]_{i+1/2}^{n+1}$  and  $[u_d^S]_{i+1/2}^{n+1}$ . The two variables are the same, other than the value of vapour saturation used in their definitions. The variable  $[u_d^N]_{i+1/2}^{n+1}$  is defined using the vapour saturation above the interface (from block  $i + 1$ ):

$$[u_d^N]_{i+1/2}^{n+1} = \frac{(1 - [S_v]_{i+1}^{n+1})C_0K_u([S_v]_{i+1}^{n+1})m([\theta]_{i+1/2})}{[S_v]_{i+1}^{n+1}([\rho_v^{ave}]_{i+1/2}^{n+1}/[\rho_l^{ave}]_{i+1/2}^{n+1})^{0.5} + 1 - [S_v]_{i+1}^{n+1}}[u_c]_{i+1/2}^{n+1} \quad (4.29)$$

while  $[u_d^S]_{i+1/2}^{n+1}$  uses the vapour saturation from the block below the interface (from block  $i$ ):

$$[u_d^S]_{i+1/2}^{n+1} = \frac{(1 - [S_v]_i^{n+1})C_0K_u([S_v]_i^{n+1})m([\theta]_{i+1/2})}{[S_v]_i^{n+1}([\rho_v^{ave}]_{i+1/2}^{n+1}/[\rho_l^{ave}]_{i+1/2}^{n+1})^{0.5} + 1 - [S_v]_i^{n+1}}[u_c]_{i+1/2}^{n+1} \quad (4.30)$$

In (4.29) and (4.30), the average interface density,  $[\rho_\beta^{ave}]_{i+1/2}^{n+1}$ , is calculated as:

$$[\rho_\beta^{ave}]_{i+1/2}^{n+1} = 0.5 ([\rho_\beta]_i^{n+1} + [\rho_\beta]_{i+1}^{n+1}) \quad (4.31)$$

and the characteristic velocity  $[u_c]_{i+1/2}^{n+1}$  is formulated numerically as:

$$[u_c]_{i+1/2}^{n+1} = \left( \frac{g[\sigma_{vl}]_{i+1/2}^{n+1} ([\rho_l^{ave}]_{i+1/2}^{n+1} - [\rho_v^{ave}]_{i+1/2}^{n+1})}{([\rho_l^{ave}]_{i+1/2}^{n+1})^2} \right)^{1/4} \quad (4.32)$$

The Bond number, used in the calculation of  $C_0K_u(S_v)$  in (4.29) and (4.30), is calculated as:

$$[N_b]_{i+1/2}^{n+1} = ([d]_{i+1/2})^2 \left( \frac{g ([\rho_l^{ave}]_{i+1/2}^{n+1} - [\rho_v^{ave}]_{i+1/2}^{n+1})}{[\sigma_{vl}]_{i+1/2}^{n+1}} \right) \quad (4.33)$$

In (4.32) and (4.33), the surface tension is calculated from the IAPWS (2014) correlation and is a function of the average interface temperature  $[T]_{i+1/2}^{n+1} = 0.5 ([T]_i^{n+1} + [T]_{i+1}^{n+1})$ . Finally, the well deviation is calculated as  $[\theta]_{i+1/2} = \cos^{-1}([\Delta z/\Delta s]_{i+1/2})$ .

To calculate the drift velocity used in (4.27), we transition smoothly between  $[u_d^S]_{i+1/2}^{n+1}$  for low vapour saturations and  $[u_d^N]_{i+1/2}^{n+1}$  for high vapour saturations, based on the value of the average vapour saturation on the interface,  $[S_v^{ave}]_{i+1/2}^{n+1}$ . To do this, we define the variable  $[U_{slip}]_{i+1/2}^{n+1}$  to smoothly transition between zero and one:

$$[U_{slip}]_{i+1/2}^{n+1} = \begin{cases} 0 & [S_v^{ave}]_{i+1/2}^{n+1} \leq b_1 \\ \frac{1}{2} \left[ 1 - \cos \left( \pi \frac{[S_v^{ave}]_{i+1/2}^{n+1} - b_1}{b_2 - b_1} \right) \right] & b_1 \leq [S_v^{ave}]_{i+1/2}^{n+1} \leq b_2 \\ 1 & [S_v^{ave}]_{i+1/2}^{n+1} \geq b_2 \end{cases} \quad (4.34)$$

Here,  $b_1$  and  $b_2$  define the range over which  $[U_{slip}]_{i+1/2}^{n+1}$  transitions from zero to one. Values of  $b_1 = 0.3$  and  $b_2 = 0.4$  were found to perform well on our counter-flow test problems. In (4.34), the average vapour saturation on an interface is defined as:

$$[S_v^{ave}]_{i+1/2}^{n+1} = 0.5 ([S_v]_i^{n+1} + [S_v]_{i+1}^{n+1}) \quad (4.35)$$

Finally, the drift velocity  $[u_d]_{i+1/2}^{n+1}$  is calculated as:

$$[u_d]_{i+1/2}^{n+1} = \left( 1 - [U_{slip}]_{i+1/2}^{n+1} \right) [u_d^S]_{i+1/2}^{n+1} + [U_{slip}]_{i+1/2}^{n+1} [u_d^N]_{i+1/2}^{n+1} \quad (4.36)$$

This implementation means that when the average vapour saturation on the interface is less than 0.3,  $[u_d]_{i+1/2}^{n+1} = [u_d^S]_{i+1/2}^{n+1}$ . When the average vapour saturation is greater than 0.4,  $[u_d]_{i+1/2}^{n+1} = [u_d^N]_{i+1/2}^{n+1}$ . Finally, when the average vapour saturation on the interface is between 0.3 and 0.4, we transition smoothly between  $[u_d^S]_{i+1/2}^{n+1}$  and  $[u_d^N]_{i+1/2}^{n+1}$ .

## 4.4 Primary variables

The discrete equations defined in the previous section are solved numerically for primary variables. These primary variables are used to calculate all of the remaining unknowns (called secondary variables) and, therefore, must completely specify the thermodynamic state of the wellbore.

The choice of these primary variables differs between modellers and depends on the form of the governing equations, the chosen constitutive equations and the numerical implementation. The three-equation conservation model requires at least three primary variables. Two are used to describe the thermal properties of the fluid. The other primary variable is a flowing quantity such as mixture velocity or total mass flow and appears dominantly in the momentum equation. Primary variables may be persistent, meaning they are the same regardless of how many phases are present. Alternatively, different combinations of primary variables may be used for single and two-phase flows, a method known as variable switching. Both of these approaches have been used in past geothermal wellbore simulators.

The best choice of primary variables for our transient wellbore simulator was not obvious. We reviewed the primary variables used in past geothermal simulators to assist with this choice. Variable switching and persistent methods are discussed in Sections 4.4.1 and 4.4.2, respectively.

When reviewing the past literature, we found that variables weighted by mass flow, for example, the flowing mass fraction or flowing enthalpy, were common choices of primary variables. We discuss why these are not suitable for use in our simulator in Section 4.4.3. Finally, we discuss our chosen primary variables in Section 4.4.4.

### 4.4.1 Primary variable switching

As mentioned above, simulators that use primary variable switching use different primary variables for single-phase and two-phase conditions. Table 4.1 summarises different combinations of primary variables that utilise this method. It is clear from Table 4.1 that pressure and temperature are generally chosen as single-phase primary variables. During

TABLE 4.1: Primary variable switching for two-phase flow of pure water.

Model	Type					
Temperature switching	Steady	$P$	$T(x_{fv})$	$Q_m$	-	
Pressure switching	Steady	$P(x_{fv})$	$T$	$Q_m$	-	
Tachimori (1982)	Steady	$P$	$T(S_v)$	$u_v$	$u_l$	
T2WELL (Pan et al., 2011)	Transient	$P$	$T(S_v)$	$u_{mix}$	-	

two-phase flow, the pressure and temperature of the fluid are related by the saturation conditions meaning one must be switched out.

In the literature, some steady-state models, for example, Upadhyay et al. (1977), Bjornsson (1987) and Aunzo et al. (1991) switch the temperature for the flowing vapour mass fraction and retain pressure. Others, for example, Barelli et al. (1982) and McGuinness (2015), switch pressure for the flowing vapour mass fraction and retain the temperature. Most steady-state models do not specify a third primary variable as the total mass flow,  $Q_m$ , is known from the boundary conditions (and feed-zones). We have included it as a primary variable in Table 4.1 as it is integral to the solution process.

Other variable switching methods have occasionally been used. For example, Tachimori (1982) solved the mass conservation and slip constitutive equation implicitly in addition to the momentum and energy equations. Tachimori's (1982) simulator, therefore, required three primary variables ( $P$ ,  $T$ ,  $u_v$  or  $u_l$ ) for single-phase flow and four primary variables ( $P$ ,  $S_v$ ,  $u_v$  and  $u_l$ ) for two-phase flow.

In the literature, T2WELL (Pan, Oldenburg, Wu and Pruess, 2011) is the only transient geothermal wellbore simulator to have used variable switching. This simulator switched temperature and vapour saturation. The third primary variable was chosen as the mixture velocity. Note, an additional primary variable, the mass fraction of  $\text{CO}_2$  is used in T2WELL. As this is used to model the  $\text{CO}_2$  component, it has been left out of the present discussion.

#### 4.4.2 Persistent primary variables

Persistent primary variables are the same regardless of the phase state of the fluid. In the steady-state literature, pressure and flowing specific mixture enthalpy have been used as persistent primary variables. For example, simulators developed by Gould (1974),

TABLE 4.2: Persistent primary variables for two-phase flow of pure water.

Model	Type				
Flowing enthalpy	Steady	$P$	$h_{fmix}$	$Q_m$	-
Gudmundsdottir (2012)	Steady	$P$	$h_{fmix}$	$u_{uni}$	-
Miller (1980 <i>b</i> )	Transient	$P$	$e_{mix}$	$Q_m$	-
García-Valladares et al. (2006)	Transient	$P$	$h_{fmix}$	$Q_m$	-
Akbar et al. (2016)	Transient	$P$	$h_{fmix}$	$u_{mix}$	-

Chierici et al. (1981), Hasan and Kabir (2010) and Franz and Clearwater (2021) use these variables. As mentioned previously, the total mass flow is known from the boundary conditions in steady-state simulation and has, therefore, been included as a primary variable.

The simulator FloWell by Gudmundsdottir (2012) uses slightly different persistent variables. It solves the mass, momentum and energy equations for  $P$ ,  $u_{uni}$  and  $h_{fmix}$ , where  $u_{uni} = Q_m/(\rho_l A)$ .

Transient simulators developed by García-Valladares et al. (2006) and Akbar et al. (2016) have both used the pressure and flowing specific mixture enthalpy as primary variables. García-Valladares et al. (2006) chose the total mass flow as the third primary variable, whereas Akbar et al. (2016) chose the mixture velocity. Miller (1980*b*) on the other hand, used pressure, the static specific mixture internal energy and the total mass flow as primary variables.

Table 4.2 summarises the persistent primary variable combinations used in the literature. It indicates that the flowing enthalpy is a very common choice of primary variable.

#### 4.4.3 Primary variables weighted by mass flow

The review of the geothermal wellbore modelling literature indicated that either the flowing vapour mass fraction,  $x_{fv}$  or the flowing enthalpy,  $h_{fmix}$  were commonly chosen as one of the primary variables in both steady-state and transient simulators. Using mass flow weighted variables when formulating or solving the governing conservation equations presents difficulties when modelling wells with zero mass flow or counter-flow. The reasons for this are discussed below, using the flowing mass fraction as an example. The same general argument applies to the flowing enthalpy as its definition,  $h_{fmix} =$

$x_{fv}h_v + x_{fl}h_l$ , makes use of the flowing mass fractions, meaning  $x_{fv}$  is calculated directly from  $h_{f_{mix}}$ .

The flowing mass fraction of phase  $\beta$  is defined as:

$$x_{f\beta} = Q_{m\beta}/Q_m \quad (4.37)$$

where,  $Q_{m\beta}$  is the mass flow of phase  $\beta$  and the total mass flow is  $Q_m = Q_{mv} + Q_{ml}$ . This definition makes the flowing mass fraction a useful variable when simulating co-current flows. As was discussed in Section 2.1.1.4, it allows the mass and volume flow of both phases to be calculated directly from the total mass flow (provided the pressure or temperature is also known). Additionally, the flowing mass fraction is typically known (or is easily calculated from the flowing enthalpy) at the wellhead in geothermal applications, as was briefly discussed in Section 2.1.1.4. Finally, it was shown in Section 3.2 that the flowing mass fractions appear explicitly in many common slip relationships.

However, the definition of  $x_{f\beta}$  in (4.37) is problematic when simulating general two-phase flow in wells. Table 4.3 shows this by giving the mass flow of each phase, total mass flow, saturation and flowing vapour mass fraction (calculated using (4.37)) for different flow scenarios.

Table 4.3 indicates that when total mass flow equals zero, then  $x_{fv}$  is undefined. This situation can occur during counter-flow, when a well is shut-in or when the flow direction changes. Additionally, when general counter-flow occurs, in which the total mass flow does not necessarily equal zero,  $x_{fv}$  has a value outside the physical bounds for a mass fraction. Finally, the flowing mass fraction cannot differentiate between transitions from two-phase to single-phase conditions and transitions between the co-current and counter-flow regimes. The last two lines of Table 4.3 give the mass flow, vapour saturation and flowing mass fractions for the flow transitions between two-phase and single-phase conditions. Here, the mass flow of the disappearing phase (e.g., liquid when two-phase is transitioning to vapour) is zero. Comparing these cases with the conditions at the boundary between the counter-flow and co-current flow regimes, we see, for example, that  $x_{fv}$  has a value of one when transitioning between counter-flow and up-flow and when transitioning between two-phase and vapour conditions. This is because the liquid

TABLE 4.3: Possible values of flowing vapour mass fraction,  $x_{fv}$ , for flow scenarios that are possible during two-phase flow.

Flow scenario	$Q_{mv}$	$Q_{ml}$	$Q_m$	$S_v$	$x_{fv}$
Co-current up-flow	$>0$	$>0$	$>0$	$0 < S_v < 1$	$0 < x_{fv} < 1$
Co-current down-flow	$<0$	$<0$	$<0$	$0 < S_v < 1$	$0 < x_{fv} < 1$
Counter-flow	$>0$	$<0$	$Q_m > Q_{ml} \ \& \ Q_m < Q_{mv}$	$0 < S_v < 1$	$x_{fv} < 0$ or $x_{fv} > 1$
$Q_m = 0$ (e.g., stable counter-flow)	$>0$	$<0$	0	$0 < S_v < 1$	Undefined
Counter-flow/up-flow regime boundary	$>0$	0	$Q_{mv}$	$0 < S_v < 1$	1
Counter-flow/down-flow regime boundary	0	$<0$	$Q_{ml}$	$0 < S_v < 1$	0
Two-phase/vapour phase transition	$\neq 0$	0	$Q_{mv}$	1	1
Two-phase/liquid phase transition	0	$\neq 0$	$Q_{ml}$	0	0

mass flow is zero in both cases, which means that  $x_{fv}$  does not uniquely define the transition to vapour conditions. The flowing mass fraction, therefore, cannot be used for identifying phase transitions.

Given the issues with using the flowing mass fraction (or flowing enthalpy) as a primary variable, we decided that these variables should not be used when formulating or solving the governing conservation equations if counter-flow or zero-mass flow cases are of interest. As these cases commonly occur during transient wellbore flow, for example, opening and closing the well, it seems better to use a statically defined variable such as vapour saturation. Table 4.3 indicates that vapour saturation stays within physical bounds for all cases and only takes a value of zero or one during transitions between two-phase and single-phase conditions.

#### 4.4.4 Preferred primary variables

A different approach was taken in this work than those from the literature described above. Our approach is to solve the slip model as a fourth equation implicitly for a fourth primary variable. This method is beneficial for several reasons. Firstly, it provides implicit knowledge of an additional primary variable. This means that the flow direction of both phases is known explicitly from the primary variables (without using the flowing mass fraction or flowing enthalpy). Secondly, as we discussed previously, not all empirical slip parameters are formulated in terms of the same variables and, therefore, may not be able to be calculated explicitly (depending on the chosen primary variables). This makes implementing different slip models more complex as either the primary variables

TABLE 4.4: Combinations of primary variables tested in this work.

Velocity formulation	$P$	$T(S_v)$	$u_v$	$u_l$
Volume flux formulation	$P$	$T(S_v)$	$F_{Vv}$	$F_{Vl}$
Mixed formulation	$P$	$T(S_v)$	$u_v$	$F_{Vl}$

TABLE 4.5: Primary variable values to determine the current phase-state of the fluid.

P	T	$S_v$	Phase state
$P > P_{sat}(T)$	$T < T_{sat}(P)$	0	Single-phase liquid
$P < P_{sat}(T)$	$T > T_{sat}(P)$	1	Single-phase vapour
$P = P_{sat}(T)$	$T = T_{sat}(P)$	$0 < S_v < 1$	Two-phase conditions

must be changed, some unknowns must be lagged by a time step or the equation for slip must be solved implicitly anyway.

Always solving the slip equation implicitly avoids some of the issues discussed above. However, we found that the formulation of the slip equation and choice of primary variables had a significant effect on the numerical performance of the simulator. This is discussed further in Section 6.1.

As mentioned above, solving the slip equation implicitly requires a fourth primary variable. This was also done for one previous simulator, i.e., the steady-state model by Tachimori (1982). They used  $P$ ,  $T(S_v)$ ,  $u_v$  and  $u_l$  as primary variables. We initially used these primary variables in our simulator. However, after several issues were encountered, other choices for primary variables were explored.

The three different primary variable combinations tested in this work are given in Table 4.4. Two of the primary variables remain the same for all three cases. For single-phase flow, pressure and temperature are used. They are switched to pressure and vapour saturation for two-phase conditions. This process is described in Section 4.4.4.1 below. These primary variables are the standard choice in geothermal reservoirs simulators (when using the pure water equation of state) and have proven to result in a robust method for dealing with multi-phase systems (Pruess et al., 2012; Croucher, 2020). Choosing these primary variables also allows existing thermodynamic packages to be used and simplifies future integration with existing reservoir codes. The phase state of a wellbore element is determined explicitly from these primary variables. Their values in different phases are given in Table 4.5.



The two remaining primary variables are flow variables and appear predominantly in the momentum equation. We will, therefore, refer to them as *flowing primary variables*. The three combinations of flowing primary variables tested were the phase velocities, phase volume fluxes and a mixed formulation, which used the vapour velocity and liquid volume flux. The numerical performance of the three different combinations was compared. The main results from this investigation were that the choice of primary variables and the numerical formulation of the constitutive slip equation had a significant impact on the numerical performance of our simulator. We found that the best choice of primary variables for our implementation of Shi et al.'s (2005) drift-flux model was the mixed formulation ( $P$ ,  $T$  swapped with  $S_v$ ,  $u_v$  and  $F_{VL}$ ). The investigation that resulted in this choice is presented in Section 6.1.

#### 4.4.4.1 Primary variable switching method

As described above, our simulator uses primary variable switching. For pure water simulations, the primary variables are pressure and temperature for single-phase flow, while pressure and vapour saturation are used when two-phase conditions exist. While pressure is retained as a primary variable, it must be recalculated to ensure that it is within the new thermodynamic region. The remaining primary variables (vapour velocity and liquid volume flux) are persistent and do not require switching.

The method used to switch primary variables affects the numerical performance of the simulator as methods that result in discontinuities and inconsistencies in primary variables over the phase transition may present numerical difficulties and require smaller time steps when transitioning between phases. The switching method used in our simulator avoids significant discontinuities and is based on the method used in the reservoir simulator Waiwera (Croucher et al., 2018; Croucher, 2020).

Table 4.5 shows the values which the primary variables may take for liquid, vapour and two-phase conditions. Transitions between phase states occur when the primary variables step over these bounds. Single-phase liquid will transition to two-phase conditions when the fluid pressure drops below the saturation pressure. Likewise, vapour conditions will transition to two-phase when the fluid pressure increases above the saturation pressure.

TABLE 4.6: Pressure, temperature and saturation conditions during phase transitions. Transitions from single-phase to two-phase conditions are identified using the pressure. Transitions from two-phase to single-phase conditions are identified using the vapour saturation.

P	T	$S_v$	Transition
$P_x < P_{sat}(T_x)$	$T_x$	0	Liquid to two-phase transition
$P_x > P_{sat}(T_x)$	$T_x$	1	Vapour to two-phase transition
$P_x$	$T_{sat}(P_x)$	$S_{vx} < 0$	Two-phase to liquid transition
$P_x$	$T_{sat}(P_x)$	$S_{vx} > 1$	Two-phase to vapour transition

Transitions from two-phase to single-phase conditions occur when the vapour saturation steps outside the interval between zero and one. These conditions are summarised in Table 4.6 and the numerical procedure for switching primary variables is outlined below.

A transition occurs when the single-phase pressure and temperature "step over" the two-phase saturation curve during a Newton step. This step across the saturation curve occurs when  $P_{k+1} < P_{sat}(T_{k+1})$ , where  $k$  is the index of the Newton iteration. This is shown diagrammatically in Figure 4.5 A) for the transition between liquid and two-phase conditions.

Once the transition is recognised, we must switch the temperature primary variable with vapour saturation. We also must ensure that the pressure and vapour saturation primary variables are within the two-phase region. To do this, we calculate the new 'two-phase' pressure and temperature at the point at which the Newton step crosses the saturation curve. This point is where the straight line between  $(T_k, P_k)$  and  $(T_{k+1}, P_{k+1})$  intersects with  $P_{sat}(T)$ , shown by  $(P_x, T_x)$  in Figure 4.5 A). This intersect is formulated numerically as:

$$P_k + \frac{P_{k+1} - P_k}{T_{k+1} - T_k}(T - T_k) = P_{sat}(T) \quad (4.38)$$

This equation is non-linear and is, therefore, solved using Brent's method to find  $T = T_x$ . The new two-phase pressure is then calculated as  $P_x = P_{sat}(T_x)$ . The vapour saturation primary variable is set as  $S_{vx} = 1E - 6$ .

The same process is used when transitioning from vapour to two-phase conditions. However, the transition occurs when  $P > P_{sat}(T)$ . The vapour saturation is set as  $S_{vx} = 1 - 1E - 6$  and the new two-phase pressure is calculated using (4.38).

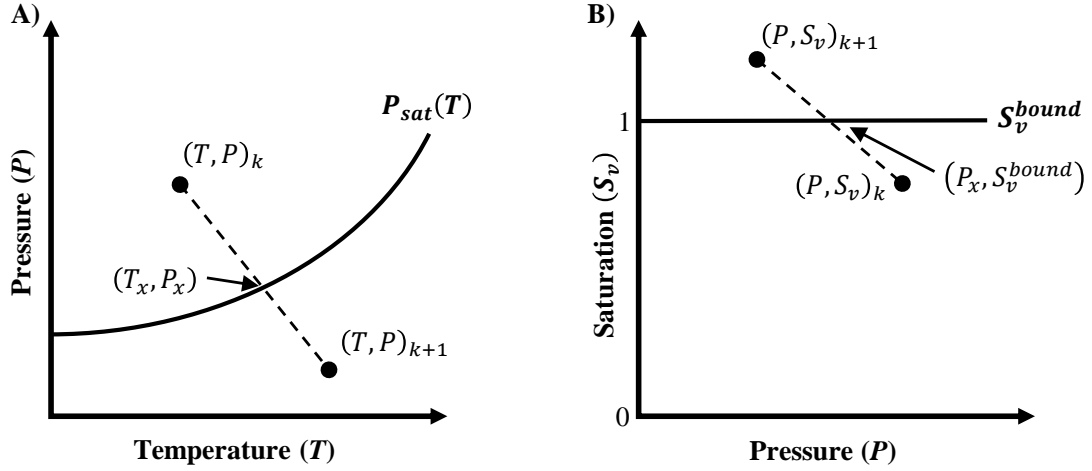


FIGURE 4.5: Variable switching for A) phase transitions from liquid to two-phase conditions and B) phase transitions from two-phase to vapour conditions.

Transitions from two-phase to single-phase conditions are identified using the vapour saturation primary variable. Following a Newton step, a vapour saturation greater than one indicates the two-phase block should transition to vapour conditions. This case is shown in Figure 4.5 B). Likewise, if vapour saturation drops below zero, a transition to liquid conditions occurs.

When a transition away from two-phase conditions occurs, we must estimate a new single-phase pressure and temperature. The vapour saturation primary variable is then switched with the new single-phase temperature. To do this, we calculate the pressure at which the Newton step crosses the boundary between the two-phase and single-phase regions (denoted by  $S_v^{bound}$  in Figure 4.5). This is formulated as:

$$P_x = \left( \frac{S_v^{bound} - S_{v,k}}{S_{v,k+1} - S_{v,k}} \right) (P_{k+1} - P_k) + P_k \quad (4.39)$$

Here,  $S_v^{bound}$  is zero or one for transitions to liquid or vapour, respectively. The new single-phase temperature is calculated from the saturation relationship ( $T_x = T_{sat}(P_x)$ ). This means that the new values of pressure and temperature are still at saturation conditions. Therefore, the pressure is offset by a small amount ( $P = (1 \pm 1E-6) * P_x$ ) to ensure the block is within the single-phase region.

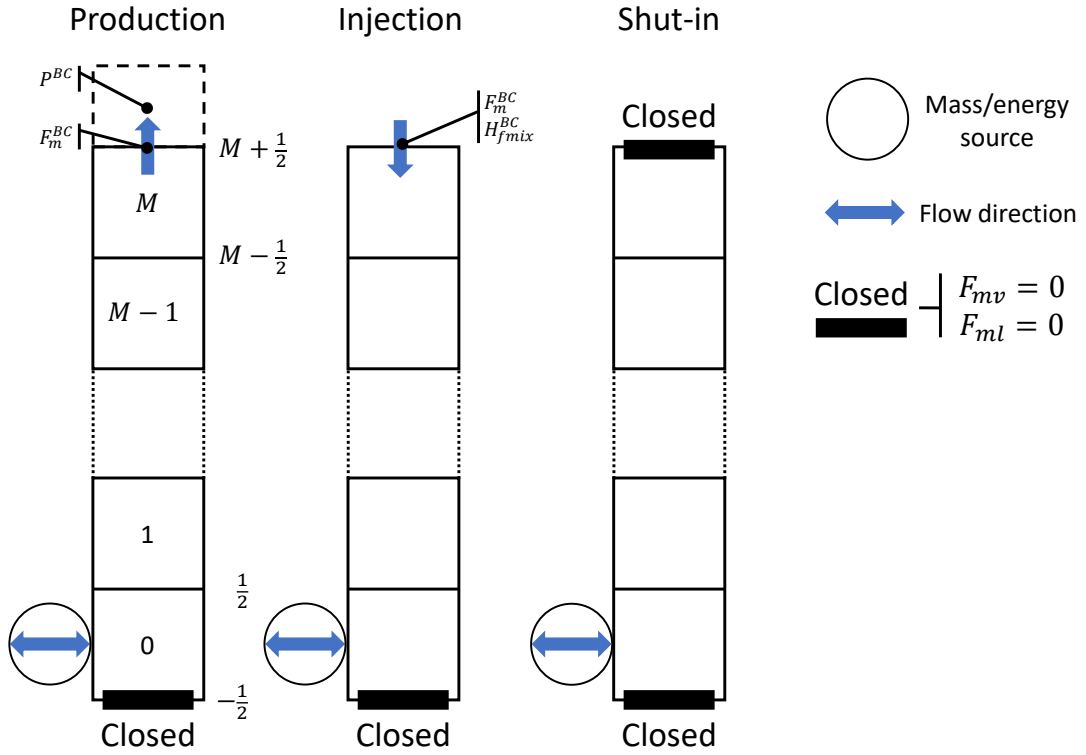


FIGURE 4.6: Diagrammatic representation of production, injection and shut-in boundary conditions.

## 4.5 Boundary conditions

Boundary conditions describe the behaviour of the wellbore flow at a fixed point in space, which constrains the general flow equations for a specific problem. Physically, the boundary conditions describe the inputs and output of the well. Below we discuss boundary conditions used to model production, injection and the special case of shut-in conditions. Additional boundary conditions, which model the atmosphere, are discussed later on in Section 7.2.3 when we present our air-water equation of state.

### 4.5.1 Production boundary conditions at the wellhead

During production, mass flow or pressure are controlled at the wellhead. In a well, fluid is not typically added through the bottom of the well. Instead, fluid is added over feed-zone intervals where the well intersects with a permeable section of the formation. Therefore, we used a closed bottomhole, and the properties of the in-flowing fluid are defined using source terms. A source term can be defined for any block in the wellbore, meaning a single feed-zone may span multiple blocks.

The discrete mass and energy conservation equations at the wellhead (in block  $i = M$ ) are the same as are given in (4.1) and (4.5). However, the upwinded densities, saturations and enthalpies at the wellhead boundary ( $M + 1/2$ ), which are used to define the mass and energy fluxes, are always taken from the block below. They are defined as:

$$[\rho_\beta]_{M+1/2}^{n+1} = [\rho_\beta]_M^{n+1} \quad (4.40)$$

$$[S_\beta]_{M+1/2}^{n+1} = [S_\beta]_M^{n+1} \quad (4.41)$$

$$[H_\beta]_{M+1/2}^{n+1} = [H_\beta]_M^{n+1} \quad (4.42)$$

The formulation of the momentum equation differs depending on whether mass flow or pressure is specified at the wellhead. The implementation of the pressure and mass flow boundary conditions are discussed in Sections 4.5.1.1 and 4.5.1.2, respectively.

#### 4.5.1.1 Wellhead pressure boundary condition

Pressure can be prescribed at the wellhead as a function of time. This condition is useful for modelling start-up processes as, in these cases, the mass flow at the wellhead is often unknown. It is also useful for long term production scenarios in which the well is operating at a constant pressure equal to the separator pressure. Similarly, the wellhead pressure boundary condition is used when opening the well to atmospheric conditions.

The wellhead pressure,  $P_{BC}^{n+1}$ , is specified in the pressure gradient term within the momentum conservation equation. This equation is formulated as:

$$\begin{aligned} [R_{BC}]_{4M+4}^{n+1} = & \frac{[F_{mv} + F_{ml}]_{M+1/2}^{n+1} - [F_{mv} + F_{ml}]_{M+1/2}^n}{\Delta t} + \frac{P_{BC}^{n+1} - P_M^{n+1}}{\Delta s_M} \\ & + \frac{1}{[V]_{M+1/2}} \left( [AF_{mv}u_v + AF_{ml}u_l]_{M+1/2}^{n+1} - [AF_{mv}u_v + AF_{ml}u_l]_{M-1/2}^{n+1} \right) \\ & + \left[ \frac{2}{r} \tau \right]_{M+1/2}^{n+1} + [\rho_v S_v + \rho_l S_l]_M^{n+1} g \frac{\Delta z_M}{\Delta s_M} = 0. \end{aligned} \quad (4.43)$$

Here, the index  $M$  refers to the wellhead block, as is shown in Figure 4.6. The wellhead pressure boundary condition is denoted by  $P_{BC}^{n+1}$ . The wellhead pressure is specified at

the centre of a "ghost block" above the wellhead interface, as is shown in Figure 4.6. Note that  $[V]_{M+1/2}$  is assumed to equal  $[V]_M$ . The mass flux of each phase is defined in (4.3), however, the upwinded density and saturation given in (4.40) and (4.41) are used.

#### 4.5.1.2 Wellhead mass flux boundary condition

The mass flux boundary condition prescribes the total mass flux (or mass flow) at the wellhead interface as a function of time. To do this, the momentum conservation equation on the wellhead interface is replaced by the mass flux boundary condition:

$$[R_{BC}]_{4M+4}^{n+1} = [F_{mv} + F_{ml}]_{M+1/2}^{n+1} - [F_m]_{BC}^{n+1} = 0. \quad (4.44)$$

When mass flow is specified on the wellhead, the mass flux is calculated as  $[F_m]_{BC}^{n+1} = [Q_m]_{BC}^{n+1} / [A]_{M+1/2}$ .

Equation (4.44) is not appropriate for modelling no-flow conditions at the wellhead (e.g., shut-in cases) because this boundary condition may be satisfied when the phase mass fluxes are non-zero and equal and opposite (i.e., by counter-flow). Non-zero phase mass flows at the wellhead will result in the transport of momentum and energy across the wellhead boundary, despite the total mass flow being zero. Instead, the flow of both phases must equal zero. The wellhead boundary conditions for shut-in conditions are discussed in Section 4.5.3 below.

#### 4.5.1.3 Wellhead slip equation

The constitutive model for slip on the wellhead interface is also solved on the wellhead boundary when the well is not shut-in. Again, the interface variables that are typically upwinded are taken from block  $M$ . The numerical implementation of the drift-flux model is:

$$[R_{slip}]_{4M+5}^{n+1} = [u_v]_{i+1/2}^{n+1} - [C_0]_{M+1/2}^{n+1} \left( [S_v]_M^{n+1} [u_v]_{M+1/2}^{n+1} + [F_{Vl}]_{M+1/2}^{n+1} \right) - [u_d]_{M+1/2}^{n+1} = 0 \quad (4.45)$$

Here,  $[u_d]_{M+1/2}^{n+1}$  is not calculated using the method that was described in Section 4.3. Instead, it is simply calculated using the variables from block  $M$ :

$$[u_d]_{M+1/2}^{n+1} = \frac{(1 - [S_v]_M^{n+1})[C_0 K_u([S_v]_M^{n+1})m([\theta]_M)]}{[S_v]_M^{n+1}([\rho_v]_M^{n+1}/[\rho_l]_M^{n+1})^{0.5} + 1 - [S_v]_M^{n+1}} [u_c]_M^{n+1} \quad (4.46)$$

#### 4.5.2 Injection boundary conditions at the wellhead

Injection scenarios play an important role in the management of geothermal resources. In most cases, it is liquid water that is injected at the wellhead. For example, separated geothermal water is injected back into the reservoir. Liquid water is also injected during injection tests, which are used to infer reservoir characteristics based on wellbore measurements taken at different injection rates. However, two-phase fluid may be injected when completing well-to-well discharge stimulation. In this case, two-phase fluid from a discharging well is injected into a non-discharging well in an attempt to increase well temperatures sufficiently for the well to flow on its own. Therefore, for our simulator, general injection conditions can be specified at the wellhead.

During injection simulations, the flowing mixture enthalpy,  $[H_{f_{mix}}]_{BC}^{n+1}$ , and mass flux,  $[F_m]_{BC}^{n+1}$ , of the in-flowing fluid are specified as boundary conditions at the wellhead. The mass flux is specified in the same way as described in Section 4.5.1.2 above. The wellhead enthalpy is specified in the energy conservation equation for block  $M$ :

$$\begin{aligned} & \frac{[S_v \rho_v H_v + S_l \rho_l H_l - P]_M^{n+1} - [S_v \rho_v H_v + S_l \rho_l H_l - P]_M^n}{\Delta t} \\ & + \frac{1}{[V]_i} \left( [A]_{M+1/2}^{n+1} [F_m]_{BC}^{n+1} [H_{f_{mix}}]_{BC}^{n+1} - [AF_{mv} H_v + AF_{ml} H_l]_{M-1/2}^{n+1} \right) \\ & + [F_{mv} + F_{ml}]_M^{n+1} g \frac{\Delta z_M}{\Delta s_M} + [q_{heat}]_M^{n+1} - [q_{ener}]_i^{n+1} = 0. \quad (4.47) \end{aligned}$$

#### 4.5.3 Closed boundary conditions

Closed boundary conditions (no-flow conditions) prevent flow through a boundary. In our simulator, the bottom boundary of the well is always assumed to be closed, and sources of mass and energy from the reservoir are modelled using the source terms. We have retained the residual equations and primary variables on this bottom interface for flexibility.

To specify no-flow conditions through the bottom boundary, we set the vapour velocity and liquid volume flux to be zero:

$$R_0 = [u_v]_{-1/2}^{n+1} = 0 \quad (4.48)$$

and,

$$R_1 = [F_{Vl}]_{-1/2}^{n+1} = 0 \quad (4.49)$$

Additionally, closed (no-flow) boundary conditions are required at the wellhead to model scenarios such as shutting in a flowing well and the heating up of closed wells. Again, we must enforce flow in both phases to equal zero. For the wellhead boundary, we replace the momentum conservation equation with:

$$R_{4M+4} = [u_v]_{M+1/2}^{n+1} = 0 \quad (4.50)$$

and the slip equation with:

$$R_{4M+5} = [F_{Vl}]_{M+1/2}^{n+1} = 0 \quad (4.51)$$

These conditions ensure that there is no mass, momentum or energy flow through the boundary. We switch to these no-flow boundary conditions (i.e., shut the well) if the total mass flow reaches zero when using either the pressure or mass flux boundary conditions.

## 4.6 Solution procedure

This section discusses the numerical procedure used to solve the governing conservation equations, and the constitutive model for slip, for our chosen primary variables. We solve these equations simultaneously using the multi-variate Newton-Raphson method. This method is explained in Section 4.6.1 below. We then briefly discuss the calculation of gradients in the Jacobian matrix, convergence criterion and time stepping in the following sections.



#### 4.6.1 Multi-variate Newton-Raphson method

The Newton-Raphson method iteratively updates the array of primary variables,  $x$ , to drive the residuals, which describe the imbalance in the discrete conservation equations, to zero using the following linear system:

$$\mathbf{J}\Delta\mathbf{x} = -\mathbf{R} \quad (4.52)$$

Here  $\mathbf{J}$  is the Jacobian matrix and  $\mathbf{R}$  is the array of residuals calculated using the discretised conservation equations. This linear system is solved for the update vector,  $\Delta x$ , which represents the change in primary variables. Here, the residual vector is assembled from the residuals defined previously in the chapter. For example, for the case where the total mass flux is specified on the top boundary, the residual vector is:

$$\mathbf{R} = \begin{bmatrix} R_0 \\ R_1 \\ \vdots \\ R_{4i} \\ R_{4i+1} \\ R_{4i+2} \\ R_{4i+3} \\ R_{4i+4} \\ R_{4i+5} \\ \vdots \\ R_{4M+4} \\ R_{4M+5} \end{bmatrix} = \begin{bmatrix} \text{BH BC} \\ \text{BH BC} \\ \vdots \\ [\text{Mom}]_{i-1/2} \\ [\text{Slip}]_{i-1/2} \\ [\text{Mass}]_i \\ [\text{Ener}]_i \\ [\text{Mom}]_{i+1/2} \\ [\text{Slip}]_{i+1/2} \\ \vdots \\ \text{WH BC} \\ \text{WH Slip} \end{bmatrix} = \begin{bmatrix} (4.48) \\ (4.49) \\ \vdots \\ (4.10) \\ (4.27) \\ (4.1) \\ (4.5) \\ (4.10) \\ (4.27) \\ \vdots \\ (4.44) \\ (4.45) \end{bmatrix} \quad (4.53)$$

The Jacobian matrix,  $\mathbf{J}$ , contains derivatives of residuals with respect to the primary variables. It is defined as:

$$\mathbf{J} = \begin{bmatrix} \frac{\partial R_0}{\partial x_0} & \cdots & \frac{\partial R_0}{\partial x_{4M+5}} \\ \vdots & \ddots & \vdots \\ \frac{\partial R_{4M+5}}{\partial x_0} & \cdots & \frac{\partial R_{4M+5}}{\partial x_{4M+5}} \end{bmatrix} \quad (4.54)$$

The Newton-Raphson method uses the Jacobian to drive the convergence of the residual equations to zero for each time step. This means that an inaccurate or poorly calculated Jacobian can result in slow or failed convergence. In our simulator, the Jacobian is calculated approximately using finite differencing. This involves perturbing the primary variable  $x_j$  by a small amount  $dx_j$  and taking the forward difference:

$$J_{ij} = \frac{\partial R_i}{\partial x_j} = \frac{R_i(x_j + dx_j) - R_i(x_j)}{dx_j}. \quad (4.55)$$

This method can be prone to truncation and round-off errors. Decreasing the step size,  $dx_j$ , will reduce the truncation error, however, it will also increase the round-off error. There is an optimal size of  $dx_j$  that minimises the truncation and round-off errors for each term in the Jacobian. However, this optimal value will change depending on the residual equation and the primary variable. This is because both the governing equations and primary variables can have very different orders of magnitude. For example, typical wellbore pressures can range from  $1 \times 10^5$  Pa to  $2 \times 10^7$  Pa, whereas the saturation varies between 0 and 1. For this reason,  $dx_j$  is estimated as  $dx_j = \pm 1E - 6(x_j + 1)$ . Note that we always calculate  $dx_j$  to ensure the primary variable steps away from the phase boundaries. For example, for the pressure primary variable,  $dx_j$  is taken as positive in the liquid region and negative in the vapour region. This avoids phase transitions when calculating the gradients.

The primary variables are updated iteratively using:

$$\mathbf{x}_{k+1} = \mathbf{x}_k + \Delta \mathbf{x} = \mathbf{x}_k - \mathbf{J}_k^{-1} \mathbf{R}_k, \quad (4.56)$$

where  $k$  is the index of the Newton iteration.

The convergence of the Newton-Raphson procedure is used to automatically adjust the time step during a simulation. This is essential for efficient computation as the time-scales of different wellbore processes can vary significantly. We use a simple method based on the number of Newton iterations required for convergence. If the current time step converges in less than four Newton iterations, then the time step is increased. Conversely, if the residuals have not converged to a suitable tolerance after seven Newton

iterations (i.e., the current primary variables do not adequately satisfy the conservation equations), then the time step is repeated with a reduced time increment. The time step is repeatedly dropped until the time step converges within seven iterations.

#### 4.6.2 Convergence criterion

The convergence criterion defines the point at which the numerical solution adequately satisfies the conservation equations. As noted previously, the residuals provide a measure of this. Therefore, we consider the residual vector when judging the convergence of our solution.

The residual vector,  $R$ , must be normalised because the order of magnitude of each residual equation differs significantly from one another. The residual for the mass conservation equation is weighted by the amount of mass in an element,  $[\rho_v S_v + \rho_l S_l]_i^{n+1}$ . The residual for the energy conservation equation is normalised using the amount of energy in the block  $[\rho_v S_v h_v + \rho_l S_l h_l - P]_i^{n+1}$ . The residual for the momentum equation cannot be normalised by the total momentum of the flow as the momentum of the fluid is zero when mass flow is zero. This can result in numerical errors associated with division by small numbers. When flow tends towards zero, the dominant term in the momentum residual is the hydrostatic pressure gradient. Therefore, the residual is normalised using  $[\rho_{mix}^{ave}]_{i+1/2}^{n+1} g$  where the average density is calculated using (4.13). Finally, we do not normalise the slip equation as it has a relatively small order of magnitude (the same order as the vapour velocity).

A time step is considered to be converged when:

$$\|R_{norm}\|_{inf} \leq 1.0E - 6 \quad (4.57)$$

This condition ensures the largest normalised residual is below the desired tolerance of 1.0E-6.

## 4.7 Summary

This chapter presents the numerical method used to solve the conservation equations for transient flow in a geothermal wellbore. Our formulation is fully implicit in time

and requires upwinding for stability. Two different methods of upwinding were presented in this work. The first had discrete transitions between upwinding directions and the second transitions smoothly.

Our model solves the equation for slip simultaneously with the three discrete conservation equations for four primary variables. This method provides explicit knowledge of the upwinding direction of both phases. Experimentation showed that the best primary variables for our simulator were pressure, temperature (swapped with vapour saturation for two-phase conditions), vapour velocity and liquid volume flux.

The numerical method described in this section was continually improved over the course of this work. We discuss some of the challenges faced during the development of this numerical implementation in Chapter 6.

## Chapter 5

# Testing a transient geothermal wellbore model

Testing is an important part of the development of any new numerical simulator. This chapter presents the problems used to test our wellbore simulator. First, Section 5.1 presents analytical solutions for simplified wellbore flow, which were used to verify the numerical implementation of our simulator. Following this, simulation results are compared to steady-state pressure and temperature profiles for a range of geothermal wells. These simulations show that our simulator can reproduce real world wellbore flow. Finally, Section 5.3 presents a set of transient test cases used during the development of our simulator. These test cases were developed to ensure our simulator could model a wide range of flow conditions and include production, injection and counter-flow scenarios.

### 5.1 Model verification

Model verification ensures that the numerical model defined in Chapter 4 is programmed correctly. To do this, we derived analytical solutions for simplified forms of the single-phase conservation equations. These are then used to verify the numerical implementation of the simulator.

### 5.1.1 Case 1: constant density model

A simple linear model can be derived for the steady flow of a single-phase isothermal fluid. As this case is single-phase and isothermal, the energy equation is discarded. Additionally, the fluid density and frictional effects are constant, and a vertical well with a constant diameter is used. Applying these assumptions, (2.42) and (2.43) give:

$$\frac{dP}{ds} = - \left( \frac{f}{4r} \frac{F_m |F_m|}{\rho} + \rho g \right). \quad (5.1)$$

Integrating (5.1) with respect to  $s$  gives:

$$P(s) = P_0 - s \left( \frac{f}{4r} \frac{F_m |F_m|}{\rho} + \rho g \right). \quad (5.2)$$

Here,  $P_0$  is the wellhead pressure, which is known as a boundary condition, and  $f$  is the coefficient of friction, fixed at 2.5E-2. Simulations were run for both liquid and vapour conditions in a 1500 m vertical wellbore with a diameter of 0.216 m, discretised into 10 elements. A constant wellhead pressure of 8 bar was use, while the mass flux was varied.

Figures 5.1 and 5.2 show that the analytical model and numerical results match well for a variety of mass flow rates. Although simple, this solution helps to verify that the

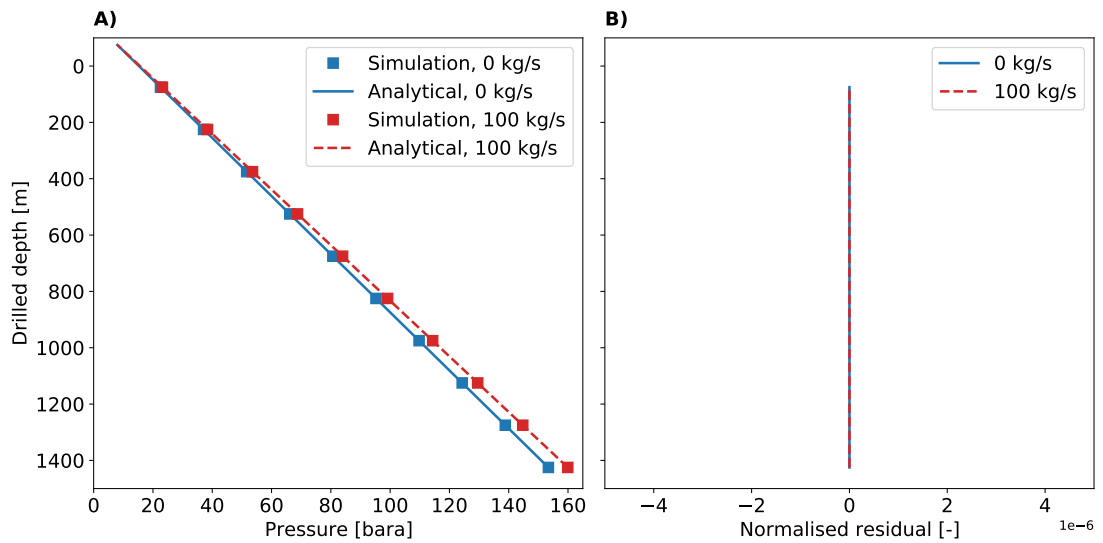


FIGURE 5.1: Comparison of numerical and analytical solutions for liquid flow for verification Case 1. Plot A) compares the numerical and analytical pressures and B) plots the normalised pressure residuals.

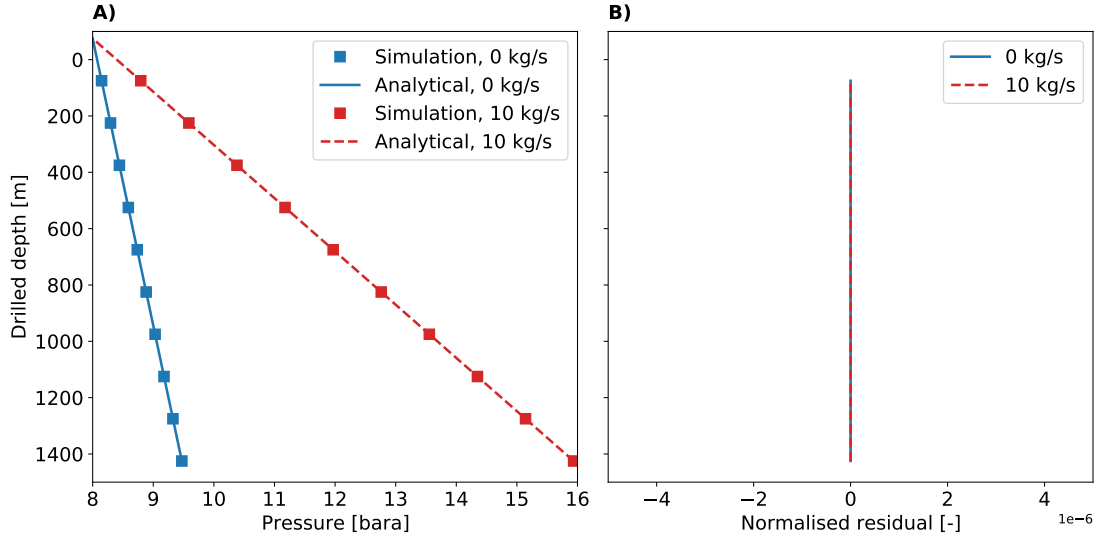


FIGURE 5.2: Comparison of numerical and analytical solutions for vapour flow for verification Case 1. Plot A) compares the numerical and analytical pressures and B) plots the normalised pressure residuals.

gravitational and friction terms have been implemented correctly and are acting in the correct direction. Obviously, the physics demands that the pressure is greater at the bottom of the well than it is at the wellhead and increasing the mass flow rate increases the friction losses and, therefore, increases the change in pressure with depth.

### 5.1.2 Case 2: linear density model

A second simple analytical solution was derived for steady, single-phase isothermal flow. In this case, the fluid density was assumed to be a linear function of pressure, such that  $\rho = mP + c$ , with  $m$  and  $c$  derived from matching the IAPWS-IF97 correlations (Dittmann, 2000). Friction effects were ignored. This is a simplified case of a semi-analytical solution presented by Pan, Webb and Oldenburg (2011). Simplifying the single-phase mass equation (2.42) and momentum equation (2.43) using these assumptions gives:

$$\frac{dP}{ds} = -\frac{\rho g}{F_m^2 \frac{d}{dP}(1/\rho) + 1}. \quad (5.3)$$

Inverting (5.3) and integrating with respect to pressure gives an analytical expression for drilled length,  $s$ , in terms of pressure,

$$s(P) = C - \frac{1}{mg} \ln|\rho| - \frac{F_m^2}{2g} \frac{1}{\rho^2}, \quad (5.4)$$

where,

$$C = \frac{1}{mg} \ln|\rho_0| + \frac{F_m^2}{2g} \frac{1}{\rho_0^2}. \quad (5.5)$$

Here,  $\rho_0$  is the density calculated from the wellhead pressure and  $m$  is the gradient of density with respect to pressure. The lengths of the wellbores were 4000 m and 1500 m for the liquid and vapour simulations, respectively. Both were discretised into 50 elements. Figure 5.3 presents the comparison between the analytical and numerical solutions for liquid water flowing at 20 kg/m<sup>2</sup>/s.

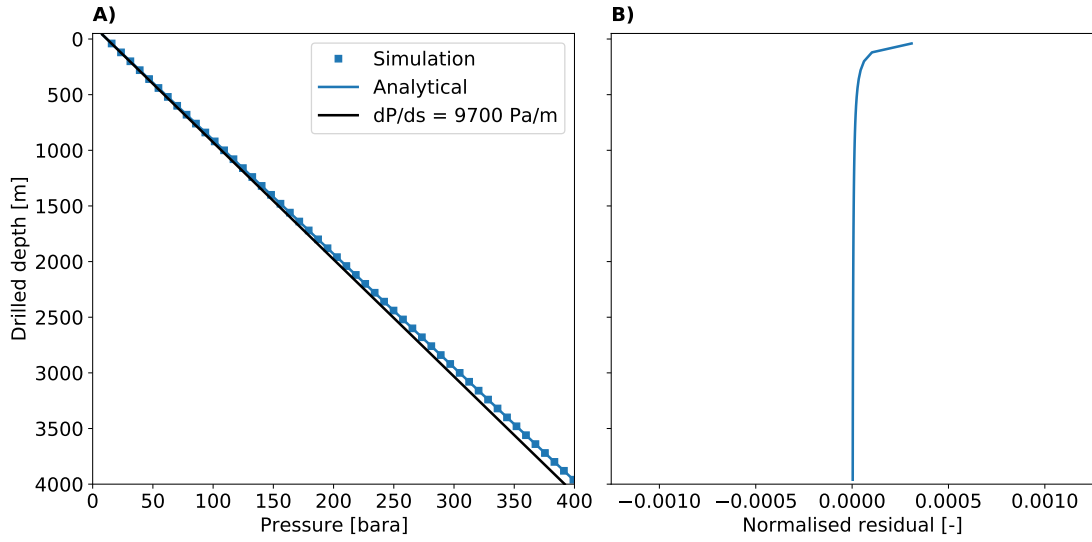


FIGURE 5.3: Comparison of numerical and analytical solutions for liquid flow for verification Case 2. Plot A) compares the numerical and analytical solutions for pressure vs. drilled depth and B) plots the normalised residuals for the drilled depth.

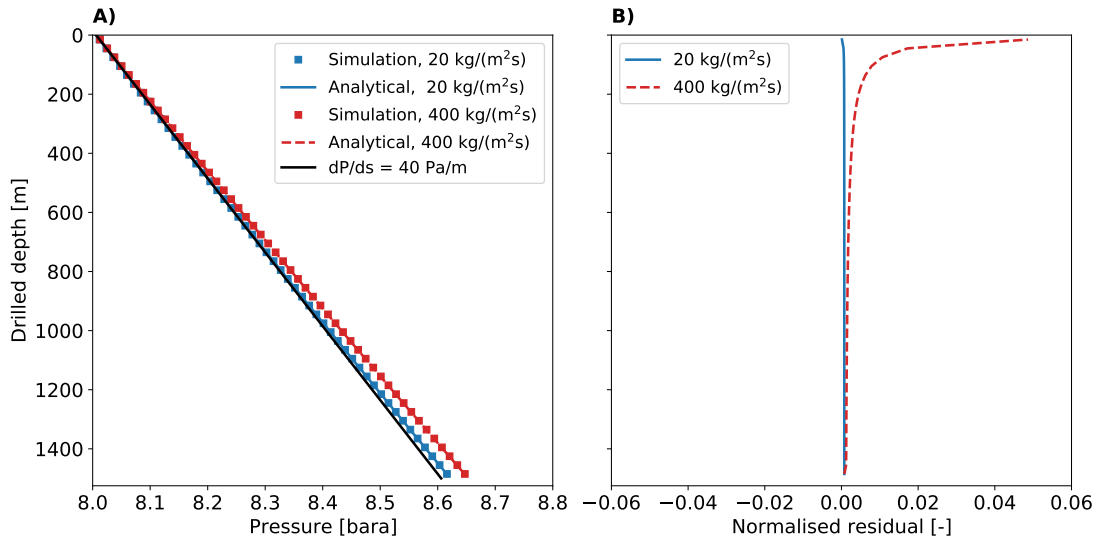


FIGURE 5.4: Comparison of numerical and analytical solutions for vapour flow for verification Case 2. Plot A) compares the numerical and analytical solutions for pressure vs. drilled depth and B) plots the normalised residuals for the drilled depth.



A good match is achieved with a maximum relative error of 0.03% between the analytical and numerical solutions for depth. Changes in mass flux have little influence on the pressure profile due to the low compressibility of water and the corresponding results have not been presented.

Figure 5.4 compares the analytical and numerical solutions for the vapour case at two different mass fluxes. A good match is achieved for both cases with maximum percentage errors of 0.07% and 0.4% for the  $F_m$  equal to 20 kg/m<sup>2</sup>/s and 400 kg/m<sup>2</sup>/s, respectively.

### 5.1.3 Case 3: Ramey's solution for wellbore heat transport

Ramey (1962) presented an analytical approximation for wellbore temperatures during steam injection. Ramey's method was presented for geothermal applications by Horne and Shinohara (1979) for both production and injection cases. This method assumes the fluid has a constant density and heat capacity and flows at a steady rate. The reservoir was assumed to be radially symmetric and to have a constant vertical temperature gradient.

For production cases, Horne and Shinohara (1979) derived the temperature in the wellbore, given the assumptions above, as:

$$T(s) = T_{res} + aA \left( 1 - \exp \left( \frac{s_{BH} - s}{A} \right) \right). \quad (5.6)$$

Here,  $T_{res}$  is the formation temperature (which is a linear function of depth),  $s_{BH}$  is the value of  $s$  at the bottom of the well and  $a$  is the vertical temperature gradient in the formation. The coefficient  $A$  is defined as:

$$A = \frac{Q_m c_p (k_{res} + rU f(t))}{2\pi r U k_{res}}. \quad (5.7)$$

Here,  $Q_m$  is the total mass flow,  $c_p$  is the specific heat capacity of the wellbore fluid,  $k_{res}$  is the thermal conductivity of the formation,  $r$  is the wellbore radius and  $f(t)$  is the non-dimensional time function.

The simulations used specific heat capacities of 3.425 kJ/kg/K and 1.95 kJ/kg/K for the liquid and vapour simulations, respectively. Both the liquid and vapour simulations were run with a formation thermal conductivity ( $k_{res}$ ) of 2.422 W/m/K and an overall heat transfer coefficient ( $U$ ) of 20 W/m<sup>2</sup>/K. The non-dimensional time function by Chiu and Thakur (1991), given in (3.72), was used.

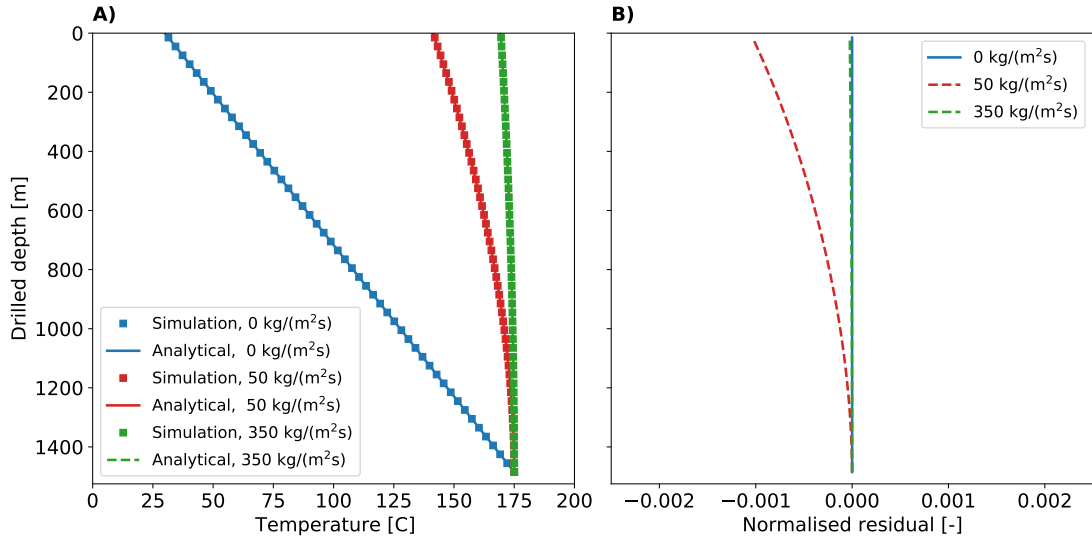


FIGURE 5.5: Comparison of numerical and analytical solutions for liquid flow for verification Case 3. Plot A) compares the numerical and analytical temperatures and B) plots the normalised temperature residuals.

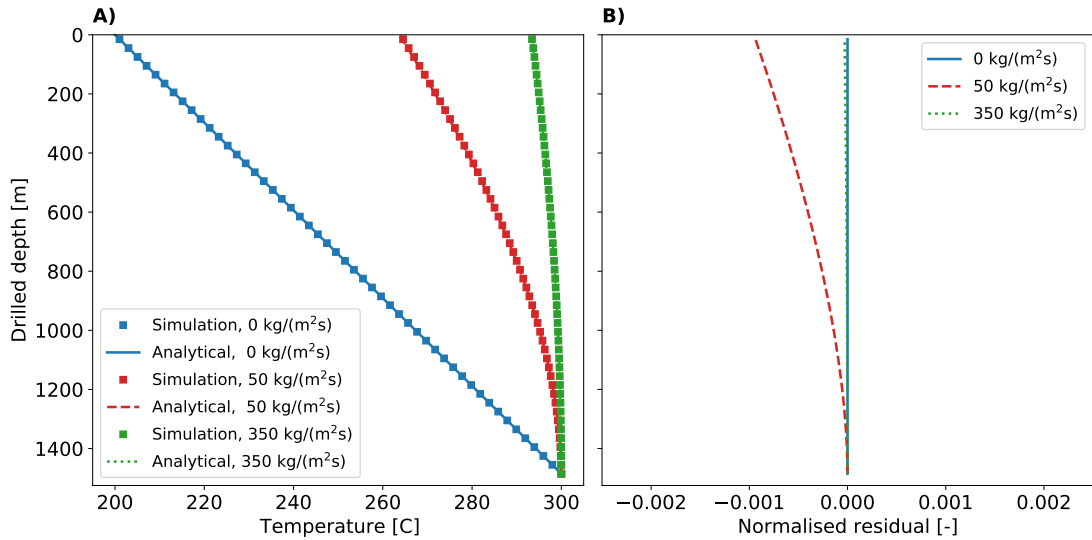


FIGURE 5.6: Comparison of numerical and analytical solutions for liquid flow for verification Case 3. Plot A) compares the numerical and analytical temperatures and B) plots the normalised temperature residuals.

All simulations were run with a wellhead pressure of 8 bar at 0 kg/m<sup>2</sup>/s, 50 kg/m<sup>2</sup>/s or 350 kg/m<sup>2</sup>/s for 1.0E7 seconds. The bottom-hole temperatures were 175 °C and 300 °C for the liquid and vapour simulations, respectively.

The reservoir temperature profiles varied linearly from 30 °C to 175 °C for the liquid cases and from 200 °C to 300 °C for the vapour cases. As expected, the wellbore temperature profile approaches the reservoir temperature profile for a closed well, as shown by the 0 kg/m<sup>2</sup>/s cases in Figures 5.5 and 5.6. As the mass flux increases, less heat is lost to the formation relative to the heat flow up the well, which results in higher wellbore temperatures near the surface.

The simulations matched the analytical solutions well. For the liquid flow cases, given in Figure 5.5, the maximum difference between the analytical and simulated temperature values was 0.1% and 0.01% for  $F_m$  equal to 50 kg/m<sup>2</sup>/s and 350 kg/m<sup>2</sup>/s, respectively. For the vapour flow cases, given in Figure 5.6, the maximum difference was 0.08% and 0.01% for  $F_m$  equal to 50 kg/m<sup>2</sup>/s and 350 kg/m<sup>2</sup>/s, respectively.

## 5.2 Model validation

Validation assesses the ability of the simulator to reproduce real-world observations. Simulation results were compared to steady pressure and temperature measurements taken from a variety of geothermal fields, which have a wide range of properties. Typically, the quality of the match between measured and simulated data is assessed by plotting the simulated pressure and temperature profiles against the measured data. García-Valladares et al. (2006) note that "by eye" comparisons are affected by the scale on which the results are plotted. We use the mean sum of residual squares, defined as:

$$\text{MRSS} = \frac{1}{N} \sum_{i=1}^N (\varphi_i^{\text{sim}} - \varphi_i^{\text{meas}})^2, \quad (5.8)$$

and the mean normalised sum of residual squares:

$$\text{MNRSS} = \frac{1}{N} \sum_{i=1}^N \left( \frac{\varphi_i^{\text{sim}} - \varphi_i^{\text{meas}}}{\varphi_i^{\text{meas}}} \right)^2, \quad (5.9)$$

as measures of fit (Aster et al., 2013). Here, the superscripts *sim* and *meas* refer to the simulated and measured values for either pressure or temperature, the subscript *i* refers to the *i*th observation and *N* is the total number of observations.

### 5.2.1 East Mesa 6-1

Well 6-1 at East Mesa (USA) is 2133 m deep and has a uniform internal diameter of 0.2215 m. No information was given for the cement, so we assumed it was 0.314 m in diameter (the internal diameter of 13 5/8 inch casing) and extended the entire length of the well.

For the numerical model, the well was discretised into 100 uniform elements. The well-head pressure was fixed at 1.5 bara. Fluid was added at a rate of 12.9 kg/s with an enthalpy of 850.4 kJ/kg (which corresponds to a temperature of 198.5 °C) into the bottom block of the model. The shut-in wellbore temperature profile, given by Ortiz-Ramirez (1983), was used as a far-field reservoir temperature and is shown in Figure 5.7.

Figure 5.7 shows that the simulated steady-state profiles for EM 6-1 match the measured pressure and temperatures well. A good match to the data was achieved. For pressure, the MRSS and MNRSS values are 0.9330 and 0.0085, respectively, and for temperature, the MRSS and MNRSS values are 1.314 and 0.0092, respectively.

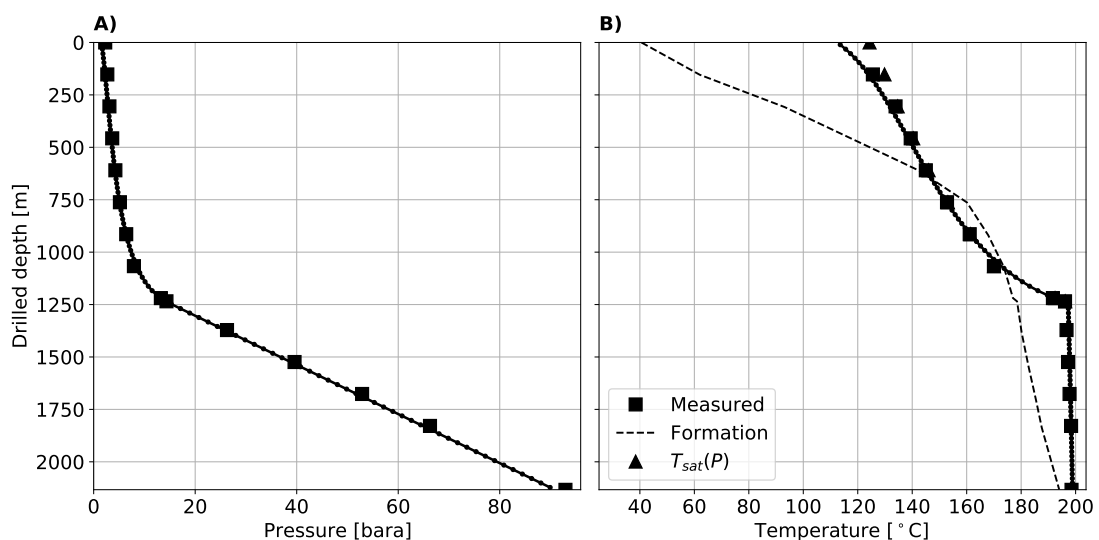


FIGURE 5.7: Comparison of simulated pressure and temperature profiles with measured data for well EM 6-1.

### 5.2.2 Krafla KJ-11

Well KJ-11 at Krafla (Iceland) is a classic example of a well with multiple feed-zones, each with very different characteristics. The data for this well were sourced from Bjornsson (1987) and are shown in Figure 5.8. Well testing indicated that feed-zones exist between the depths of 850 and 1050 m, at 1500 m and below 1800 m, however, mass flow and fluid parameters at the feed-zones were not available. Additionally, mass flow and enthalpy at the wellhead were not measured.

Because of the uncertainty in the conceptual model for this well, Bjornsson (1987) presented several interpretations of the downhole data. The case of influx from all feeds was chosen as a validation case. KJ-11 has a depth of 2217 m with an internal diameter of 0.214 m for the top 750m and an internal diameter of 0.117 m from a depth of 750 m to the bottom-hole. The cement diameter was assumed to be 0.314 m above 750 m and 0.122 m below this point.

No information on the formation temperature was available. In the absence of data, we

TABLE 5.1: KJ-11 Feed parameters estimated by Bjornsson (1987).

Name	Drilled depth [m]	Mass flow [kg/s]	Enthalpy [kJ/kg]
Feed 1	840 - 930	7.80	670
Feed 2	1730 - 1770	21.0	950
Feed 3	2180 - 2220	1.20	1312

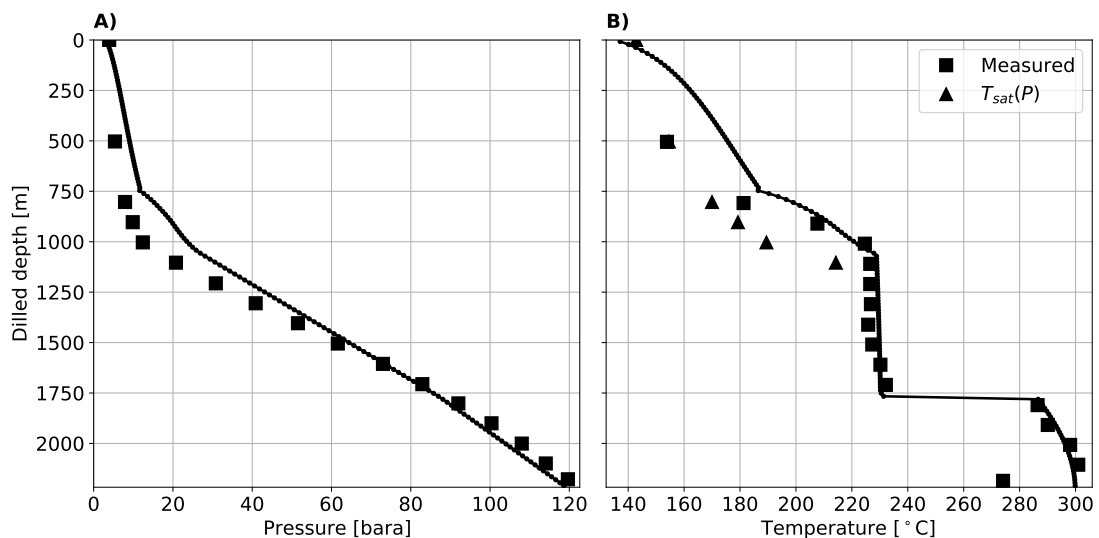


FIGURE 5.8: Comparison of simulated pressure and temperature profiles with measured data for well KJ-11.

have assumed a linear conductive temperature profile between a surface temperature of 25 °C and the bottomhole temperature measured in KJ-22 (295 °C). A fixed wellhead pressure of 3 bara was applied on the top boundary. The depth, mass flow and enthalpy of each feed, estimated by Bjornsson (1987), are given in Table 5.1.

Figure 5.8 presents the comparison between measured downhole data and the results of the wellbore simulation. For the pressure, a reasonable match was achieved for the bottom of the well. However, pressure is overestimated above 1500 m. The MRSS and MNRSS values for pressure are 35.70 and 0.2066, respectively. Similarly, a good match for temperature is achieved below 1000 m. However, temperatures are significantly overestimated at the top of the well. The MRSS and MNRSS values are 97.44 and 0.2220, respectively. These MRSS and MNRSS values mean that this model shows the worst fit to the data of any of the wells presented in this work. However, it was deemed satisfactory given the uncertainty in both the conceptual model of the feed-zones and the operating conditions under which the measurements were taken (Bjornsson, 1987).

### 5.2.3 Krafla KJ-22

Data for well KJ-22, also from the Krafla field in Iceland, were sourced from Hadgu (1989). This data included the wellbore structure and boundary conditions, given in Table 5.2 and the feed properties given in Table 5.3. No information on the formation temperature was available. In the absence of data, we have assumed a linear conductive temperature profile between a surface temperature of 25 °C and the bottomhole temperature measured in KJ-22 (190 °C). The model was discretised into 100 elements.

Figure 5.8 compares the pressure and temperature profiles against the measured data from Hadgu (1989). For the pressure, we have a satisfactory match above 600 m, however, pressure is off-set by approximately 4 – 5 bar below 700 m. For pressure, the MRSS and MNRSS are 12.47 and 0.0104, respectively. For temperature, the MRSS and MNRSS values are 11.57 and 0.0082, respectively. This is likely to be caused by over-estimating the vapour saturation and, therefore, under-estimating the gravitational component of pressure drop in the two-phase region of the well. The saturation of the flow is affected by the choice of the empirical model for slip, which means that a different empirical model may produced a slightly better fit to the data for this well.

TABLE 5.2: Simulation parameters for well KJ-22.

Drilled depth [m]	Wellbore diameter [m]	Wellhead pressure [bara]	Total flow rate [kg/s]
0 – 550	0.22	8.4	25.5
550 – 1200	0.16		

TABLE 5.3: Feed-zone parameters and locations for KJ-22.

Name	Drilled depth [m]	Mass flow [kg/s]	Enthalpy [kJ/kg]
Feed 1	610 – 650	11.00	1600*
Feed 2	800 – 825	0.95.0	1600*
Feed 3	1090 – 1125	11.00	875
Feed 4	1185 – 1200	2.55	815

\* The enthalpy values of feeds 1 and 2 were obtained from a nearby well.

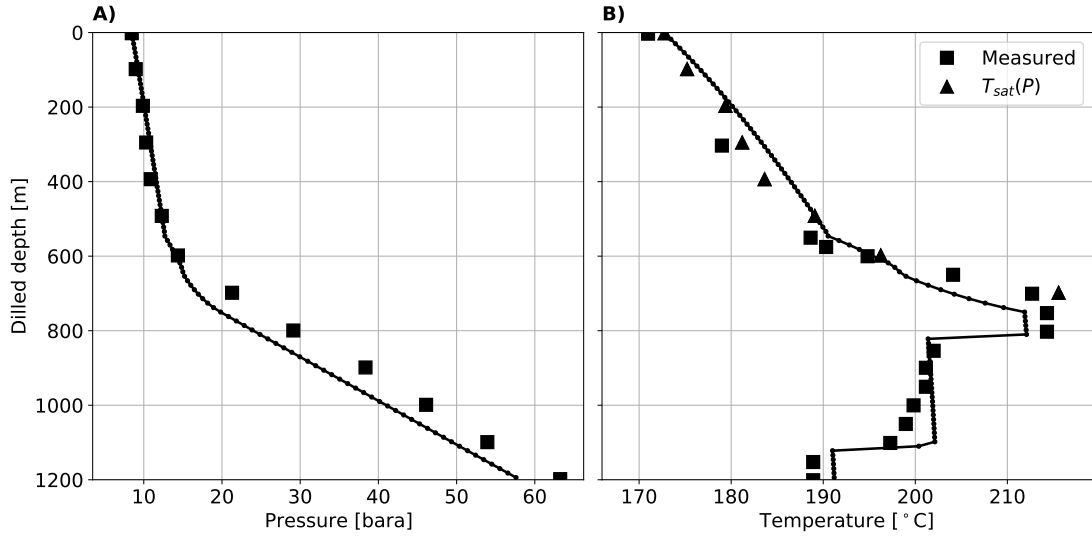


FIGURE 5.9: Comparison of simulated pressure and temperature profiles with measured data for well KJ-22.

#### 5.2.4 Los Azufres AZ-18

Data for well AZ-18, located in the Los Azufres field in Mexico, were sourced from García-Valladares et al. (2006). AZ-18 is characterised by high salt and high gas content (6949 ppm as NaCl and 7.5wt% as CO<sub>2</sub>). AZ-18 is a vertical well with an internal diameter of 0.220 m above 959 m and 0.157 below this point. This well is modelled with a 250 block grid with uniform spacing. Formation temperatures were not provided by García-Valladares et al. (2006). In the absence of data, we have assumed a linear conductive temperature profile between a surface temperature of 25 °C and the bottomhole temperature measured in AZ-18 (265 °C). Fluid is added to the well in the bottom block

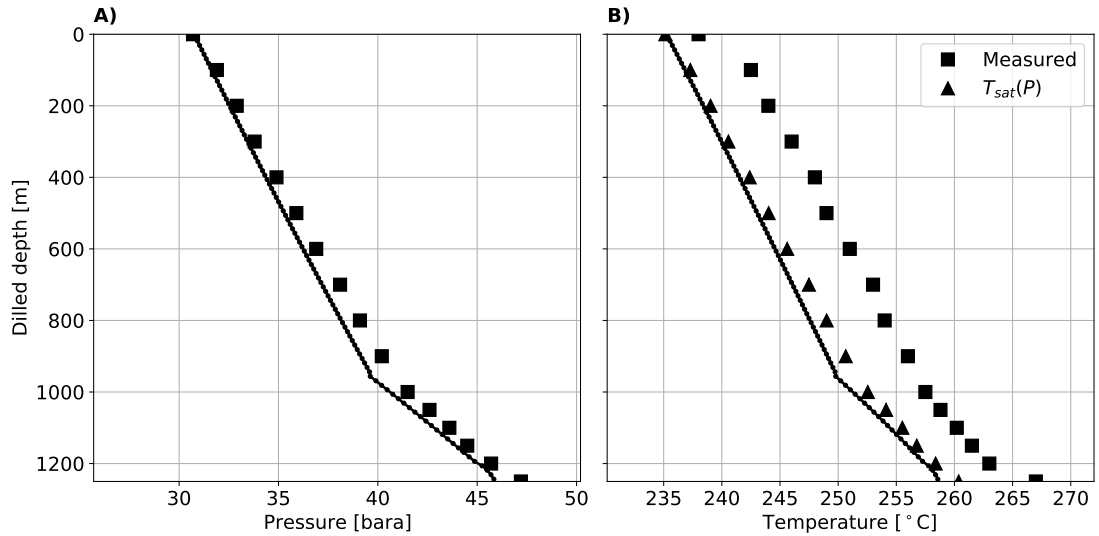


FIGURE 5.10: Comparison of simulated pressure and temperature profiles with measured data for well AZ-18.

TABLE 5.4: Simulation parameters for well AZ-18.

Drilled depth [m]	Wellbore inclination [ $\theta$ ]	Wellbore diameter, ID [m]	Mass flow rate [ $\text{kg s}^{-1}$ ]	Feed Enthalpy [kJ/kg]
959	0	0.220	26.7	1620
1250	0	0.157		

of the model (1245 – 1250 m) with an enthalpy of 1620 kJ/kg at a rate of 26.7 kg/s. The wellhead pressure was fixed at 31 bara.

A very good pressure match is achieved with MRSS and MNRSS values of 0.5598 and 0.0003, respectively. Although, our model underestimates the pressure gradient above 900 m slightly. The temperature profile is offset by approximately 5°C from the measured data. Comparison of the measured temperatures to the saturation temperatures (calculated from the measured pressures) suggests that, as expected, the presence of gas and salt in the fluid is influential in this case.



TABLE 5.5: Simulation parameters for well H-1.

Depth [m]	Wellbore inclination [ $\theta$ ]	Wellbore diameter, ID [m]	Mass flow rate [ $\text{kg s}^{-1}$ ]	Bottom-hole temp. [C]
814	0	0.220	28	274.2
918	0	0.157		
1200	5.1	0.157		

### 5.2.5 Los Humeros H-1

Data for well H-1, located in the Los Humeros field in Mexico, were sourced from García-Valladares et al. (2006). These included flowing pressure and temperature profiles, wellbore structure and inflowing conditions. These are presented in Table 5.5.

Well H-1 is vertical above 918 m and deviated at an angle of  $5.1^\circ$  below this point. The diameter of the well changes from 0.220 m to 0.157 m at 918 m. This geometry of H-1 is given in Table 5.5. This well was modelled numerically with a 100 block grid. Formation temperatures were not provided by García-Valladares et al. (2006). In the absence of data, we have assumed a linear conductive temperature profile between a surface temperature of  $25^\circ\text{C}$  and the bottomhole temperature measured in H-1 ( $273^\circ\text{C}$ ).

A wellhead pressure of 21 bara was initially used to ensure a pressure match at the wellhead. The simulation results for this case are shown in black in Figure 5.11. For this case, we have a poor fit for both pressure and temperature at most depths. We also have two-phase fluid at the bottom of the well, whereas the data sourced from García-Valladares et al. (2006) suggests fluid enters the well as a liquid.

García-Valladares et al. (2006) use the bottomhole pressure as their boundary condition. Increasing the wellhead pressure in our model to 25.5 bara gives a better match to their results. In this case, for the pressure data, the MRSS and MNRSS values are 7.433 and 0.0134, respectively. For the temperature, the MRSS and MNRSS values are 8.996 and 0.01357, respectively. Figure 5.11 shows the simulation matches data relatively well below a depth of 600 m. The pressure gradient with respect to depth is under-estimated above this point, leading to a maximum pressure difference of approximately 5 bar located at the wellhead. Again, this is likely to be due to the presence of salt and high amounts of  $\text{CO}_2$  in the production fluid.

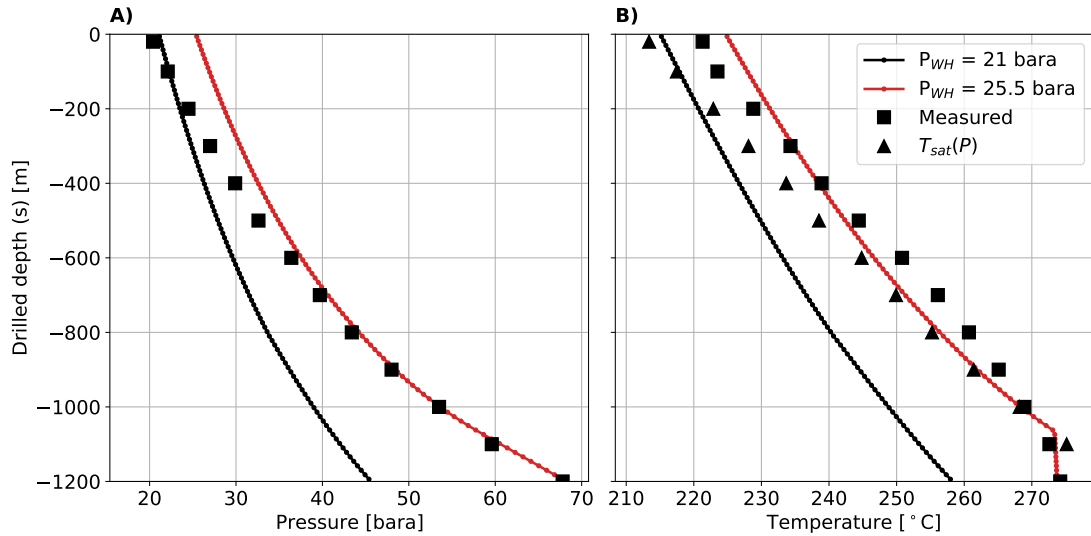


FIGURE 5.11: Comparison of simulated pressure and temperature profiles with measured data for well H-1.

### 5.2.6 Los Humeros H-37

Data for H-37, a high-enthalpy two-phase well located in the Los Humeros field in Mexico, were sourced from García-Valladares et al. (2006). These data included downhole pressure and temperature measurements as well as in-flowing fluid conditions. Well H-37 is 1198 m long with a constant diameter of 0.22 m. It is vertical for the first 850 m and deviated at an angle of  $15^\circ$  below this point.

Fluid was added at 7.8 kg/s with a flowing enthalpy of 2592 kJ/kg to the bottom block of the well. A wellhead pressure of 30.5 bara was used. Formation temperatures were not provided by García-Valladares et al. (2006). In the absence of data, we have assumed a linear conductive temperature profile between a surface temperature of 25 °C and the bottomhole temperature measured in H-37 (240 °C). However, García-Valladares et al. (2006) note that formation heat transfer has little impact on simulation results when this well is flowing at 7.8 kg/s.

TABLE 5.6: Simulation parameters for well H-37.

Drilled depth [m]	Wellbore inclination [ $\theta$ ]	Wellbore diameter, ID [m]	Mass flow rate [kg s <sup>-1</sup> ]	Feed Enthalpy [kJ/kg]
0 - 850	0	0.22	7.8	2592
850 - 1198	15	0.22		

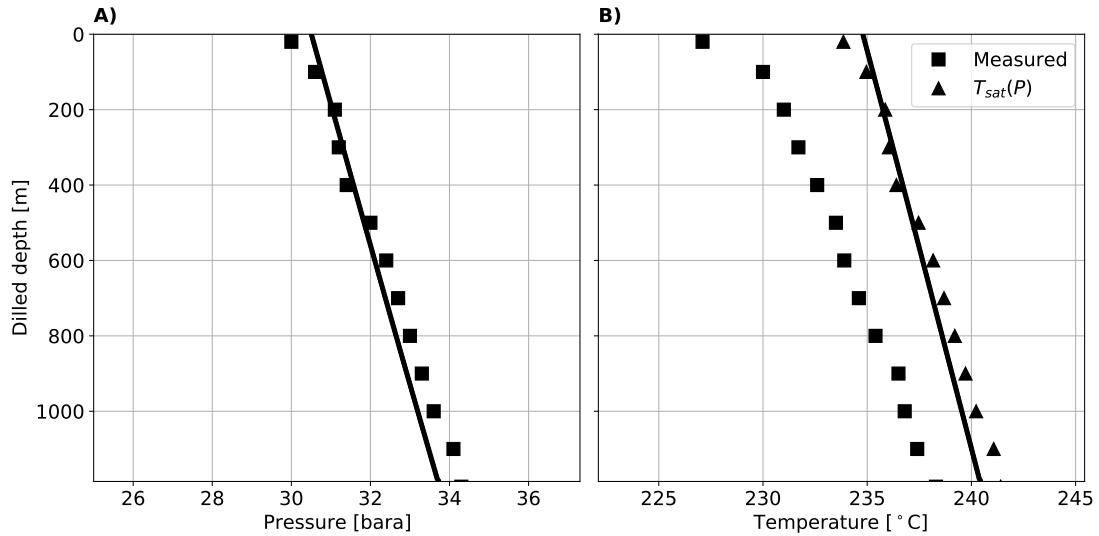


FIGURE 5.12: Comparison of simulated pressure and temperature profiles with measured data for well H-37.

A good pressure match was achieved, with MRSS and MNRSS values of 0.1389 and 0.0001, respectively. As was the case with AZ-18, the simulation does not match the measured temperature data well. This is likely to be due to the high salt and gas content (1370 ppm as NaCl and 1.4wt% as CO<sub>2</sub>). The MRSS and MNRSS values were 17.21 and 0.0005, respectively.

### 5.2.7 WELL-A

WELL-A is an anonymised well for which the data were obtained via personal communication. It has a total mass flow of 180.5 kg/s, the highest of any tested. WELL-A has a wellhead elevation of 450 mRL and a total length of 1635 m. The well track is shown in Figure 5.13 A). It is vertical above -600 mRL and deviated at approximately 32.5° below this point. Figure 5.13 B) shows the radius of the well, which changes from 0.1699 m to 0.1365 at -510 m. Figure 5.13 B) shows the cement radius in grey. Heat exchange with the formation was not modelled for this case because reservoir temperature data was unavailable. This assumption has little impact on the results of this simulation because the high mass flow rate (650 t/h) means the reservoir heat transfer term is small compared to the energy flux within the well.

The fluid inflow was modelled using source terms. No information on the feed properties other than their approximate location was given. The feed locations are shown in Figure

TABLE 5.7: Estimated feed-zone properties and locations for WELL-A.

Name	Elevation [mRL]	Mass flow [kg/s]	Enthalpy [kJ/kg]
Wellhead	450		
Feed 1	-525 to -550	60.185	1236
Feed 2	-1010 to -1025	118.620	1276
Feed 3	-1050 to -1075	1.500	1263
Feed 4	-1150 to -1180	0.250	1251

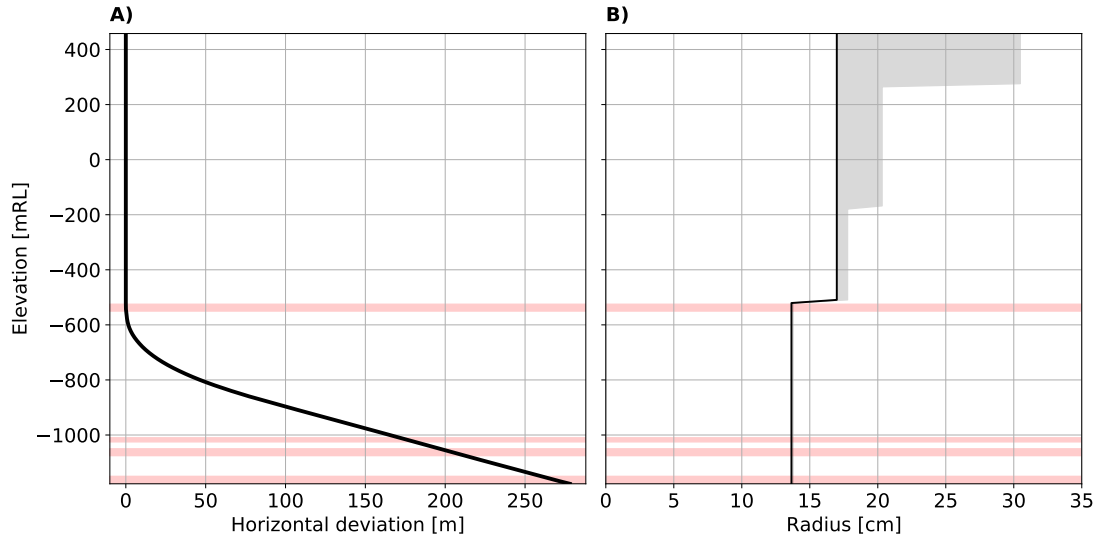


FIGURE 5.13: A) The well track showing the deviation. B) The wellbore radius, with the cement radius shown in grey. Feed-zone locations are shown in red.

5.13. The mass flow contributions and enthalpy values give in Table 5.7 were found to produce a very good fit to the pressure and temperature data, as shown in Figure 5.14. For the pressure, the MRSS and MNRSS values are 1.619 and 0.0004, respectively. For the temperature, the MRSS and MNRSS values are 0.3272 and 0.0004, respectively.

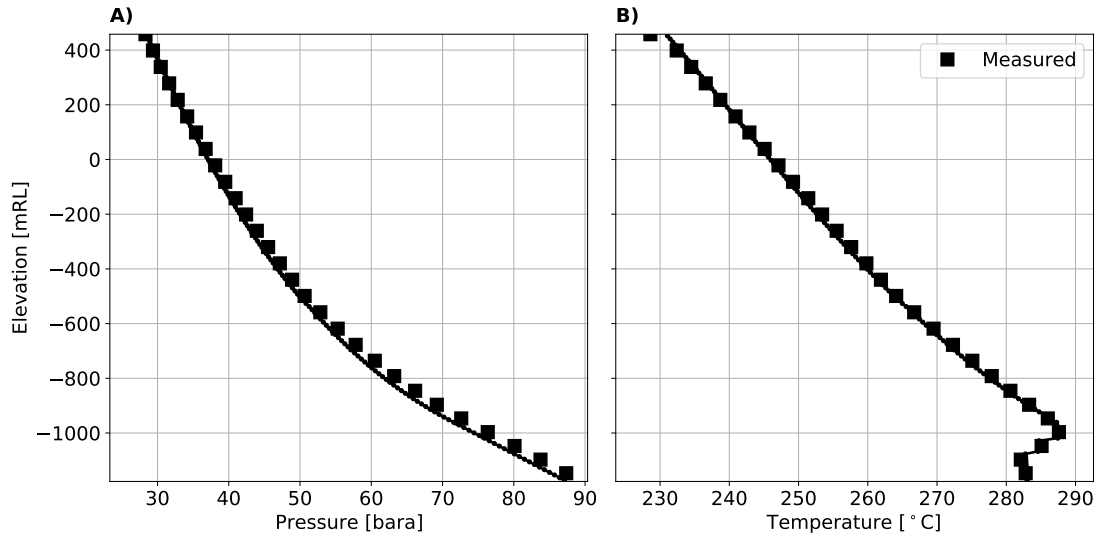


FIGURE 5.14: Comparison of simulated pressure and temperature profiles with measured data for Well-A.

TABLE 5.8: Summary of MRSS and MNRSS values for the validation problems.

	Pressure		Temperature	
	MRSS	MNRSS	MRSS	MNRSS
KJ-22	8.830	0.0081	19.14	0.0066
KJ-11	35.70	0.2066	97.44	0.2220
EM-6-1	0.9330	0.0085	1.314	0.0092
AZ-18	0.5598	0.0003	37.58	0.0009
H-1	7.433	0.0134	8.996	0.0136
H-37	0.1389	0.0001	17.21	0.0005
Well A	1.619	0.0004	0.3272	0.0004

### 5.2.8 Summary

In this section, we compared simulation results to steady pressure and temperature profiles. The wells we considered cover a wide range of flow rates, diameters and enthalpies. The quality of fit that we attained varied between cases. The mean sum of squares (MRSS) and mean normalised sum of squares (MNRSS) were used to assess the quality of fit. These parameters are summarised in Table 5.8.

Overall we were able to match the measured data relatively well. We note that the case with the worst fit, KJ-11, is also the case with the highest uncertainty in both the conceptual model and operating conditions under which the data were collected. As suggested by Hasan and Kabir (2010), the quality of data is very influential on the ability of a model to match measured data.

For wells AZ-18 and H-37, we were able to obtain a good match to the measured pressure data, however, the simulated temperatures were offset from the measured temperatures in both cases. This is likely to be due to the presence of salt and non-condensable gasses in the Los Humeros and Los Azufres fields. Given these considerations, we are satisfied that our simulator can accurately represent production in geothermal wells.

### 5.3 Transient test cases

The main objective of the research discussed in this thesis was to develop a simulator capable of modelling the wide variety of transient flow scenarios that are possible within a geothermal well. This section defines a set of 12 test cases and presents the results that cover a range of production, injection and shut-in scenarios. These problems include examples of co-current up-flow, co-current down-flow and counter-flow occurring within the well. In addition to these cases, three other test cases are discussed in Appendix C. These additional cases were designed to test specific down-flow scenarios that do not occur in the other test cases.

Section 5.3.1 discusses production cases that involve transitions between liquid and two-phase flow. Section 5.3.2 presents production cases that involve transitions between vapour and two-phase conditions. Section 5.3.3 presents injection cases for liquid, vapour and two-phase conditions. Finally, Section 5.3.4 presents two examples of counter-flow in geothermal wells. These test cases are summarised in Table 5.9.

The test cases presented below were also useful when developing and refining the simulator. Specifically, they were used to:

- compare the numerical performance of different combinations of primary variables - see Section 6.1,
- develop the discrete formulation of the drift velocity required to simulate counter-flow scenarios - see Section 6.2,
- improve the numerical performance of upstream weighting methods - see Section 6.3, and
- investigate counter-flow processes in transient geothermal wells - see Section 8.1.

These test cases were used as benchmark problems on which to test stages in simulator development, and will be useful benchmark problems when testing future simulator developments.

All of the test cases described below were obtained using the numerical methods described in Chapter 4. Heat flux between the well and formation, when modelled, is calculated as described in Section 3.4. The properties of the formation and wellbore completion, given in Table 5.10, are the same in all cases. Finally, when required, the relative permeability of a feed is calculated using Grant's Curves, which are given in Section 3.5, using  $S_{lr} = 0.5$  and  $S_{sr} = 0.1$ .

TABLE 5.9: Summary of the transient processes that are modelled in test cases discussed in Section 5.3.

	Test Case														
	1	2	3	4	5	6	7	8	9	10	11	12	13	14	15
Production scenario	x	x	x	x	x	x	x	x			x				x
Injection scenario									x	x			x	x	
Closed wellhead scenario			x									x			
Up-flow process	x	x	x	x	x	x	x	x							x
Down-flow process		x							x	x			x	x	x
Counter-flow process			x					x			x	x			
Liquid/two-phase transition	x	x	x	x					x	x		x		x	x
Vapour/two-phase transition					x	x	x	x	x	x			x		
Multi-feed scenarios				x		x	x	x					x	x	x
Pressure boundary cond.		x		x	x	x	x	x			x				x
Mass flow boundary cond.	x		x						x	x		x	x	x	

TABLE 5.10: Reservoir and wellbore parameters required for analytical heat flux calculations.

Symbol	Units	Description	Value
$k_{res}$	W/K/m	Formation heat conductivity	2.422
$k_{cem}$	W/K/m	Cement heat conductivity	1.400
$\rho_{res}$	kg/m <sup>3</sup>	Formation density	2600
$c_{res}$	J/K/kg	Formation specific heat capacity	1000

### 5.3.1 Liquid production

This section discusses four production test cases, which all feature transitions between liquid and two-phase conditions. Our simulator must be able to model cases such as these, as they are very common in real world applications.

Figure 5.15 shows the phase state and flow direction combinations that are possible when transitions between liquid and two-phase conditions occur during up-flow. In Figure 5.15, Scenarios A) and D) show the liquid up-flow and co-current two-phase up-flow. Both of these fundamental flow scenarios occur in Test Cases 1 – 4. Scenario B) shows liquid flowing up into a two-phase block. This scenario can occur, for example, when flashing begins at the wellhead after opening a well to flow and progresses down the well. This scenario is shown clearly in Test Case 1 and Test Case 4. Scenario C) shows two-phase up-flow into a liquid block. This can occur, for example, when flashing begins deep in the well due to the influx of hot fluid from the reservoir. This process is modelled in Test Case 2.

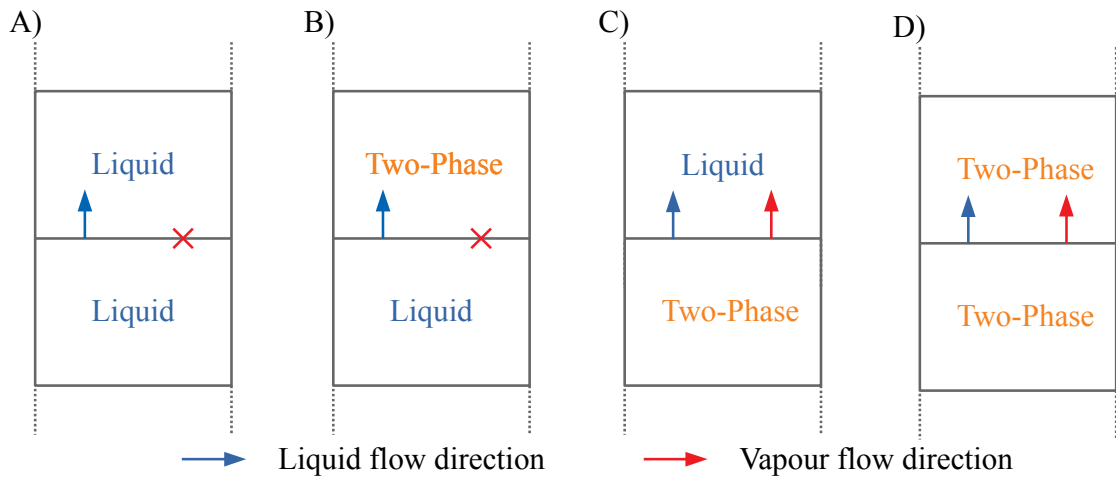


FIGURE 5.15: The possible phase state and flow direction combinations for liquid and two-phase up-flow, showing A) pure liquid up-flow, B) up-flow from a liquid block into a two-phase block, C) two-phase up-flow into a liquid block and D) two-phase up-flow.



TABLE 5.11: Simulation and wellbore parameters for Test Case 1.

Wellhead elevation	0 mRL
Inclination angle	0 °
Length	2133 m
Wellbore diameter	0.2215 m
Cement diameter	0.314 m
Pipe roughness	4.5E-05 m
Formation temperature	Figure 5.16 B)
Wellhead boundary conditions	Transient mass flux
Bottomhole boundary condition	Closed
Source model	Lumped model (3.78)
Feed parameters	Table 5.12
Initial conditions	Figure 5.16
Discretisation	Uniform, 100 blocks

### 5.3.1.1 Test Case 1: 198.5 °C liquid production

Test Case 1 is a simple example that models the start-up of production in a well accessing a deep liquid reservoir. The wellbore properties given in Table 5.11 are based on the well 6-1 (East Mesa) validation example. The well is vertical with a constant diameter of 0.2215 m. The cement diameter is 0.314 m and extends the entire length of the well, as shown in Figure 5.16 C).

The feed properties given in Table 5.12 do not represent the East Mesa field. The productivity of the feed ( $\alpha$ ) was chosen so that the flowing pressure and temperature profiles from the simulation were similar to those measured in well 6-1 when 210 bara was chosen as the feed pressure. This feed pressure was chosen to ensure that the shut-in conditions were liquid with a water level above the wellhead.

The initial conditions used for this test case are given in Figure 5.16. These correspond to a static liquid column with a linear temperature profile between 100 and 200 °C. The formation temperature is also given in Figure 5.16 B).

Flow is initiated by slowly increasing the mass flux at the wellhead. The mass flux is increased to 0.388 kg/s (10 kg/s/m<sup>2</sup>) linearly over 3 hours and then, over the next 1150 days, the mass flow is increased to 13.68 kg/s (355 kg/s/m<sup>2</sup>). This slow increase in mass flux results in a very slow flashing process within the well. It is, therefore, a good test of the performance of our simulator for flows with a low vapour saturation.

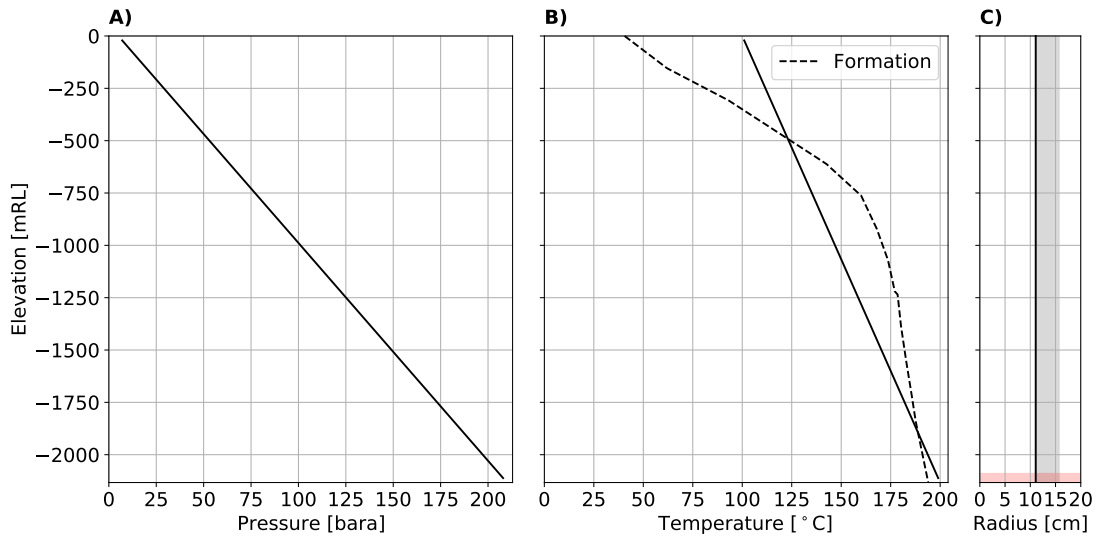


FIGURE 5.16: Initial conditions for Test Case 1 showing A) pressure and B) temperature. Plot C) shows the wellbore structure with the cement radius shown in grey.

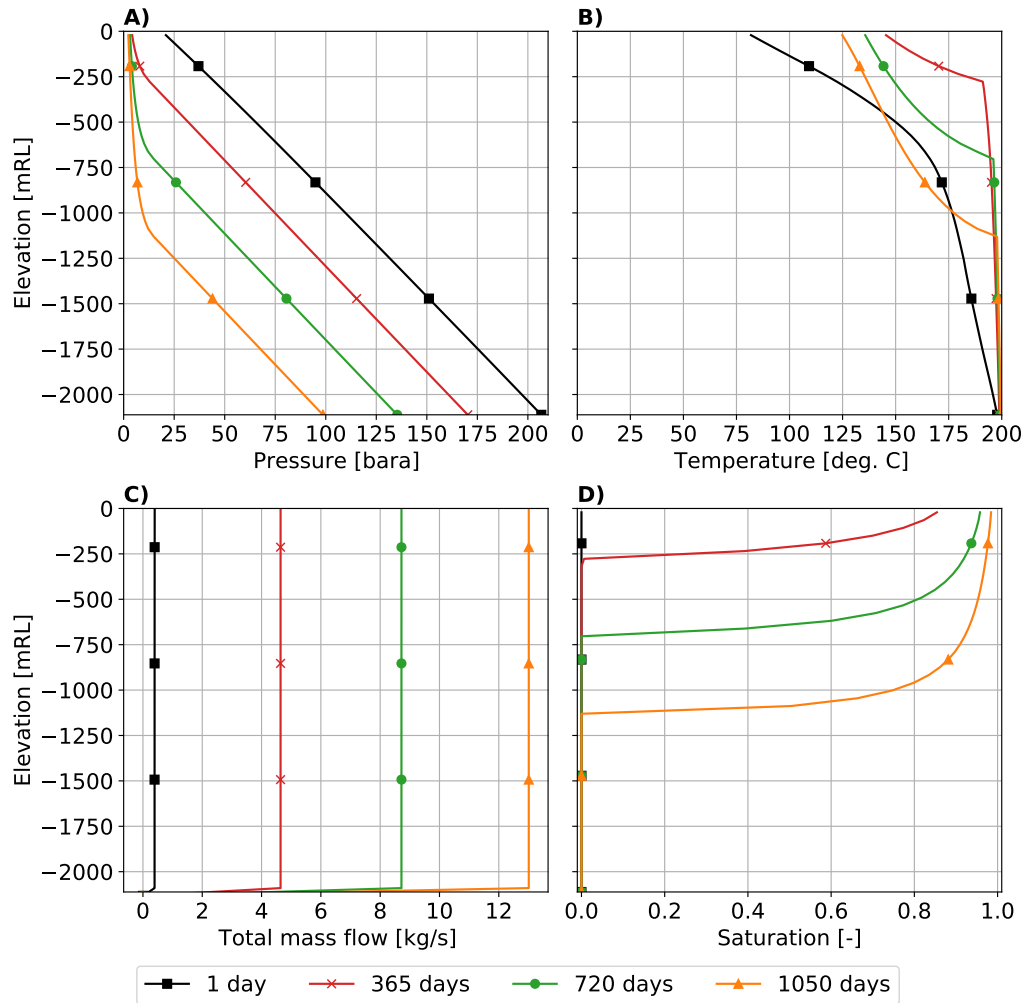


FIGURE 5.17: Plots of A) pressure B) temperature C) total mass flow rate and D) vapour saturation for Test Case 1, which show the two-phase region slowly progressing down the well.

TABLE 5.12: Feed-zone properties and locations for Test Case 1.

Location	$\alpha$ [kg/s/Pa]	Elevation [mRL]	P [bara]	T [°C]	$S_v$ [-]
Bottomhole	1.168E-06	-2090 to -2133	210	198.5	0

Figure 5.17 shows how pressure, temperature, mass flow and saturation change as mass flow at the wellhead is slowly increased. The plots show that flashing begins at the wellhead as the pressure in the well drops. The flash point slowly progresses down the well as mass flow increases, taking approximately 680 days to progress from -250 mRL down to approximately -1200 mRL. This is a much slower process than those shown in Test Case 2, for example (see below).

### 5.3.1.2 Test Case 2: 300 °C liquid production

Test Case 2 is similar to Test Case 1 but with a higher enthalpy inflow. It models the start-up of flow from a hot, liquid reservoir in a 1000 m well. In this case, boiling begins at depth due to the influx of hot fluid. It tests the ability of our simulator to model rapid transient processes associated with flashing in the wellbore. Additionally, this test case ensures that our simulator can model two-phase up-flow into a liquid block (shown as C) in Figure 5.15).

This simulation starts from the static, shut-in conditions shown in Figure 5.18. The reservoir feed-zone is located in the bottom 50 m of the well and has the properties given in Table 5.14. Additional wellbore and simulation parameters are given in Table 5.13.

In Figure 5.18 B), the temperatures in the bottom of the well deviate slightly from the formation temperatures because the feed is spread over multiple blocks. In this case, fluid flows in from the top half of the feed-zone interval, then flows down and out into the bottom half of the feed interval. The inflow of mass is equal and opposite to the outflow.

Flow in the well is started by dropping the wellhead pressure from the shut-in pressure of 14 bara to 4.3 bara over 100 seconds. The drop in wellhead pressure causes a drop in bottomhole pressure and an influx of liquid water at 300 °C, which begins slowly flowing

TABLE 5.13: Simulation and wellbore parameters for Test Case 2.

Wellhead elevation	0 mRL
Inclination angle	0 °
Length	1000 m
wellbore diameter	0.2205 m above -660 mRL 0.1594 m below -660 mRL
Cement diameter	0.314 m above -660 mRL 0.1694 m below -660 mRL
Pipe roughness	4.5E-05 m above -660 mRL 9.0E-05 m below -660 mRL
Formation temperature	Figure 5.18 B)
Wellhead boundary conditions	Transient pressure
Bottomhole boundary condition	Closed
Source model	Productivity model (3.74)
Feed parameters	Table 5.14
Initial conditions	Figure 5.18
Discretisation	Uniform, 200 blocks

TABLE 5.14: Feed-zone properties and locations for Test Case 2.

Location	PI [-]	Elevation [mRL]	P [bara]	T [°C]	$S_v$ [-]
Bottomhole	1.0E-13	-950 to -1000	100	300	0

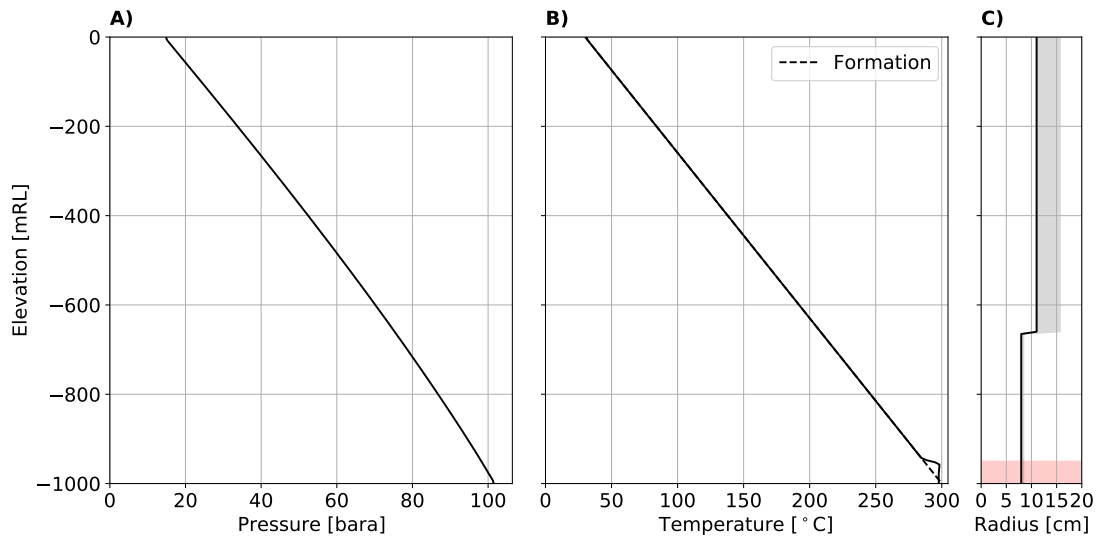


FIGURE 5.18: Initial conditions for A) pressure and B) temperature for Test Case 2. Plot C) shows the feed locations and the wellbore structure, in which the cement radius is shown in grey.

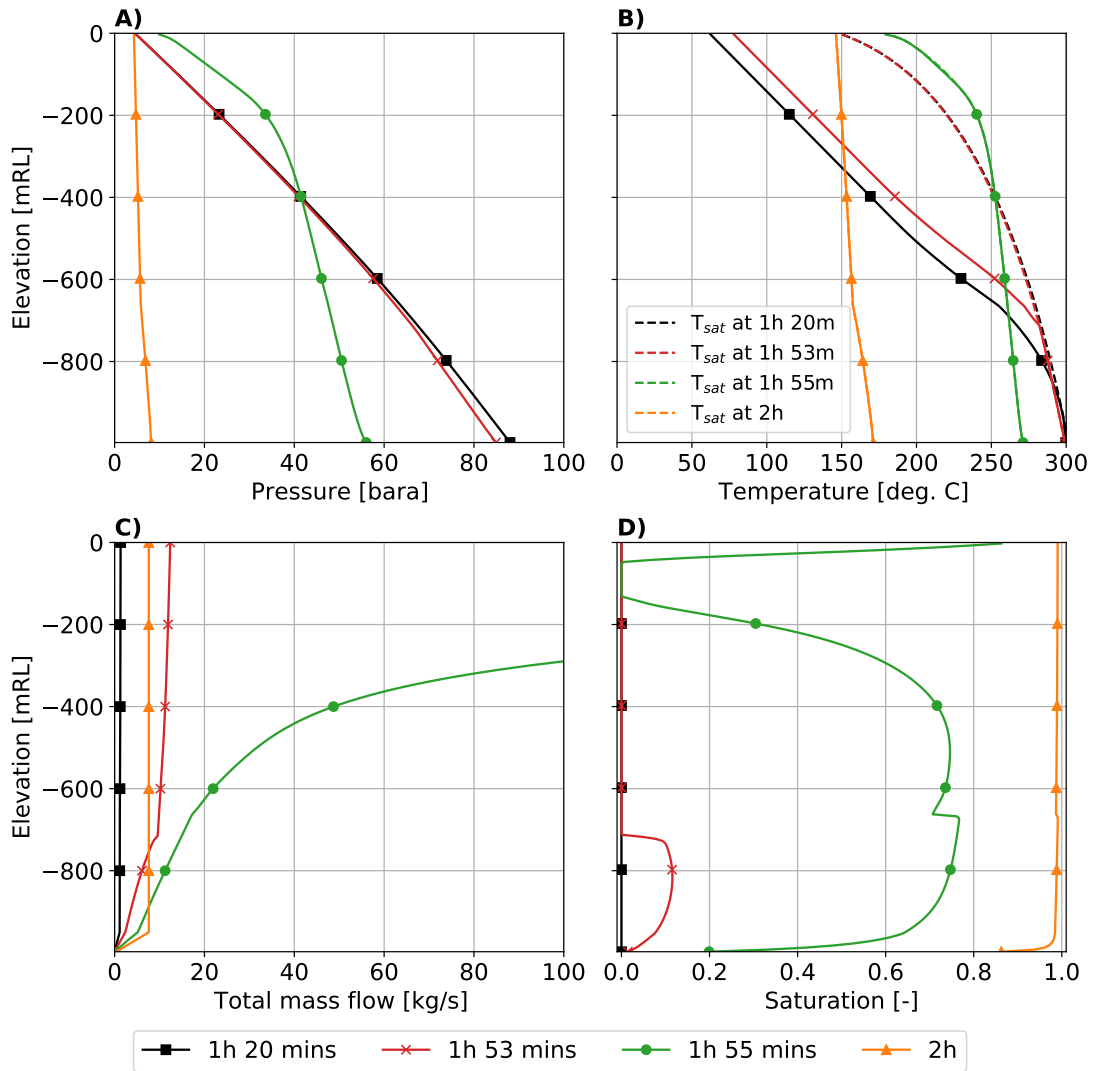


FIGURE 5.19: Plots of A) pressure B) temperature C) total mass flow rate and D) vapour saturation at various times, which show the rapid flashing process that occurs in Test Case 2.

up the well. Figure 5.19 shows that after approximately 1 hour 20 minutes, the conditions at the bottom of the well have warmed and are just below saturation conditions. Boiling begins shortly after this time at a depth of approximately 900 m. This boiling causes a drop in fluid density in this region, reducing the hydrostatic pressure at the bottom of the well and increasing influx.

After an additional 30 minutes (1 hour 53 minutes in Figure 5.19) rapid flashing begins in the well. This causes rapid fluid expansion to occur deep in the well, causing acceleration of the two-phase fluid flow and forcing the liquid water above the two-phase zone up the well. This causes a large increase in mass flow at the wellhead, shown by the 1 hour 55

minute profile in Figure 5.19 C).

After only two additional minutes (1 hour 55 minutes in Figure 5.19) flashing has progressed approximately 600 m up the well to -150 mRL. Nearly steady flowing conditions are reached after another 5 minutes (2 hours in Figure 5.19).

### 5.3.1.3 Test Case 3: wellbore shut-in

Test Case 3 simulates the rapid shut-in of the well described for Test Case 2. This simulation is complex because of the rapid transition processes that occur after the shutting in of the well, which include counter-flow. It is important to be able to model this case because it is a fundamental wellbore operation that is associated with wellbore testing procedures. This section outlines the set up of the test case and provides a summary of the interesting processes that occur in this simulation. A detailed discussion of the simulation results is given in Section 8.1.3, where we explain the role of counter-flow processes in different shut-in scenarios.

Test Case 3 uses the same wellbore, formation and feed properties as Test Case 2. These are given in Tables 5.13 and 5.14 above. However, Test Case 3 starts from flowing conditions after 60 days of production at 7.6325 kg/s. These conditions are shown in Figures 5.20 and 5.21.

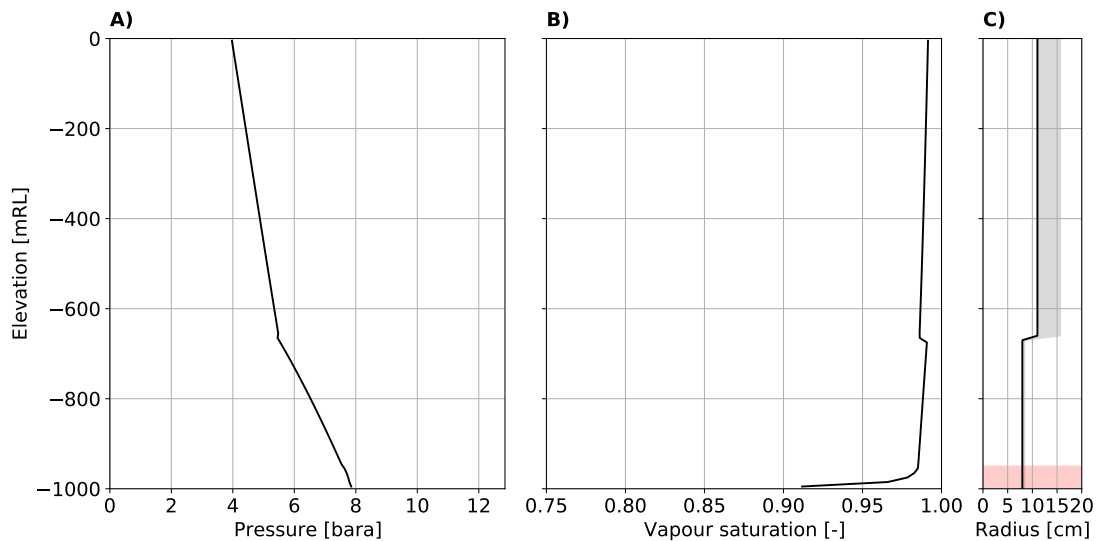


FIGURE 5.20: Initial conditions for A) pressure and B) vapour saturation for Test Case 3. Plot C) shows the feed locations and the wellbore structure, in which cement radius is shown in grey.

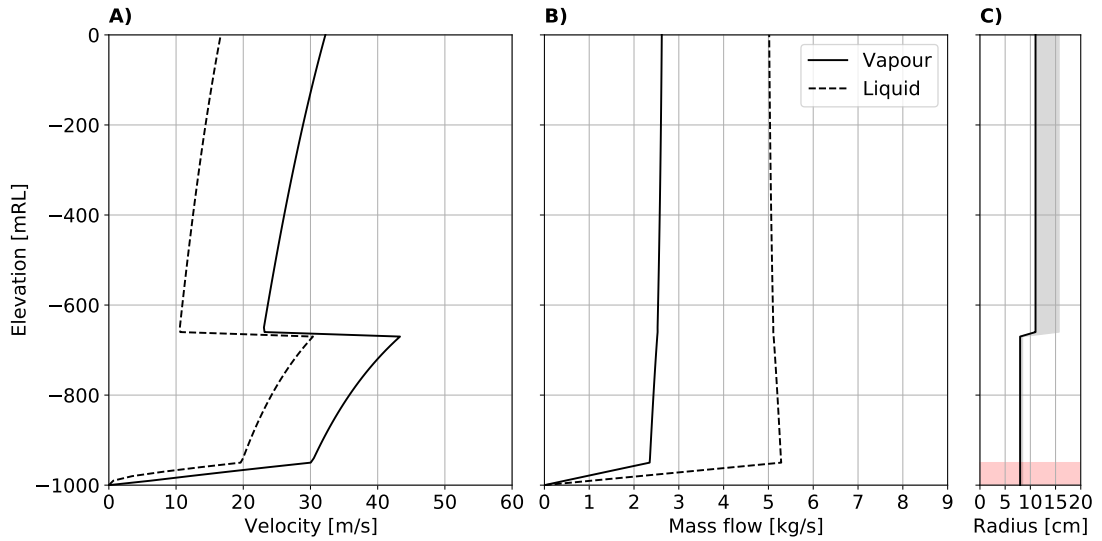


FIGURE 5.21: Initial conditions for A) phase velocities and B) phase mass flow rates for Test Case 3. Plot C) shows the feed locations and the wellbore structure, in which the cement radius is shown in grey.

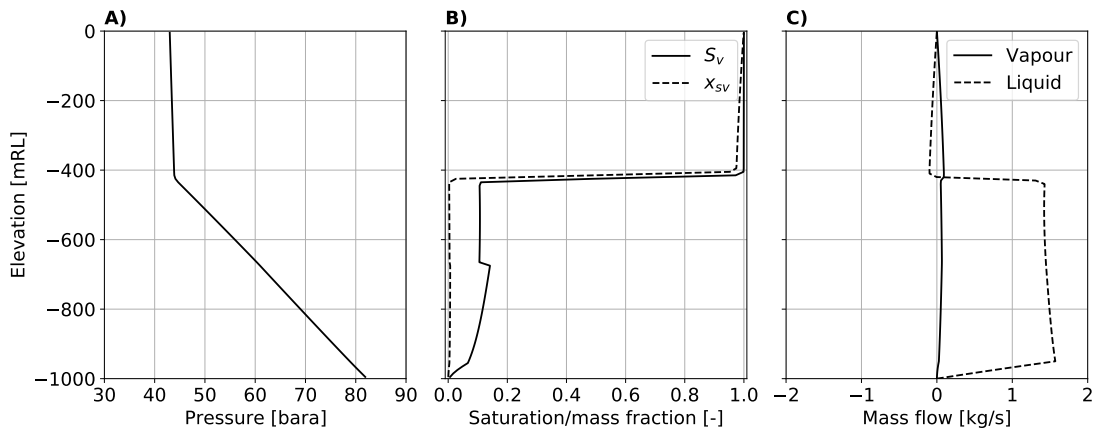


FIGURE 5.22: Plots of A) pressure, B) static vapour mass fraction and vapour saturation and C) the mass flow rates of each phase one hour after shut-in for Test Case 3.

To shut in the well, the total mass flow at the wellhead is decreased linearly from 7.6325 kg/s ( $200 \text{ kg/m}^2/\text{s}$ ) to zero over a period of 60 seconds. This simulates a rapid closure procedure that is at the limit of what is physically possible. When the mass flow boundary condition reaches a value of zero, the shut-in boundary conditions discussed in Section 4.5.3 are used. These ensure that the mass flows of both phases across the wellhead boundary are zero.

The results of this simulation show that counter-flow processes occur after the well is shut-in. Counter-flow allows the less dense vapour to accumulate at the top of the well while the liquid phase accumulates rapidly at the bottom. This process is shown in Figure

5.22, which plots the conditions in the well approximately one hour after shut-in. The plot of static vapour mass fraction in Figure 5.22 B) shows that at this time, low vapour saturation conditions exist below -450 mRL and high vapour saturation conditions exist above this elevation. This is also shown by the change in pressure gradient at -450 mRL.

As time progresses, influx from the reservoir and heat loss to the formation condenses the vapour column at the top of the well back to liquid conditions. It requires 5 hours 30 minutes for the entire well to condense back to liquid conditions after the shutting in of the well. This process is discussed in more detail in Section 8.1.3.

#### 5.3.1.4 Test Case 4: multi-feed production

Test Case 4 models a multi-feed well as it starts to flow. The wellbore structure, including the location of feed-zones, was taken from the KJ-11 validation example given in Section 5.2.2. The wellbore radius and feed-zone locations are shown in Figure 5.23 C) and additional simulation parameters are given in Table 5.15. The feed-zone parameters are given in Table 5.16 below. The pressure, enthalpy and productivity assigned to each feed were chosen to give interesting behaviour and do not represent the Krafla geothermal field. Mainly, they were chosen to allow inter-zonal flow at low mass flow rates.

TABLE 5.15: Simulation and wellbore parameters for Test Case 4.

Wellhead elevation	0 mRL
Inclination angle	0 °
Length	2217 m
Wellbore diameter	0.214 m
	0.117 m
Cement diameter	0.314 m
	0.122 m
Pipe roughness	4.5E-05 m
	9.0E-05 m
Formation temperature	Figure 5.23 B)
Wellhead boundary conditions	2.5 bara
Bottomhole boundary condition	Closed
Source model	Lumped model (3.78)
Feed parameters	Table 5.16
Initial conditions	Figures 5.23 and 5.24
Discretisation	Uniform, 150 blocks



TABLE 5.16: Feed-zone properties and locations for Test Case 4.

Location	Elevation [mRL]	$\alpha$ [kg/s/Pa]	P [bara]	$h_{f_{mix}}$ [kJ/kg]
Shallow	-890 to -930	1.00E-06	95	770
Mid	-1730 to -1770	3.20E-06	160	950
Deep	-2180 to -2220	3.00E-07	185	1312

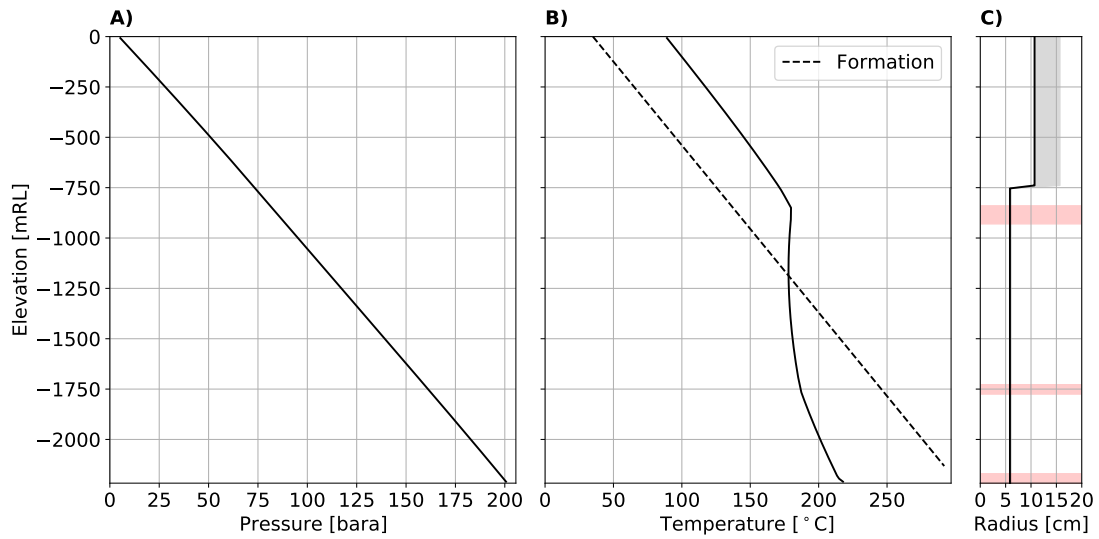


FIGURE 5.23: Initial conditions for A) pressure and B) temperature for Test Case 4. Plot C) shows the feed locations and the wellbore structure, in which the cement radius is shown in grey.

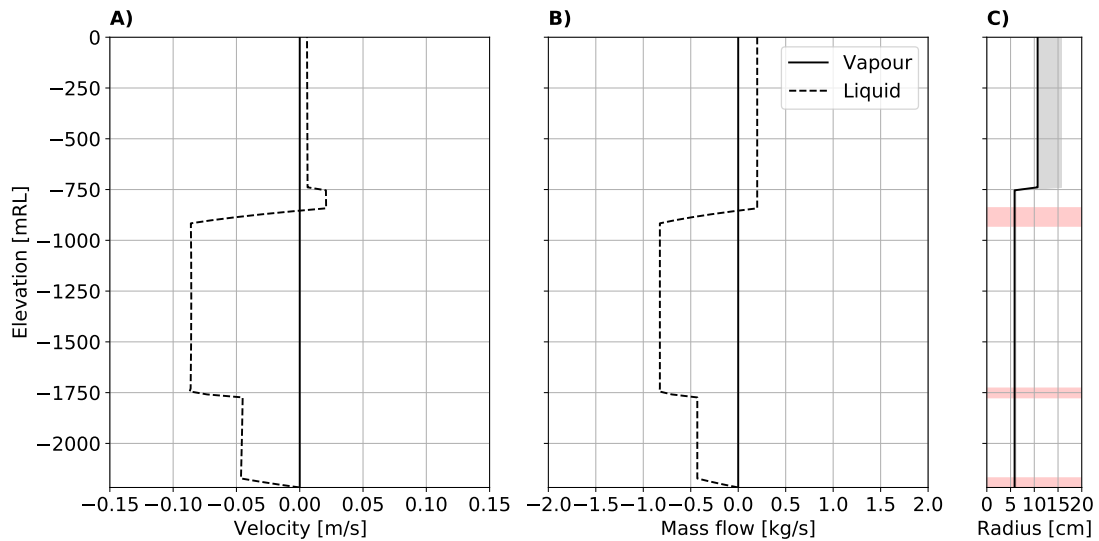


FIGURE 5.24: Initial conditions for A) phase velocities and B) phase mass flows rates for Test Case 4. Plot C) shows the feed locations and the wellbore structure, in which the cement radius is shown in grey.

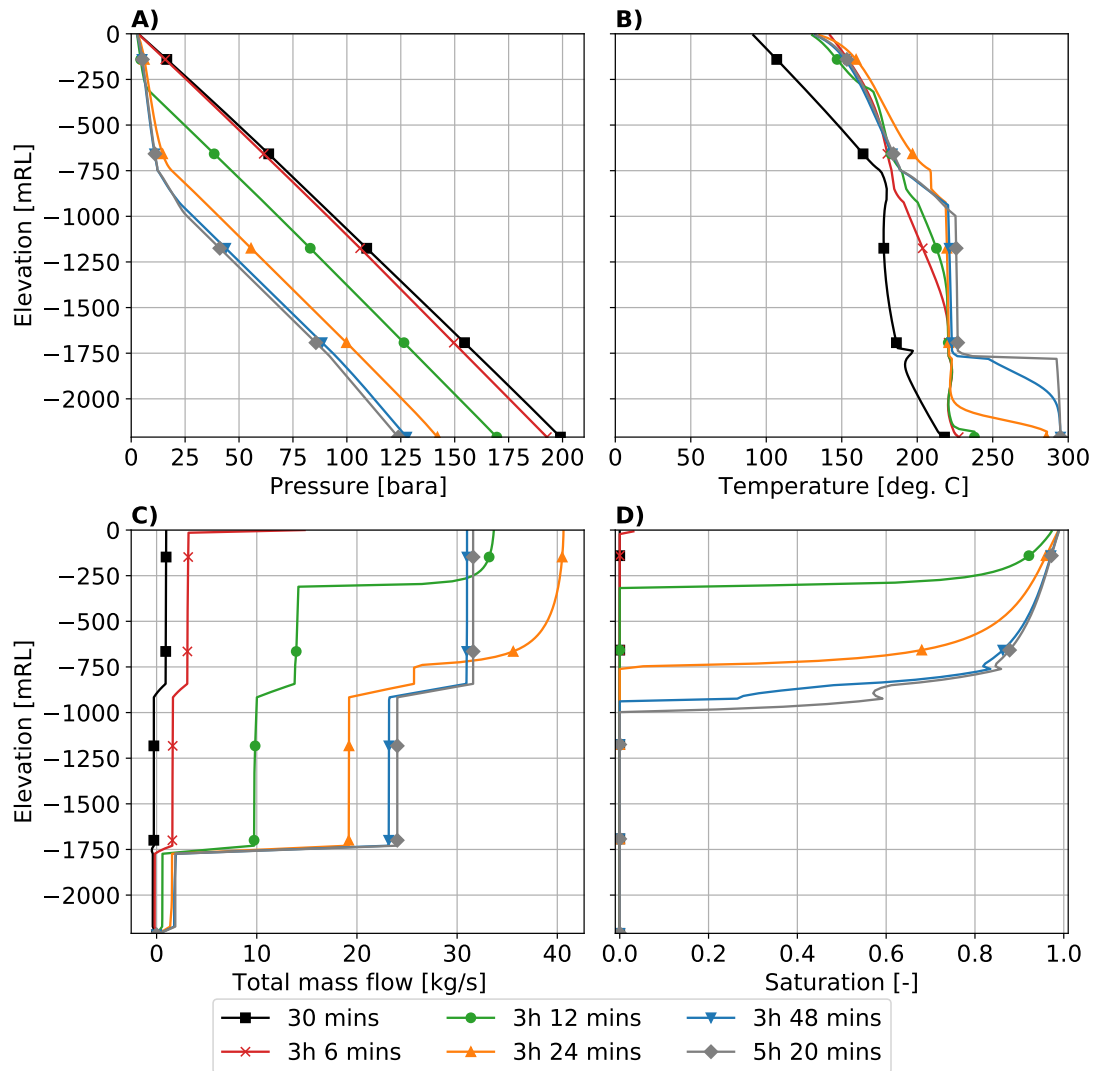


FIGURE 5.25: Simulated profiles for A) pressure, B) temperature, C) mass flow and D) vapour saturation during Test Case 4.

The initial state of the wellbore is given in Figures 5.23 and 5.24. The well has a small positive mass flow of 0.2 kg/s leaking from the wellhead and internal circulation between the feed-zones. Fluid enters the well via the shallow feed, flowing to the surface and down to the middle and deep feeds. This inter-zonal flow significantly alters the initial wellbore temperature profile, which does not reflect the reservoir temperatures (a linear temperature profile between 30 – 295 °C, as shown in Figure 5.23 B)).

Flow in the well is started by dropping the wellhead pressure from its initial value of 4.8 bara to 2.5 bara. This value is held constant throughout the simulation. Figure 5.25 shows profiles for pressure, temperature, saturation, and mass flow at various times during the simulation. After approximately 30 minutes, production has begun from the

middle feed. This is shown in Figure 5.25 B) by the increase in temperature at -1750 mRL caused by the hot in-flowing fluid. After approximately 3 hours and 6 minutes, the temperature in the well has risen sufficiently for flashing to begin at the wellhead. Following this, the wellbore flashes rapidly due to the higher enthalpy fluid from the middle feed.

Over the next 15 – 20 minute period, the well flashes along a length of approximately 650 m. During this flashing process, large changes in the overall fluid density cause a significant drop in wellbore pressures and a large increase in the total mass flow rate. By 5 hours and 20 minutes, steady-state conditions are reached. At this time, the vapour saturation profile in Figure 5.25 D) shows the effect of the influx of cool water at approximately -1000 mRL. Also, the effects can be seen of the change in wellbore radius at approximately -750 mRL.

Although Test Case 4 is relatively simple, it demonstrates the ability of the simulator to model flows with rapid changes in fluid properties over large sections of the well. Additionally, it highlights the use of a transient simulator for studying the interaction between major feeds and how this interaction affects the mass flow rate and enthalpy of the produced fluid.

### 5.3.2 Vapour production

This section discusses four vapour production test cases. These cases were developed early on in our research when it became clear that early versions of our simulator had difficulty in modelling transitions between two-phase and vapour conditions. We determined that this issue was caused by the choice of primary variables that we were using at the time. The issue of the choice of primary variables is discussed in detail in Section 6.1. These vapour production cases, although relatively simple, are fundamental to this investigation and show that our simulator can now model these transitions.

Figure 5.26 shows the three different combinations of phase and flow direction that two-phase and vapour flow can take during co-current production. In Figure 5.26, Scenario A) shows pure vapour up-flow, B) shows up-flow from a vapour block into a two-phase block and C) shows two-phase up-flow into a vapour block. Test Cases 5 – 8 all demonstrate Scenario A), Test Case 8 clearly demonstrates Scenario B) and Test Case 7 is an example of Scenario C).

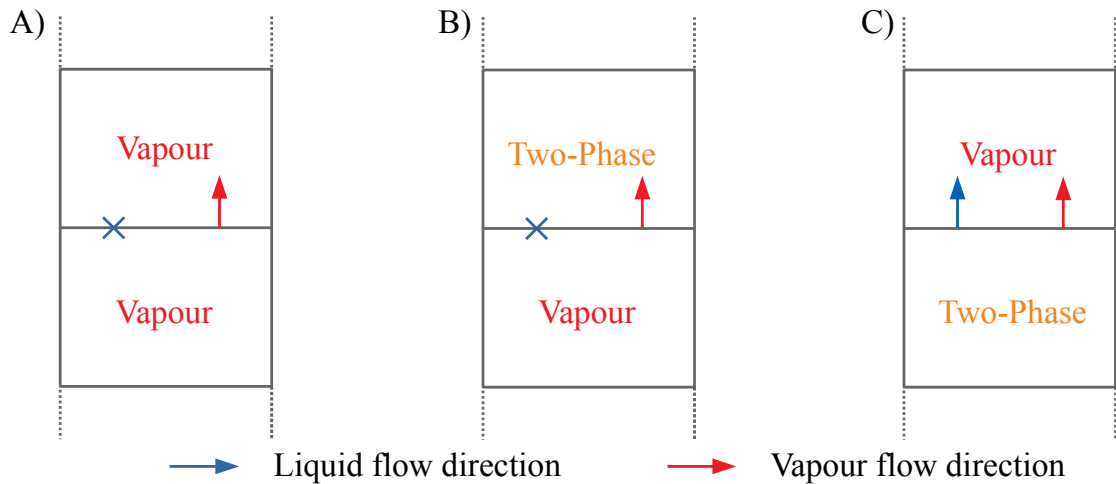


FIGURE 5.26: The possible phase state and flow direction combinations for vapour up-flow, showing A) pure vapour up-flow, B) up-flow from a vapour block into a two-phase block and C) two-phase up-flow into a vapour block.

### 5.3.2.1 Test Case 5: single-feed vapour production

Test Case 5 simulates transitions between single-phase vapour and two-phase flow along the entire length of the wellbore. This is achieved by transitioning the feed-zone, located at the bottom of the well, from vapour to two-phase conditions. This test case uses the same 1000 m well that was used in Test Cases 2 and 3. The simulation parameters for Test Case 5 are summarised in Table 5.17. Reservoir heat transfer is not included for this case as omitting this term made it easier to control flashing and condensing within the well.

The transient feed-zone conditions used to transition flow in the well between two-phase and vapour conditions are given in Table 5.18. At the beginning of the simulation, the feed produces 300 °C vapour. Then the pressure and temperature are increased and decreased, respectively, over a period of five years until saturation conditions are reached. Over the next five years, the vapour saturation of the feed is decreased from 1.0 to 0.5, where it is held constant for a further five year. This process is then reversed over the next 10 years to return the well to the vapour conditions used at the start.

TABLE 5.17: Simulation and wellbore parameters for Test Case 5.

Wellhead elevation	0 mRL
Inclination angle	0 °
Length	1000 m
wellbore diameter	0.2205 m above 660 -mRL 0.1594 m below 660 -mRL
Pipe roughness	4.5E-05 m above 660 -mRL 9.0E-05 m below 660 -mRL
Wellhead pressure condition	5.5 bara
Bottomhole flow condition	Closed
Reservoir heat transfer	None
Discretisation	Uniform, 100 elements
Source model	PI model given in (3.74)
Feed Parameter	Table 5.18
Initial Conditions	Vapour inflow conditions in Figures 5.27 and 5.28

TABLE 5.18: Feed-zone properties and locations for Test Case 5.

Elevation [mRL]	PI [m <sup>3</sup> ]	Time [years]	P [bar]	T [°C]	Sv [-]
-950 to -1000	1E-12	0	20	300	1
		5	40	250.3325	1
		10 - 15	40	250.3325	0.5
		20	40	250.3325	1
		25	20	300	1

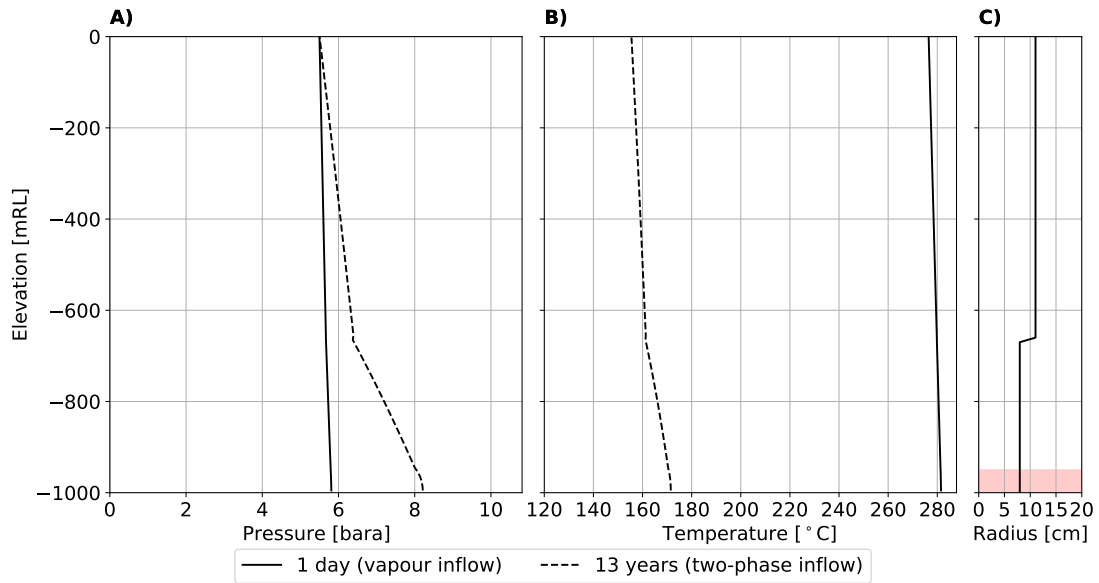


FIGURE 5.27: A comparison of A) pressure and B) temperature within the well for the vapour inflow conditions and the two-phase inflow conditions for Test Case 5.

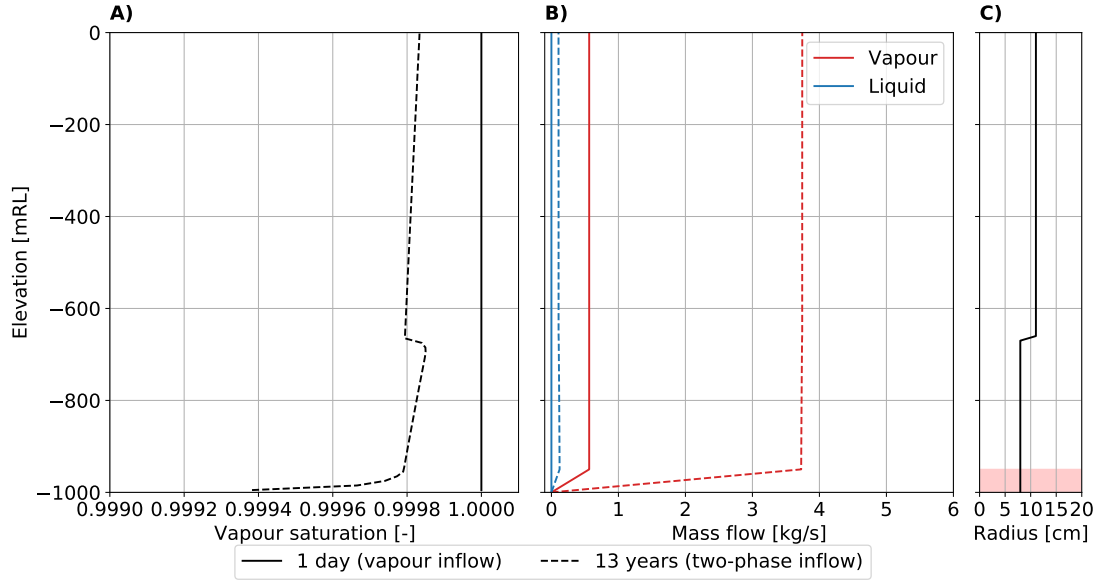


FIGURE 5.28: A comparison of A) vapour saturation and B) phase mass flow rates within the well for the vapour inflow conditions and the two-phase inflow conditions for Test Case 5.

Figures 5.27 and 5.28 compare the conditions within the well when vapour inflow occurs (at 0 and 25 years) to the conditions when two-phase inflow occurs (at 10 to 15 years). As expected, pressures at the bottom of the well are higher when there is two-phase inflow. This is due to a decrease in the vapour saturation at all depths, although Figure 5.28 A) shows that vapour saturation is still very high in all locations. This test case verifies that our simulator can model slow transient processes when vapour saturation within the well is high.

### 5.3.2.2 Test Case 6: fast flashing and condensing

Like Test Case 5, Test Case 6 was developed to test transitions between two-phase and vapour conditions. However, the reservoir parameters are varied more quickly in this case.

Test Case 6 simulated flow in a 200 m well with a constant diameter of 0.2205 m. A low resolution model with 30 blocks is used to allow fast computation. Additional wellbore and simulation parameters are given in Table 5.19.

TABLE 5.19: Simulation and wellbore parameters for Test Case 6.

Wellhead elevation	0 mRL
Inclination angle	0 °
Length	200 m
wellbore diameter	0.2205 m
Pipe roughness	4.5E-05 m
Wellhead pressure condition	3.5 bara
Bottomhole flow condition	Closed
Reservoir heat transfer	None
Discretisation	Uniform, 30 blocks
Source model	PI model given in (3.74)
Feed Parameter	Table 5.20
Initial Conditions	Two-phase conditions given in Figures 5.29 and 5.30

TABLE 5.20: Feed-zone properties and locations for Test Case 6.

Name	PI [m <sup>3</sup> ]	Elevation [mRL]	Time [hours]	P [bar]	T [°C]	S <sub>v</sub> [-]
Deep Feed	1E-12	-180 to -200	0 – 200	20.0	212.3747	0.0
			248	20.0	212.3747	1.0
			296	20.0	300	1.0
			296 – 344	20.0	300	1.0
			392	20.0	212.3747	1.0
			440	20.0	212.3747	0.0
Shallow Feed	1E-12	-50 to -60	All times	20.0	300	1.0

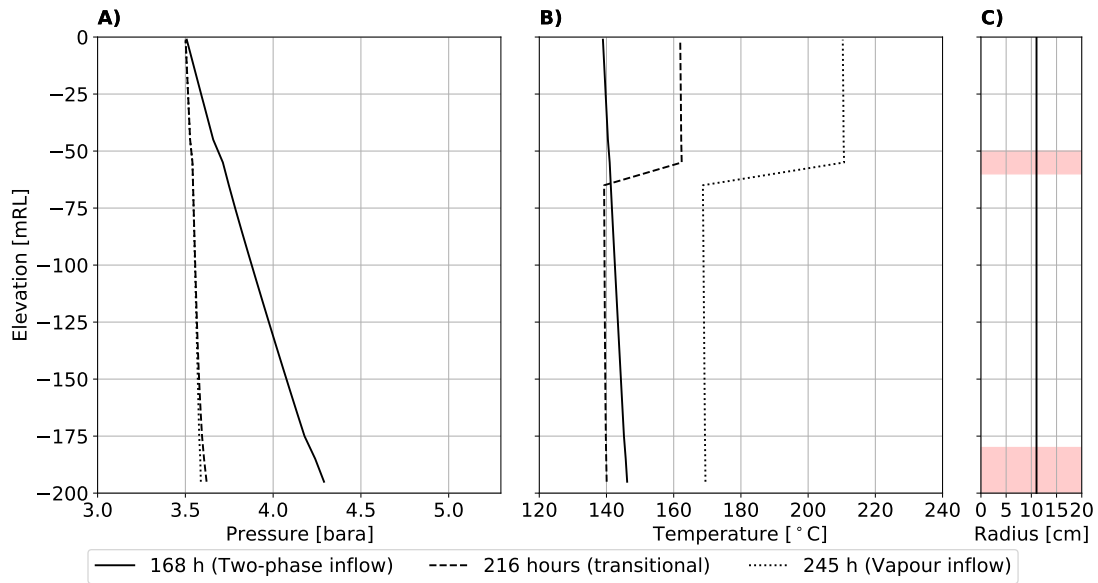


FIGURE 5.29: A comparison of A) pressure and B) temperature within the well for the two-phase inflow conditions, vapour inflow condition and transitioning between the two states, for Test Case 6.

Fluid enters the well via two feeds. The shallow feed produces pure vapour at 300 °C at all times. The deep feed transitions from two-phase to vapour conditions and then back to two-phase conditions. Two-phase conditions are produced from the deep feed for the first 200 hours. After this, the feed-zone parameters are transitioned linearly in 48 hour increments until 300 °C vapour is produced. This process is repeated in reverse to return the well to the same two-phase conditions that existed at the start of the simulation. These feed properties are summarised in Table 5.20.

Figures 5.29 and 5.30 compare the conditions in the well when i) two-phase fluid is produced from the deep feed, ii) the well is transitioning from two-phase flow to vapour flow and iii) vapour flow exists in the entire well. Figure 5.30 A) shows the addition of hot vapour from the shallow feed increases the vapour saturation at the top of the well. Saturation in the well increases as the deep feed transitions to vapour conditions, which is shown by the transitional profile in Figure 5.30 A). This plot indicates that the transition to vapour begins at the wellhead and progresses down the well. This is an example of flow scenario B) in Figure 5.26.



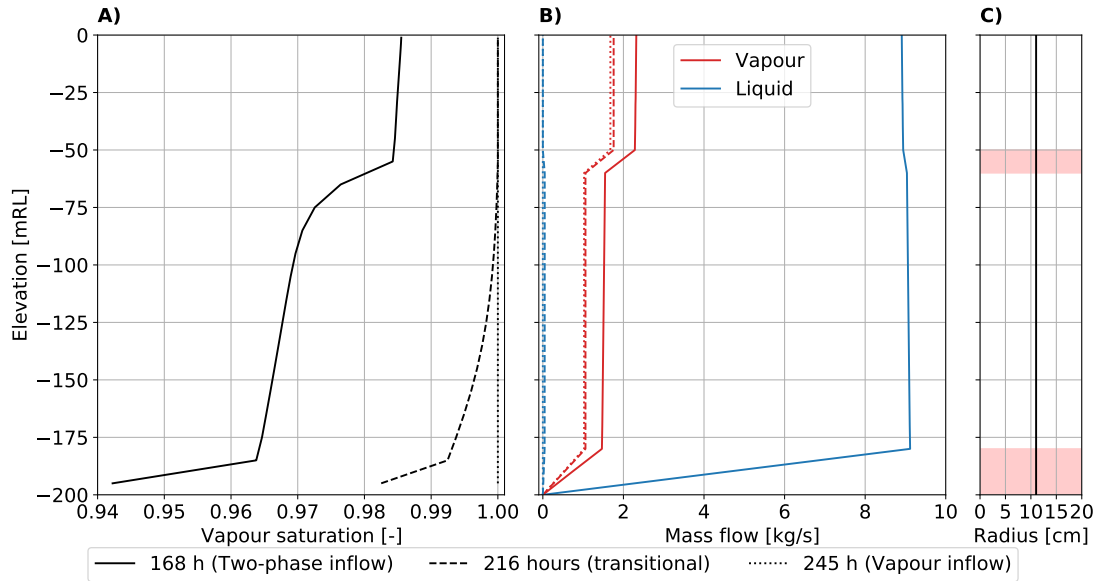


FIGURE 5.30: A comparison of A) vapour saturation and B) phase mass flow rates within the well for the two-phase inflow conditions, vapour inflow condition and transitioning between the two states, for Test Case 6.

### 5.3.2.3 Test Case 7: deep two-phase feed

Test Case 7 builds on Test Case 5 by adding a shallow vapour feed. The deep feed-zone slowly transitions from vapour conditions to two-phase conditions, as defined in Table 5.22. This causes the well to condense to two-phase conditions below the shallow feed, while above, the well remains in single-phase vapour conditions. This case was developed specifically to ensure that we can model flows which feature interfaces between two-phase and vapour blocks (the case given in Figure 5.26 C)).

TABLE 5.21: Simulation and wellbore parameters for Test Case 7.

Wellhead elevation	0 mRL
Inclination angle	0 °
Length	1000 m
wellbore diameter	0.2205 m above -660 mRL 0.1594 m below -660 mRL
Pipe roughness	4.5E-05 m above -660 mRL 9.0E-05 m below -660 mRL
Wellhead pressure condition	5.5 bara
Bottomhole flow condition	Closed
Reservoir heat transfer	None
Discretisation	uniform, 100 blocks
Source model	PI model given in (3.74)
Feed Parameter	Table 5.22
Initial Conditions	Vapour inflow conditions in Figures 5.31 and 5.32

TABLE 5.22: Feed-zone properties and locations for Test Case 7.

Name	PI [m <sup>3</sup> ]	Elevation [mRL]	Time [days]	P [bar]	T [°C]	Sv [-]
Deep Feed	1E-12	-950 to -1000	242	20	300	1
			670	40	250.3326	1
			6242	40	250.3326	0.5
Shallow Feed	1E-12	-400 to -450	All times	20	300	1

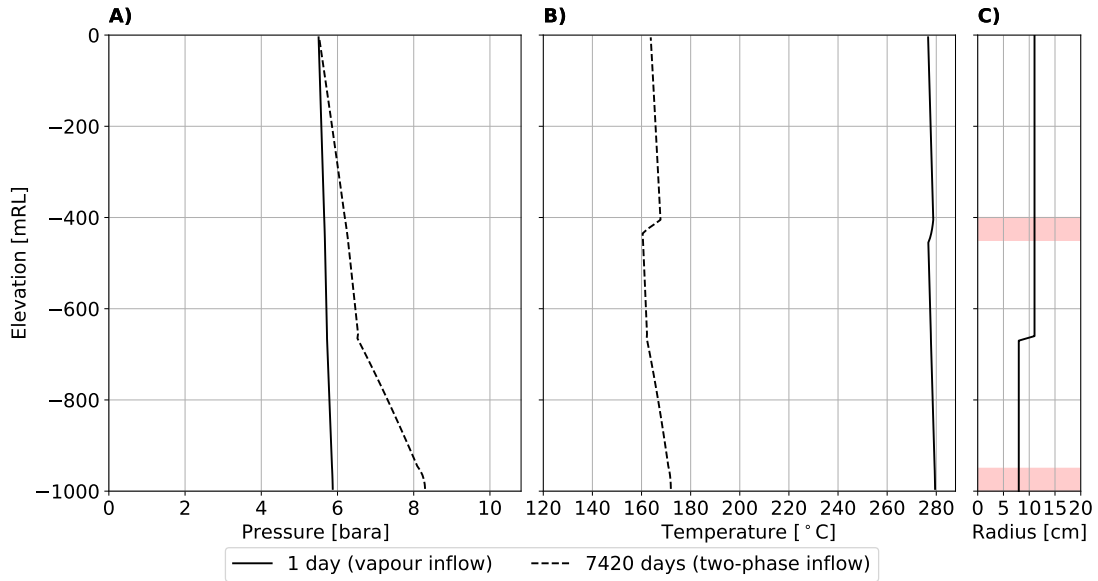


FIGURE 5.31: A comparison of A) pressure and B) temperature within the well for the vapour inflow conditions and the two-phase inflow conditions for Test Case 7.

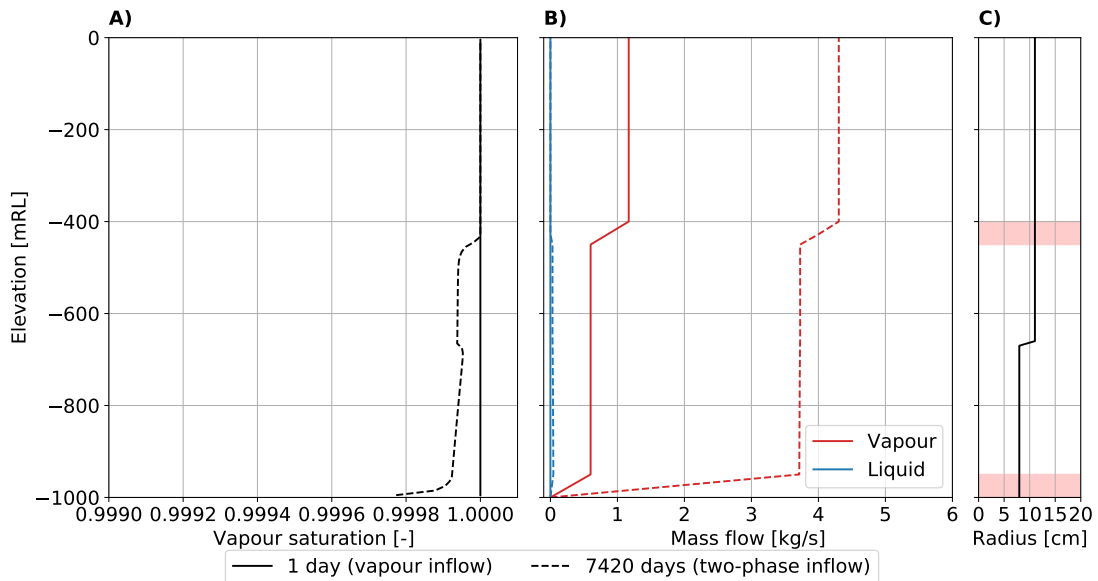


FIGURE 5.32: A comparison of A) vapour saturation and B) phase mass flow rates within the well for the vapour inflow conditions and the two-phase inflow conditions for Test Case 7.

Figures 5.31 and 5.32 compare the conditions within the well when both feeds are producing vapour to the case when the deep feed is producing two-phase conditions. Figure 5.32 A) shows the transition between two-phase and vapour conditions at approximately -450 mRL, which is due to the addition of high enthalpy vapour at this elevation. Figure 5.32 B) plots the mass flows of each phase. It shows that there is co-current up-flow in the two-phase fluid below -450 mRL, although the liquid up-flow is very small due to the high vapour saturation of the fluid. This confirms that our simulator is capable of modelling cases with two-phase up-flow into a vapour column (flow scenario C) in Figure 5.26).

#### 5.3.2.4 Test Case 8: shallow two-phase feed

Test Case 8 is similar to Test Case 7 except, in this case, it is the shallow feed that transitions to two-phase conditions. These transient feed conditions are given in Table 5.24. This causes a two-phase zone to develop above a column of vapour. The productivity index of the deep feed has been increased to  $1.64\text{E-}12 \text{ m}^3$ . This prevents liquid down-flow from the two-phase region at the top of the well, which could result in the condensation of the vapour column below.

The results of Test Case 8 are given in Figures 5.33 and 5.34. Figure 5.34 A) shows that a two-phase zone has developed due to the addition of two-phase fluid between -400 mRL and -450 mRL. This test case shows that our simulator is capable of modelling cases with single-phase vapour up-flow into a two-phase fluid zone (flow scenario B) in Figure 5.26).

Further examination of Figure 5.34 A) indicates that the two-phase column extends down to -520 mRL, 70 m below the bottom of the two-phase feed located at -450 mRL. This is caused by a small liquid down-flow from the two-phase column at the top of the well, which slowly condenses the top of the vapour column. This liquid down-flow is evident between -450 mRL and -520 mRL in the plot of the liquid mass flow rate, given in Figure 5.34 B).

TABLE 5.23: Simulation and wellbore parameters for Test Case 8.

Wellhead elevation	0 mRL
Inclination angle	0 °
Length	1000 m
wellbore diameter	0.2205 m above 660 m 0.1594 m below 660 m
Pipe roughness	4.5E-05 m above 660 m 9.0E-05 m below 660 m
Wellhead pressure condition	5.5 bara
Bottomhole flow condition	Closed
Reservoir heat transfer	None
Discretisation	uniform, 100 blocks
Source term model	PI model given in (3.74)
Feed parameter	Table 5.24
Initial conditions	Vapour conditions given in Figures 5.33 and 5.34

TABLE 5.24: Feed-zone properties and locations for Test Case 8.

Name	PI [m <sup>3</sup> ]	Elevation [mRL]	Time [days]	P [bar]	T [°C]	Sv [-]
Shallow feed	1E-12	-400 to -450	242	20	300	1
			670	40	250.3326	1
			6242	40	250.3326	0.5
Deep feed	1.64E-12	-950 to -1000	All times	20	300	1

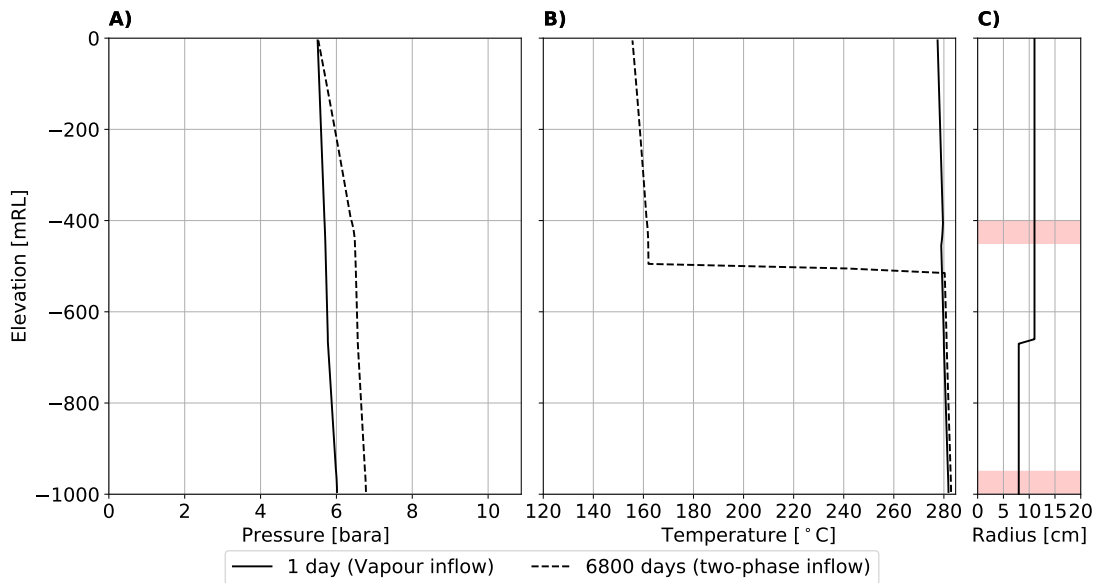


FIGURE 5.33: A comparison of A) pressure and B) temperature within the well for the vapour inflow conditions and the two-phase inflow conditions for Test Case 8.

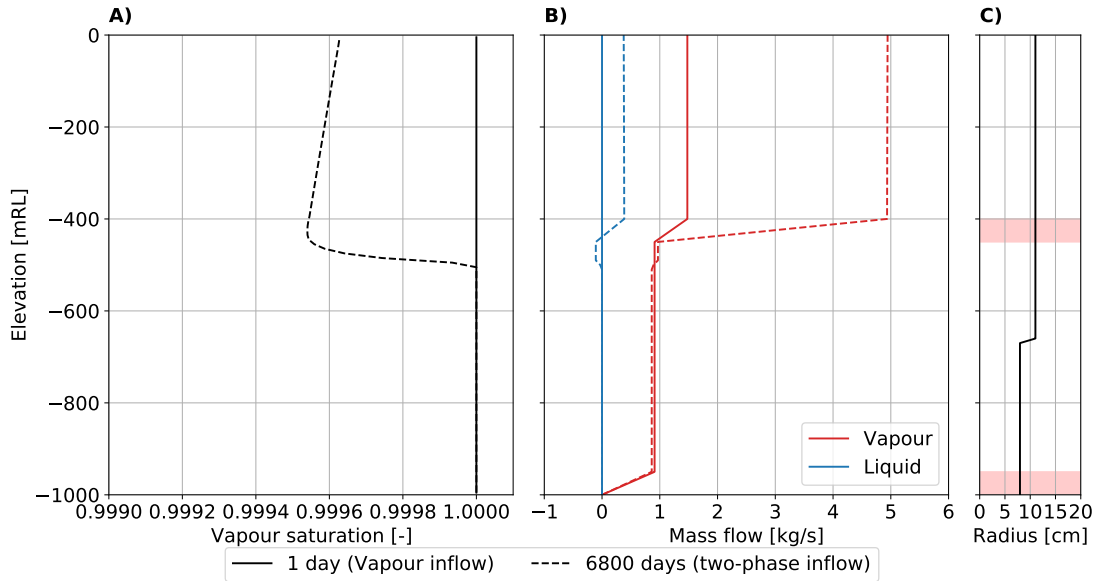


FIGURE 5.34: A comparison of A) vapour saturation and B) phase mass flow rates within the well for the vapour inflow conditions and the two-phase inflow conditions for Test Case 8.

### 5.3.3 Injection cases

While not as common as production cases, injection plays an important role in wellbore testing, field management (e.g., the re-injection of liquid water) and discharge stimulation (e.g., well to well stimulation and air compression). Therefore, it is important that our simulator is able to model injection cases and, more generally, the down-flow of fluid in geothermal wells.

Figure 5.35 shows the different combinations of phase and flow direction that are possible during down-flow. In Figure 5.35, Scenarios A), C) and E) correspond to liquid, two-phase and vapour down-flow, respectively. Scenario B) shows two-phase down-flow into a liquid block. This may occur, for example, during well to well stimulation, in which hot geothermal fluid is injected into a non-discharging well. Scenario D) shows liquid down-flow into a two-phase block. This may occur, for example, during an injection test when a two-phase (or vapour) feed is not suppressed by the liquid injection. Scenarios F) and G) show vapour down-flow into a two-phase block and two-phase down-flow into a vapour block, respectively. Physically realistic cases in which scenarios E), F) and G) occur for flows of hot water vapour are not very obvious. However, the down-flow of water vapour is similar to the down-flow of air. This is required to model air injection at

the wellhead, which is used when simulating discharge stimulation in Section 8.2.3. It is, therefore, important to verify that our simulator can model cases such as these.

Section 5.3.3.1 presents Test Case 9, which models the injection of low enthalpy fluid. This case verifies that our simulator can model scenarios A), B) and C) in Figure 5.35. Section 5.3.3.2 discusses Test Case 10, which verifies that our simulator can model scenarios C), E) and G). Test Cases 13 and 14, presented in Appendix C, were developed to test scenarios D) and F).

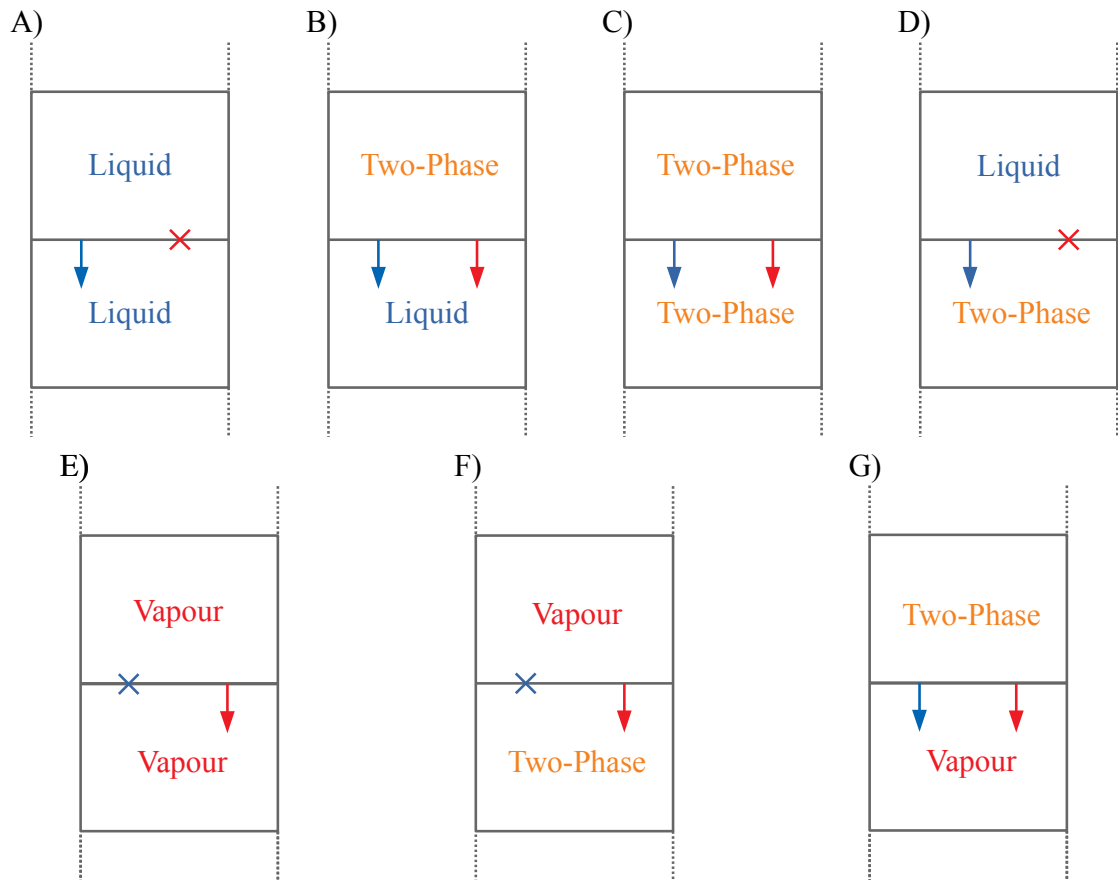


FIGURE 5.35: The possible phase state and flow direction combinations for vapour up-flow, showing A) liquid down-flow B) two-phase down-flow into a liquid block, C) two-phase down-flow, D) liquid down-flow into a two-phase block, E) vapour down-flow, F) vapour down-flow into a two-phase block and G) two-phase down-flow into a vapour block.

### 5.3.3.1 Test Case 9: low enthalpy injection

Test Case 9 simulates the injection of low enthalpy fluid at the wellhead. The test well has a length of 100 m and a diameter of 0.2 m. This case demonstrates flow Scenarios A), B) and C) in Figure 5.35 above. It also verifies that our simulator can model transitions from liquid to two-phase conditions during down-flow.

This simulation is run by prescribing the mass flow and flowing enthalpy of the injection fluid using the conditions described in Section 4.5.2. We simulate transitions between liquid and two-phase conditions by slowly increasing the enthalpy of the fluid injected at the wellhead. These conditions are summarised in Table 5.26. Mass flow exits the well via a feed in the bottom block of the model. The feed conditions, which correspond to a liquid reservoir at 15 bara, are given in Table 5.27. Reservoir heat transfer is not included for this case as omitting this term made it easier to control boiling within the well.

TABLE 5.25: Simulation and wellbore parameters for Test Case 9.

Wellhead elevation	0 mRL
Inclination angle	0 °
Length	100 m
wellbore diameter	0.2 m
Pipe roughness	4.5E-05 m
Bottomhole flow condition	Closed
Reservoir heat transfer	None
Discretisation	Uniform, 100 blocks
Source term model	Lumped parameter model (3.78)
Feed parameters	Table 5.27
Wellhead mass flow	Table 5.26
Wellhead flowing enthalpy	Table 5.26
Initial conditions	Figure 5.36

TABLE 5.26: Mass flow and flowing enthalpy boundary conditions prescribed at the wellhead for Test Case 9.

Time [s]	0	60	600	3600
Flowing enthalpy [kJ/kg]	125	125	125	900
Mass flow rate [kg/s]	0	0	-10	-10

TABLE 5.27: Feed-zone properties and locations for Test Case 9.

Name	Elevation [mRL]	$\alpha$ [kg/s/Pa]	$P$ [bar]	$T$ [°C]	$S_v$ [-]
bottomhole feed	-99 to -100	1E-5	15	150	0

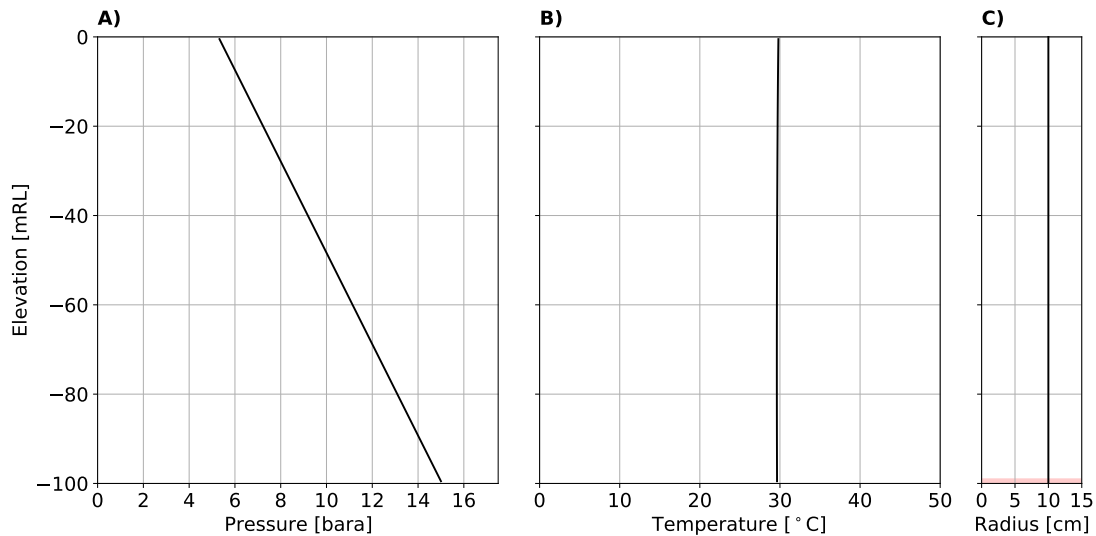


FIGURE 5.36: Initial conditions for Test Case 9 showing A) pressure and B) temperature. The wellbore radius and feed location are shown in plot C).

The simulation starts as a static column of liquid at 30 °C. These conditions are shown in Figure 5.36. The well remains shut for the first 60 seconds of the simulation. Following this, the injection mass flow is increased linearly up to 10 kg/s after 600 seconds. This fluid has an enthalpy of 125 kJ/kg (liquid water at 30 °C). Over the next 59 minutes, the enthalpy of the injected fluid is increased linearly from 125 kJ/kg to 900 kJ/kg. The injection mass flow rate is kept constant at 10 kg/s.

Figure 5.37 shows how the conditions within the well change in response to the injection boundary conditions. After 55 minutes (shown in black), temperatures in the well, shown in Figure 5.37 B), have increased and conditions at the wellhead are just below saturation conditions. Pressure in the well, shown in Figure 5.37 A), has also increased over this time. This increase in pressure creates the over-pressure at the bottomhole required for the feed to accept 10 kg/s of fluid.

Figure 5.37 D) shows that boiling begins at the wellhead and progresses down the well. This boiling causes fluid expansion, which increases wellbore pressures and accelerates the liquid column down the well. This increase in mass flow is shown in Figure 5.37 C). After 30 minutes of injection at 900 kJ/kg (1 hour 30 minutes in Figure 5.37), flow in the well has stabilised. The two-phase injected fluid flows down the well. It condenses to liquid at a depth of approximately 30 m. This is the depth where the pressure in the well is equal to the pressure of saturated liquid water with an enthalpy of 900 kJ/kg.



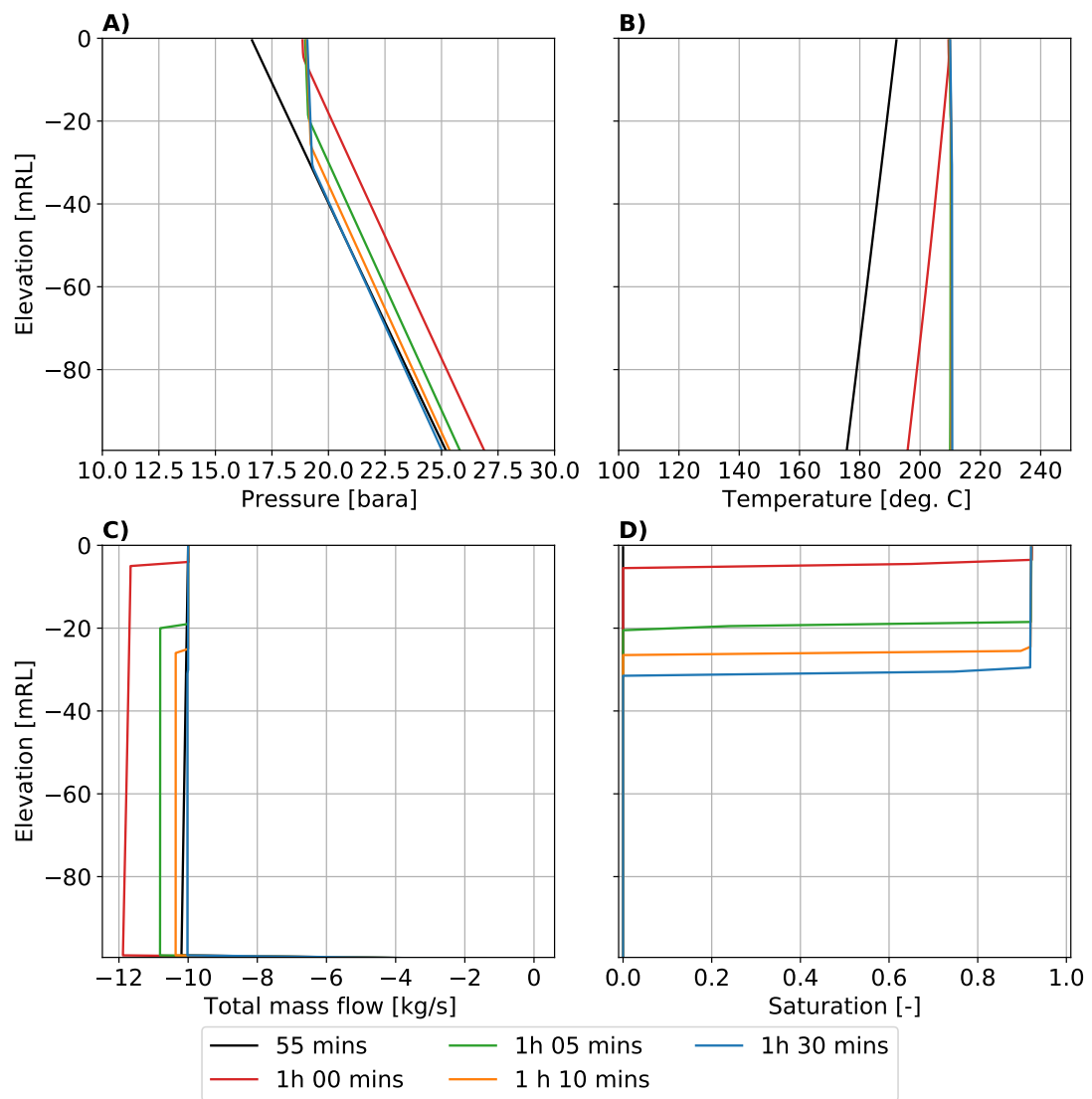


FIGURE 5.37: Results showing A) pressure, B) temperature, C) total mass flow and D) vapour saturation for Test Case 9.

### 5.3.3.2 Test Case 10: high enthalpy injection

Test Case 10 simulates the injection of high-enthalpy fluid at the wellhead. This simple test case was developed to ensure that our simulator could model vapour down-flow and phase changes from vapour and two-phase conditions (Scenarios G) in Figure 5.26).

Test Case 10 uses the same well as Test Case 9, however, different wellhead boundary conditions and feed-zone parameters are used. The feed properties, which correspond to a vapour feed at 15 bara, are given in Table 5.28. Additional simulation parameters are given in Table 5.29.

For this case, the injection enthalpy at the wellhead is varied with time to force the wellbore flow to condense from vapour to two-phase. These injection conditions are given in Table 5.30. Reservoir heat transfer is not included for this case as omitting this term made it easier to control condensing within the well.

TABLE 5.28: Feed-zone properties and locations for Test Case 10.

Name	Elevation [mRL]	$\alpha$ [kg/s/Pa]	$P$ [bar]	$T$ [°C]	$S_v$ [-]
bottomhole feed	-99 to -100	5E-6	15	250	1

TABLE 5.29: Simulation and wellbore parameters for Test Case 10.

Wellhead elevation	0 mRL
Inclination angle	0 °
Length	100 m
wellbore diameter	0.2 m
Pipe roughness	4.5E-05 m
Bottomhole flow condition	Closed
Reservoir heat transfer	None
Discretisation	Uniform, 100 blocks
Source term model	Lumped parameter model given in (3.78)
Feed parameter	Table 5.28
Wellhead mass flow	Table 5.30
Wellhead flowing enthalpy	Table 5.30
Initial conditions	Figure 5.38

TABLE 5.30: Mass flow and flowing enthalpy boundary conditions prescribed at the wellhead for Test Case 10.

Time [s]	0	100	1000
Flowing enthalpy [kJ/kg]	2900	2900	2760
Mass flow rate [kg/s]	-3	-3	-3

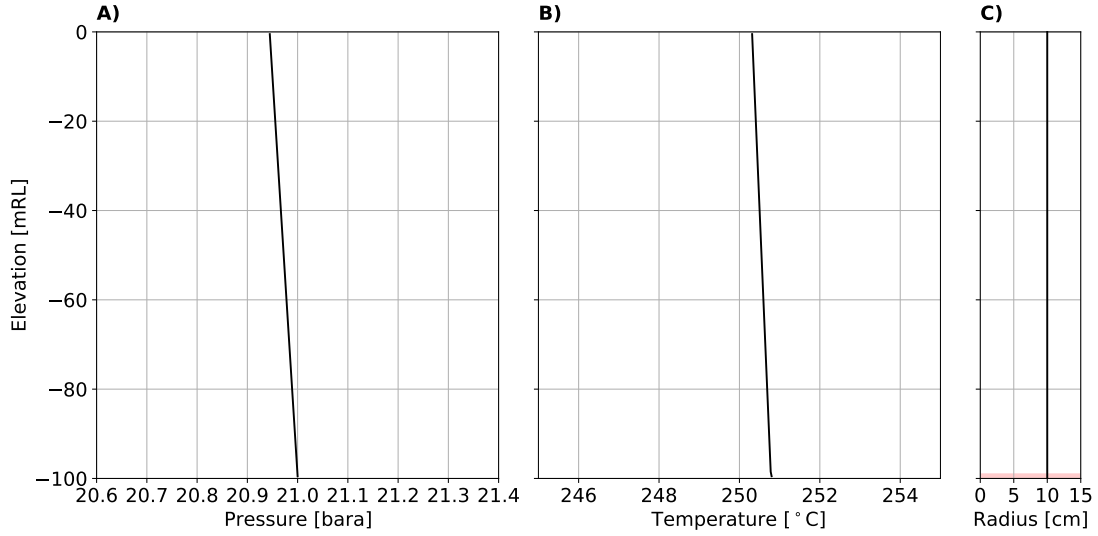


FIGURE 5.38: Initial conditions for Test Case 10 showing A) pressure and B) temperature. The wellbore radius and feed location are shown in plot C).

The simulation starts from the flowing vapour conditions shown in Figure 5.38. These correspond to vapour with an enthalpy of 2900 kJ/kg flowing at 3 kg/s.

Figure 5.39 shows the results of this simulation. After 100 seconds of injection at 2900 kJ/kg, the wellhead enthalpy is decreased to 2760 kJ/kg over the next 900 seconds (15 minutes). As expected, temperatures in the well drop considerably as the enthalpy of the injected fluid is decreased. After 11 minutes, the wellhead temperature has dropped to approximately 218 °C, 3 °C above saturation conditions.

The flow condenses from vapour to two-phase conditions when saturation conditions are reached at the wellhead. Figure 5.39 D), which plots static mass fraction, shows the flow condensing from vapour to two-phase conditions, confirming that our simulator can model this process.

Figure 5.39 A) shows that the mass flow at the bottom of the well decreases slightly as the wellbore flow cools and condenses. This behaviour can be explained by considering the mass conservation equation, which states that:

$$\frac{\partial \rho_{mix}}{\partial t} + \frac{1}{A} \frac{\partial Q_m}{\partial s} = 0. \quad (5.10)$$

When the density of the fluid increases (due to the decrease in enthalpy of the injected fluid) the mass flow gradient with depth must be negative. As a result, the total mass

flow decreases with depth while the flow is condensing. This is the opposite process to what occurs in flashing cases, where fluid expansion causes the flow to accelerate.

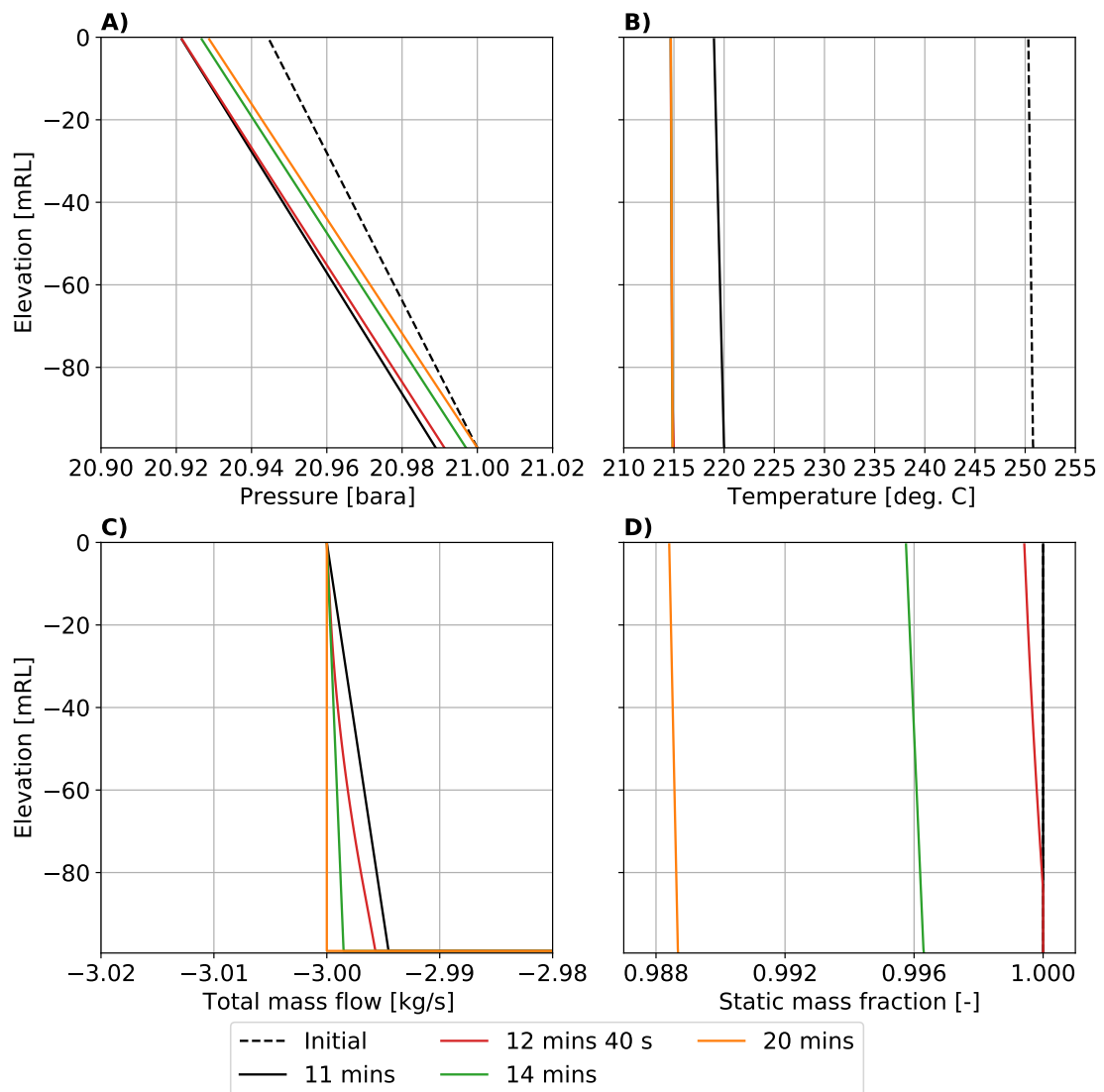


FIGURE 5.39: Results for Test Case 10 showing A) pressure, B) temperature, C) total mass flow rate and D) static mass fraction at various times.

### 5.3.4 Counter-flow cases

One of the main objectives of the research presented in this thesis was to develop a simulator capable of modelling transient counter-flow processes. In this thesis, we only consider counter-flow cases where vapour flows up while liquid flows down. The phase state and flow direction combinations that are possible during counter-flow are shown in Figure 5.40.

The two test cases described in this section were developed specifically to ensure our simulator could model counter-flow. When it became clear that we could not model some counter-flow cases with early versions of our simulator, these test cases were used to diagnose the problem and develop a solution. The details of this investigation are presented in Section 6.2.

Test Case 11, presented below in Section 5.3.4.1, models counter-flow that occurs due to boiling below the deepest feed in a well. Test Case 12 models counter-flow processes that occur as a well heats up after being shut-in. The test case set-up is discussed in Section 5.3.4.2 below, however, the results are presented later on in Section 8.1 when we discuss counter-flow processes in shut-in wells.

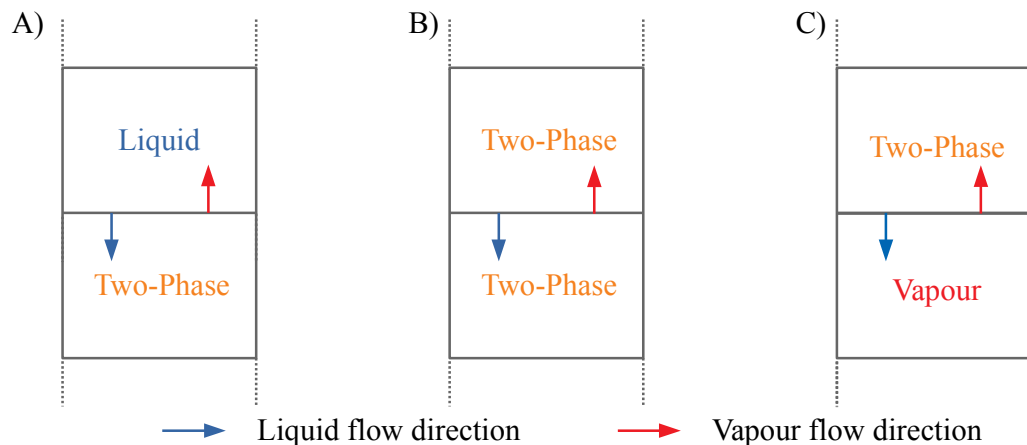


FIGURE 5.40: The phase and flow direction combinations that are possible for counter-flow. Plot A) shows vapour up-flow from a two-phase block and liquid down-flow from a liquid block, B) shows up-flow and down-flow between two-phase blocks, and C) shows vapour up-flow from a vapour block and liquid down-flow from a two-phase block.

Test Cases 11 demonstrates Scenario B) in Figure 5.40 and Test Case 12 demonstrates Scenarios A) and B). Case C) in Figure 5.40 occurs in Test Case 8, described in Section 5.3.2.4 above, where the liquid phase flowed down from the two-phase zone into the vapour column below.

#### 5.3.4.1 Test Case 11: counter-flow below feed-zone

Test Case 11 simulates two-phase flow in a 1000 m well with a constant diameter of 0.2205 m. Additional wellbore and simulation parameters are given in Table 5.31. Two-phase fluid is produced from a single feed located 200 m above the bottom of the well. Mass conservation means that the total mass flow below this feed must equal zero. This requirement is satisfied through counter-flow processes when boiling occurs below the feed.

It proved difficult to generate good initial conditions due to the location of the feed above the bottomhole and because its properties corresponded to a water level below the wellhead. It is not possible to model realistic initial conditions for these cases without including air in the simulation. We discuss the modelling of these cases in Chapters 7 and 8. This test case was intended for use with a pure-water EOS. We have, therefore, initialised the well as a simple two-phase production scenario using a second feed located

TABLE 5.31: Simulation and wellbore parameters for Test Case 11.

Wellhead elevation	0 mRL
Inclination angle	0 °
Length	1000 m
wellbore diameter	0.2205 m
Cement radius	0.314 m
Pipe roughness	4.5E-05 m
Wellhead pressure condition	5.5 bara
Bottom boundary condition	closed
Formation temperatures	Figure 5.41
Feed properties	Table 5.32
Discretisation	Uniform, 300 blocks
Initial conditions	Figures 5.41 and 5.42

TABLE 5.32: Feed properties and locations for Test Case 11. The deep feed-zone is slowly "turned off" over a period of 87.5 days.

Name	Elevation [mRL]	time [days]	P [bara]	$S_v$ [-]	PI [m <sup>3</sup> ]
Shallow	-800 to -820	all times	35	0.25	1E-12
Deep	-980 to -1000	0 - 365	35	0.25	1E-12
		365 - 447.5	35	0.25	0

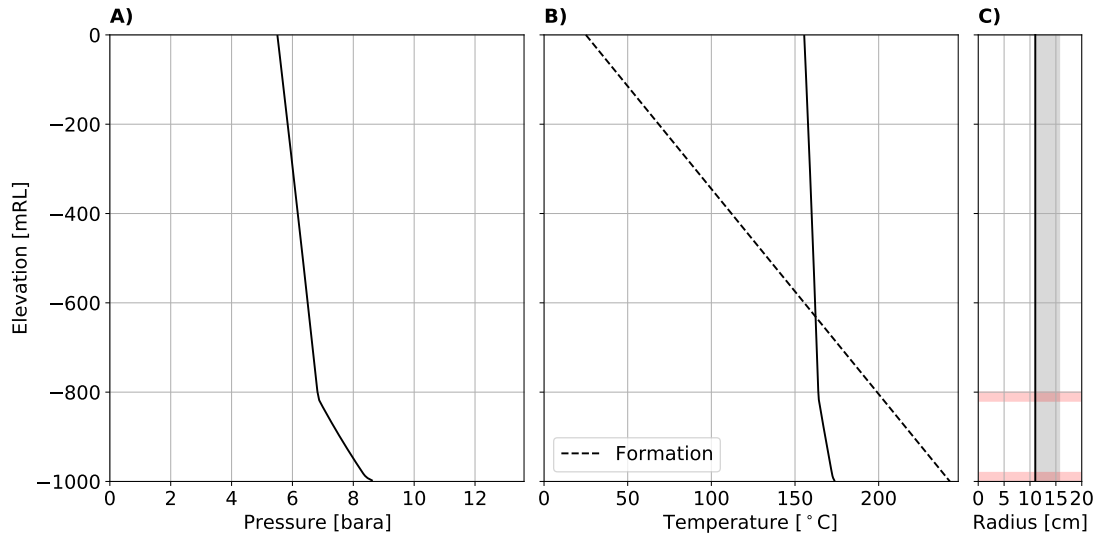


FIGURE 5.41: Initial conditions for A) pressure and B) temperature for Test Case 11. The wellbore structure and feed locations are shown in C).

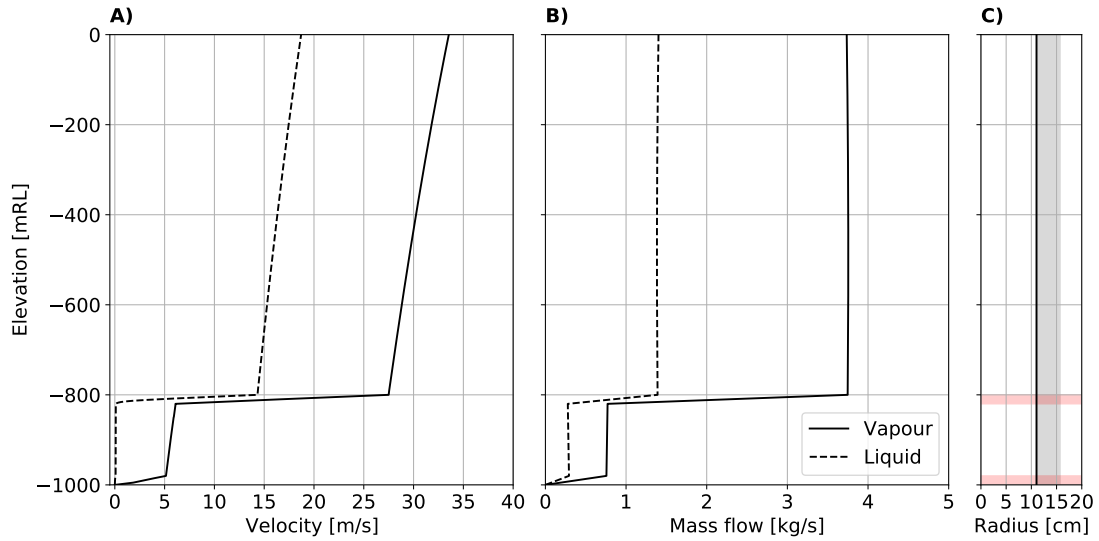


FIGURE 5.42: Initial conditions for A) phase velocity and B) phase mass flow rate for Test Case 11. The wellbore structure and feed locations are shown in C).

at the bottom of the well. The productivity of this feed was then slowly decreased to zero leaving only the feed located at -800 mRL. The feed parameters are given in Table 5.32 and the initial conditions are shown in Figures 5.41 and 5.42.

Figures 5.43 and 5.44 show the steady-state results for Test Case 11. These show that very different conditions exist in the well above and below the feed. Above the feed, there is co-current flow of two-phase fluid with a vapour saturation close to one. This causes the near vertical pressure profile above -800 mRL that is shown in Figure 5.43 A).

Figure 5.44 A) shows that two-phase flow with relatively low vapour saturation exists below the feed. Low vapour saturation increases the average density of the two-phase fluid, causing the large increase in pressure with depth below -825 mRL that is seen in Figure 5.43 A).

Figure 5.45 B) zooms in on the section of the well below the feed and shows that counter-flow occurs in this zone. Here, the mass flow rate of vapour up the well is equal and opposite to the liquid mass flow rate down. This is required to satisfy mass conservation below the feed-zone.

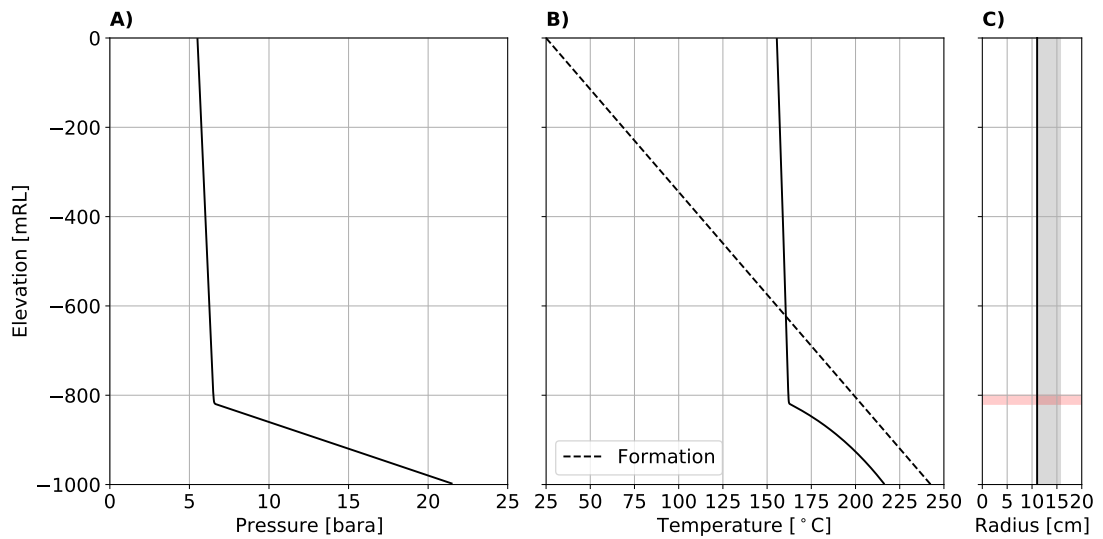


FIGURE 5.43: Steady-state results showing A) pressure and B) temperature for Test Case 11.

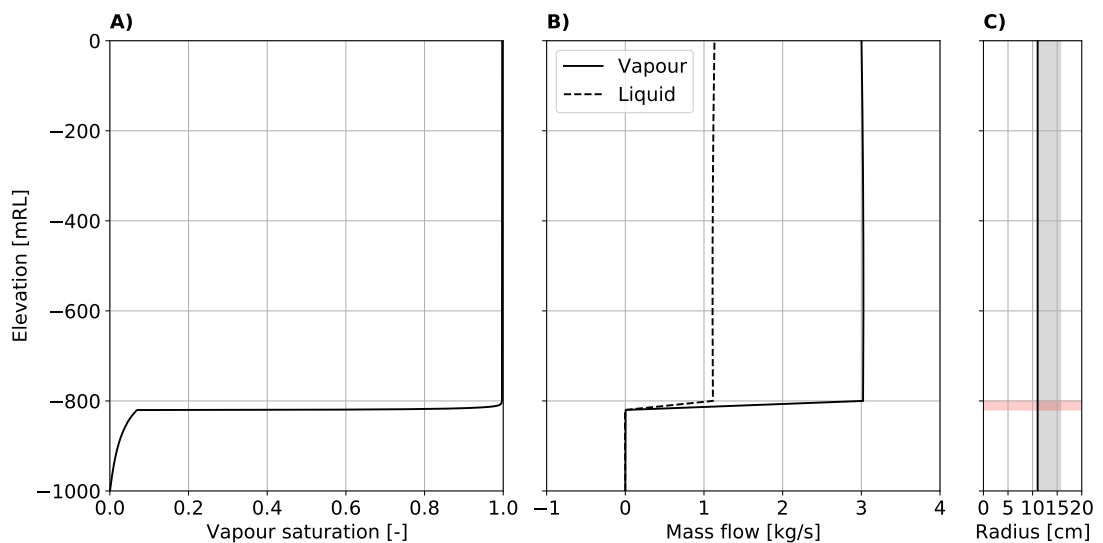


FIGURE 5.44: Steady-state profiles of A) vapour saturation and B) phase mass flow rates for Test Case 11.



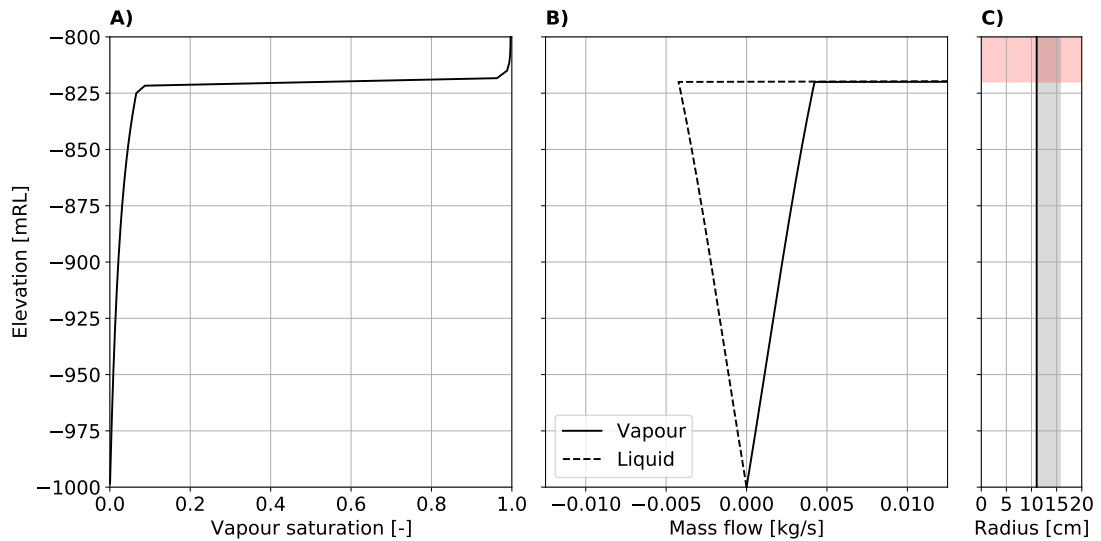


FIGURE 5.45: Steady-state profiles of A) vapour saturation and B) phase mass flow showing counter-flow occurring below the feed-zone for Test Case 11.

The comparison of the formation and wellbore temperatures in 5.43 B) indicates that there is heat transfer to the well below -650 mRL. This heat transfer causes boiling to occur in the fluid below the feed and is what drives the counter-flow process in this section of the well. We demonstrate this by changing the formation temperature profile for the problem described above and comparing the conditions below the feed. Two cases were compared to the original simulation, one with cooler formation temperatures and the other with hotter formation temperatures. For the cold case, the formation temperature profile was linear between 25 – 220 °C. For the hot case, the formation temperature was linear between 25 – 250 °C. The original case (which we presented above) has a linear formation temperature profile between 25 – 240 °C. All other simulation parameters remained the same in these simulations.

Figure 5.46 shows that increasing the formation temperatures increases vapour saturation below the feed. It also increases the rate of counter-flow (i.e., larger vapour up-flow and liquid down-flow). In this case, the higher formation temperatures increase the heat flux from the formation to this section of the well. This causes a more vigorous boiling process, which in turn increases the saturation and rate of counter-flow. Similarly, Figure 5.46 shows that decreasing the formation temperatures reduces the heat flux to this section of the well. This reduces boiling, resulting in lower vapour saturations and smaller mass flow rates below -825 mRL.

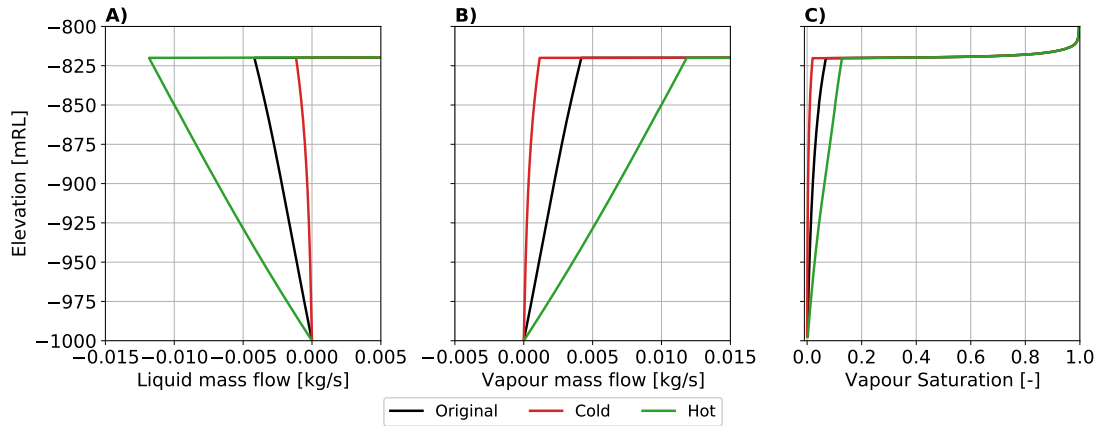


FIGURE 5.46: A comparison of A) liquid mass flow rate, B) vapour mass flow rate and C) vapour saturation for Test Case 11 using different formation temperature profiles.

#### 5.3.4.2 Test Case 12: heat up of a shut in well

Test Case 12 models heat-up processes in a shallow geothermal well that has been closed after a period of injection, a process that occurs during heating up following a completion test. This test case proved difficult to model despite being conceptually simple. Specifically, modelling no-flow conditions while two-phase fluid exists at the wellhead proved challenging. This test case allowed in-depth analysis of mass and energy fluxes occurring at the wellhead during this process, which allowed a solution to the problem of how to model these processes to be found. The problems experienced with two-phase conditions at the wellhead, and their solution, are discussed in detail in Section 6.2.

Test Case 12 simulates flow in a 100 m well with a constant diameter of 0.2 m and a completion diameter of 0.22 m. Additional model and simulation parameters are given in Table 5.33. The bottom boundary of the well is closed to flow, however, a source term in the bottom block allows fluid exchange with the reservoir. This vapour feed has a pressure of 20 bar, a temperature of 250 °C, and a productivity of 1E-6 kg/s/Pa. These conditions are summarised in Table 5.34. Finally, the formation temperature is assumed to be constant with time and is shown in Figure 5.47 B).

This case begins with the injection of 25 °C liquid water at a rate of 2 kg/s. Pressure, temperature and saturation conditions within the well after two days of injection are shown in Figure 5.47. These conditions correspond to a column of cold liquid water.

TABLE 5.33: Simulation and wellbore parameters for Test Case 12.

Wellhead elevation	0 mRL
Inclination angle	0 °
Length	100 m
discretisation	Uniform, 200 blocks
wellbore diameter	0.20 m
Cement diameter	0.22 m
Pipe roughness	4.5E-05 m
Wellhead mass flow condition	Closed
Bottomhole flow condition	Closed
Initial conditions	Figure 5.47
Formation temperature	Figure 5.47 B)

TABLE 5.34: Feed-zone properties and locations for Test Case 12.

Name	Elevation [mRL]	P [bara]	T °C	$S_v$ [-]	$\alpha$ [kg/s/Pa]
Bottomhole feed	-99.5 to -100	20	250	1.0	1.0E-06

After injecting cold water for two days, the wellhead is shut rapidly, and the well is left to heat up for 30 days.

Heat transfer from the formation causes boiling to begin at the bottom of the well. Counter-flow occurs as soon as boiling begins at the bottom of the well. Boiling progresses up the well and vapour accumulates at the wellhead. The steady wellbore conditions 30 days after shut-in are shown in Figure 5.48. Figure 5.47 B) shows that after this time, a vapour cap (which is actually high saturation two-phase fluid) has developed in the top 12 m of the well. The plot of mass flow, given in Figure 5.48 C), shows that stable counter-flow occurs within the well. Here, the vapour mass flow up the well is equal and opposite to the liquid down-flow. In this case, counter-flow transports heat up the well. This allows the vapour cap to exist at higher temperatures than the surrounding formation.

The transient evolution of the flow for this test case and the heat transport processes caused by counter-flow are discussed further in Section 8.1, where we present our investigation of counter-flow processes in shut-in geothermal wells.

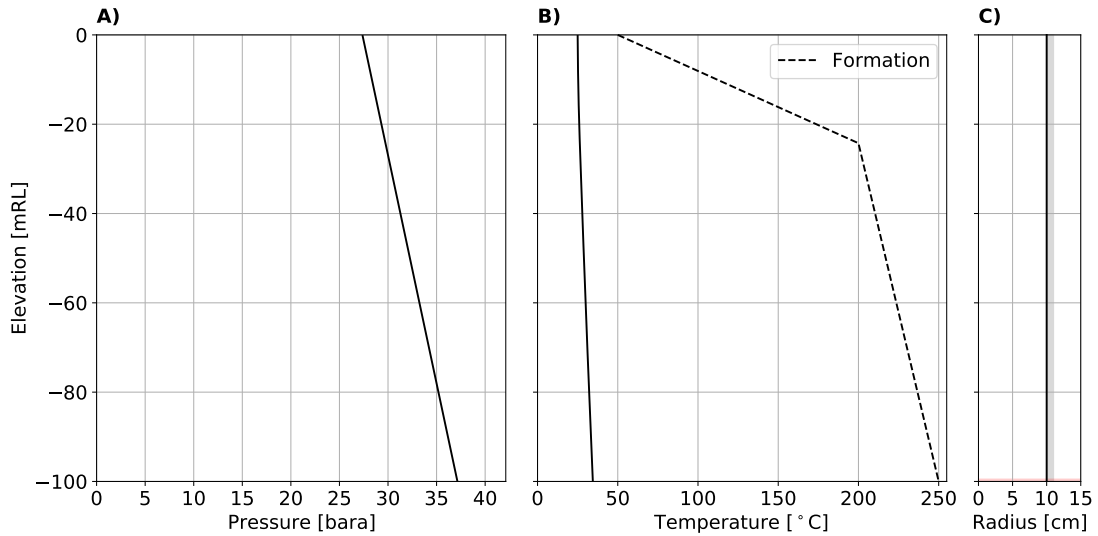


FIGURE 5.47: Initial conditions for A) pressure and B) temperature for Test Case 12.

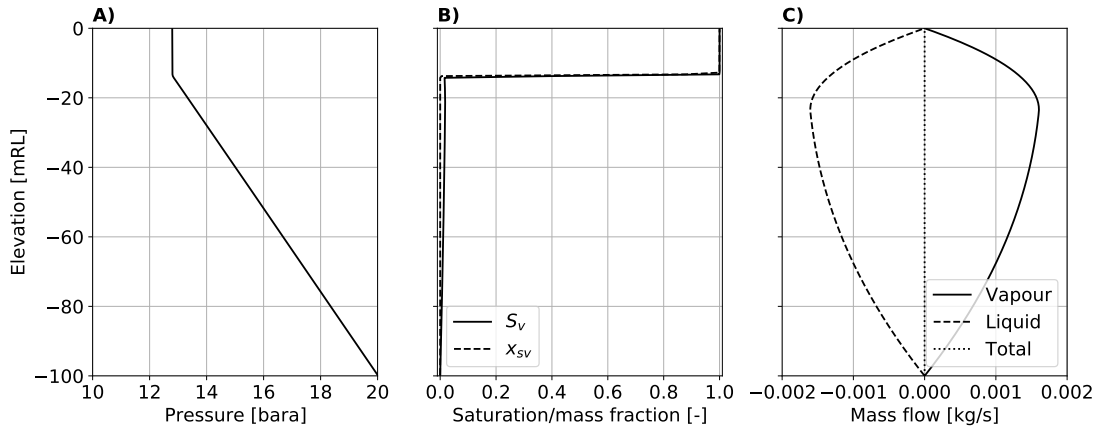


FIGURE 5.48: A) Pressure, B) static vapour mass fraction and saturation, and C) mass flow for Test Case 12 after 30 days of heating up.

## 5.4 Summary

This chapter discusses the testing of our transient geothermal wellbore simulator. First, we derived analytical solutions to the governing conservation equations for simplified flow scenarios. We tested the output of our simulator against these analytical cases to ensure the numerical method described in Chapter 4 was implemented correctly in the code. These cases also ensured that key terms such as gravity, formation heat flux and reservoir sources were acting in the correct direction.

Next, simulation results were compared to steady-state pressure and temperature data from flowing geothermal wells. Our ability to reproduce the data varied between cases.

Cases in which there was uncertainty in both the conceptual model and test conditions proved difficult to match. Additionally, cases with a significant amount of salt or CO<sub>2</sub> showed worse fits to temperature data due to the effect that these components have on the properties of the fluid mixture (e.g., density, enthalpy and the saturation relationship). Given these considerations, we were satisfied with our simulators ability to represent production cases in geothermal wells.

Finally, in Section 5.3, we presented a set of 12 test cases used in this work. These test cases were developed to verify that our simulator could model the wide range of flows scenarios that occur in geothermal wells. Three additional test cases, which target specific down-flow scenarios, are discussed in Appendix C.

These 15 test cases verify that our simulator can model:

- production and injection scenarios,
- flashing and condensing processes,
- cases with slow transient behaviour,
- cases with rapid transient behaviour (e.g., shutting in a flowing well),
- multiple feed-zones, each with very different thermodynamic properties, and
- counter-flow processes.

Of particular interest to us is the modelling of counter-flow due to boiling in geothermal wells. We demonstrated that our simulator can model this process in Section 5.3.4. In Section 8.1, we discuss examples of counter-flow in more detail and highlight why counter-flow is an important process that must be modelled when simulating the behaviour of geothermal wells.

The test cases presented in Section 5.3 were also used to troubleshoot issues with early versions of our simulator. These investigations are discussed in the following chapter.

These test cases do not include scenarios where the water level is below the wellhead. A simulator capable of modelling mixtures of water and NCGs is required to model these

cases. We discuss the extension of our simulator to model air-water mixtures in Chapter 7 and provide examples of cases with water levels below the wellhead in Chapter 8.

## Chapter 6

# Further investigations of the numerical implementation of our transient geothermal wellbore simulator

Chapter 4 presented the numerical implementation used in our simulator. However, as is the case with any simulator, the final numerical implementation is the product of successive refinement. This chapter discusses some of the interesting decisions we made about the numerical implementation during the research project discussed in this thesis. Section 6.1 discusses how the choice of different primary variables affects the numerical performance of our simulator. Section 6.2 discusses issues that we faced when calculating the drift velocity for cases with counter-flow and the solution we found to these problems. Finally, Section 6.3 discusses smaller changes relating to the upstream weighting methods that improved the numerical performance of our simulator.

### 6.1 Primary variable selection

In Section 4.4 we introduced the concept of primary variables. As discussed there, we use pressure, temperature (swapped for vapour saturation), vapour velocity and liquid

TABLE 6.1: Combinations of primary variables tested in this work.

Velocity formulation	$P$	$T(S_v)$	$u_v$	$u_l$
Volume flux formulation	$P$	$T(S_v)$	$F_{Vv}$	$F_{Vl}$
Mixed formulation	$P$	$T(S_v)$	$u_v$	$F_{Vl}$

volume flux as primary variables in our simulator. This combination of primary variables was chosen based on the investigation presented in this section, which was carried out after we experienced convergence issues for cases with high vapour saturation when using the velocity formulation. Given these issues, we tried the volume flux formulation. This showed better performance for high vapour saturation cases but worse performance for low vapour saturation cases. Finally, a mixed formulation was tested, which used the vapour velocity and the liquid volume flux as primary variables. This combination resulted in good numerical performance for all of the test cases.

In this section, we discuss why the different combinations of primary variables, summarised in Table 6.1, perform differently. Before doing this, we present the differences in the numerical formulation of the secondary variables and the formulation of the drift-flux model for each combination of primary variables.

We use Test Cases 1 – 8, which are described in Sections 5.3.1 and 5.3.2, to compare the numerical performance of the three implementations. In Section 6.1.4 we compare the results of this comparison and discuss why different combinations of primary variables perform well for different cases.

### 6.1.1 Velocity formulation

The velocity formulation calculates the vapour and liquid velocities,  $[u_v]_{i+1/2}^{n+1}$  and  $[u_l]_{i+1/2}^{n+1}$ , as primary variables. When these variables are used, the volume flux of each phase is calculated from the velocity using:

$$[F_{V\beta}]_{i+1/2}^{n+1} = [S_\beta]_{i+1/2}^{n+1} [u_\beta]_{i+1/2}^{n+1}, \quad (6.1)$$

where the interface saturation,  $[S_\beta]_{i+1/2}^{n+1}$ , is upwinded as defined in (4.15).



The average velocity of a phase in block  $i$  is the average of the interface velocities and is calculated as:

$$[u_\beta]_i^{n+1} = \frac{1}{2} \left( [u_\beta]_{i+1/2}^{n+1} + [u_\beta]_{i-1/2}^{n+1} \right). \quad (6.2)$$

This allows the average mass flux, used in the energy conservation equation, to be calculated as:

$$[F_{m\beta}]_i^{n+1} = [\rho_\beta S_\beta]_i^{n+1} [u_\beta]_i^{n+1}. \quad (6.3)$$

In the velocity formulation, the drift-flux constitutive model is implemented differently depending on the average interface vapour saturation. When  $[S_v^{ave}]_{i+1/2}^{n+1} \leq 0.8$ , we solve the following version of the drift-flux equation for the vapour velocity:

$$[u_v]_{i+1/2}^{n+1} - [S_v u_v + S_l u_l]_{i+1/2}^{n+1} - [u_d^{ave}]_{i+1/2}^{n+1} = 0, \quad (6.4)$$

Here, we have made the simplification  $[C_0]_{i+1/2}^{n+1} = 1$ . The drift velocity,  $[u_d^{ave}]_{i+1/2}^{n+1}$ , is formulated as:

$$[u_d^{ave}]_{i+1/2}^{n+1} = \frac{(1 - [S_v^{ave}]_{i+1/2}^{n+1})[C_0 K_u]([S_v^{ave}]_{i+1/2}^{n+1})m([\theta]_{i+1/2})}{[S_v^{ave}]_{i+1/2}^{n+1}([\rho_v^{ave}]_{i+1/2}^{n+1}/[\rho_l^{ave}]_{i+1/2}^{n+1})^{0.5} + 1 - [S_v^{ave}]_{i+1/2}^{n+1}} [u_c]_{i+1/2}^{n+1}, \quad (6.5)$$

where an averaged interface variable is defined as  $[\varphi^{ave}]_{i+1/2} = ([\varphi]_i + [\varphi]_{i+1})/2$ . This formulation of  $u_d$  is what was used when our experiments with the choice of primary variables were undertaken. However, it differs from what is currently used in our simulator. This is discussed further in Section 6.2 below.

When  $[S_v^{ave}]_{i+1/2}^{n+1} > 0.8$ , we solve the drift-flux equation for the liquid velocity (3.11) (assuming  $[C_0]_{i+1/2}^{n+1} = 1$ ), which is defined as:

$$[u_l]_{i+1/2}^{n+1} - [S_v u_v + S_l u_l]_{i+1/2}^{n+1} + \frac{[S_v]_{i+1/2}^{n+1}}{1 - [S_v]_{i+1/2}^{n+1}} [u_d^{ave}]_{i+1/2}^{n+1} = 0. \quad (6.6)$$

Again, we have made the assumption that  $[C_0]_{i+1/2}^{n+1} = 1$  and  $[u_d^{ave}]_{i+1/2}^{n+1}$  is defined in (6.5).

This equation switch is made because (6.4) results in a nearly singular Jacobian matrix when the vapour saturation approaches one. This problem is discussed further in Section

6.1.4. By experimentation, we found that the saturation at which this switch was made did not influence the numerical performance of the simulator significantly (provided that this switch was completed before vapour saturation became close to one). Therefore, we chose to switch these equations when the vapour saturation was equal to 0.8.

Although (6.6) does not result in a singular Jacobian when  $[S_v]_{i+1/2}^{n+1} \approx 1$ , it suffers from errors associated with division by small numbers. To prevent this issue, we solve:

$$[u_l]_{i+1/2}^{n+1} - \frac{1 - [S_v]_{i+1/2}^{n+1}}{1 - S_v^{max}} [S_v u_v + S_l u_l]_{i+1/2}^{n+1} + \frac{[S_v]_{i+1/2}^{n+1}}{1 - S_v^{max}} [u_d]_{i+1/2}^{n+1} = 0, \quad (6.7)$$

where  $S_v^{max} = 0.9999$ , for cases in which  $[S_v]_{i+1/2}^{n+1} \geq 0.9999$ . Equation (6.7) is also used by T2WELL to prevent errors associated with division by small numbers when calculating the liquid velocity as a secondary variable using (3.16).

Equation (6.7) was used rather than multiplying (6.6) through by  $(1 - [S_v]_{i+1/2}^{n+1})$  because this multiplication would mean that all of the terms in (6.6) would tend towards zero as the vapour saturation tended towards 1. This would result in a nearly singular Jacobian (i.e., the same issue as with (6.4)).

When  $[S_v]_{i+1/2}^{n+1} = 1$ , we switched out the drift flux relationship and solved:

$$[u_l]_{i+1/2}^{n+1} = 0. \quad (6.8)$$

Similarly, for cases where  $[S_v]_{i+1/2}^{n+1} = 0$ , we solved:

$$[u_v]_{i+1/2}^{n+1} = 0. \quad (6.9)$$

This equation switching ensured that the velocity of the non-present phase was zero.

### 6.1.2 Volume flux formulation

The volume flux formulation calculates the liquid and vapour volume fluxes,  $[F_{Vv}]_{i+1/2}^{n+1}$  and  $[F_{Vl}]_{i+1/2}^{n+1}$ , as primary variables. The velocity of a phase is calculated as a secondary

variable, and is defined by:

$$[u_\beta]_{i+1/2}^{n+1} = \begin{cases} [F_{V\beta}]_{i+1/2}^{n+1}/[S_\beta]_{i+1/2}^{n+1} & , [S_\beta]_{i+1/2}^{n+1} \neq 0 \\ 0 & , [S_\beta]_{i+1/2}^{n+1} = 0 \end{cases}. \quad (6.10)$$

The average volume flux at the block centre is the average of the interface fluxes, such that:

$$[F_{V\beta}]_i^{n+1} = \frac{1}{2} \left( [F_{V\beta}]_{i+1/2}^{n+1} + [F_{V\beta}]_{i-1/2}^{n+1} \right). \quad (6.11)$$

The average volume flux in block  $i$  is then used to calculate the mass flux of phase in  $i$  as:

$$[F_{m\beta}]_i^{n+1} = [\rho_\beta]_i^{n+1} [F_{V\beta}]_i^{n+1}, \quad (6.12)$$

and the velocity of a phase in block  $i$  as:

$$[u_\beta]_i^{n+1} = \begin{cases} [F_{V\beta}]_i^{n+1}/[S_\beta]_i^{n+1} & , [S_\beta]_i^{n+1} \neq 0 \\ 0 & , [S_\beta]_i^{n+1} = 0 \end{cases}. \quad (6.13)$$

Formulating (6.4) in terms of the phase volume fluxes, using (6.13), gives:

$$[u_v]_{i+1/2}^{n+1} - [F_{Vv} + F_{Vl}]_{i+1/2}^{n+1} - [u_d^{ave}]_{i+1/2}^{n+1} = 0, \quad (6.14)$$

where  $[u_v]_{i+1/2}^{n+1}$  is calculated from the vapour volume flux using (6.10).

When  $[S_v]_{i+1/2}^{n+1} = 1$ , we switched out the drift flux relationship and solved:

$$[F_{Vl}]_{i+1/2}^{n+1} = 0. \quad (6.15)$$

Similarly, for cases where  $[S_v]_{i+1/2}^{n+1} = 0$ , we solved:

$$[F_{Vv}]_{i+1/2}^{n+1} = 0. \quad (6.16)$$

This equation switching ensured the volume-flux of the non-present phase was zero.

### 6.1.3 Mixed formulation

The mixed formulation uses  $[u_v]_{i+1/2}^{n+1}$  and  $[F_{Vl}]_{i+1/2}^{n+1}$  as primary variables and combines the two formulations described above. The secondary variables for the vapour phase are calculated from  $[u_v]_{i+1/2}^{n+1}$  using the procedure outlined in Section 6.1.1. The secondary variables for the liquid phase are calculated from  $[F_{Vl}]_{i+1/2}^{n+1}$  using the procedure outlined in Section 6.1.2.

Finally, the slip equation is formulated in terms of the mixed primary variables as:

$$[u_v]_{i+1/2}^{n+1} - [F_{Vl}]_{i+1/2}^{n+1} - [S_v u_v]_{i+1/2}^{n+1} - [u_d^{ave}]_{i+1/2}^{n+1} = 0. \quad (6.17)$$

When  $[S_v]_{i+1/2}^{n+1} = 1$ , we switched out the drift flux relationship and solved:

$$[F_{Vl}]_{i+1/2}^{n+1} = 0. \quad (6.18)$$

Similarly, for cases where  $[S_v]_{i+1/2}^{n+1} = 0$ , we solved:

$$[u_v]_{i+1/2}^{n+1} = 0, \quad (6.19)$$

instead of the drift flux equation. This equation switching ensured the flow of the non-present phase was zero.

Note that this equation switching was dropped shortly after completing the primary variable investigation discussed in this section. This is because switching these equations hindered the numerical performance of the simulator and is not required when using the mixed formulation. This is discussed further in Section 6.3.1 below.

### 6.1.4 Results

The numerical performance of the three formulations is compared using three metrics. These are the total number of time steps, linear solves (Newton iterations), and equation of state (EOS) errors that occur during a simulation.

EOS errors include cases when the primary variables step outside of thermodynamic bounds (excluding phase transitions). Cases where both upstream weighted interface

saturations are zero ( $[S_v]_{i+1/2}^{n+1} = [S_l]_{i+1/2}^{n+1} = 0$ ), which can occur when a vapour block is directly adjacent to a liquid block or when non-physical flow scenarios occur (e.g., vapour down-flow and liquid up-flow), are also included as EOS errors. Our simulator does not allow cases where liquid and vapour conditions exist in adjacent blocks as it was unclear how to correctly handle the drift flux model and the upwinding direction in these cases (especially when forcing the non-present phase velocities to be zero). Instead, the time step is automatically dropped until two-phase conditions develop between the liquid and vapour zones. Thus far, we have always found there to be at least one two-phase block between the liquid and vapour zones, even when simulating air caps above cold columns of water, where the possibility of liquid and vapour blocks existing next to one another seems most likely.

Figures 6.1 A) and 6.1 B) show that the velocity formulation performs significantly better than the volume flux formulation for Test Cases 1 – 4. The performance of the mixed formulation is slightly better than the velocity formulation. Figure 6.1 C) shows the number of EOS errors are similar for all formulations.

Test Case 1, described in Section 5.3.1.1, shows the greatest difference between methods. The volume flux method takes 567 time steps and 1938 linear solves compared to 177 time steps and 288 linear solves taken by the mixed method. The test cases indicated that slow convergence was occurring when one or more blocks are transitioning from liquid to two-phase conditions. This is a surprising result, because the very slow flashing process that occurs in Test Case 1 makes it the simplest of the four cases.

Figure 6.1 D) shows the poor numerical performance of the volume flux formulation for Test Case 1 by comparing the time stepping of the three formulations. During the volume flux simulation, the time step drops every time a block flashes. By comparison, the time step does not drop when the velocity or mixed formulations are used.

Figures 6.2 A) and 6.2 B) show the total number of time steps and linear solves taken for Test Cases 5 – 8. They indicate that the volume flux formulation performs significantly better than the velocity formulation for cases with transitions between two-phase and vapour conditions (i.e., for cases with high vapour saturation). In all cases, the volume flux formulation requires fewer time steps and fewer linear solves. The performance of

TABLE 6.2: Results of Test Cases 1 – 4 for the velocity, volume flux and mixed formulations.

	Mixed			Velocity			Volume Flux		
	Steps	Solves	Err.	Steps	Solves	Err.	Steps	Solves	Err.
Test Case 1	177	288	0	177	293	0	567	1938	0
Test Case 2	222	475	5	224	483	5	289	885	1
Test Case 3	220	422	14	231	455	16	250	554	14
Test Case 4	239	795	3	248	837	3	510	1999	2

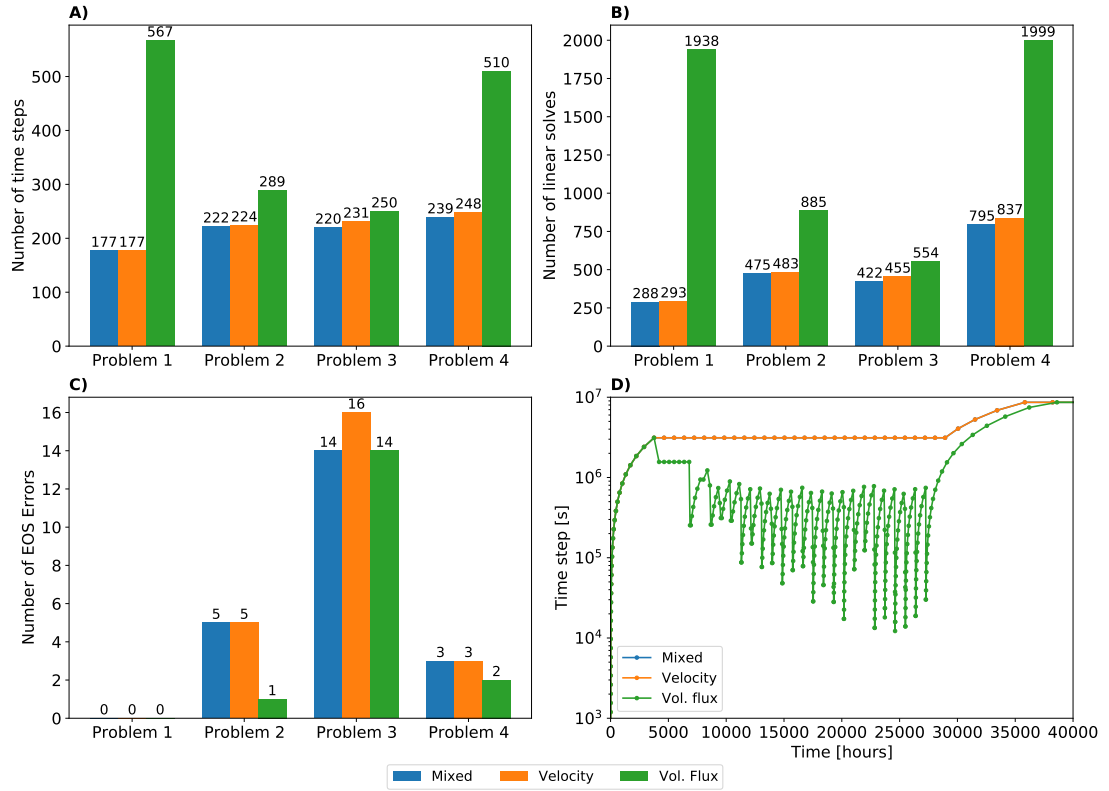


FIGURE 6.1: Comparisons of the total number of A) time steps, B) linear solves and C) EOS errors for Test Cases 1 – 4 for the velocity, volume flux and mixed formulations. Plot D) compares the time stepping for Test Case 1.

TABLE 6.3: Results of Test Cases 5 – 8 for the velocity, volume flux and mixed formulations. The \* indicates that the simulation was stopped prior to completion.

	Mixed			Velocity			Volume Flux		
	Steps	Solves	Err.	Steps	Solves	Err.	Steps	Solves	Err.
Test Case 6	135	286	8	228	628	21	135	286	8
Test Case 5	63	123	0	1156	3895	48	63	123	0
Test Case 7	64	125	0	945	3132	61	64	125	0
Test Case 8	83	184	4	5800*	33919	9	83	184	4

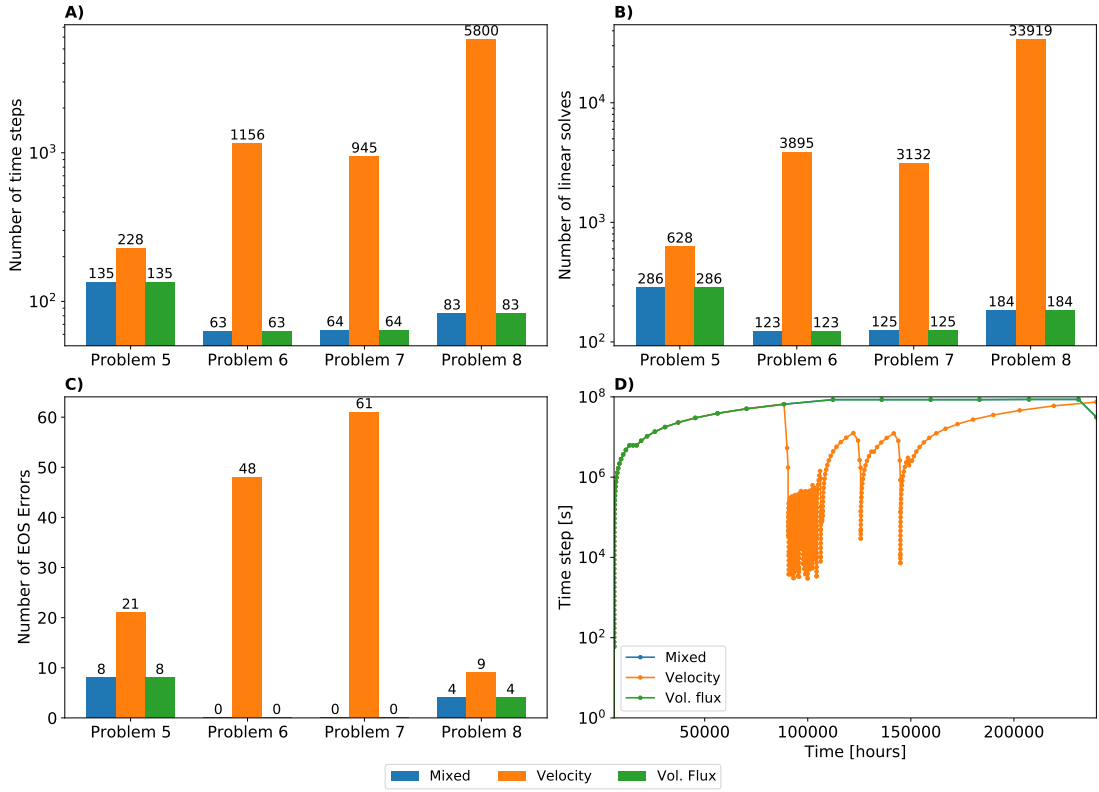


FIGURE 6.2: Comparisons of the total number of A) time steps, B) linear solves and C) EOS errors for Test Cases 5 – 8 for the velocity, volume flux and mixed formulations. Plot D) compares the time stepping for Test Case 7.

the mixed formulation is identical to that of the volume flux formulation. It is also interesting to note that for Test Cases 6 and 7, the number of EOS errors that occur when using the velocity formulation is much higher than when the other formulations are used. This indicates that the solution (the primary variables) is frequently stepping outside the thermodynamic bounds of the equation of state. We found that this was because of large, erroneous steps in the primary variables. These steps are calculated using the Jacobian (see the description of the Newton Raphson method in Section 4.6), which is a matrix comprised of derivatives that describe how the discrete conservation equations change with respect to the primary variables. These inaccurate steps suggest that some of the gradients (i.e., some of the elements in the Jacobian matrix), which we estimate using finite differences, may be inaccurate.

The poor performance of the velocity formulation is highlighted by the time stepping comparison for Test Case 7 given in Figure 6.2 D). Here, the time step is reduced every time a block condenses from vapour to two-phase conditions when using the velocity

formulation. By comparison, the volume flux and mixed formulations allow the entire bottom section of the well to condense in a single time step for this problem.

The worst performance of the velocity formulation is for Test Case 8. Here, the simulation was stopped after 5800 time steps. At this point, it had completed over 33,900 linear solves but was less than half complete. By comparison, the volume flux and mixed formulations required only 83 time steps and 184 linear solves. This poor performance makes the velocity formulation unusable for this case.

### 6.1.5 Discussion

The results presented above indicate that the velocity formulation showed satisfactory numerical performance for Cases 1 – 4 (with liquid/two-phase transitions) and unsatisfactory performance for Cases 5 – 8 (with vapour/two-phase transitions). The volume flux formulation performed well for Cases 5 – 8 but worse than the velocity formulation for Cases 1 – 4. The mixed formulation performed well for all cases. The differences in numerical performance for each method can be explained by considering the derivatives of the constitutive slip equation with respect to the primary variables used in each formulation. As discussed in Section 4.6, these derivatives are some of the components of the Jacobian matrix, which is used in the Newton-Raphson method to update the primary variables and drive the residuals towards zero.

First we consider the gradients of the drift flux relationship for the velocity formulation. The derivatives of (6.4), with respect to the vapour and liquid velocities are:

$$\frac{\partial}{\partial u_v} (u_v - (S_v u_v + S_l u_l) - u_d) = 1 - S_v - \frac{\partial u_d}{\partial u_v}, \quad (6.20)$$

and

$$\frac{\partial}{\partial u_l} (u_v - (S_v u_v + S_l u_l) - u_d) = -S_l - \frac{\partial u_d}{\partial u_l}. \quad (6.21)$$

In our case,  $\partial u_d / \partial u_l$  and  $\partial u_d / \partial u_v$  are zero as the equation for  $u_d$  by Shi et al. (2005) is a function of saturation and pressure when  $C_0 = 1$ .



When  $S_v \approx 1$ , it is clear from (6.20) and (6.21) that:

$$\frac{\partial}{\partial u_v} (u_v - (S_v u_v + S_l u_l) - u_d) = 1 - S_v \approx 0, \quad (6.22)$$

and

$$\frac{\partial}{\partial u_l} (u_v - (S_v u_v + S_l u_l) - u_d) = -S_l = S_v - 1 \approx 0. \quad (6.23)$$

These near-zero gradients result in a nearly singular Jacobian, which causes inaccurate primary variable updates and, ultimately, the failure of the simulation. This is the reason that (6.4) must be switched with (6.6) for high saturation cases when using the velocity formulation.

By comparison, the gradients of (6.6) with respect to the phase velocities when  $S_v \approx 1$  are:

$$\frac{\partial}{\partial u_v} \left( u_l - (S_v u_v + S_l u_l) + \frac{S_v}{1 - S_v} u_d \right) = -S_v + \frac{S_v}{1 - S_v} \frac{\partial u_d}{\partial u_v} \approx -1, \quad (6.24)$$

and the derivative with respect to liquid velocity is:

$$\frac{\partial}{\partial u_l} \left( u_l - (S_v u_v + S_l u_l) + \frac{S_v}{1 - S_v} u_d \right) = 1 - S_l + \frac{S_v}{1 - S_v} \frac{\partial u_d}{\partial u_l} \approx 1. \quad (6.25)$$

These gradients are non-zero and do not result in a singular Jacobian. However, the velocity implementation still shows poor numerical performance for Test Cases 5 – 8. The gradient of (6.6) with respect to vapour saturation is:

$$\frac{\partial}{\partial S_v} \left( u_l - (S_l u_l + S_v u_v) + \frac{S_v}{1 - S_v} u_d \right) = u_l - u_v + \frac{u_d}{(1 - S_v)^2} + \frac{S_v}{1 - S_v} \frac{\partial u_d}{\partial S_v}. \quad (6.26)$$

As  $(1 - S_v) \lesssim 1E-6$  when transitioning between two-phase and pure vapour, the gradient given by (6.26) is very large compared to the magnitude of (6.6), which can result in inaccurate primary variable updates and poor convergence. Limiting the size of  $S_v$  in the denominator, as is done in (6.7), reduces but does not prevent this problem.

When the vapour saturation is low (as occurs in Cases 1 – 4), the gradients given by (6.20) and (6.21) are non-zero and (6.26) has a similar order of magnitude to (6.6).

As a result, the velocity formulation has satisfactory numerical performance for these problems.

Similarly, the poor numerical performance shown by the volume flux formulation for Test Cases 1 – 4 can be explained by considering the gradient of (6.14) with respect to  $F_{Vv}$  and  $S_v$ . These derivatives are:

$$\frac{\partial}{\partial F_{Vv}} \left( \frac{F_{Vv}}{S_v} - (F_{Vv} + F_{Vl}) - u_d \right) = \frac{1}{S_v} - 1 - \frac{\partial u_d}{\partial F_{Vv}}, \quad (6.27)$$

where  $\partial u_d / \partial F_{Vv}$  is zero, and:

$$\frac{\partial}{\partial S_v} \left( \frac{F_{Vv}}{S_v} - (F_{Vv} + F_{Vl}) - u_d \right) = \frac{F_{Vv}}{S_v^2} - \frac{\partial u_d}{\partial S_v}. \quad (6.28)$$

For cases with low vapour saturation, i.e., when  $S_v \approx 0$ , both (6.27) and (6.28) are large compared to the magnitude of (6.4). This means small changes in the vapour volume flux or the vapour saturation result in large changes in the residual equation, which can result in inaccurate updates of the primary variables and poor numerical performance. This explains why Test Case 1 has the worst numerical performances out of Cases 1 – 4 for the volume flux formulation, as each block spends a greater length of time with a low vapour saturation due to the slow evolution of flashing in this problem.

The mixed formulation shows good performance regardless of whether vapour saturation is low or high. This is because the mixed formulation avoids the issues with the gradients discussed above. For example, the gradients with respect to  $u_v$ ,  $F_{Vl}$  and  $S_v$  are:

$$\frac{\partial}{\partial u_v} (u_v - F_{Vl} - S_v u_v - u_d) = u_v - S_v, \quad (6.29)$$

$$\frac{\partial}{\partial F_{Vl}} (u_v - F_{Vl} - S_v u_v - u_d) = -1, \quad (6.30)$$

and

$$\frac{\partial}{\partial S_v} (u_v - F_{Vl} - S_v u_v - u_d) = -u_v - \frac{\partial u_d}{\partial S_v}, \quad (6.31)$$

respectively.

Thus, our investigation showed that the mixed formulation ( $P$ ,  $T(S_v)$ ,  $u_v$  and  $F_{Vl}$ ) is the

best choice of primary variables of those we tested. The poor numerical performance of the velocity and volume flux formulations was explained by considering the approximate gradients of the constitutive slip equation with respect to the primary variables when the vapour saturation is close to zero or one, which can occur during phase transitions.

The discussion above indicates that the formulation of the slip equation and the choice of primary variables can have a large impact on the performance of a geothermal wellbore simulator. The basic analysis presented above can be used to help guide the choice of primary variables when implementing different slip relationships. For example, if the relative velocity equation,  $u_r = u_v - u_l$ , is used to model slip, then the velocity formulation would be likely to perform well for all cases. By contrast, the volume flux formulation would be likely to perform worse than the velocity formulation at both high and low saturations. The mixed formulation would be likely to have similar performance to the velocity formulation for low vapour saturations and similar performance to the volume flux formulation for high vapour saturations.

## 6.2 Calculation of the drift velocity for counter-flow simulations

In Section 4.3.1, we presented the method used in our simulator to calculate the drift velocity, which was developed after early versions of our simulator struggled to model counter-flow. This method differs from early implementations of our simulator. Originally, the drift velocity on an interface,  $[u_d]_{i+1/2}^{n+1}$ , was calculated using average interface variables, such that:

$$[u_d^{ave}]_{i+1/2}^{n+1} = \frac{(1 - [S_v^{ave}]_{i+1/2}^{n+1})[C_0 K_u([S_v^{ave}]_{i+1/2}^{n+1})m([\theta]_{i+1/2})]}{[S_v^{ave}]_{i+1/2}^{n+1}([\rho_v^{ave}]_{i+1/2}^{n+1}/[\rho_l^{ave}]_{i+1/2}^{n+1})^{0.5} + 1 - [S_v^{ave}]_{i+1/2}^{n+1}}[u_c]_{i+1/2}^{n+1}, \quad (6.32)$$

where an averaged interface variable is defined as  $[\varphi^{ave}]_{i+1/2} = ([\varphi]_i + [\varphi]_{i+1})/2$ . Equation (6.32) differs from our current implementation in the treatment of the vapour saturation when calculating  $u_d$ . We discuss this further below.

The formulation given in (6.32) worked well for co-current production and injection cases. However, we had difficulty modelling counter-flow cases. For example, Test Case

11, which modelled counter-flow occurring below the deepest feed in a well, produced non-physical results and Test Case 12, which modelled the heat-up of a shut-in well, would stall when counter-flow processes began at the wellhead. Investigations showed that it was the use of the average vapour saturation,  $[S_v^{ave}]_{i+1/2}^{n+1}$ , in (6.32) which caused these problems.

In Sections 6.2.1 and 6.2.2 below, we discuss the problems faced when simulating Test Cases 11 and 12. For Test Case 11, we found that the drift velocity should be calculated using the saturation from the block below the interface,  $[S_v]_i^{n+1}$ . Test Case 12 required the drift velocity to be calculated using the vapour saturation from the block above the interface,  $[S_v]_{i+1}^{n+1}$ . Section 6.2.3 discusses the development of the drift velocity formulation presented in Section 4.3.1, which is a hybrid of these two formulations that works well for both problems.

### 6.2.1 Test Case 11: modelling counter-flow below feed-zones

Test Case 11 was the first example of counter-flow that we simulated. It models a well with a single high-enthalpy feed located approximately 200 m above the bottom of the well. In this case, conductive heat transfer from the formation causes boiling below the feed-zone. This boiling results in stable (steady-state) counter-flow in the section of the well between the bottomhole and the feed zone. Further discussion of the problem set-up and the simulation results are given in Section 5.3.4.1.

Initial simulations of this test case showed counter-flow processes in the bottom 200 m of the well. However, the results also showed a drop in vapour saturation in the block below the feed-zone. A mesh resolution study indicated that this phenomenon was confined to the mesh block immediately below the feed-zone regardless of the mesh resolution. This behaviour suggested that the drop in saturation was erroneous. Figure 6.3 compares these erroneous results to the more physical results simulated using the implementation described in Chapter 4 (which, for this case, uses the vapour saturation from block  $i$  rather than the average interface saturation when calculating the drift velocity).

Experimentation revealed that the erroneous saturation shown in Figure 6.3 was caused by using the average interface saturation when calculating the drift velocity. The flow

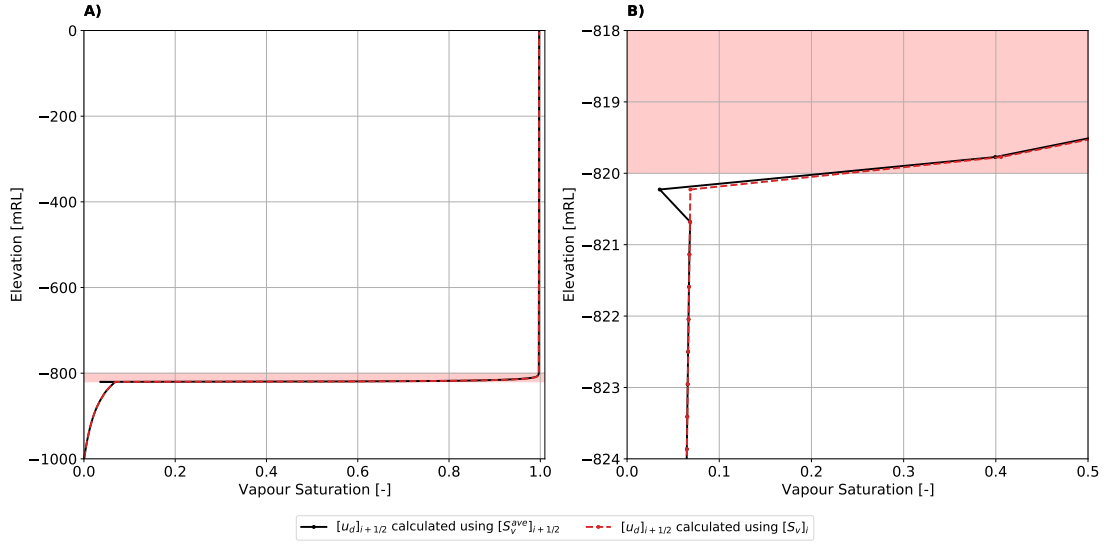


FIGURE 6.3: Comparisons of vapour saturation profiles for simulations using the average interface saturation and the upstream vapour saturation to calculate the drift velocity. Plot A) shows the entire well, while B) shows the subsection of the well where the erroneous saturation value occurs. The feed interval is highlighted in red.

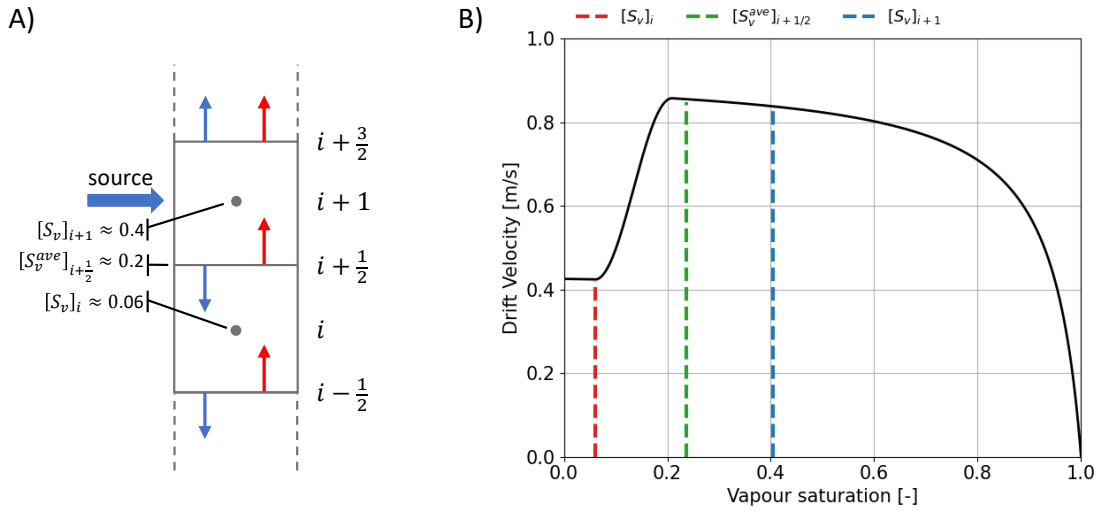


FIGURE 6.4: A) A diagrammatic representation of the flow scenario occurring for Test Case 11. B) The drift velocity calculated using the saturation from blocks  $i$  and  $i + 1$  and the average saturation at  $i + \frac{1}{2}$ .

scenario that occurs is shown diagrammatically in Figure 6.4 A). Here, the erroneous saturation occurs in block  $i$  when block  $i + 1$  is the beginning of the feed zone. In block  $i + 1$ , the flow transitions from counter-flow on the interface  $i + 1/2$  to co-current flow at  $i + 3/2$  due to the addition of high-enthalpy fluid at the feed. Figure 6.4 B) plots the drift velocity for the conditions at this point in the well. The drift velocities calculated using the saturations in block  $i$  and  $i + 1$  are shown by the red and blue lines. The green line indicates the drift velocity calculated using the averaged saturation on the interface.

Figure 6.4 indicates that the drift velocity calculated using the average saturation is approximately twice the value of  $u_d$  calculated with the vapour saturation from the block below (block  $i$ ). This larger drift velocity causes a larger vapour velocity to be calculated at  $i + 1/2$ . However, the mass flow rate of the vapour phase at  $i + 1/2$  does not increase as it is controlled by the boiling and counter-flow processes occurring below the feed. Therefore, the vapour saturation in block  $i$  must decrease to accommodate the increase in the vapour velocity at  $i + 1/2$ .

The more physically accurate solution, shown in red in Figure 6.3, results from using the saturation below the interface (block  $i$ ) rather than the average saturation at the interface  $i + 1/2$  when calculating the drift velocity. The smaller drift velocity, which is shown in red in Figure 6.4 B), results in a smaller vapour velocity. Consequently, there is no decrease in saturation, which results in a more physically accurate simulation.

We define the drift velocity calculated using  $[S_v]_i^{n+1}$  as:

$$[u_d^S]_{i+1/2}^{n+1} = \frac{(1 - [S_v]_i^{n+1})C_0K_u([S_v]_i^{n+1})m([\theta]_{i+1/2})}{[S_v]_i^{n+1}([\rho_v^{ave}]_{i+1/2}^{n+1}/[\rho_l^{ave}]_{i+1/2}^{n+1})^{0.5} + 1 - [S_v]_i^{n+1}}[u_c]_{i+1/2}^{n+1} \quad (6.33)$$

### 6.2.2 Test Case 12: heat up of a closed wellbore

Test Case 12 models the gradual heat up of a shut-in well. It was developed to test the counter-flow capabilities of our simulator and to study counter-flow processes in shut-in wells. The problem set-up is described in Section 5.3.4.2 and the results of this simulation are discussed in detail in Section 8.1.1. However, to provide context, we give a brief description of both below.

Test Case 12 simulates the heating up of a 100 m test well. The simulation begins with the well in a cold liquid state after two days of injection. After shutting the wellhead, the temperature of the liquid in the well begins to increase due to heat transfer from the reservoir. Boiling begins at the bottom of the well after approximately 21 hours. This results in counter-flow, where the liquid flows down the well as vapour flows up. The up-flow of vapour causes a net transfer of heat up the well. The boiling zone progresses up the well until it reaches the wellhead. Here, the vapour phase accumulates and forms a hot vapour cap. Note that this vapour cap is high-saturation two-phase fluid rather than pure water vapour. This must be the case in our simulator as it is a one-dimensional model and this means only one vapour mass flow rate is defined at each interface. Thus counter-flow, which transports heat to the top of the well, is only possible in two-phase flow. This heat transport process is discussed further in Section 8.1.1.

Early versions of the simulator modelled the progression of the boiling zone up the well and the counter-flow that occurred during this process. However, these early implementations of our simulator failed to capture the accumulation of the vapour phase and the growth of the gas cap that occurs once boiling begins at the wellhead. We found that the reason for this problem was the procedure for calculating the drift velocity. Specifically, it was the use of (6.32), which used the average interface saturation  $[S_v^{ave}]_{i+1/2}$  to calculate  $[u_d]_{i+1/2}$ . When this formulation was used, the simulation would repeatedly transition the top block of the numerical model between two-phase and vapour conditions. The reasons for this are discussed below.

When boiling begins in the wellhead block (block  $M$  in Figure 6.5 A)), vapour cannot flow any further and begins to accumulate, while the liquid phase flows down the well from block  $M$  into block  $M - 1$ . Vapour saturation increases in block  $M$  and the block begins to dry out. However, the vapour saturation in block  $M - 1$  does not increase because there is liquid down-flow from above, which is shown diagrammatically in Figure 6.5 A). As a result, the drift velocity, which depends strongly on saturation, differs significantly depending on whether the vapour saturation from  $M$ ,  $M - 1/2$  or  $M - 1$  is used in this calculation. This is shown in Figure 6.5 B), which plots drift velocity against vapour saturation.

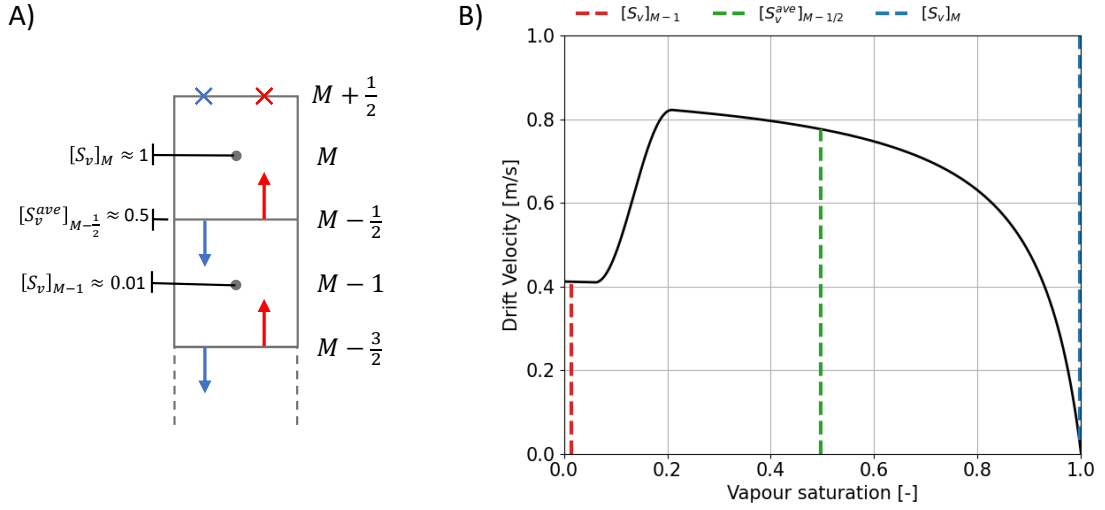


FIGURE 6.5: A) A diagrammatic representation of the flow scenario occurring for Test Case 12. B) The drift velocity calculated using the saturation from blocks  $M - 1$  and  $M$  and the average saturation at  $M - 1/2$ .

As noted above, the early implementation of our simulator used  $[S_v^{ave}]_{i+1/2}$  to calculate the drift velocity. Figure 6.5 B) shows that for this case (green dashes), the drift velocity has a value of approximately 0.8 m/s. This high drift velocity prevents the saturation in block  $M - 1$  from increasing because if the vapour saturation in this block were to increase, the vapour mass flux (and the energy flux) flowing up from block  $M - 1$  into  $M$  would also increase as  $F_{mv} = S_v \rho_v u_v$ . This would push block  $M$  further towards pure vapour conditions. However, as noted above, the block cannot transition to vapour as this stops the energy transport process that drives the development of the gas cap. Therefore, for the saturation in block  $M - 1$  to increase, the vapour velocity at  $M - 1/2$  must decrease to prevent an increase in mass and energy flux into block  $M$ . For this to occur, the drift velocity must decrease. However, Figure 6.5 B) shows that for this to happen, the average vapour saturation, and therefore the saturation in  $M - 1$ , must increase. As explained above, this cannot happen because it forces the top block to transition to vapour. This explains the phase switching behaviour observed in the unsuccessful simulations.

Instead, we found that for this case, the drift velocity at  $M - 1/2$  must be calculated using the saturation from block  $M$ , i.e., the block in which the vapour is accumulating. As block  $M$  dries out, the drift velocity will decrease as  $[S_v]_M$  increases towards one. This allows the vapour velocity at  $M - 1/2$  to decrease and the saturation in block  $M - 1$



to increase without causing a large increase in the mass and energy flux up into the top block. Block  $M - 1$  is, therefore, able to dry out, and the gas cap can grow until equilibrium conditions in the well are reached. As block  $M - 1$  dries out, the drift velocity on the interface  $M - 3/2$  must be calculated using  $[S_v]_{M-1}$ .

We define the drift velocity calculated using  $[S_v]_{i+1}^{n+1}$  on the interface  $i + 1/2$  as:

$$[u_d^N]_{i+1/2}^{n+1} = \frac{(1 - [S_v]_{i+1}^{n+1})C_0K_u([S_v]_{i+1}^{n+1})m([\theta]_{i+1/2})}{[S_v]_{i+1}^{n+1}([\rho_v^{ave}]_{i+1/2}^{n+1}/[\rho_l^{ave}]_{i+1/2}^{n+1})^{0.5} + 1 - [S_v]_{i+1}^{n+1}}[u_c]_{i+1/2}^{n+1} \quad (6.34)$$

### 6.2.3 Discussion of solution

The sections above discuss two counter-flow simulations in which the numerical formulation of the drift velocity equation is important. For Test Case 11, we found that non-physical simulation results occurred when the average saturation was used to calculate the drift velocity on the interface. More physically accurate results were achieved when the saturation from the block below the interface,  $[S_v]_i^{n+1}$ , was used to calculate the drift velocity. We defined this drift velocity as  $[u_d^S]_{i+1/2}^{n+1}$  in (6.33). For Test Case 12, we found that our simulator failed to capture the accumulation of vapour at the wellhead when the average saturation (or the saturation from the block below) was used when calculating the drift velocity. Instead, for this case, we found that the saturation from the block above an interface,  $[S_v]_{i+1}^{n+1}$ , should be used to calculate the drift velocity. We defined this drift velocity as  $[u_d^N]_{i+1/2}^{n+1}$  in (6.34).

In counter-flow cases, it seems equally valid to use the saturation from either  $i$  or  $i + 1$  when calculating  $u_d$  as, during counter-flow, the upwinded vapour properties are taken from  $i$  and the upwinded liquid properties are taken from  $i + 1$ . Therefore, the method that we use to calculate the drift velocity in our simulator is a hybrid of  $[u_d^S]_{i+1/2}^{n+1}$  and  $[u_d^N]_{i+1/2}^{n+1}$ . To do this, we define the smooth transition parameter  $[U_{slip}]_{i+1/2}^{n+1}$  as:

$$[U_{slip}]_{i+1/2}^{n+1} = \begin{cases} 0 & [S_v^{ave}]_{i+1/2}^{n+1} \leq b_1 \\ \frac{1}{2} \left[ 1 - \cos \left( \pi \frac{[S_v^{ave}]_{i+1/2}^{n+1} - b_1}{b_2 - b_1} \right) \right] & b_1 \leq [S_v^{ave}]_{i+1/2}^{n+1} \leq b_2, \\ 1 & [S_v^{ave}]_{i+1/2}^{n+1} \geq b_2 \end{cases} \quad (6.35)$$

and calculate the final drift velocity as:

$$[u_d]_{i+1/2}^{n+1} = \left(1 - [U_{slip}]_{i+1/2}^{n+1}\right) [u_d^S]_{i+1/2}^{n+1} + [U_{slip}]_{i+1/2}^{n+1} [u_d^N]_{i+1/2}^{n+1}. \quad (6.36)$$

Here,  $[U_{slip}]_{i+1/2}^{n+1}$  transitions between 0 and 1 depending on the value of the average vapour saturation on the interface ( $[S_v^{ave}]_{i+1/2}^{n+1}$ ) over the range defined by  $b_1$  and  $b_2$ . This smoothly transitions the drift velocity between  $[u_d^S]_{i+1/2}^{n+1}$  when the average interface saturation is low and  $[u_d^N]_{i+1/2}^{n+1}$  when the average interface saturation is high. The values of  $b_1$  and  $b_2$  were chosen as 0.3 and 0.4, respectively. Experimentation indicated that these values resulted in good numerical performance and physically realistic simulation results for Test Cases 11 and 12 presented above. The method also produces physically accurate results for the other cases in this thesis that demonstrate counter-flow. For example, see the results presented in Chapter 8.

## 6.3 Improving the numerical performance of our simulator for low mass flow cases

In this section, we discuss three changes that we made to the numerical formulation of our simulator to improve numerical performance. In Section 6.3.1, we discuss why we always solve the drift flux relationship (regardless of the phase-state of the fluid). In Section 6.3.2, we discuss how we determine the upwinding direction for cases with no-flow, and in Section 6.3.3 we discuss how we improved the performance of the discrete upstream weighting method for low mass flow cases.

### 6.3.1 Calculating the velocity of the non-present phase

Our simulator solves the constitutive model for slip by Shi et al. (2005) regardless of the phase state of the fluid. This differs from early versions of our simulator, which forced the velocity (or volume flux) of a non-present phase to equal zero. For example, if pure liquid was flowing in the well, we would solve  $u_v = 0$  as the fourth equation rather than the slip equation. Similarly, for pure vapour flows, we would solve  $F_{Vl} = 0$  as the fourth equation.

While this equation switching is simple and intuitive when the entire well is pure liquid or vapour, it becomes more complex when there are interfaces between two-phase and single phase zones within the well (for example, see Test Cases 1 – 8). We determined whether a phase was flowing through an interface using the upstream weighted saturation. When the upstream weighted saturation of a phase was zero, then the phase was deemed to not be flowing through the interface. The velocity of the non-flowing phase was, therefore, set to zero by switching the fourth equation.

This method worked well in most cases, however, we found that switching equations (and forcing the velocity of a phase to equal zero) could cause the flow direction and, therefore, the upwinding direction, of the non-present phase to switch after successive Newton iterations. Switching the upwinding direction changes the values of the upstream weighted variables, which causes poor or failed convergence. This behaviour was partially due to the poor selection of the upstream weighting direction for cases with zero flow. We discuss this further in the following section.

Instead, we found it was better to solve the drift-flux equation regardless of the phase state of the flow. This was made possible by our choice of primary variables. For the mixed primary variables, the drift flux relationship is well defined for the limiting cases where  $S_v = 0$  and  $S_v = 1$ .

For the flow of pure steam (when  $S_v = 1$ ), our constitutive model for slip states that:

$$u_v = F_{Vl} + u_v + u_d. \quad (6.37)$$

For the drift flux model by Shi et al. (2005),  $u_d = 0$  when  $S_v = 1$ . Therefore, (6.37) implies that  $F_{Vl} = 0$  when  $S_v = 1$ . This makes physical sense given the definition of the liquid volume flux ( $F_{Vl} = S_l u_l = (1 - S_v)u_l$ ). The liquid velocity is calculated as a secondary variable and is set to zero when  $F_{Vl}$  equals zero.

For liquid flow (when  $S_v = 0$ ), the constitutive model for slip states that:

$$u_v = F_{Vl} + u_d, \quad (6.38)$$

where  $u_d \neq 0$ . Therefore, solving (6.38) when  $S_v = 0$  will result in a non-zero vapour velocity, despite vapour not being present in the flow. While this is slightly non-physical, it does not affect the results of our simulation. This is because the vapour velocity is always weighted by vapour saturation when it appears in the governing conservation equations. As  $S_v = 0$ , a non-zero vapour velocity will have no effect on the conservation of mass, momentum and energy in this case. In fact, this non-zero vapour velocity is beneficial because it provides an estimate of the correct upwinding direction for the vapour phase when the flow flashes to two-phase conditions. This is discussed in the following section.

### 6.3.2 Upstream weighting bias

Discrete upstream weighting requires an upwinding direction to be specified when the velocity (or volume flux) of a phase is zero. This means that there is a preferential upwinding direction for a non-present phase. We call this the upwinding bias. We found this upwinding bias could cause convergence issues and non-physical simulation results, especially when we were switching the fourth equation describing slip, as we discussed in the previous section.

Initially, the upwinding direction for a non-flowing phase was assumed to be positive (i.e. flow up the well). This meant the upwinded variables of a phase were calculated as:

$$[\varphi_\beta]_{i+1/2}^{n+1} = \begin{cases} [\varphi_\beta]_i^{n+1}, & [X_\beta]_{i+1/2}^{n+1} \geq 0 \\ [\varphi_\beta]_{i+1}^{n+1}, & [X_\beta]_{i+1/2}^{n+1} < 0 \end{cases}, \quad (6.39)$$

where  $[\varphi_\beta]_{i+1/2}^{n+1}$  is a generic variable and  $[X_\beta]_{i+1/2}^{n+1}$  is the flowing primary variable of a phase (either vapour velocity or liquid volume flux). This choice made logical sense as early versions of the simulator were only used to investigate co-current production scenarios. However, we were initially unaware that this upwinding bias caused poor convergence and non-physical simulation results for cases with down-flow. This highlights the need for a diverse set of test cases when developing a new simulator, such as those that we presented in Chapter 5.

One of the problems caused by the upwinding bias is demonstrated using Test Case 9, which models two-phase injection into a column of liquid. In this case, flashing begins

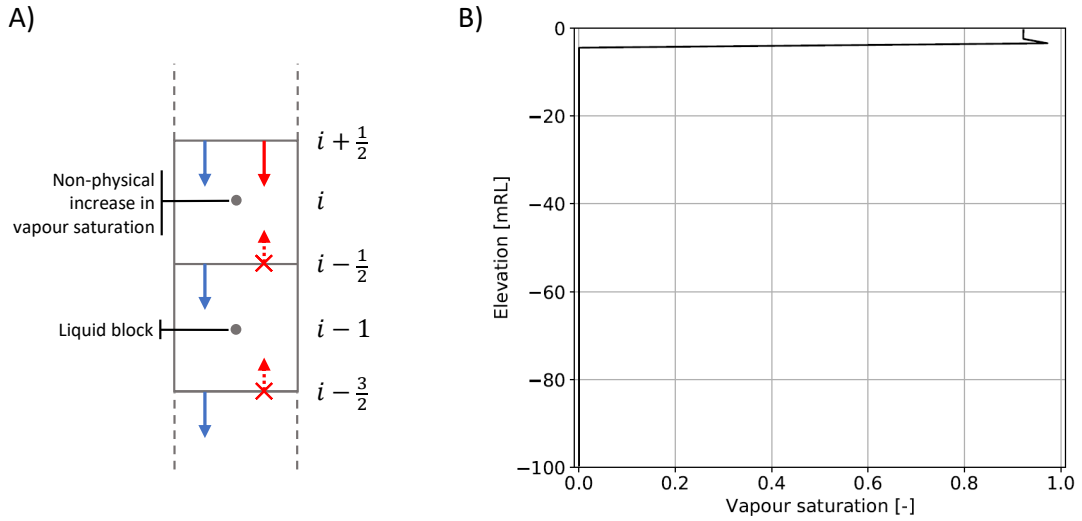


FIGURE 6.6: A) an illustration of the upstream-weighting bias. Here the dashed arrow indicates the assumed flow direction of a non present phase. B) Non-physical vapour saturation profile that results from the upstream weighting bias.

at the wellhead due to the influx of hot two-phase fluid and progresses down the well. The set-up and results of this simulation are discussed in Section 5.3.3.1.

The non-physical behaviour that results from this upstream weighting bias is shown in Figure 6.6 B). This figure plots vapour saturation as flashing progresses down the well. The results show a non-physical increase in saturation in the two-phase block above the liquid column.

Figure 6.6 A) shows an illustration of the upwinding direction for this section of the well. Here, block  $i$  has flashed from liquid to two-phase but block  $i - 1$  is liquid water. As explained above, early implementations of our simulator assumed a positive upwinding direction when the velocity of a phase was zero. Therefore, the upstream weighted variables for the vapour phase on the interface  $i - \frac{1}{2}$  are taken from block  $i - 1$ . This default upwinding direction is shown in Figure 6.6 A) by the red dashed arrow.

As discussed in the previous section, early versions of our simulator would force the vapour velocity to equal zero when the upwinded vapour saturation was zero. As a result, the vapour velocity (and vapour mass flow rate) on the interface at  $i - \frac{1}{2}$  remains zero, despite two-phase down-flow occurring above this interface. This prevents the vapour phase from flowing out of the bottom of block  $i$  and into block  $i - 1$ . Therefore,

vapour accumulates in block  $i$ , which causes the non-physical spike in saturation shown in Figure 6.6 B).

To solve this issue, we stopped forcing the velocity of the non-present phase to equal zero. This provided an estimate of the correct upwinding direction for the vapour phase (as the vapour velocity is non-zero when  $S_v = 0$ ). We also changed the method of calculating the upwinding direction when the velocity (or volume flux) of a phase is zero. We found that averaging the velocity (or volume flux) of a phase over three adjacent interfaces ( $i + 1/2$ ,  $i - 1/2$  and  $i - 3/2$  for the case in Figure 6.6 A)) provided a good estimate of the correct flow direction. This average flow direction is used when the velocity (or volume flux) of a phase is zero.

Alternatively, the hybrid upwinding method, presented in Section 4.2, does not suffer from this issue. This is because it uses a central difference approximation when the flow rate of a phase is zero. This was one of the main motivations for providing the hybrid upwinding scheme as an option in our simulator.

### 6.3.3 Discrete upstream weighting for low mass flow cases

We found that early implementations of the discrete upstream weighting method struggled to simulate test cases with very low mass flow rates. One of the reasons for this problem was that, at low flow rates, the velocity (or volume flux) primary variables would switch between very small positive and negative values for successive Newton iterations. While this change had no impact on the mass flow of a phase (which remained very close to zero) it would change the upwinding direction. This change in upwinding direction would cause the upstream weighted variables to change. This behaviour caused poor, and sometimes failed, convergence.

To prevent this behaviour, we defined a tolerance,  $X_{tol}$ , for which the upwinding direction would remain the same. In this case, an upwinded variable  $\varphi$  is defined as:

$$[\varphi_\beta]_{i+1/2}^{n+1} = \begin{cases} [\varphi_\beta]_i^{n+1}, & [X_\beta]_{i+1/2}^{n+1} > X_{tol} \\ [\varphi_\beta]_{i+1}^{n+1}, & [X_\beta]_{i+1/2}^{n+1} < -X_{tol} \end{cases}. \quad (6.40)$$

When the flowing primary variable of a phase ( $[u_v]_{i+1/2}^{n+1}$  or  $[F_{Vl}]_{i+1/2}^{n+1}$ ), is between the range defined by  $\pm X_{tol}$ , then the upwinding direction remains the same. The upwinding direction for this range is determined using the average flow direction of the surrounding interfaces, as was discussed in the previous section. Experimentation with different values of  $X_{tol}$  found that  $X_{tol} = 1 \times 10^{-6}$  provides good numerical performance.

Again, the hybrid upwinding method, presented in Section 4.2, does not suffer from this issue because it uses a central difference approximation when the flow rate of a phase is zero. Both methods are provided as options in our simulator.

## 6.4 Summary

This chapter discussed some of the investigations involving the numerical formulation of our simulator that were completed during this research. Section 6.1 presented our investigation of different primary variables that we completed after experiencing issues with an early version of our simulator. This investigation found that the best combination of primary variables for our simulator was pressure, temperature (swapped for vapour saturation for two-phase flow), vapour velocity and liquid volume flux. We explained the differences in numerical performance by considering the behaviour of the equation for phase slip for the cases when  $S_v \approx 0$  and  $S_v \approx 1$ .

Section 6.2 discussed the method for calculating the drift velocity used in our simulator. We found that the value of saturation used to calculate the drift velocity was important in counter-flow scenarios. For Test Case 11, the vapour saturation from the numerical block below an interface should be used in the calculation of the drift velocity. For Test Case 12, we found that the vapour saturation from the numerical block above the interface should be used in the calculation of the drift velocity. Therefore, we developed a hybrid formulation for the drift velocity that transitions smoothly between these cases. This formulation allowed us to successfully simulate counter-flow processes in geothermal wells.

Finally, Section 6.3 briefly discussed small changes that were made to improve the numerical performance of our simulator for cases with low mass flow. We found it was best to always solve the drift flux equation (even during single phase flow) as this helped

to prevent changes in the upwinding direction of a phase. Additionally, for the discrete upwinding method, we defined a small range around zero flow for which the upwinding direction did not change. This prevented the upwinding direction from changing when the primary variables switched between small positive and negative values for near zero flow. In this region, the upwinding direction was determined using the average flow direction from the surrounding interfaces.

To summarise, our simulator solves the drift-flux equation in all cases (even for single-phase flow). In this equation, the drift velocity is solved using the hybrid method summarised above and described in Section 6.2.3. The discrete upwinding method was improved for low mass flow cases. These improvements to the numerical formulation of our simulator were critical to the successful simulation of the test cases presented in Chapter 5.



## Chapter 7

# Modelling air-water mixtures

Non-condensable gases (NCGs) such as air and  $\text{CO}_2$  can play an important part in wellbore behaviour as they change the thermodynamic properties of the fluid mixture. Additionally, air often exists at the top of the well when it is shut-in. Therefore, a transient simulator that can account for NCGs is required if some wellbore processes are to be modelled completely (e.g., the opening and closing of a well).

Of the transient simulators reviewed in this thesis, T2WELL by Pan, Oldenburg, Wu and Pruess (2011) is the only one capable of modelling flows of a mixture of water and non-condensable gases. T2WELL was first used with the ECO2N equation of state (EOS) to model carbon sequestration problems. Although T2WELL was initially designed for low-temperature fluids with high  $\text{CO}_2$  content, it has since been extended to encompass higher temperature fluids using the ECO2H EOS (Pan et al., 2015). T2WELL has also been used in geothermal applications by Vasini et al. (2018) with the EWASG EOS, which accounts for  $\text{CO}_2$  and NaCl, to model production tests from a slim well in the Wotton Waven Field. More recently, Battistelli et al. (2020) coupled T2WELL to EOS2H to model the flow of supercritical mixtures of  $\text{CO}_2$  and water. They modelled output curves for the IDDP-1 well in the Krafla geothermal field, Iceland.

This chapter outlines the extension of our transient wellbore simulator for modelling flows of air-water mixtures. In Section 7.1, we present the conservation equations for an air-water mixture and outline the air-water equation of state. In Section 7.2, we present the

changes made to the numerical formulation that were required for modelling air-water mixtures. This includes a discussion of the discrete formulation of the conservation equations, the method we use to switch the primary variables used in this EOS, and the boundary conditions that we use to represent the atmosphere. Finally, in Section 7.3, we verify the implementation of our air-water equation of state using the analytical solution for two-phase flow of air-water mixtures presented by Pan, Webb and Oldenburg (2011).

## 7.1 Conservation Equations for air-water mixtures

Mass conservation equations are required for both the air and water components when modelling air-water mixtures. The conservation of mass equation for the air component is:

$$\frac{\partial}{\partial t} [\rho_l S_l x_l^a + \rho_v S_v x_v^a] + \frac{1}{A} \frac{\partial}{\partial s} [A \rho_l S_l u_l x_l^a + A \rho_v S_v u_v x_v^a] - q_{mass}^a = 0, \quad (7.1)$$

and the conservation of mass equation for the water component is:

$$\frac{\partial}{\partial t} [\rho_l S_l x_l^w + \rho_v S_v x_v^w] + \frac{1}{A} \frac{\partial}{\partial s} [A \rho_l S_l u_l x_l^w + A \rho_v S_v u_v x_v^w] - q_{mass}^w = 0. \quad (7.2)$$

In (7.1) and (7.2), the mass fraction of component  $\kappa$  in phase  $\beta$  is represented by  $x_\beta^\kappa$ , defined as:

$$x_\beta^\kappa = \frac{M_\beta^\kappa}{M_\beta}, \quad (7.3)$$

where  $M_\beta^\kappa$  is the mass of component  $\kappa$  in phase  $\beta$  and  $M_\beta$  is the total mass of phase  $\beta$ .

It follows from (7.3) that:

$$x_\beta^w + x_\beta^a = 1 \quad (7.4)$$

The static (in place) mass fraction of a component  $x^\kappa$  is defined as:

$$x_s^\kappa = \frac{M^\kappa}{M} \quad (7.5)$$

where,  $M^\kappa$  is the total mass of the component  $\kappa$  and  $M$  is the total mass of the mixture.

The total mass of a component,  $M^\kappa$ , is the sum of the mass of the component in both

phases, i.e.:

$$M^\kappa = M_v^\kappa + M_l^\kappa. \quad (7.6)$$

Substituting (7.3) and (7.6) into (7.5) provides a way of calculating the static component mass fraction in terms of the phase mass fractions:

$$x_s^\kappa = \frac{M_v^\kappa + M_l^\kappa}{M} = x_v^\kappa \frac{M_v}{M} + x_l^\kappa \frac{M_l}{M} = \frac{\rho_v S_v x_v^\kappa + \rho_l S_l x_l^\kappa}{\rho_v S_v + \rho_l S_l} = x_v^\kappa x_{sv} + x_l^\kappa x_{sl}. \quad (7.7)$$

Here, the static mass fraction of phase  $\beta$ ,  $x_{s\beta}$ , is defined in the same way as discussed in Section 2.1.1.4, i.e.,  $x_{s\beta} = M_\beta/M = (S_\beta \rho_\beta)/\rho_{mix}$ .

In (7.1) and (7.2),  $\rho_l$  and  $\rho_v$  are the densities of the liquid and vapour phases. They are the mass-averaged density of the air and water components and are defined in (7.10) and (7.18) below for the liquid and vapour phases, respectively. The saturation and average velocity of phase  $\beta$  are given by  $S_\beta$  and  $u_\beta$ , respectively. We assume that the dissolved air flows at the same velocity as the liquid phase,  $u_l$ , while gaseous air and water vapour have the same average velocity,  $u_v$ .

The mass exchange between the reservoir and the wellbore for a component  $\kappa = a, w$  is given by  $q_{mass}^\kappa$  in (7.1) and (7.2). It is defined as:

$$q_{mass}^\kappa = x_{f,feed}^\kappa q_{mass}. \quad (7.8)$$

Here,  $x_{f,feed}^\kappa$  is the flowing mass fraction of the component  $\kappa$  and  $q_{mass}$  is the total mass source, defined in the same way as in (3.78). The flowing enthalpy of the air-water mixture must also be specified for the feed.

In (7.8), and in general, the flowing mass fraction of a component is defined as the ratio of the mass flow rate of a component to the total mass flow rate. Therefore,  $x_f^\kappa$  is defined as:

$$x_f^\kappa = \frac{Q_m^\kappa}{Q_m} = \frac{F_m^\kappa}{F_m}. \quad (7.9)$$

The conservation of momentum and energy equations are unchanged in form from (2.54) and (2.55), however, the calculations of average phase densities and enthalpies are adjusted to account for the presence of air. These variables are defined below.

### 7.1.1 Air-water equation of state

Calculating the properties of an air-water mixture requires an additional primary variable. We use the partial pressure of air in addition to the total pressure, temperature (swapped with vapour saturation for two-phase flow), vapour velocity and liquid volume flux as primary variables.

The phase state of an air-water mixture is identified in a similar way to what was discussed in Section 4.4.4.1 for pure water simulations. However, it is now the partial pressure of water that is used to determine the phase state of the mixture. Liquid conditions occur when the partial pressure of water is greater than the saturation pressure (calculated using the temperature primary variable), vapour conditions occur when the partial pressure of water is less than the saturation pressure, and two-phase conditions occur when the partial pressure of water is equal to the saturation pressure. These conditions are summarised in Table 7.1. As was the case for the pure water EOS, transitions between phase states occur when the primary variables step outside of the ranges defined in Table 7.1. These transitions, and the methods used to switch the primary variables, are discussed in Section 7.2.2.

Below, we describe the method for calculating the secondary variables for an air-water mixture. This method can be easily adapted for other NCGs by simply adjusting the thermodynamic correlations used to describe the properties of the NCG (e.g., those for density, enthalpy, viscosity, Henry's coefficient and the heat of solution).

TABLE 7.1: Primary variable values used to determine the current phase-state of the fluid.

$P^w = P - P^a$	$T$	$S_v$	Phase state
$P^w > P_{sat}(T)$	$T < T_{sat}(P^w)$	0	Liquid
$P^w < P_{sat}(T)$	$T > T_{sat}(P^w)$	1	Vapour
$P^w = P_{sat}(T)$	$T = T_{sat}(P^w)$	$0 < S_v < 1$	Two-phase

### 7.1.1.1 Liquid phase

The effect of dissolved air on the liquid density and dynamic viscosity,  $\rho_l$  and  $\mu_l$ , are assumed negligible, therefore:

$$\rho_l = \rho_l^w, \quad (7.10)$$

and

$$\mu_l = \mu_l^w. \quad (7.11)$$

Here,  $\rho_l^w$  and  $\mu_l^w$  are the density and dynamic viscosity of liquid water, which are calculated using the IAPWS-97 thermodynamic equations as functions of the partial pressure of water,  $P^w$ , and temperature,  $T$  (Dittmann, 2000). The partial pressure of water is calculated from Dalton's law of partial pressure, therefore:

$$P^w = P - P^a. \quad (7.12)$$

Here, the total pressure,  $P$ , and the partial pressure of air,  $P^a$ , are calculated as primary variables for all fluid states. The physical meaning of  $P^a$  is somewhat different under single-phase liquid conditions, where it corresponds to the pressure required to keep all of the air in solution.

The calculation of fluid properties requires the temperature of the fluid. This is calculated as a primary variable for single-phase flow. When two-phase conditions exist, the temperature of the fluid mixture is the saturation temperature,  $T_{sat}$ , of the water component calculated using the IAPWS-97 formulation:

$$T = T_{sat}(P^w). \quad (7.13)$$

Calculation of the liquid enthalpy must take air into account. It is calculated using the component mass fractions:

$$h_l = x_l^w h_l^w + x_l^a (h_l^a + h_{sol}^a), \quad (7.14)$$

where,  $h_l^w$  is the enthalpy of liquid water,  $h_l^a$  is the enthalpy of air in the liquid phase and  $h_{sol}^a$  is the heat of solution. For air, the heat of solution is assumed to be zero.

Essentially the same method discussed here for water-air mixtures can be used for water-CO<sub>2</sub> mixtures, and for CO<sub>2</sub>, the heat of solution is not zero.

The mass fraction of air in the liquid phase is calculated using Henry's law. First, the mole fraction of air,  $m_l^a$ , is calculated as:

$$m_l^a = \frac{P^a}{k_h}, \quad (7.15)$$

where  $P^a$  is the partial pressure of air and  $k_h$  is Henry's Coefficient, which for air is assumed to have a constant value of  $10^{10}$  Pa (Pruess et al., 2012). Then the mass fraction of air in the liquid phase,  $x_l^a$ , is calculated from the mole fraction using the molecular weights of air and water,  $MW^a$  and  $MW^w$ :

$$x_l^a = \frac{m_l^a MW^a}{m_l^a MW^a + (1 - m_l^a) MW^w}. \quad (7.16)$$

Finally, the mass fraction of water in the liquid phase,  $x_l^w$ , is calculated using (7.4) as:

$$x_l^w = 1 - x_l^a. \quad (7.17)$$

#### 7.1.1.2 Vapour phase

The average density of the air-water vapour mixture is calculated using Dalton's law:

$$\rho_v = \rho_v^w + \rho_v^a. \quad (7.18)$$

Here, the water vapour density,  $\rho_v^w$ , is calculated using the IAPWS-97 equations (Dittmann, 2000) as a function of  $P^w$  and  $T$ , and the air density,  $\rho_v^a$ , is calculated as a function of  $P^a$  and  $T$  using the ideal gas law. Again, the temperature is known as a primary variable for single-phase flow and from (7.13) when two-phase conditions exist.

The mass fraction of air in the vapour phase is calculated as the ratio of air density to total density:

$$x_v^a = \frac{\rho_v^a}{\rho_v^w + \rho_v^a}. \quad (7.19)$$

After calculating the mass fraction of air with (7.19), the mass fraction of water in the vapour phase is calculated as:

$$x_v^w = 1 - x_v^a. \quad (7.20)$$

The average vapour enthalpy is weighted by the component mass fractions, therefore:

$$h_v = x_v^w h_v^w + x_v^a h_v^a. \quad (7.21)$$

Here,  $h_v^w$  is the enthalpy of water vapour and  $h_v^a$  is the enthalpy of air. The enthalpy of water vapour is calculated as a function of  $P^a$  and  $T$  using the IAPWS-97 relationships for pure water (Dittmann, 2000). The enthalpy of air is calculated as a function of temperature using the formula given by Irvine and Liley (1984) (in kJ/kg):

$$h_v^a = \sum_{N=0}^3 (A_N T^N) - h_{triple}^a, \quad (7.22)$$

where the coefficients denoted by  $A_N$  are given in Table 7.2 and  $h_{triple}^a$  is the enthalpy of air at the triple point of water (0.01 °C), which is equal to approximately 273.15 kJ/kg. Subtracting  $h_{triple}^a$  shifts the formula for the enthalpy for air given by Irvine and Liley (1984) to equal zero at the triple point of water so that it is consistent with the IAPWS-97 formulation.

Finally, the viscosity of the air-water vapour mixture,  $\mu_v$ , is calculated in the same way as in the geothermal reservoir simulators TOUGH2 (Pruess et al., 2012) (EOS3) and Waiwera (Croucher, 2020). These simulators use an equation by Hirschfelder et al. (1954) based on kinetic gas theory to calculate the viscosity of the air-water vapour mixture. Pruess et al. (2012) modified the original formulation by using an empirical relationship for the viscosity of the water vapour rather than using the first order approximation suggested by Hirschfelder et al. (1954). We make the same modification and use the IAPWS-08 formulation for the viscosity of water vapour (Huber et al., 2009). The equations for calculating  $\mu_v$  are given in Appendix D.

TABLE 7.2: Coefficients for calculating the enthalpy of air (Irvine and Liley, 1984).

$A_0$	$A_1$	$A_2$	$A_3$
12.074	0.924502	0.115984E-3	-0.563568E-8

## 7.2 Numerical implementation

The following section discusses the changes we made to the numerical formulation of our simulator to include air. Section 7.2.1 presents the discrete mass conservation equations, Section 7.2.2 discusses how we perform primary variable switching during phase transitions, and Section 7.2.3 discusses the boundary conditions that we use to represent the atmosphere in our simulations.

### 7.2.1 Discrete conservation equations

The discrete mass conservation equation for the air component is:

$$\begin{aligned} & \frac{1}{\Delta t} \left( [S_v \rho_v x_v^a + S_l \rho_l x_l^a]_i^{n+1} - [S_v \rho_v x_v^a + S_l \rho_l x_l^a]_i^n \right) \\ & + \frac{1}{[V]_i} \left( [AF_{mv} x_v^a + AF_{ml} x_l^a]_{i+1/2}^{n+1} - [AF_{mv} x_v^a + AF_{ml} x_l^a]_{i-1/2}^{n+1} \right) - [q_{mass}^a]_i^{n+1} = 0, \end{aligned} \quad (7.23)$$

and the discrete conservation equation for the water component is:

$$\begin{aligned} & \frac{1}{\Delta t} \left( [S_v \rho_v x_v^w + S_l \rho_l x_l^w]_i^{n+1} - [S_v \rho_v x_v^w + S_l \rho_l x_l^w]_i^n \right) \\ & + \frac{1}{[V]_i} \left( [AF_{mv} x_v^w + AF_{ml} x_l^w]_{i+1/2}^{n+1} - [AF_{mv} x_v^w + AF_{ml} x_l^w]_{i-1/2}^{n+1} \right) - [q_{mass}^w]_i^{n+1} = 0. \end{aligned} \quad (7.24)$$

Here, the mass fractions of component  $\kappa$  in phase  $\beta$ ,  $x_{\beta}^{\kappa}$ , are defined at the centre of block  $i$ . The mass fraction on the interface,  $[x_{\beta}^{\kappa}]_{i+1/2}^{n+1}$ , is upstream weighted based on the direction of flow of the phase. The method used is the same as what was described in Section 4.2. All other variables are calculated in the same way as was described in Chapter 4.

TABLE 7.3: Pressure, temperature and saturation primary variables during phase transitions.

$P^w = P_x - P_x^a$	T	$S_v$	Transition
$P^w < P_{sat}(T_x)$	$T_x$	0	Liquid to two-phase transition
$P^w > P_{sat}(T_x)$	$T_x$	1	Vapour to two-phase transition
$P^w$	$T_{sat}(P^w)$	$S_{vx} < 0$	Two-phase to liquid transition
$P^w$	$T_{sat}(P^w)$	$S_{vx} > 1$	Two-phase to vapour transition



### 7.2.2 Phase transitions

As discussed in Section 7.1.1, we determine the phase state of an air-water mixture using the partial pressure of water. A transition occurs from single-phase to two-phase conditions when the water pressure and temperature "step over" the saturation curve during a Newton step. For transitions from liquid to two-phase conditions, this step across the saturation curve occurs when  $P_{k+1}^w < P_{sat}^w(T_{k+1})$ . This is shown diagrammatically in Figure 7.1 A).

As with the pure water EOS, we find the partial pressure of water by solving for the point where the straight line between  $(T_k, P_k^w)$  and  $(T_{k+1}, P_{k+1}^w)$  intersects with  $P_{sat}^w(T)$ , shown by  $(T_x, P^w)$  in Figure 7.1 A). This intersect is formulated as:

$$P_k^w + \frac{P_{k+1}^w - P_k^w}{T_{k+1} - T_k}(T - T_k) = P_{sat}^w(T). \quad (7.25)$$

This equation (rearranged for zero on the right hand side) is solved using Brent's method to find  $T = T_x$ . The new water partial pressure is then  $P^w = P_{sat}^w(T_x)$ .

Next, we calculate the proportion of the Newton step required to reach the saturation curve. This is formulated as:

$$\Lambda = \frac{d_1}{d_2} = \sqrt{\frac{(P^w - P_k^w)^2 + (T_x - T_k)^2}{(P_{k+1}^w - P_k^w)^2 + (T_{k+1} - T_k)^2}}, \quad (7.26)$$

where the distances  $d_1$  and  $d_2$  are shown in Figure 7.1 A). The step in the air partial pressure primary variable is scaled using this ratio, meaning:

$$P_x^a = P_k^a + \Lambda(P_{k+1}^a - P_k^a). \quad (7.27)$$

Finally, the new total pressure is calculated by summing the partial pressures, such that:

$$P_x = P_x^a + P^w, \quad (7.28)$$

and the vapour saturation primary variable is set as  $S_{vx} = 1E - 6$ .

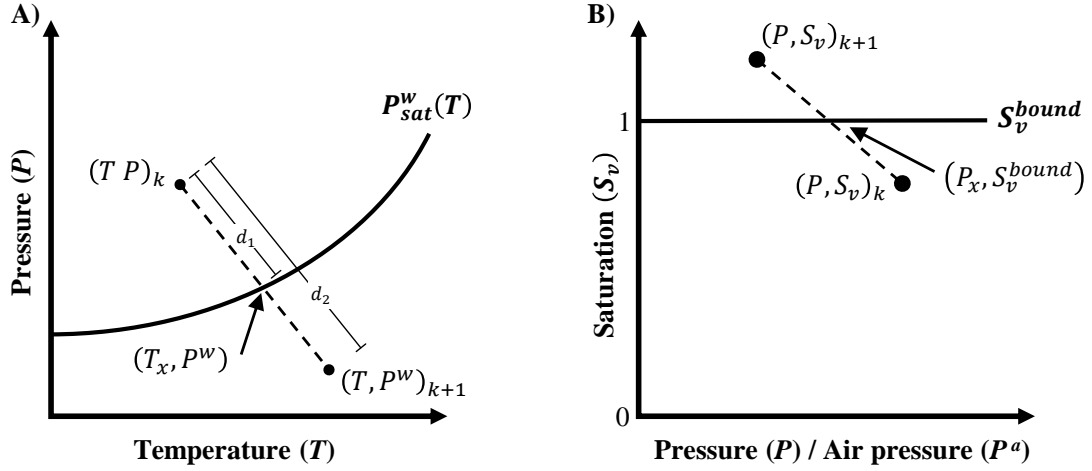


FIGURE 7.1: Variable switching for A) phase transitions from liquid to two-phase conditions and B) phase transitions from two-phase to vapour conditions for the air-water EOS.

A similar process is used when transitioning from vapour to two-phase conditions. However, the transition occurs when  $P^w > P_{sat}(T)$  and the new two-phase vapour saturation is set as  $S_{vx} = 1 - 1E - 6$ .

Transitions from two-phase to single-phase flow are completed in much the same way as in the pure water EOS. The point where the total pressure and the air partial pressure cross the saturation bound ( $S_v^{bound} = 0$  and  $S_v^{bound} = 1$  for liquid and vapour transitions, respectively) is calculated from:

$$P_x = \left( \frac{S_v^{bound} - S_{vk}}{S_{v,k+1} - S_{vk}} \right) (P_{k+1} - P_k) + P_k, \quad (7.29)$$

and

$$P_x^a = \left( \frac{S_v^{bound} - S_{vk}}{S_{v,k+1} - S_{vk}} \right) (P_{k+1}^a - P_k^a) + P_k^a. \quad (7.30)$$

The new water partial pressure is then calculated as  $P^w = P_x - P_x^a$ . The new water partial pressure is used to calculate the new single-phase temperature as  $T_x = T_{sat}(P^w)$ . Finally, we recalculate the total pressure with a small perturbation to ensure that the primary variables are within the single-phase region, such that:

$$P_x = (1 \pm 1E - 6) \times P^w + P_x^a. \quad (7.31)$$

### 7.2.3 Atmospheric boundary conditions

Including air in our simulations allows us to represent the atmosphere numerically. We use two different atmospheric boundary conditions, which are shown diagrammatically in Figure 7.2. The first, discussed in Section 7.2.3.1, uses a source term to replicate wellhead operations for shut-in wells. The second boundary condition, discussed in Section 7.2.3.2, is used to model cases where the wellhead is open to atmospheric conditions.

#### 7.2.3.1 One-way atmospheric feed

In this research, we simulate cases in which the shut-in water-level is below the wellhead, for example, see Sections 8.1.2 and 8.2. To simulate these cases, we require initial conditions that accurately represent the state of the shut-in well. These initial conditions are found using simulations which use a “one-way atmospheric feed” that controls the flow of air in and out of the wellhead. This is discussed further below.

A geothermal well is typically shut-in by injecting cold water to suppress up-flow and

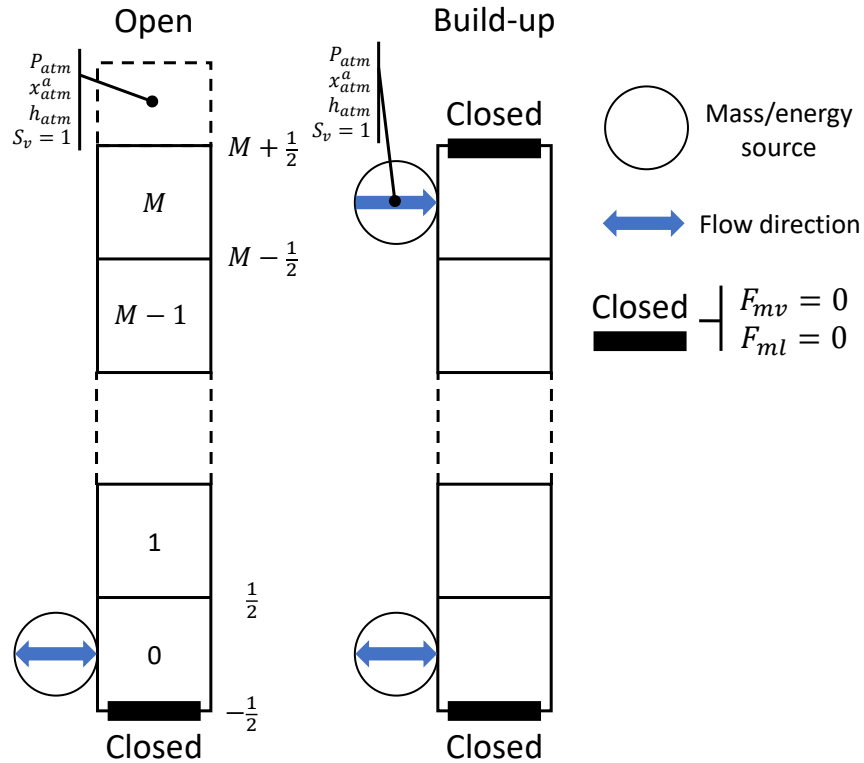


FIGURE 7.2: Diagrammatic representation of the atmospheric boundary conditions discussed in Sections 7.2.3.1 and 7.2.3.2.

then closing the wellhead. If the water level begins to drop after shut-in, the wellhead pressure will drop below atmospheric conditions. If this occurs, the wellhead is opened slightly, allowing a small amount of air into the well. This allows the wellhead pressure to return to atmospheric conditions and for the water level to drop. The water level will continue to drop until equilibrium conditions are reached, which occur when the net mass flow in the well is zero. After the water level stabilises, the well is left closed to heat up. If boiling occurs at any point during the heat-up process, pressure in the well will increase. In some cases, the increase in pressure is sufficient for a well to self-discharge. This is discussed in Section 8.1.2. In other cases, pressure will not build up and the well must be stimulated. Discharge stimulation methods using air are discussed further in Section 8.2.

We represent the wellhead control process described above using a "one-way atmospheric feed" prescribed in the top block of the wellbore model. The wellhead boundary is closed to flow using the conditions discussed in Section 4.5.3. This is shown diagrammatically in Figure 7.2. The atmospheric feed allows air to be drawn into the well but prevents outflow. This allows us to simulate wells with water levels below the wellhead and determine whether a well will require stimulation in order to flow.

The properties of the atmospheric feed, which represent atmospheric conditions at 25 °C, are given in Table 7.4. Here, the flowing mass fraction of air,  $x_f^a$ , is set to 0.9999 rather than one (i.e., pure air) because our numerical procedure requires the partial pressure of water to be non-zero. Otherwise, the saturation temperature cannot be calculated, meaning the phase state of the flow cannot be determined.

Modelling the inflow of air using the method described above requires the productivity value,  $\alpha$ , to be specified for the atmospheric feed. The value chosen for  $\alpha$  will affect the relationship between wellhead pressure and the rate at air enters the well. Choosing a very small value means that a larger pressure drop is required to draw in air at the wellhead. We also found large values for  $\alpha$  could induce small oscillations in the wellhead pressure. Our experimentation found that choosing  $\alpha$  to be of the same order of magnitude as the productivity of the reservoir feeds provided satisfactory performance.

TABLE 7.4: Parameters and location of the atmospheric feed.

Location	$P$ [bara]	$h_{f_{mix}}$ [kJ/kg]	$x_f^a$ [-]
Wellhead block	1.01325	25	0.9999

Also, as the feed is prescribed in the top block of the wellbore model, it is located slightly below the **wellhead**.

### 7.2.3.2 Open to atmospheric conditions

In some cases, we want to simulate the opening of a well to atmospheric conditions, for example, when simulating the stimulation of non-discharging wells, which is discussed in Section 8.2.

The discrete mass and energy conservation equations at the wellhead (in block  $i = M$ ) are the same as those given in (7.23), (7.24) and (4.5). However, if down-flow occurs for either phase on the top boundary, the in-flowing fluid is air at atmospheric conditions. Therefore, the upwinded parameters at the wellhead are defined as:

$$[S_\beta]_{M+1/2}^{n+1} = \begin{cases} [S_\beta]_M^{n+1}, & [X_\beta]_{M+1/2}^{n+1} > 0 \\ [S_\beta]_{atm}, & [X_\beta]_{M+1/2}^{n+1} < 0 \end{cases} \quad (7.32)$$

$$[\rho_\beta]_{M+1/2}^{n+1} = \begin{cases} [\rho_\beta]_M^{n+1}, & [X_\beta]_{M+1/2}^{n+1} > 0 \\ [\rho_\beta]_{atm}, & [X_\beta]_{M+1/2}^{n+1} < 0 \end{cases} \quad (7.33)$$

$$[x_\beta^\kappa]_{M+1/2}^{n+1} = \begin{cases} [x_\beta^\kappa]_M^{n+1}, & [X_\beta]_{M+1/2}^{n+1} > 0 \\ [x_\beta^\kappa]_{atm}, & [X_\beta]_{M+1/2}^{n+1} < 0 \end{cases} \quad (7.34)$$

$$[H_\beta]_{M+1/2}^{n+1} = \begin{cases} [H_\beta]_M^{n+1}, & [X_\beta]_{M+1/2}^{n+1} > 0 \\ [H_\beta]_{atm}, & [X_\beta]_{M+1/2}^{n+1} < 0 \end{cases} \quad (7.35)$$

The atmospheric pressure,  $P_{atm}^{n+1}$  bara, is specified in the pressure gradient term within the momentum conservation equation. This equation is formulated as:

$$\begin{aligned}
 [R_{BC}]_{4M+4}^{n+1} = & \frac{[F_{mv} + F_{ml}]_{M+1/2}^{n+1} - [F_{mv} + F_{ml}]_{M+1/2}^n}{\Delta t} + \frac{P_{atm}^{n+1} - P_M^{n+1}}{\Delta s_M} \\
 & + \frac{1}{[V]_{M+1/2}} \left( [AF_{mv}u_v + AF_{ml}u_l]_{M+1/2}^{n+1} - [AF_{mv}u_v + AF_{ml}u_l]_{M+1/2}^n \right) \\
 & + \left[ \frac{2}{r} \tau \right]_{M+1/2}^{n+1} + [\rho_v S_v + \rho_l S_l]_M^{n+1} g \frac{\Delta z_M}{\Delta s_M} = 0. \quad (7.36)
 \end{aligned}$$

Here, the index  $M$  refers to the wellhead block, as shown in Figure 7.2. The atmospheric pressure boundary condition is denoted by  $P_{atm}^{n+1}$ . The atmospheric pressure is specified at the centre of a "ghost block" above the wellhead interface, as is shown in Figure 7.2.

### 7.3 Model verification

Our implementation of the air-water EOS was validated using the semi-analytical solution given by Pan, Webb and Oldenburg (2011). This solution is derived by considering steady-state, isothermal flow within a vertical well with a constant diameter. It is assumed that there is no mixing between the phases, which means  $x_{fv}$  remains constant with depth. This is a relatively good approximation in this case as air has low solubility in **liquid** water. With these assumptions, the momentum conservation equation simplifies to:

$$\frac{d}{ds} \left( \frac{h}{\rho_{mix}} \right) + \frac{dP}{ds} = -\frac{f F_m^2}{4r \rho_{mix}} - \rho_{mix} g. \quad (7.37)$$

Here,  $h/\rho_{mix}$  is the momentum flux of the fluid and  $h$  is defined as:

$$h = F_m^2 + \frac{x_{fv} \rho_l}{a_1} u_d^2, \quad (7.38)$$

where  $a_1$  is an intermediate parameter defined as:

$$a_1 = \frac{1 - x_{fv}}{\rho_l} + \frac{u_d}{F_m} = \frac{x_{fv}(1 - S_v)}{S_v \rho_v}. \quad (7.39)$$

The vapour saturation can be defined in terms of  $a_1$  as:

$$S_v = \frac{x_{fv}}{x_{fv} + a_1 \rho_v}, \quad (7.40)$$

which is required for the solution procedure outlined below.

The momentum flux derivative can be expanded as:

$$\frac{d}{ds} \left( \frac{h}{\rho_{mix}} \right) = \frac{\partial}{\partial P} \left( \frac{h}{\rho_{mix}} \right) \frac{dP}{ds} + \frac{\partial}{\partial T} \left( \frac{h}{\rho_{mix}} \right) \frac{dT}{ds}. \quad (7.41)$$

Pan, Webb and Oldenburg (2011) assume that  $dT/ds$  is constant. We assume isothermal flow, meaning  $dT/ds = 0$  °C/m, therefore, the momentum conservation equation simplifies to:

$$\left( \frac{\partial}{\partial P} \left( \frac{h}{\rho_{mix}} + 1 \right) \right) \frac{dP}{ds} = -\frac{f F_m^2}{4r \rho_{mix}} - \rho_{mix} g. \quad (7.42)$$

Rearranging for  $dP/ds$ , and inverting gives:

$$\frac{ds}{dP} = -\frac{1 + \frac{\partial}{\partial P} \left( \frac{h}{\rho_{mix}} \right)}{\rho_{mix} g + \frac{f F_m^2}{4r \rho_{mix}}}. \quad (7.43)$$

Finally, integrating (7.43) with respect to  $s$  gives:

$$s(P) = s_0 - \int_{P_0}^P \frac{1 + \frac{\partial}{\partial P} \left( \frac{h}{\rho_{mix}} \right)}{\rho_{mix} g + \frac{f F_m^2}{4r \rho_{mix}}} dP, \quad (7.44)$$

which can be evaluated using numerical integration. Pan, Webb and Oldenburg (2011) outline the following steps to calculate the depth from (7.44):

- Step 1: For a series of  $P$ , calculate the values of  $\rho_\beta(P, T)$  from the EOS
- Step 2: Solve (7.40) implicitly for  $S_v$  given  $\rho_\beta$ ,  $x_{fv}$  and  $F_m$
- Step 3: Calculate  $\rho_{mix}$ ,  $h$  and the integrand of (7.44)
- Step 4: Calculate  $s(P)$  by integration of (7.44)

Simulation results are compared to the analytical solution presented in (7.44) to verify the implementation of the air-water equation of state. The parameters for the verification simulations are given in Table 7.5. Figure 7.3 shows a very good agreement between the analytical and numerical solution.

TABLE 7.5: Simulation and wellbore parameters for air-water verification simulation.

Inclination angle	0 °
Length	1000 m
wellbore diameter	0.1 m
Pipe roughness	2.4E-5 m
Temperature	20 °C (isothermal)
Wellhead pressure condition	1 bara
Flowing mass fraction ( $x_{fv}$ )	0.5
Total mass flux	50 kg/s/m <sup>2</sup>
Drift-flux relationship	Shi et al. (2005)

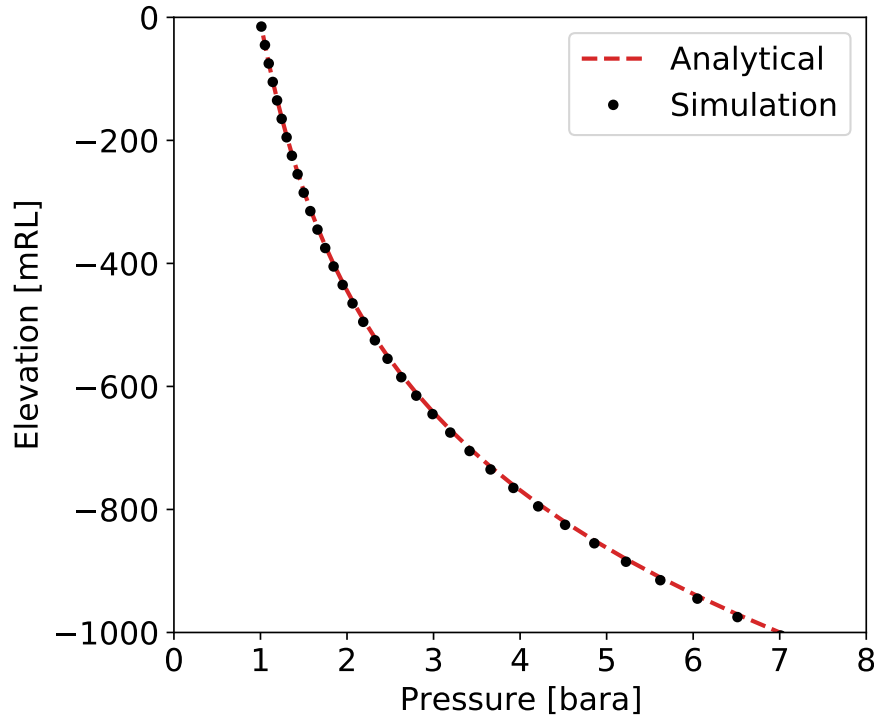


FIGURE 7.3: Comparison of simulation results with the semi-analytical solution defined by Pan, Webb and Oldenburg (2011).

Further verification was completed to ensure that simulation results using the air-water equation of state made physical sense. Firstly, the test cases presented in Chapter 5 were run using the air-water equation of state with no air. The simulation results were compared to the pure water EOS results. This ensured that the air-water EOS produced the same results as the pure water EOS when air was not present in the simulation. Secondly, we added small amounts of air to the source terms for the production test cases presented in Section 5.3.1. The results were compared to the pure water simulations to ensure that the air-water simulation results were physically realistic. Test Case 3 is discussed below as an example.



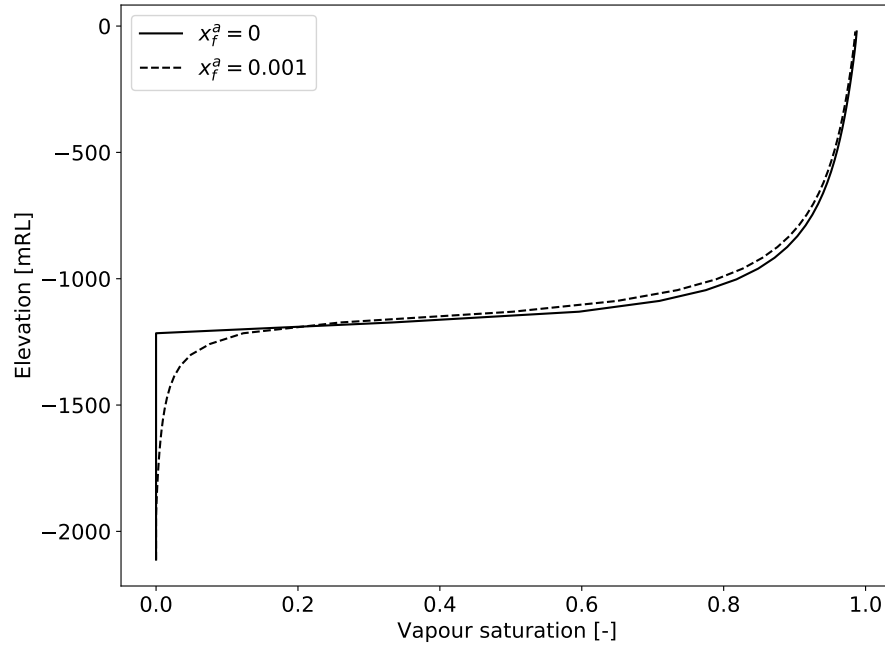


FIGURE 7.4: Comparison of the steady-state vapour saturation for Test Case 3 with no air and 0.1% air.

For Test Case 3, the flowing mass fraction of air in the feed-zone was set at 0.1% for the air-water case. The enthalpy of the feed was kept constant for the air and no air simulations. Figure 7.4 compares the steady-state vapour saturation for the air-water and pure water simulations. For the air-water case, air enters the well dissolved in the liquid water via the feed at the bottom of the well. As the liquid flows up the well, the pressure drops, and the air comes out of solution. This is shown in Figure 7.4 by two-phase conditions beginning at approximately -1900 mRL in the air-water case rather than -1200 mRL as was the case with pure-water. As the amount of air in the simulation is small, the pressure and temperature profiles are very similar to the pure water simulation. Therefore, the large increase in vapour saturation caused by the flashing of the water component still occurs at approximately -1200 mRL for the air-water case. These results match our expectations of the physical process that occurs when a small amount of air is present in the flow of hot geothermal fluid.

## 7.4 Summary

This chapter discussed the extension of our simulator for modelling flows of air-water mixtures. Section 7.1 presented the conservation of mass equations for the individual air and water components. It also outlined the method of calculating the secondary variables for flows of air and water from the primary thermodynamic variables. Our method used the total pressure, partial pressure of air, temperature (swapped with vapour saturation for two-phase flow), vapour velocity and liquid volume flux as primary variables.

Section 7.2 discussed the changes to our numerical formulation that were required to simulate air-water mixtures. This included discussions of the discrete conservation of mass equations for each phase, how we recognise phase transitions and our method for switching the primary variables. We also discussed two wellhead boundary conditions that we use to represent the atmosphere. The first condition approximated wellhead operations using a source term to allow air into the well if the wellhead pressure drops below atmospheric conditions. This allows the water level to drop within the well and allows the simulation of cases with air caps. The second wellhead boundary condition models the case when the wellhead is open to atmospheric conditions.

Finally, in Section 7.3 we discussed the verification of our air-water equation of state. This was completed by comparing simulation results to the semi-analytical solution by Pan, Webb and Oldenburg (2011), which describes the idealised flow of isothermal air-water mixtures.

One of our main motivations for including air in our simulator is that it is required to simulate wells with air caps at the wellhead. This occurs when the reservoir is under-pressured (i.e., the pore pressure in the feed is less than the fluid pressure in a full wellbore). We present two examples of wells with air caps in the following chapter.

## Chapter 8

# Wellbore modelling case studies

So far in this thesis, we have discussed the formulation, implementation and testing of our transient geothermal wellbore simulator. This chapter presents case studies that highlight the uses and capabilities of our simulator.

Section 8.1 discusses counter-flow processes that occur in shut-in geothermal wells. First, we discuss the counter-flow that occurs as a small, shut-in test well heats up. We show that the energy transport resulting from counter-flow is required to produce the hot gas cap that can occur within a shut-in geothermal well. We then demonstrate that the same process can occur in more realistic shut-in wells. Finally, we use simulation to explain the role of counter-flow during the shutting in of a flowing well.

In Section 8.2, we discuss the stimulation of geothermal wells that will not self-discharge. We simulate air-lifting and air injection stimulation methods on a case study well. These simulations provide examples of the practical applications of our transient simulator. They also serve as good test problems for our air-water equation of state as they involve rapid transient process and counter-flow.

## 8.1 Counter-flow processes in shut-in wells

One of the main objectives of this work was to develop a simulator capable of modelling counter-flow processes within a geothermal well. Throughout this thesis, we have highlighted the modelling decisions that we made based on this requirement. This includes our choice of empirical slip model (Section 3.2), our choice of primary variables (Section 4.4) and the numerical implementation of the drift velocity formula (Section 6.2). In this section, we present a preliminary investigation into the role of counter-flow processes in shut-in geothermal wells.

In Section 8.1.1, we present a simulation of a shut-in geothermal well as it heats up (Test Case 12). The numerical modelling of shut-in wells is of interest because pressure and temperature data taken from these wells is used to infer reservoir characteristics and to calibrate numerical reservoir models (Grant and Bixley, 2011). Section 8.1.2 presents simulations of the opening of a well to flow, starting from realistic shut-in initial conditions. These initial conditions feature boiling and inter-zonal flow. Finally, in Section 8.1.3, we simulate the shutting in of a flowing well. Counter-flow occurs during this process.

### 8.1.1 Modelling wellbore heat-up (Test Case 12)

Test Case 12 models heat-up processes in a shallow geothermal well that has been closed after a period of injection. This test case is described fully in Section 5.3.4.2, however, we summarise the important parameters below.

Test Case 12 was developed to investigate shut-in wellhead conditions and counter-flow processes within the well. The well is only 100 m deep with a constant internal diameter of 0.2 m and a completion diameter of 0.22 m. A vapour feed with a pressure of 20 bar, a temperature of 250 °C, and a productivity of 1E-6 kg/s/Pa is located in the bottom block of the model. The deliverability model used allows fluid to enter and exit the well during heat-up. Finally, the formation temperature profile is constant with time. It is shown in Figure 8.1 B).

Test Case 12 begins with the injection of 25 °C liquid water at a rate of 2 kg/s at the wellhead. Pressure, temperature and saturation conditions within the well after two days

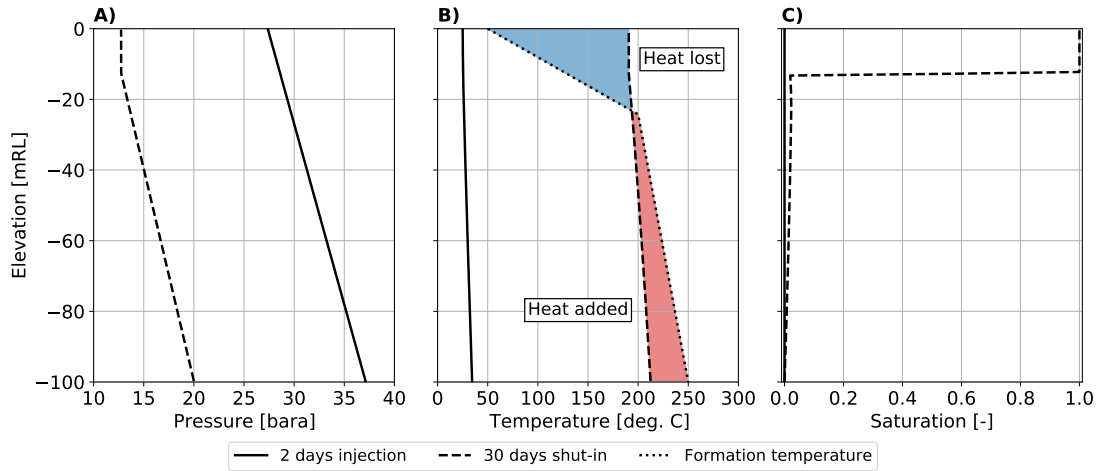


FIGURE 8.1: Wellbore conditions for Test Case 12 for A) pressure, B) temperature and C) vapour saturation after 2 days of injection and after 30 days of being shut-in.

of injection are shown in Figure 8.1. These conditions correspond to a column of cold liquid water. After cold water is injected for two days, the wellhead is shut rapidly, and the well is left for 30 days to heat up.

Figure 8.1 compares the pressure, temperature and saturation in the wellbore after two days of injection with the conditions 30 days after shut-in. This comparison indicates that after being shut in, the wellbore has heated up and developed a hot vapour zone at its top. The role of counter-flow in this process is discussed below using Figure 8.2, which plots the mass flows of each phase at various times. The saturation within the well is shown diagrammatically to the right of each mass flow plot in Figure 8.2.

Figure 8.2 A) plots the liquid and vapour mass flows 21 hours after shut-in. By this time, temperatures within the well have increased from the cold injection conditions shown in Figure 8.1 B) to saturation conditions, and boiling has just begun at the bottom of the well. At this stage, the liquid phase is flowing down the well and the vapour phase is bubbling up through the liquid.

Figure 8.2 B) shows that after seven more hours (approximately 28 hours after shut-in), boiling has progressed up the well to a depth of 12 m. Counter-flow is evident in the well below this point. Figure 8.2 B) shows that there is a net down-flow of fluid below 12 m, as the liquid down-flow is greater than the vapour up-flow. This is due to the two-phase fluid expanding as it boils, which increases the pressure in the well, forcing

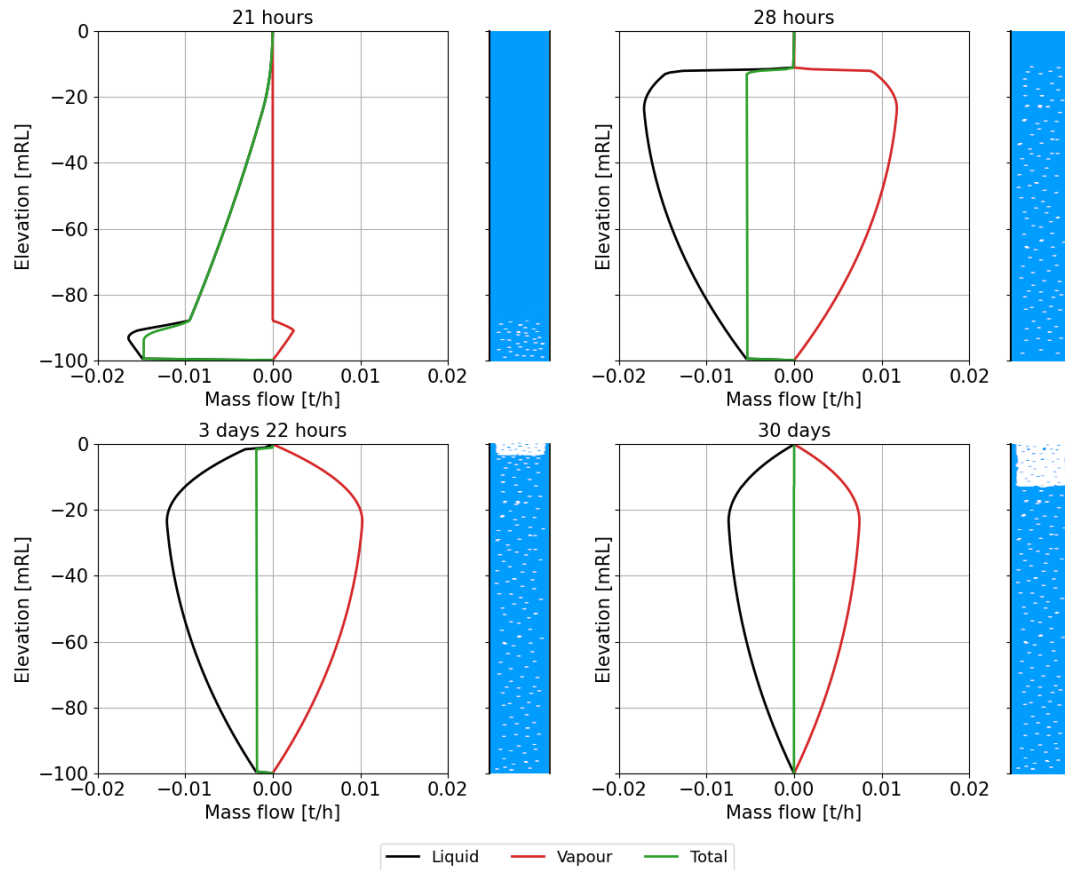


FIGURE 8.2: Plots of the liquid, vapour, and total mass flow A) 21 hours, B) 28 hours, C) 3 days and 22 hours and D) 30 days after shut-in for Test Case 12. These plots show that counter-flow occurs within the well as it heats up. The corresponding wellbore saturation is shown diagrammatically to the right of each mass flow plot.

fluid down and out of the well. The counter-flow occurring below 12 m transports energy up the well, heating the liquid above the boiling zone. This is because the high enthalpy vapour phase transports more energy up the well than the lower enthalpy liquid phase transports down.

Figure 8.2 C) shows that boiling reaches the wellhead approximately three days and 22 hours after shut-in. Boiling takes longer to progress up this last 12 m of the well because, in this region, heat is lost to the formation due to its low temperature. This means the heating of the top 20 m is caused solely by the net upwards heat transfer that results from counter-flow.

After reaching the wellhead, vapour begins to accumulate, causing a hot gas cap to form. Note that this gas cap is high saturation two-phase fluid rather than pure water vapour. This must be the case in our test problem as it is one-dimensional. This means that

only one mass flow rate (and flow direction) for the vapour is defined at each interface. Therefore, counter-flow, which transports heat to the top of the well, is not possible within a column of pure vapour. As more vapour accumulates at the top of the well, the interface between the high and low saturation regions moves down the well. Physically, the low vapour saturation section below this interface has bubbles of vapour moving up through the water, which is balanced by a small down-flow of liquid. The vapour boils off the top of the low vapour saturation column into the high vapour saturation zone. Here, the vapour slowly rises and loses heat to the formation. This heat loss causes some of the vapour to condense to liquid which flows back down the well.

Figure 8.2 D) shows that the well has reached steady-state conditions after being shut-in for 30 days. At this time, stable counter-flow occurs at all depths. Here, the vapour up-flow is equal and opposite to the liquid down-flow, and mass flow to the feed is zero. This is required to satisfy mass conservation for a shut-in single-feed well. Figure 8.1 C) shows that a hot vapour cap has developed in the top 12.5 m of the well. Comparing the temperature profile at 30 days with the formation temperature in Figure 8.1 B) indicates that the processes occurring within the well are driven by heat transfer between the wellbore and the formation. In this case, the well is essentially acting as a long heat exchanger. Heat is added to the well in the region highlighted in red in Figure 8.1 B). Counter-flow processes transport heat up the well where it is lost to the formation in the area highlighted in blue.

The results of this simulation show that counter-flow processes start as soon as boiling begins in the well. They suggest that the vapour cap that can exist in a geothermal well develops because of convective heat transport due to counter-flow that occurs in the two-phase fluid. For this reason, counter-flow processes cannot be ignored when simulating the shutting-in of a geothermal wellbore, even though the mass flows that occur during this process are small.

TABLE 8.1: Wellbore and simulation parameters for the case described in Section 8.1.2, which simulates opening a realistic well to flow.

Wellhead elevation	0 mRL
Length	1000 m
Inclination angle	0 °
Wellbore diameter	0.2205 m above -660 mRL 0.16 m below -660 mRL
Cement diameter	0.314 m above -660 mRL 0.17 below -660 mRL
Pipe roughness	4.5E-5 m above -660 mRL 9.0E-5 m below -660 mRL
Discretisation	Uniform, 200 blocks
Feed-zone parameters	Table 8.2
Formation temperatures	Figure 8.3
Bottomhole boundary condition	Closed

TABLE 8.2: Feed-zone properties for the case described in Section 8.1.2, which simulates opening a realistic well to flow.

Feed location	Elevation [mRL]	$\alpha$ [kg/s/Pa]	P [bara]	$h_{f_{mix}}$ [kJ/kg]	$x_f^a$
Atmospheric feed	0 to -10	8.3E-07	1.01325	25	0.9999
Shallow	-490 to -500	8.3E-07	33.00	1034	0
Deep	-990 to -1000	8.3E-07	66.82	1251	0

### 8.1.2 Modelling wellbore start-up from realistic shut-in conditions

In this section, we demonstrate that the processes discussed in Section 8.1.1 also occur in more complex, more realistic wells. In this case, we simulate flow in a 1000 m well with a diameter of 0.2205 m above -660 mRL. The diameter decreases to 0.16 m below -660 mRL. Other model and simulation parameters are given in Table 8.1. The formation temperature profile for this case is shown in Figure 8.3 B). It has a linear transition from 25 – 100 °C over the first 100 m of the formation. Below this point, the formation temperature follows the boiling point for depth profile. This well has two feed-zones that allow transfer of mass and energy to and from the reservoir. The properties of both feeds are given in Table 8.2. They correspond to saturated liquid water conditions for their depth based on the temperature profile given in Figure 8.3 B).

Figures 8.3 and 8.4 show the wellbore conditions 30 days after being shut-in. These conditions were simulated by shutting the wellhead after a period of cold water injection. For this well, the wellhead pressure drops below atmospheric conditions after shut-in. We use an additional ‘one-way atmospheric feed’ located in the top block of the model to control the flow of air into and out of the well when this occurs. This boundary condition,



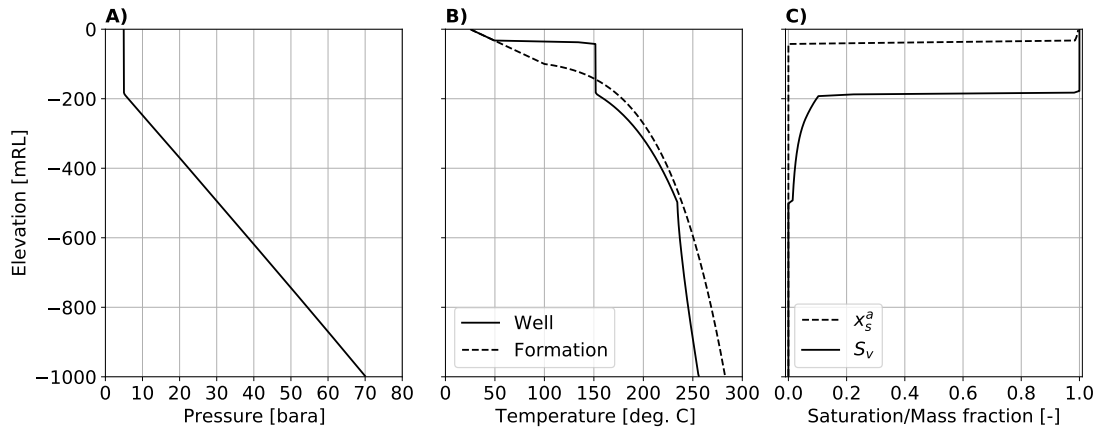


FIGURE 8.3: Plots of A) pressure, B) wellbore and formation temperature, and C) vapour and air mass fractions vs. elevation for the wellbore described in Section 8.1.2 after 30 days of heat-up.

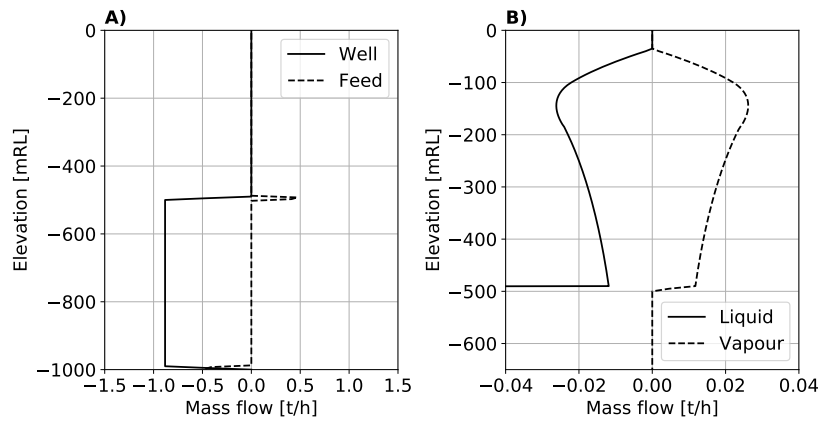


FIGURE 8.4: Plots of A) total mass flow rate within the well, showing inter-zonal flow. B) Mass flow rates for the liquid and vapour phases between 0 and -600 mRL, showing counter-flow exists in the wellbore described in Section 8.1.2 after 30 days of heat-up.

which is described in Section 7.2.3.1, allows air into the well when the wellhead pressure drops below atmospheric pressure but does not allow outflow. This simulates opening the wellhead slightly for a short period of time to release a vacuum that has developed after shut-in, then shutting the well and allowing it to heat up. The conditions of this feed, which correspond to air at 25 °C, are given in Table 8.2.

The shut-in conditions given in Figures 8.3 and 8.4 show several interesting features. Firstly, inter-zonal flow occurs between the two feeds. Figure 8.4 A) indicates that fluid enters the well via the shallow feed at -500 mRL at approximately 230 °C. It flows down the well at 0.8 t/h and exits via the deep feed at the same rate. This down-flow is evident in the near-isothermal temperature profile for the bottom 500 m of the well, shown in

Figure 8.3 B). Secondly, boiling occurs in the well between -20 mRL and -500 mRL. Figure 8.4 B) shows that counter-flow occurs in this section of the well. The comparison of the well and formation temperatures in Figure 8.3 B) indicates that, in this case, the isothermal temperatures between -30 mRL and -200 mRL do not reflect the reservoir temperatures. Instead, this high-temperature, high vapour saturation, two-phase column is attributed to boiling in the wellbore and the heat transfer that it causes. This is the same heat transfer process that was discussed in Section 8.1.1 above.

Similarly, the non-isothermal temperatures in the low saturation boiling zone between -200 mRL and -500 mRL do not reflect the reservoir temperatures. Differences range from approximately 2 °C at -500 mRL to approximately 15 °C at -200 mRL. Finally, Figure 8.4 C) indicates that the top 30 m of the well is occupied by air, which was drawn into the well after shut-in. There is no circulation or counter-flow in this section of the well. As a result, there is no energy transport from the hotter region of the well below, meaning this section of the well is at reservoir temperatures.

The shut-in conditions described above are used as the initial conditions when simulating the opening of this well to flow. Figure 8.3 A) indicates that the boiling which occurs while this well is heating up causes the wellhead pressure to increase from atmospheric conditions to approximately 5.0 bara. This over-pressure makes it possible to start the well by simply opening the wellhead. Figure 8.5 shows how this process evolves with time. The well is opened to flow by dropping the wellhead pressure boundary condition from 5.0 bara to 1.01325 bara over 60 seconds. The depressurisation of the well causes rapid flashing processes to occur at -200 mRL. The two-phase fluid expands as it flashes, causing the rapid increase in mass flow at -200 mRL that is shown in Figure 8.5 C). After 30 seconds, vapour saturation has increased between -200 mRL and -500 mRL as hot fluid is transported up the well. The production of hot two-phase fluid causes the wellhead temperature to increase from 25 °C to 130 °C over this 30 second period. After 3.5 minutes, the flash-point has reached the bottom of the well. This flashing causes the average density of the fluid to decrease, which results in a significant drop in pressure in the bottom half of the well. This pressure drop causes hot geothermal fluid to be produced from both feeds. After 5 minutes, we start linearly increasing the wellhead pressure boundary condition to 6.0 bara. This simulates slowly switching production

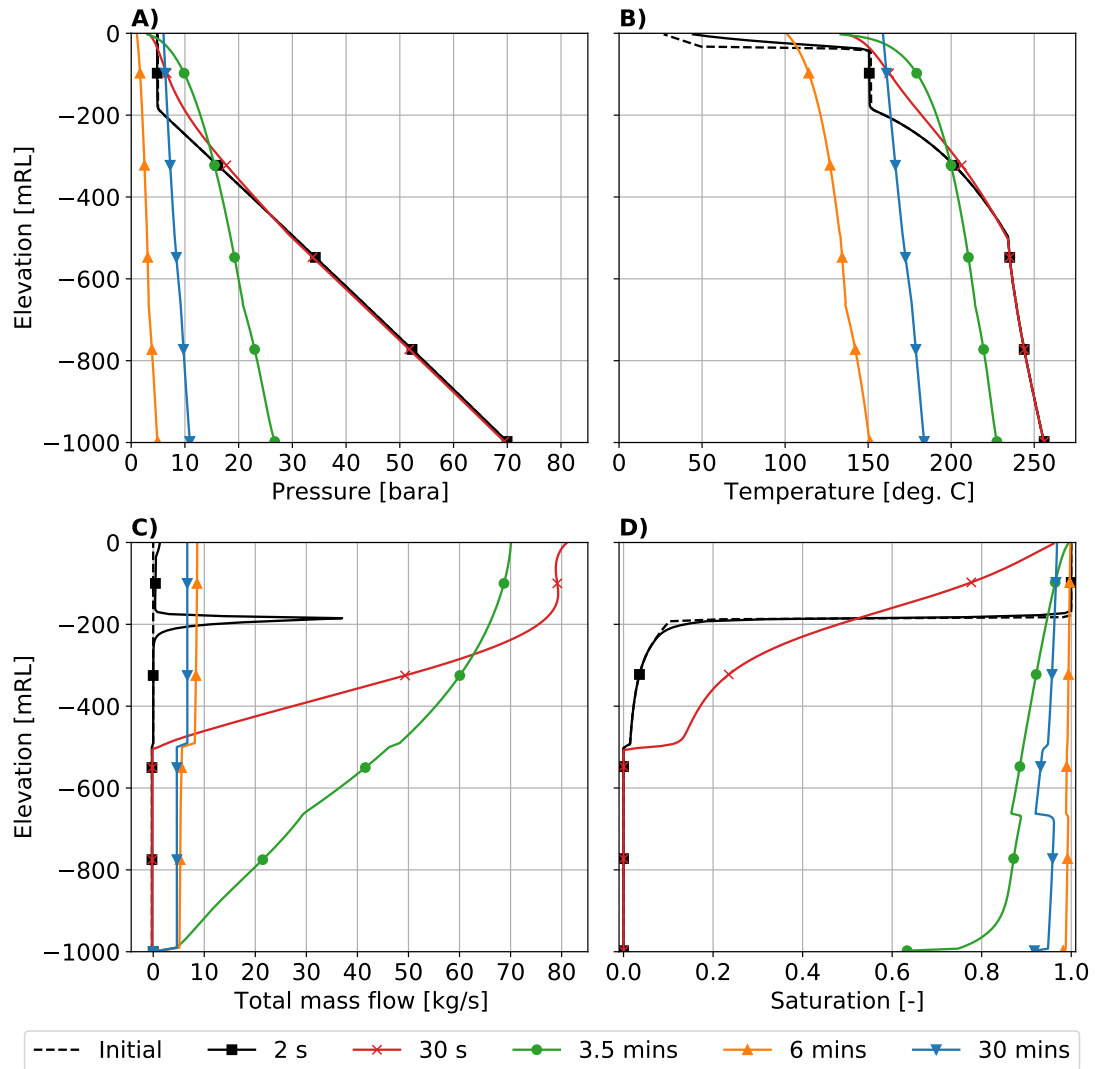


FIGURE 8.5: Profiles of A) pressure, B) temperature, C) total mass flow and D) vapour saturation as the well described in Section 8.1.2 is opened to flow.

from a silencer at atmospheric pressure to the surface network, which operates at the separator pressure. After 30 minutes, production from the well has stabilised and reached operating conditions.

This case study highlights the fact that a simulator requires counter-flow capabilities to completely model even the most fundamental wellbore processes, in this case, opening a well to flow. Additionally, the initial conditions used for this case study, which were found using simulation, highlight some of the difficulties faced when interpreting shut-in data from hot geothermal wells. We suggest that simulation of shut-in wells could be used to aid and confirm the interpretation of this data.

### 8.1.3 Modelling wellbore shut-in (Test Case 3)

Test Case 3 models the rapid shut-in of a flowing geothermal well. The well is 1000 m long and fed by a hot liquid feed at the bottom of the well. Initially, the well is flowing steadily with a total mass flow rate of 7.6325 kg/s (200 kg/m<sup>2</sup>/s). After 60 days of production at this rate, the mass flow boundary condition is decreased linearly from 7.6325 kg/s to zero over 60 seconds. Further information on the initial conditions, simulation parameters and feed-zone conditions are given in Section 5.3.1.3.

Shutting in the well causes rapid pressure, temperature, saturation and mass flow transients within the well, which are shown in Figures 8.6 and 8.7 below. Here, the steady flowing conditions at 60 days are shown by the dashed lines. The remaining profiles show the wellbore conditions at various times after 60 days.

After 22 seconds (i.e., while the wellhead is still being closed), the wellhead mass flow boundary condition is approximately 4.915 kg/s. The decrease in mass flow causes the two-phase flow to compress and increases pressures within the well. This compression is shown by the non-linear total mass flow profile in Figure 8.6 C) (in black).

After 1 minute 15 seconds (15 seconds after the well is shut completely), pressure in the well has increased further. Figure 8.7 shows that counter-flow is occurring above -600 mRL at this time. Figure 8.7 A) (in red) shows liquid down-flow below -100 mRL. Liquid down-flow above -100 mRL is small because this section of the well has already dried out. Meanwhile, Figure 8.7 B) shows that the vapour flows up the well, although at a lower rate. This results in a net down-flow of mass, which is shown in Figure 8.6 C).

Over the next 12 minutes, the counter-flow described above results in the separation of the phases. Liquid accumulates at the bottom of the well and vapour accumulates at the top. This is shown (in green) in Figure 8.6 D) by the decrease in vapour saturation below -600 mRL. In this section of the well, the static vapour mass fraction is less than 2.5 %. A high vapour saturation column exists above this point, which is shown in Figure 8.6 by the rapid increase in vapour saturation at -600 mRL. In this section of the well, the static vapour mass fraction is above 97 %. The separation of the phases into low and high vapour saturation columns is also evident in the pressure profiles in Figure 8.6 A), where the change in pressure gradient corresponds to the interface between the low

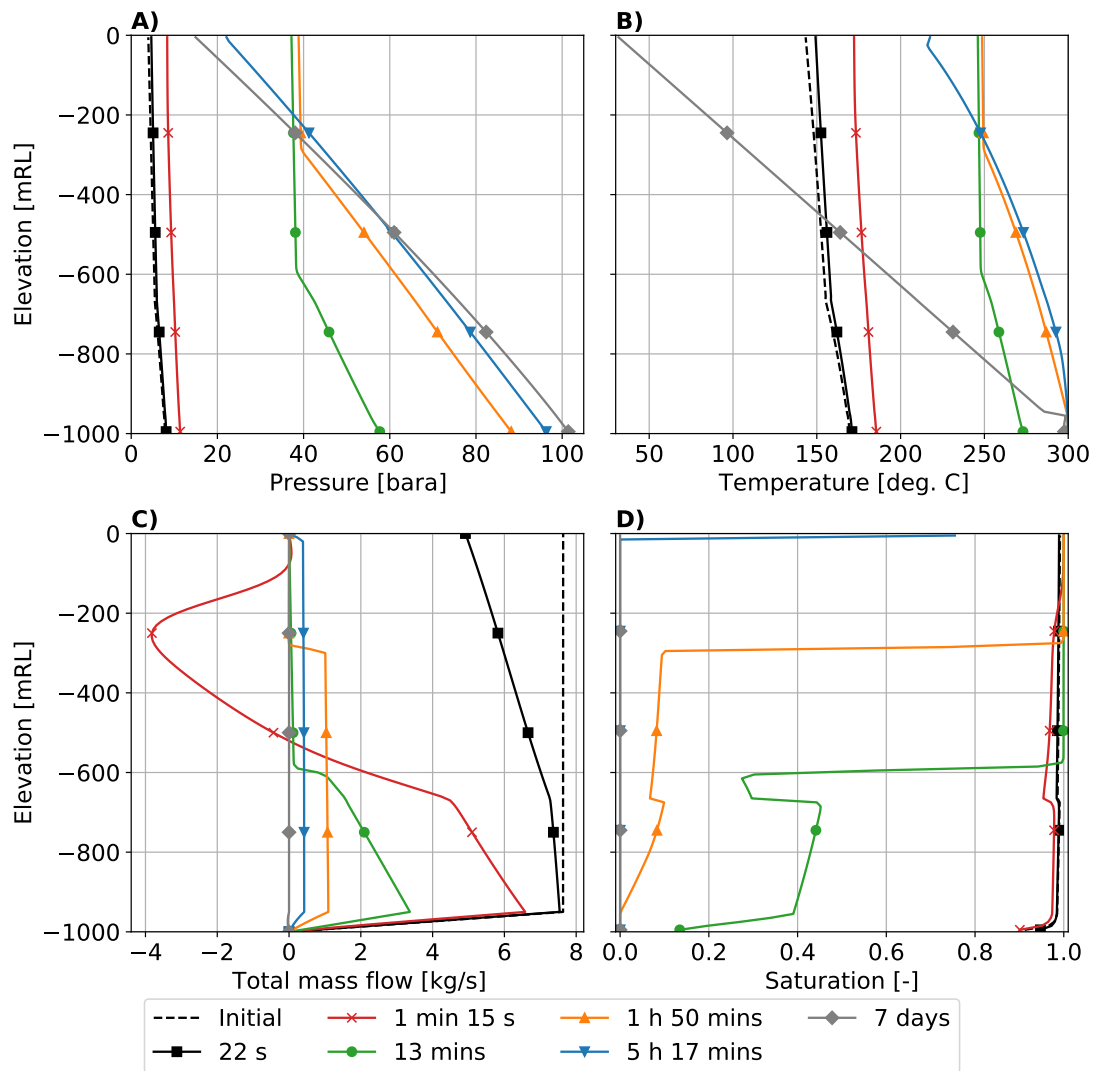


FIGURE 8.6: Wellbore profiles of A) pressure B) temperature C) total mass flow and D) vapour saturation at different times after 60 days of production.

and high vapour saturation columns. Note that the decrease in vapour saturation at -660 mRL in Figure 8.6 D) at all times is caused by a change in well diameter at this elevation.

After 1 hour and 50 minutes (shown in yellow), the water level in the well has risen from -600 mRL to -300 mRL. Figure 8.6 D) shows that vapour saturation below -300 mRL has decreased further over this period. The increase in the height of the low vapour saturation column is caused by the inflow of fluid from the feed-zone at the bottom of the well at approximately 1 t/h as shown in Figure 8.6 C). Additionally, heat loss to the formation slowly condenses the vapour cap, causing a small down-flow of liquid, which is shown in Figure 8.7 A).

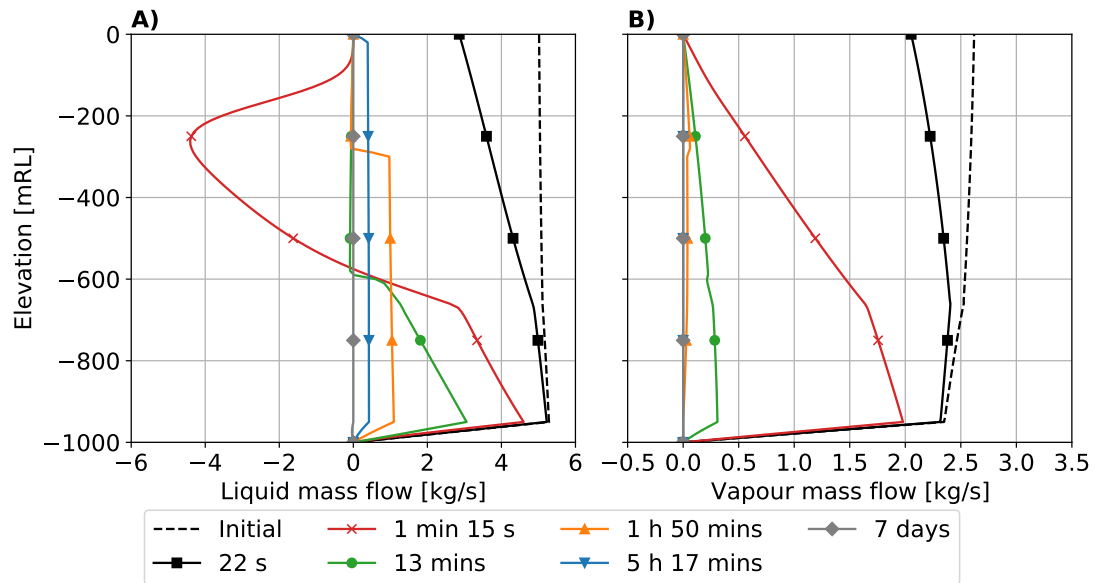


FIGURE 8.7: Wellbore profiles of A) liquid mass flow and B) vapour mass flow at different times after 60 days of production.

After 5 hours 17 minutes (shown in blue), the majority of the well is liquid water, and two-phase fluid only exists in the top 10 m of the well. Bottomhole pressures rise as the height of the liquid column increases. This reduces the influx from the feed-zone further to approximately 0.5 kg/s. After a further 15 minutes, the top of the well has condensed to liquid conditions.

Over the next seven days, heat transfer to the formation slowly cools the liquid column until the temperatures in the well are equal to the reservoir temperatures. The isothermal temperature profile at the bottom of the well is caused by the feed being spread over multiple blocks. Here, fluid flows in from the top half of the feed-zone interval, then flows down and out into the bottom half of the feed interval. The inflow of mass is equal and opposite to the outflow.

#### 8.1.4 Discussion

This section discusses the modelling of counter-flow due to boiling in shut-in geothermal wells. The importance of this process in geothermal applications has not been discussed in the literature. Test Case 12 studied a shallow geothermal well while it heated up. This case indicated that counter-flow processes occurred as soon as boiling began at the bottom of the well. The resulting energy transport heated the top section of the well

and caused a hot vapour cap to form. Counter-flow played the same role in the initial conditions used to simulate the opening of a realistic multi-feed well to flow, which was discussed in Section 8.1.2. We have concluded that shut-in conditions for geothermal wellbores with boiling cannot be modelled accurately without modelling counter-flow, despite the fact that the mass flows that occur during these counter-flow processes are very small.

Currently, pressure and temperature data from shut-in wells are interpreted manually using industry expertise to gain information about the characteristics of the reservoir. The cases presented above show that processes such as boiling in the wellbore and inter-zonal flow can obscure reservoir temperatures and present difficulties when analysing wellbore data. We suggest that wellbore simulation should be used to aid and confirm the interpretation of temperatures in shut-in wellbores. The simulations discussed above indicate that if a wellbore simulator is to be used in this capacity, it must be able to simulate counter-flow processes.

The counter-flow processes that occur as a well heats up are driven by formation heat transfer, a process that we approximate with the analytical model discussed in Section 3.4. Wellbore heat-up simulations could be improved by representing heat transfer in the formation numerically. A more accurate representation of heat flux in these simulations will change how wellbore conditions evolve over time, especially as extended periods of injection will modify the formation temperature close to the well. However, improving the representation of formation heat transfer in our model will not change the main conclusion of this section. Namely, that counter-flow is a fundamental heat transfer process that must be modelled when two-phase flow occurs within shut-in geothermal wells.

Finally, in Section 8.1.3 we modelled the rapid shutting-in of a flowing geothermal wellbore. This simulation showed that counter-flow processes occurred after shutting the wellhead. In this case, counter-flow allowed liquid to accumulate in the bottom of the well, while vapour accumulated in the top of the well. This case and the simulation of the opening of a well to flow highlight that a transient geothermal wellbore simulator must be able to model counter-flow processes to simulate the wide range of flow scenarios that

are possible within a geothermal well, including processes as fundamental as opening and closing a well to flow.

## 8.2 Modelling discharge stimulation of geothermal wells

Most geothermal wells are self-discharging, meaning that flow is initiated by first shutting the well, allowing it to heat up and build pressure and then simply opening the wellhead to flow. However, non-self-discharging wells fail to build sufficient pressure after being shut-in. Instead, the top section of the well is filled with cold air, and the water level may be hundreds of metres below the wellhead. These non-self-discharging wells can occur in conventional liquid-dominated geothermal systems and have been reported in Indonesia, the Philippines, Costa Rica, Iceland, Iran, Mexico, Kenya and New Zealand (Mubarok and Zarrouk, 2017).

The inability of a well to flow can be caused by a combination of several factors, including (Mubarok and Zarrouk, 2017):

- Deep natural water levels, e.g. due to high elevation terrain,
- Slow temperature recovery after well testing,
- Cold temperatures in the shallow formation,
- Damage to the well during drilling,
- Low reservoir permeability, and
- Significant pressure or temperature decline in the reservoir

If a well will not self-discharge for any of the reasons listed above, then it must be stimulated. Two methods of discharge stimulation are gas lifting and air compression. The cost of a typical air compression program is approximately 50,000 USD. By comparison, gas lift programs, which are typically seen as a last resort when other stimulation methods do not work, can cost anywhere between 150,000 – 500,000 USD per well, depending on the cost of mobilising a coiled tubing unit (Mubarok and Zarrouk, 2017). Given the high cost of these methods, it is worthwhile to use numerical simulation to provide low-cost insight to aid decision making.



Numerical simulation of air compression and air-lifting processes requires a transient wellbore simulator with air-water capabilities to: 1) model the air cap in the top section of the shut-in well, and 2) model the injection of air at either the wellhead or at depth to stimulate flow. We discussed the extension of our simulator for modelling air-water mixtures in Chapter 7.

Section 8.2.1 presents the stationary conditions that are used as initial conditions. Discharge stimulation using air-lifting and air compression are then discussed in Sections 8.2.2 and 8.2.3, respectively. The same wellbore is used for both simulations, and its properties are given in Tables 8.3 and 8.4.

### 8.2.1 Initial conditions

When shut-in, non-self-discharging wells have a water level below the wellhead. It is important that the correct initial conditions, which include the column of air at the top of the well, are used. Otherwise, it is unlikely that the simulation will accurately represent the stimulation process. The initial conditions and conceptual model of the well are discussed below.

TABLE 8.3: Reservoir and atmospheric feed for the discharge stimulation simulations in Sections 8.2.2 and 8.2.3.

Name	Elevation [mRL]	$P$ [bara]	$h_{f_{mix}}$ [kJ/kg]	$\alpha$ [kg/s/Pa]	$x_f^a$ [-]
Atmospheric feed	0 to -10	1.01325	25	3E-06	0.9999
Reservoir	-990 to -1000	60	1085	3E-06	0

TABLE 8.4: Wellbore and simulation parameters for the discharge stimulation simulations in Sections 8.2.2 and 8.2.3.

Wellhead elevation	0 mRL
Length	1000 m
Inclination	0 °
Diameter	0.2 m
Completion diameter	0.3 m
Discretisation	Uniform, 100 elements
Slip model	Shi et al. (2005)
Feed-zones	Table 8.3
Pipe roughness	4.5E-05
Bottomhole boundary	Closed
Formation temperatures	Figure 8.8 B)

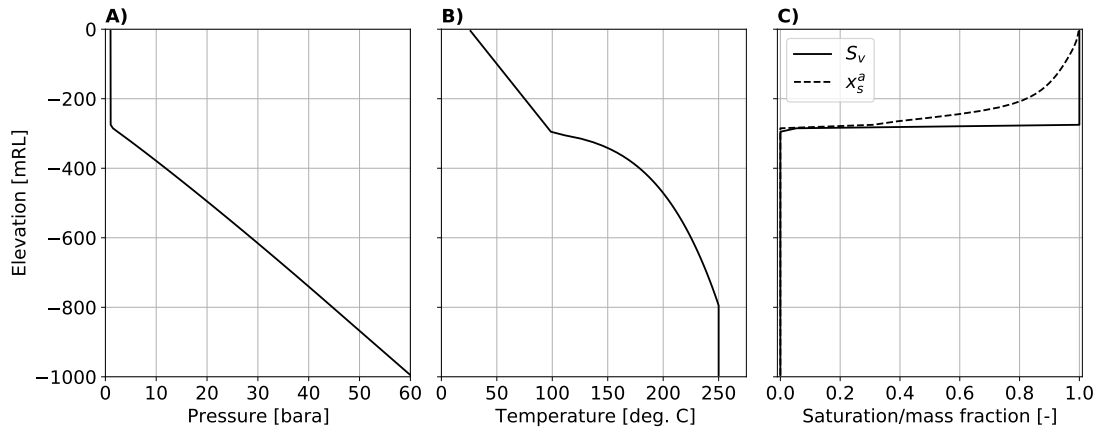


FIGURE 8.8: Initial conditions for A) pressure, B) temperature and C) vapour saturation and air mass fraction for a well with a water level below the wellhead.

We use a 1000 m vertical well with a constant diameter of 0.2 m to demonstrate the simulation of discharge stimulation. Additional wellbore and simulation properties are given in Table 8.4. The reservoir is modelled using a single feed, with properties given in Table 8.3, located at the bottom of the well. These feed properties correspond to liquid water at approximately 60 bara and 250 °C. The formation temperature profile, shown in Figure 8.8 B), is constant with time and corresponds to a liquid-dominated geothermal system. Here, the top 300 m has a linear transition between 25 – 100 °C. Below this depth, it has the boiling point for depth profile with a maximum temperature of 250 °C. The inflow and outflow of air through the wellhead is controlled with a ‘one-way atmospheric feed’. As discussed in Section 7.2.3.1, this allows air into the well if the wellhead pressure drops below atmospheric conditions, but prevents flow out of the well. The properties of the atmospheric feed are given in Table 8.3 and correspond to 25 °C air at sea level. The productivity of the atmospheric feed was chosen to be the same as the reservoir productivity.

To simulate the initial conditions for this well, we first inject liquid water at 25 °C, then shut the wellhead for a period of 30 days. After shut-in, the hydrostatic pressure of the liquid column in the well is greater than the bottomhole feed-zone pressure. As a result, wellbore fluid flows out into the feed. This reduces the pressure in the wellhead block slightly, so that it is below the pressure of the atmospheric feed. This activates the feed and draws air into the well. The water level continues to drop until equilibrium conditions are reached, which occur when the net mass flow into the well is zero.

Simulating the wellhead in this way allows us to predict whether a well is likely to self-discharge, or whether it will require stimulation. Unlike the test case presented in Section 8.1.2, which models the opening of a realistic well to flow, this test case failed to build up pressure after 30 days of being shut. Figure 8.8 A) shows the wellhead pressure only increases to 1.4 bara due to a small amount of boiling, and the shut-in water level is approximately 275 m below the wellhead. This is shown by the change in pressure gradient in Figure 8.8 A) and the rapid increase in vapour saturation in Figure 8.8 C). We discuss the stimulation of this wellbore using gas lifting and air injection below.

### 8.2.2 Gas lifting

Gas lifting involves pumping a compressed gas to some depth below the water level in the well using a coiled tubing unit. While air has been used in past gas lifting operations, nitrogen is a more common choice of gas because it is chemically stable and non-corrosive (Mubarok and Zarrouk, 2017). However, as air is approximately 80% nitrogen, the density, solubility, and heat capacity of the two gases are similar, meaning air-water simulations can be used to gain valuable insight into gas lifting in geothermal wells.

The air-lifting of a geothermal well has been simulated by Akbar et al. (2016), however, their simulation did not explicitly model air. Instead, they initialised the entire wellbore with an approximate air-water mixture, which had a modified density and heat capacity. We present a more physically accurate simulation of air-lifting, which starts from the realistic static conditions given in Figure 8.8. Air was injected at a depth of 705 m, approximately 425 m below the water level, at different mass flow rates until sustainable flow was achieved. In Section 8.2.2.1, we discuss air injection at a mass flow rate of 0.01 kg/s, which failed to stimulate the well. In Section 8.2.2.2, we discuss how sustained discharge is achieved by increasing the mass flow rate to 0.05 kg/s.

#### 8.2.2.1 Failed lift

Initially, air was injected at a mass flow rate of 0.01 kg/s at a depth of 705 m for 30 minutes. It was found that this rate, depth and time period of injection was insufficient to raise the water level to the wellhead and stimulate discharge. Instead, Figure 8.9 A),

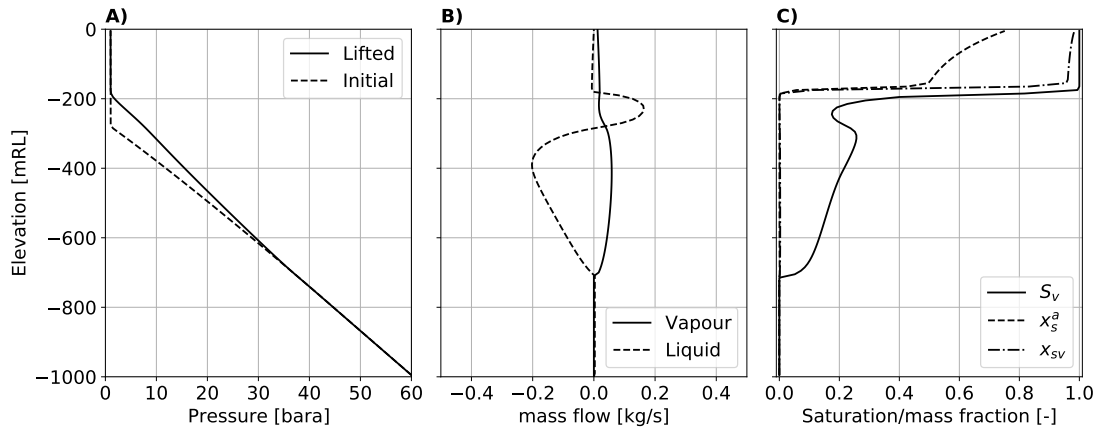


FIGURE 8.9: Conditions after 30 minutes of air-lifting at 0.01 kg/s for A) pressure, B) liquid and vapour mass flow rates and C) vapour saturation,  $S_v$ , static vapour mass fraction,  $x_{sv}$ , and static air mass fraction,  $x_s^a$  for the well described in Section 8.2.1.

which compares the initial pressure to the pressure at 30 minutes, shows that the water level was only lifted by approximately 100 m. This lift failed because, at this injection rate, the velocity of the air rising through the liquid is not large enough to entrain the water and prevent down-flow in the liquid phase. This down-flow is shown in Figure 8.9 B) which plots the phase mass flows.

The injected air, which has mixed with a small amount of water vapour, rises slowly from the top of the liquid column located at -200 mRL. As the air-water vapour mixture flows towards the wellhead, it loses energy to the cooler formation. This causes some of the water vapour to condense, which is shown in Figure 8.9 C) by the increase in static air mass fraction from 50% to 75% between the water level and the wellhead. This results in a small down-flow of liquid condensate in the top 200 m of the well, which is shown in Figure 8.9 B).

### 8.2.2.2 Successful lift

The well was successfully discharged by increasing the rate of air injection to 0.05 kg/s. The results of this simulation are shown in Figure 8.10 and are discussed below. Note that the drop in temperature at -700 mRL in Figure 8.10 B) is caused by injecting cold air at 25 °C.

Figure 8.10 C) shows (in black) that three minutes of injection at the increased rate of 0.05 kg/s has caused up-flow above -700 mRL. At this increased flow rate, the velocity of

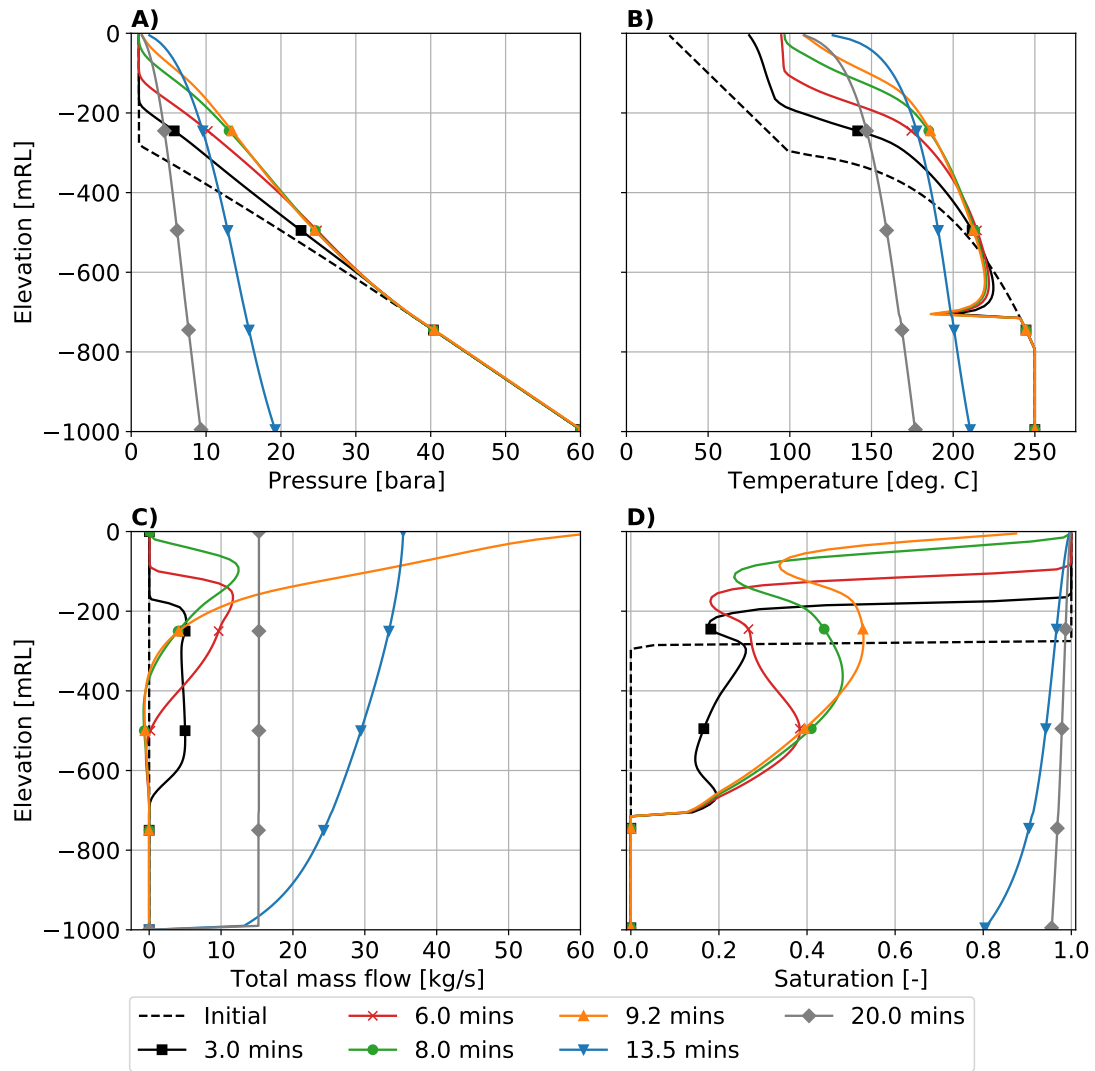


FIGURE 8.10: Results of successful air-lifting with an air mass flow rate of 0.05 kg/s showing A) pressure, B) temperature, C) total mass flow and D) vapour saturation at various times for the well described in Section 8.2.1.

the vapour phase is large enough to begin dragging the liquid up the well. Additionally, the expansion of the gas as it progresses up the well displaces the water above it.

After approximately 9 minutes of injection, the water level reaches the wellhead, as shown by the pressure profiles in Figure 8.10 A) and the drop in wellhead saturation in Figure 8.10 D) (shown in orange). Shortly after this time, sufficient heat has been transported up the well for flashing to begin at the wellhead. This causes a significant increase in mass flow at the wellhead, as shown in Figure 8.10 C) (similarly in orange). This flashing is required for the wellbore to flow without additional air injection. Pressures drop rapidly as flashing progresses down the well. Figure 8.10 A) shows (in blue) that

after 13.5 minutes of injection, approximately 4 minutes after the onset of flashing, the bottomhole pressure has dropped below 20 bara, and hot geothermal fluid is produced at 12 kg/s from the feed-zone. After 20 minutes, the well has reached stable conditions and no longer requires stimulation.

### 8.2.3 Air compression

During air compression, air is injected at the wellhead to depress the water level and force fluid into the reservoir. After allowing the cold fluid to be heated by the reservoir, the wellhead is opened to flow. The rapid drop in wellbore pressures causes production from the feed-zone and an influx of hot fluid. Flashing induced in the well by the inflowing fluid is hopefully sufficient to sustain low hydrostatic pressures and continue production. The wellhead pressure required to stimulate flow varies depending on the feed properties and the length and temperature of the fluid column. We model air compression using two separate simulations. The first simulation models the compression of the liquid column, and the second simulates opening the well to flow. The simulations are discussed in Sections 8.2.3.1 and 8.2.3.2 and the results are shown in Figures 8.11 and 8.12, respectively.

#### 8.2.3.1 Compression simulation

The compression simulation starts from the stable initial conditions given in Figure 8.8 above. Air is injected at the wellhead at a fixed rate of 0.05 kg/s for 5 hours using a source term in the top block of the wellbore model. Injecting air increases the wellhead pressure, which increases bottom-hole pressure, forcing fluid into the feed-zone and lowering the water level. After compression, Figure 8.11 A) shows the wellhead pressure has risen to approximately 27 bara, and Figure 8.11 C) shows the water level has dropped 300 m down to -600 mRL. The well remains shut-in for 24 h to allow time for it to heat up.

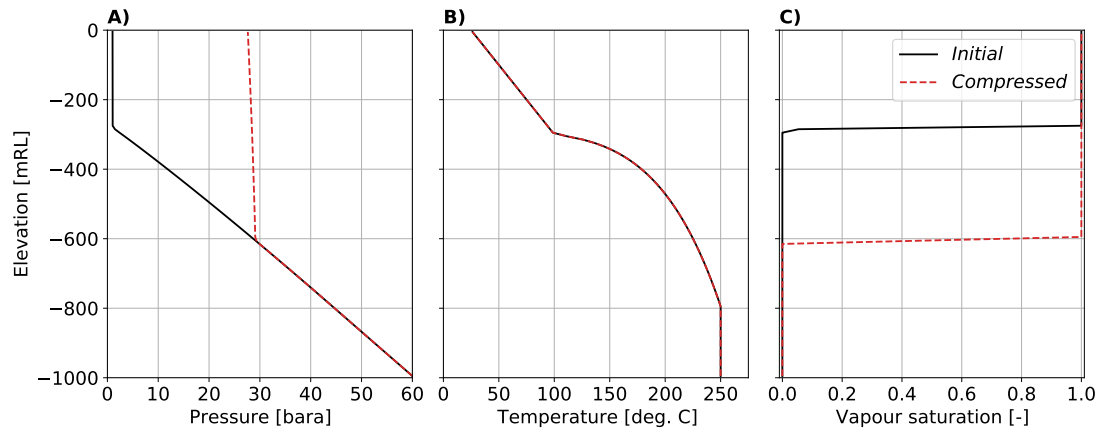


FIGURE 8.11: A) pressure, B) temperature and C) vapour saturation and mass fraction profiles before and after air compression (0.05 kg/s injected for five hours) for the well described in Section 8.2.1.

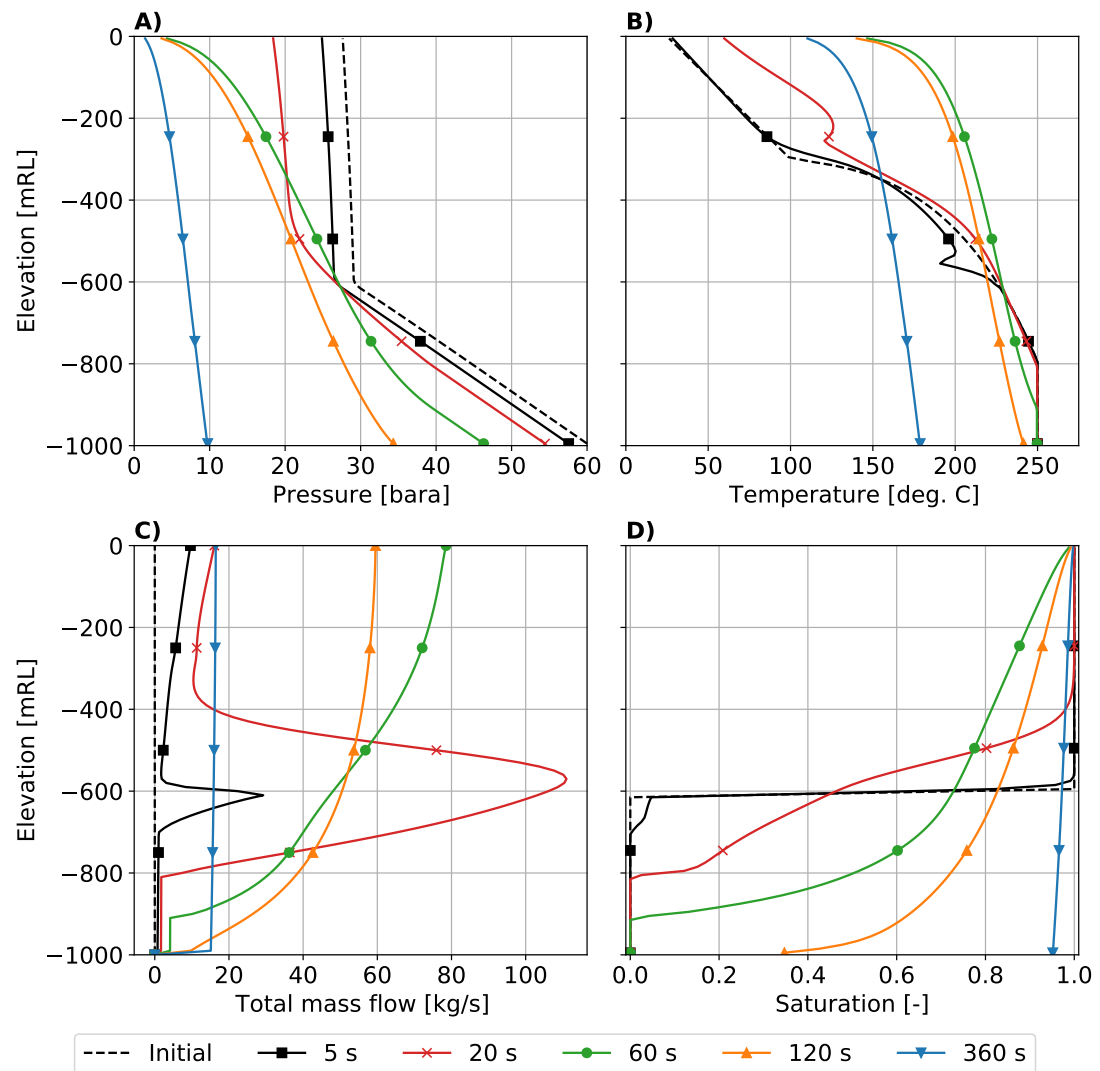


FIGURE 8.12: Results of discharge stimulation with a compressed pressure of 27 bara showing A) pressure, B) temperature, C) total mass flow and D) vapour saturation at various times after opening the well described in Section 8.2.1.

### 8.2.3.2 Depressurisation simulation

Wellbore flow is initiated by dropping the wellhead pressure from the compressed value of 27 bara to atmospheric conditions (1.01325 bara) linearly over 60 seconds. Figure 8.12 A) shows that reducing the wellhead pressure causes the pressure to drop at all depths. Figure 8.12 D), which shows vapour saturation, indicates that this pressure drop initiated a rapid flashing process almost immediately at the air-water interface. This is because the liquid at this depth is at 225 °C and has a saturation pressure of approximately 25 bara (only 2 - 3 bara below the compressed pressure). The onset of rapid flashing causes fluid expansion and the acceleration of the two-phase fluid up the well, as shown by the large increase in mass flow in Figure 8.12 C). During this process, extending over 60 seconds, the wellhead temperature increases from 25°C to 150°C. This rapid heating would place considerable thermal stress on the well. Figure 8.12 D) shows that the entire well has flashed after two minutes, which decreases the bottomhole pressure further, causing overpressure in the feed and the production of hot geothermal fluid. After six minutes, the feed produces fluid at approximately 15 kg/s, and the wellbore flow has stabilised.

### 8.2.4 Discussion

In this section, we discussed the modelling of two methods of stimulating a non-self-discharging well. These were air-lifting and air compression, neither of which have previously been simulated for geothermal wells using an air-water equation of state. Our test case was relatively simple and designed to showcase the simulation of these methods using an air-water equation of state. It was also intended to highlight the importance of using realistic initial conditions, including the correct water level. Despite being a conceptually simple well, the simulations of discharge stimulation involved complex wellbore processes. For example, counter-flow in the failed gas-lift simulations, sharp changes in vapour saturation moving with time and space in the compression simulation, and very rapid flashing processes in the depressurisation simulation. This demonstrates the ability of our simulator to model complex flows of air-water mixtures.

The case presented above has relatively high formation temperatures in the bottom third of the well. In other cases, the temperatures in non-self-discharging wells are significantly



lower than in our example, meaning hot geothermal fluid must be produced from the reservoir before flashing will occur. This leads to more prolonged and more difficult stimulation procedures. Internal circulation between feeds can have a similar effect. These effects can be so pronounced that, in some cases, air compression will not induce flow and stimulation using gas lifting can be difficult. The case studies present in this chapter show that our simulator is capable of modelling the complex processes that occur during discharge stimulation. This makes it a useful tool to aid decision making for more difficult stimulation procedures, for example, to determine whether stimulation via air compression is likely to be successful or whether air-lifting will be required.

### 8.3 Summary

This chapter demonstrates that our simulator can model complex transient processes that occur within geothermal wells. In Section 8.1 we investigated cases of counter-flow. The main conclusion from this investigation was that counter-flow plays a fundamental role in shut wells, even though the mass flows that occur during this process are very small. In the heat-up simulations for a shut-in well, counter-flow transported heat to the top of the well, which allowed a hot gas cap to exist alongside cold formation temperatures. The initial conditions used to simulate the opening of a well to flow, discussed in Section 8.1.2, showed that these counter-flow processes are important in more realistic wells. They also highlight that the temperature profiles taken from shut-in wells do not necessarily reflect reservoir conditions when processes such as boiling and inter-zonal flow occur. Finally, in Section 8.1.3, we modelled the shutting-in of a flowing geothermal well. In this case, counter-flow caused the liquid phase to accumulate at the bottom of the well and vapour to accumulate at the wellhead.

Section 8.2 discussed the stimulation of a non-self-discharging well using air-lifting and injection. The initial conditions used for the discharge simulations were found using simulation. It was important that these initial conditions represent the correct water level within the well. To do this, a "one way atmospheric feed" was used to approximate wellhead operations by allowing air into the well but preventing outflow. This allowed the water level to drop and allowed us to determine whether the well would build pressure over time or whether it would require stimulation. The well was successfully induced

to flow using both stimulation methods. The simulations included complex wellbore processes such as counter-flow, moving interfaces between air and water columns and very rapid flashing processes. These simulations are good examples of the ability of our simulator to model complex flows of air-water mixtures.

## Chapter 9

# Conclusions

The research presented in this thesis targets the development of a new transient geothermal wellbore simulator. In this chapter, we discuss the conclusions drawn from this research. Section 9.1 discusses the findings from our review of the governing conservation equations and constitutive equations that are used in geothermal wellbore modelling. Section 9.2 summarises the numerical implementation and testing of our simulator. Section 9.3 summarises the conclusions drawn from our studies of counter-flow processes in geothermal wells and discharge stimulation. Section 9.4 discusses the direction of our future research into geothermal wellbore modelling, and Section 9.5 summarises the main achievements of this research.

### 9.1 Model formulation

The first step in this research was to determine the best form of the conservation equations to solve in our geothermal wellbore simulator. Our literature review indicated that many variations of multi-phase flow models have been used, however, there is limited information about how each model was derived, what assumptions were made in their derivation and how they relate to other models presented in the literature.

To clarify these problems, conservation equations from the geothermal wellbore modelling literature were compared to the three equation model, a physically accurate form

of the mass, momentum and energy conservation equations. We found that some formulations of the momentum equation commonly used in steady-state models do not correctly conserve momentum flux. Additionally, some simulators do not correctly conserve momentum across changes in wellbore area.

Comparisons on our test cases of the approximate momentum flux terms with the physically accurate model indicated that the approximation of momentum flux terms affects the results of wellbore simulations. However, the impact of incorrectly conserving momentum is relatively small for moderate mass flows and relatively high wellhead pressures.

We also found that some models use approximate representations of kinetic energy, using average variables. However, we found that this approximation made little difference to the results of our test case simulations.

Despite the results of these investigations indicating that the impact of these modelling assumptions on simulation results was relatively small, we do not think the use of approximate conservation equations is justified or necessary when developing a new transient wellbore simulator. Therefore, we used a formulation of the mass, momentum and energy equations that correctly conserved these quantities.

Constitutive equations are required in geothermal wellbore simulators to describe phase slip, pipe friction, wellbore heat transfer and reservoir sources. These were discussed in Chapter 3. Of particular interest to us was selecting a slip model capable of modelling complex flow scenarios such as counter-flow. We found the drift flux model, with empirical parameters given by Shi et al. (2005), was the most appropriate model of those we considered. The correlation by Shi et al. (2005) was chosen because of its smooth nature, ability to model counter-flow, and optimisation for flow in wide-diameter pipes.

## 9.2 Numerical implementation and testing

Our numerical implementation of the equations governing flow in geothermal wellbores is fully implicit in time. We also solve the constitutive equation for slip simultaneously with the three discrete conservation equations for four primary variables. This method

provides explicit knowledge of the upwinding direction of both phases. Experimentation showed that the best primary variables for our simulator were pressure, temperature (swapped with vapour saturation for two-phase conditions), vapour velocity and liquid volume flux. Vapour saturation was used rather than the more common choice of flowing mass fraction because the flowing mass fraction is not well defined for counter-flow cases or cases with zero mass flow. The partial pressure of air is included as a fifth primary variable when simulating the flow of air-water mixtures.

Chapter 5 discussed the testing of our simulator. We verified our simulator was programmed correctly using analytical solutions for simplified single-phase steady-state flow. A semi-analytical verification case for the flow of air-water mixtures was also presented following the development of our air-water equation of state. We then validated our model against steady-state pressure and temperature data from flowing wells. Finally, we presented a set of 15 test cases, which demonstrated that our simulator can model the diverse range of flow conditions that are possible within geothermal wells, including production, injection and counter-flow scenarios. These test cases were used during the development of our simulator to determine the best primary variable combination for our simulator and troubleshoot issues experienced with modelling counter-flow. In the future, these test cases will provide a benchmark for simulator development and for comparisons between simulators.

### 9.3 Wellbore modelling case studies

We used our simulator to investigate counter-flow processes that occur in geothermal wells. The main conclusion from this investigation was that counter-flow plays a fundamental role in the shutting in of a well, despite the fact that the mass flows occurring during this process are very small. In the heat-up simulations for a shut-in test well, counter-flow transported heat to the top of the well, which allowed a high-temperature, high-saturation two-phase zone to exist alongside cold formation temperatures. The initial conditions used to simulate the opening of a well to flow showed that these counter-flow processes are also important in full-scale geothermal wells. These case studies also highlighted that the temperature profiles taken from shut-in wells do not necessarily reflect reservoir conditions when boiling and inter-zonal flow processes occur. In the final

counter-flow case, we modelled the shutting in of a flowing geothermal well. In this case, counter-flow caused the liquid phase to accumulate at the bottom of the well and the vapour phase to accumulate at the wellhead. We, therefore, concluded that a geothermal wellbore simulator must be able to model counter-flow processes if it is to be used to simulate the shutting in of wells. This has implications for the simulation of cases that are of interest to the geothermal industry, for example, using simulation to aid the interpretation of wellbore data, pressure transient analysis, the analysis of completion testing, and discharge stimulation.

We also used our simulator to model the stimulation of a non-self-discharging well by using air-lifting and air compression. These simulations required the use of an air-water equation of state, the implementation of which was discussed in Chapter 7. This equation of state can be easily modified to model different NCG components.

Simulation was used to obtain realistic conditions, including the water level, within a shut-in well. These simulations were used to predict whether or not a well required stimulation. They were also used as initial conditions for the simulations of discharge stimulation. These simulations made use of a one-way feed-zone located at the wellhead that allowed air into the well when the wellhead pressure dropped below the atmospheric pressure but prevented outflow when the well started to pressurise. We simulated the successful discharge of a test well, with a water level 300 m below the wellhead, using air-lifting and air compression. These simulations included complex wellbore behaviour such as counter-flow, moving interfaces between the columns of air and water, and very rapid flashing processes, all well represented by our simulator.

## 9.4 Future work

In this section, we discuss the direction of our future research into geothermal wellbore modelling. Section 9.4.1 discusses transient geothermal wellbore processes that we intend to investigate. Section 9.4.2 discusses the research associated with improving the representation of the reservoir in our simulator. Finally, Section 9.4.3 outlines the future research into the formulation of our geothermal wellbore simulator.

#### 9.4.1 Transient wellbore investigations

Our investigations indicated that counter-flow must be modelled when simulating the shutting-in of a well. However, our experimentation also indicated that counter-flow processes can play a role during production scenarios. For example, in some cases, counter-flow may influence transient cycling processes, in which the mass flow rate, pressure and enthalpy at the wellhead oscillate with time. In other cases, counter-flow may cause the accumulation of liquid at the bottom of a well resulting in the suppression of production from deep feeds. These hypotheses require further investigation. This thesis demonstrates that our simulator is capable of undertaking these investigations.

Another interesting future application of our transient wellbore simulator is the modelling of processes leading to loss-of-control incidents during geothermal drilling. These can occur due to the circulation of hot fluids from deep in the well towards the surface, which causes flashing processes to begin within the well. The influx of high-enthalpy fluid from a shallow feed can cause similar effects. In other cases, loss of circulation can cause the fluid level, and thus the pressure, in a well to suddenly drop, which allows flashing processes to begin (Finger and Blankenship, 2010). To model these processes, a simulator must be able to represent multiple feed-zones, rapid flashing processes caused by the influx of fluid, changes in water level, and potentially counter-flow. In this thesis, we have demonstrated that our simulator is capable of modelling processes such as these. Numerical investigations of loss-of-control incidents would provide a greater understanding of the nature of these processes, which may help to improve their recognition and management. Simulations such as these will also provide a valuable educational resource that demonstrates how these processes differ from loss-of-control incidents that occur in oil and gas wells.

One of our main interests moving forward is the simulation of transient wellbore behaviour during completion testing. Completion testing occurs directly after drilling finishes and is used to identify feeds, assess the need for intervention, and estimate the future performance of the well. Pressure transient analysis undertaken on data gathered during injection testing can be affected by inter-zonal flow, which in some cases can be

difficult or impossible to suppress (Zarrouk and McLean, 2019). If the inflow is high-enthalpy, boiling may occur during testing. The impact of these processes can, in some cases, be difficult to identify. In other cases, it can lead to misinterpretation of the data (Zarrouk and McLean, 2019). Numerical investigations of injection cases that feature inter-zonal flow and boiling would help to improve the understanding of how these processes impact the data collected during injection testing. A greater understanding of these processes could help to identify their occurrence from measured wellbore data. To simulate these processes, a simulator must be able to model injection at the wellhead, inter-zonal flow and counter-flow processes. The reservoir is influential during completion testing. Therefore, simulations of these processes would benefit from an improved representation of the reservoir. We discuss this in the following section.

#### **9.4.2 Improved modelling of the reservoir**

Currently, our simulator uses approximate analytical models to represent the reservoir. Specifically, a simple productivity model based on radial Darcy flow is used to model the reservoir feeds, and the heat conduction between the well and formation is approximated analytically using the model by Ramey (1962). We intend to investigate how more accurate representations of these reservoir processes affect the results of the simulations presented in this thesis. The complexity of the formation representation should be increased progressively. First, 1D radial mass and energy conservation equations should be used to represent each reservoir feed-zone. Following on from this, 1D radial heat conduction equations should be used to represent the heat transfer between the reservoir and well in non-feed-zone layers.

These 1D radial equations cannot model the vertical heat and mass transfer that occurs in geothermal reservoirs. A 3D numerical representation of the reservoir is required to model this process (similar to what is available in T2WELL). Therefore, our long-term goal is to couple our transient wellbore simulator with the Waiwera reservoir simulator. This would require studying different methods for coupling reservoir and wellbore simulators, for example, loose-lagged, semi-implicit and fully implicit methods. The impact of these different coupling methods on simulation results should be assessed, and the scenarios for which each method is appropriate should be determined.



### 9.4.3 Improved modelling of transient flow in geothermal wells

As we discussed in Chapter 3, the constitutive models used in geothermal wellbore simulation require an in-depth review. Of particular interest to us is the constitutive equation for modelling phase slip. This review should present and compare the slip models used in geothermal wellbore modelling. Such a review should assess the ability of each model to reproduce data from flow in vertical and deviated pipes with wide diameters. Comparisons of the predictive ability of each correlation on geothermal wellbore data should be aimed at determining under what conditions each correlation performs well. Finally, verification data for each correlation currently used in geothermal wellbore simulators should be presented to help ensure that these relationships are programmed correctly.

The numerical formulation used in our simulator is fully implicit in time and solves the constitutive model for slip simultaneously with the governing conservation equations. This implementation differs from other transient geothermal wellbore simulators. Future work includes investigating how different numerical formulations impact geothermal wellbore simulations. For example, assessing the impact of solving the slip equation simultaneously as a fourth equation and comparing our fully-implicit formulation to semi-implicit formulations used in other simulators. We wish to determine how different formulations such as these affect simulation results and the numerical performance of a geothermal wellbore simulator. Additionally, we want to determine under what conditions different numerical formulations are beneficial. The test cases discussed in Chapter 5 will provide a benchmark for these comparisons.

A recent study by Pereira and Fowler (2020) suggested that non-equilibrium dynamics influence the point at which gas exsolves from the liquid phase in oil and gas wells. As this process is similar to flashing in geothermal wells, their work suggests that non-equilibrium fluid dynamics may influence geothermal wellbore simulation. While we believe factors such as the accurate representation of the reservoir would be more influential on the results of geothermal wellbore simulation, it would be valuable to assess the impact of more complex two-phase models on flow within geothermal wells.

## 9.5 Achievements

This thesis discussed the development, testing and applications of our transient geothermal wellbore simulator. We have shown our simulator is suitable for modelling cases of interest to the geothermal industry, including:

- Completion testing, which may include inter-zonal flow and counter-flow processes.
- Simulation of discharge from wells that are difficult to stimulate.
- Cycling processes, in which we suspect that counter-flow will be influential.
- Loss-of-control incidents in geothermal wells.
- The shutting in of geothermal wells, which can be required for initial conditions, during simulations of completion testing and loss-of-control incidents, and may also be useful to aid the interpretation of data from geothermal wells.

The geothermal wellbore simulators presented in the literature have not demonstrated that they are able to simulate counter-flow caused by boiling processes, which we have shown to be important in geothermal wells. By comparison, between the test cases presented in Chapter 5 and the transient investigations presented in Chapter 8, we have demonstrated that our simulator is capable of modelling a wide range of complex transient flows that may occur in cases such as those listed above.

## Appendix A

# Derivations of the conservation equations

The one-dimensional, area-averaged conservation equations are derived by integrating three-dimensional conservation equations over the cross-sectional area of the pipe. In general, the cross-sectional average of a variable  $f$  is defined as:

$$\langle f \rangle_A \equiv \frac{1}{A} \int_A f(x, y, z, t) dA. \quad (\text{A.1})$$

Here,  $x$ ,  $y$  and  $z$  are Cartesian coordinates,  $t$  is time, and  $A$  is the cross-sectional area of the pipe.

The derivation of the area averaged conservation equations requires the product of variables to be averaged over the cross-sectional area of the pipe. In general, the average of the products does not equal the product of the averages, i.e. for any variables  $f = \langle f \rangle_A + f'$  and  $g = \langle g \rangle_A + g'$  (Berry et al., 2014):

$$\langle fg \rangle_A = \langle f \rangle_A \langle g \rangle_A + \langle f'g' \rangle_A. \quad (\text{A.2})$$

However, Berry et al. (2014) notes that the covariance terms that result from the averaging process are usually assumed to be negligible, i.e.  $\langle f'g' \rangle_A = 0$  and  $\langle fg \rangle_A = \langle f \rangle_A \langle g \rangle_A$ . We make the same approximation when developing our transient geothermal wellbore

simulator and make use of the notational simplification  $\langle f \rangle \Rightarrow f$  in the remainder of this thesis.

Using the notation defined in Section 2.1.1, Berry et al.'s (2014) mass, momentum and energy balance equations, as well as the saturation evolution equation, can be written for the liquid phase as:

$$\frac{\partial S_l \rho_l A}{\partial t} + \frac{\partial S_l \rho_l u_l A}{\partial s} = -\Gamma A_{int} A, \quad (\text{A.3})$$

$$\begin{aligned} \frac{\partial S_l \rho_l u_l A}{\partial t} + \frac{\partial S_l A (\rho_l u_l^2 + P_l)}{\partial s} = & \\ & P_{int} A \frac{\partial S_l}{\partial s} + P_l S_l \frac{\partial A}{\partial s} + A \lambda (u_v - u_l) \\ & - \Gamma A_{int} u_{int} A - F_{wall,l} - F_{f,v} + S_l \rho_l A \mathbf{g} \cdot \hat{\mathbf{n}}_{axis}, \quad (\text{A.4}) \end{aligned}$$

$$\begin{aligned} \frac{\partial S_l \rho_l e_{Tl} A}{\partial t} + \frac{\partial S_l u_l A (\rho_l e_{Tl} + P_l)}{\partial s} = & \\ & P_{int} u_{int} A \frac{\partial S_l}{\partial s} - \bar{P}_{int} A \mu (P_l - P_v) + \bar{u}_{int} A \lambda (u_v - u_l) \\ & + \Gamma A_{int} \left( \frac{P_{int}}{\rho_{int}} - h_{Tl,int} \right) A + Q_{int,l} + Q_{wall,l}, \quad (\text{A.5}) \end{aligned}$$

and

$$\frac{\partial S_l A}{\partial t} + u_{int} A \frac{\partial S_l}{\partial s} = A \mu (P_l - P_v) - \frac{\Gamma A_{int} A}{\rho_{int}}. \quad (\text{A.6})$$

Similarly, the conservation equations for the vapour phase are written as:

$$\frac{\partial S_v \rho_v A}{\partial t} + \frac{\partial S_v \rho_v u_v A}{\partial s} = \Gamma A_{int} A, \quad (\text{A.7})$$

$$\begin{aligned} \frac{\partial S_v \rho_v u_v A}{\partial t} + \frac{\partial S_v A (\rho_v u_v^2 + P_v)}{\partial s} = & \\ & P_{int} A \frac{\partial S_v}{\partial s} + P_v S_v \frac{\partial A}{\partial s} + A \lambda (u_l - u_v) \\ & + \Gamma A_{int} u_{int} A - F_{wall,v} - F_{f,l} + S_v \rho_v A \mathbf{g} \cdot \hat{\mathbf{n}}_{axis}, \quad (\text{A.8}) \end{aligned}$$

$$\begin{aligned} \frac{\partial S_v \rho_v e_{T_v} A}{\partial t} + \frac{\partial S_v u_v A (\rho_v e_{T_v} + P_v)}{\partial s} = \\ P_{int} u_{int} A \frac{\partial S_v}{\partial s} - \bar{P}_{int} A \mu (P_v - P_l) + \bar{u}_{int} A \lambda (u_l - u_v) \\ - \Gamma A_{int} \left( \frac{P_{int}}{\rho_{int}} - h_{T_v, int} \right) A + Q_{int, v} + Q_{wall, v}, \quad (\text{A.9}) \end{aligned}$$

and

$$\frac{\partial S_v A}{\partial t} + u_{int} A \frac{\partial S_v}{\partial s} = A \mu (P_v - P_l) + \frac{\Gamma A_{int} A}{\rho_{int}}. \quad (\text{A.10})$$

For two-phase flow, the saturation of one phase is always known from the relationship  $S_l + S_v = 1$ . Therefore, either (A.6) or (A.10) is not required (typically (A.6) is discarded) reducing the total number of equations to seven.

In Equations (A.3)–(A.10),  $A_{int}$  is the interfacial surface area per unit volume of two-phase mixture and  $\Gamma$  is the net transfer of mass is the net mass transfer per unit interfacial area from the liquid to the vapour phase. The interface pressure and average interface pressure are  $P_{int}$  and  $\bar{P}_{int}$ , respectively. Similarly,  $u_{int}$  and  $\bar{u}_{int}$  are the interface velocity and average interface velocity. The total phase enthalpy at the interface is given by  $h_{T\beta, int}$ . Frictional forces are modelled by  $F_{wall, \beta}$ , which is the friction force from the wall acting on phase  $\beta$ , and  $F_{f, \beta^*}$ , which is the friction force acting on phase  $\beta$  by phase  $\beta^*$ . Finally,  $Q_{int, \beta}$  and  $Q_{wall, \beta}$  represent the heat transfer to phase  $\beta$  from the interface and wall, respectively. The pressure and velocity relaxation coefficients are given by  $\mu$  and  $\lambda$ , respectively. These parameters describe how the two-phase system approaches thermodynamic equilibrium (Berry et al., 2014). The term  $\mathbf{g} \cdot \hat{\mathbf{n}}_{axis}$  is the component of gravity in the axial direction, which is equal to  $-g \, dz/ds$  in our notation.

This set of seven equations is reduced to a set of six equations by assuming the pressure of the liquid and vapour phases are equal (i.e.,  $P_l = P_v = P_{int} = P$ ). Summing (A.6) and (A.10) gives:

$$\frac{\partial S_l A + S_v A}{\partial t} + u_{int} A \frac{\partial S_l + S_v}{\partial s} = 0 \quad (\text{A.11})$$

Noting that  $S_v + S_l = 1$  means that all terms in (A.11) are zero. This leaves six equations describing the conservation of mass, momentum and energy of each phase.

Assuming that the temperatures of the phases are equal to the saturation temperature (i.e.,  $T_l = T_v = T_{sat}(P)$ ) and that a slip model can provide an adequate description

of two-phase processes allows us to simplify this set of six equations to a set of three equations, which described the behaviour of the fluid mixture. These manipulations are given in Sections A.1, A.2 and A.3 below.

## A.1 Mixture conservation of mass

The mass conservation of a fluid mixture, given the assumptions discussed above, is reached simply by summing the phase mass balances:

$$\frac{\partial}{\partial t}[S_l \rho_l A + S_v \rho_v A] + \frac{\partial}{\partial s}[S_l \rho_l u_l A + S_v \rho_v u_v A] = 0 \quad (\text{A.12})$$

In our model, the wellbore cross-sectional area,  $A$ , is constant with time. Removing it from the time derivative and dividing the equation by  $A$  gives:

$$\frac{\partial}{\partial t}[S_l \rho_l + S_v \rho_v] + \frac{1}{A} \frac{\partial}{\partial s}[S_l \rho_l u_l A + S_v \rho_v u_v A] = 0 \quad (\text{A.13})$$

which is the same as that mass conservation equation that we use in our simulator (without the external source of mass).

### A.1.1 Mass conservation in terms of mixture variables

To write (A.13) in terms of mixture variables, we first note the definitions of the mixture density,  $\rho_{mix}$ , and the mixture velocity  $u_{mix}$ . These are defined as:

$$\rho_{mix} = \rho_l S_l + \rho_v S_v \quad (\text{A.14})$$

and

$$u_{mix} = \frac{F_m}{\rho_{mix}} = \frac{\rho_l u_l S_l + \rho_v u_v S_v}{\rho_{mix}} \quad (\text{A.15})$$

Noting that  $F_m = u_{mix} \rho_{mix} = S_l \rho_l u_l + S_v \rho_v u_v$ , and substituting these definitions into (A.13) results in:

$$\frac{\partial \rho_{mix}}{\partial t} + \frac{1}{A} \frac{\partial}{\partial s}[A \rho_{mix} u_{mix}] = 0 \quad (\text{A.16})$$

## A.2 Mixture conservation of momentum

The conservation of momentum equation for a two-phase mixture is reached by summing the momentum conservation equations for each phase ((A.4) and (A.8)). Summing these equations gives:

$$\begin{aligned}
& \frac{\partial(S_l \rho_l u_l A + S_v \rho_v u_v A)}{\partial t} + \frac{\partial(S_l A (\rho_l u_l^2 + P_l) + S_v A (\rho_v u_v^2 + P_v))}{\partial s} = \\
& \quad P_{int} A \frac{\partial S_l}{\partial s} + P_{int} A \frac{\partial S_v}{\partial s} \\
& \quad + P_l S_l \frac{\partial A}{\partial s} + P_v S_v \frac{\partial A}{\partial s} + A \lambda(u_v - u_l) + A \lambda(u_l - u_v) \\
& \quad - \Gamma A_{int} u_{int} A + \Gamma A_{int} u_{int} A - F_{fwall,l} - F_{fwall,v} - F_{f,v} - F_{f,l} \\
& \quad + S_l \rho_l A \mathbf{g} \cdot \hat{\mathbf{n}}_{axis} + S_v \rho_v A \mathbf{g} \cdot \hat{\mathbf{n}}_{axis} \quad (A.17)
\end{aligned}$$

Simplifying this equation by noting that pressures are equal ( $P = P_l = P_v = P_{int}$ ), the velocity relaxation terms are equal and opposite (i.e.,  $A \lambda(u_v - u_l) + A \lambda(u_l - u_v) = 0$ ), and factorising results in:

$$\begin{aligned}
& \frac{\partial(S_l \rho_l u_l A + S_v \rho_v u_v A)}{\partial t} + \frac{\partial(S_l A (\rho_l u_l^2 + P) + S_v A (\rho_v u_v^2 + P))}{\partial s} = \\
& \quad P A \frac{\partial(S_l + S_v)}{\partial s} + (S_l + S_v) P \frac{\partial A}{\partial s} - F_{fwall,l} - F_{fwall,v} - F_{f,v} - F_{f,l} \\
& \quad + (S_l \rho_l + S_v \rho_v) A \mathbf{g} \cdot \hat{\mathbf{n}}_{axis} \quad (A.18)
\end{aligned}$$

Substituting in the relationship  $S_l + S_v = 1$  means the first term on the right-hand side of (A.18) reduces to zero:

$$\begin{aligned}
& \frac{\partial S_l \rho_l u_l A + S_v \rho_v u_v A}{\partial t} + \frac{\partial S_l A (\rho_l u_l^2 + P) + S_v A (\rho_v u_v^2 + P)}{\partial s} = \\
& \quad P \frac{\partial A}{\partial s} - F_{fwall,l} - F_{fwall,v} - F_{f,v} - F_{f,l} + (S_l \rho_l + S_v \rho_v) A \mathbf{g} \cdot \hat{\mathbf{n}}_{axis} \quad (A.19)
\end{aligned}$$

Expanding the spatial derivative (term 2) on the left hand side of (A.19) results in:

$$\begin{aligned} \frac{\partial(S_l \rho_l u_l A + S_v \rho_v u_v A)}{\partial t} + \frac{\partial(AS_l \rho_l u_l^2 + AS_v \rho_v u_v^2)}{\partial s} + \frac{\partial AP}{\partial s} = \\ P \frac{\partial A}{\partial s} - F_{fwall,l} - F_{fwall,v} - F_{f,v} - F_{f,l} \\ + (S_l \rho_l + S_v \rho_v) A \mathbf{g} \cdot \hat{\mathbf{n}}_{axis} \quad (\text{A.20}) \end{aligned}$$

Then expanding the third term on the left hand side of (A.20) using the product rule and simplifying gives:

$$\begin{aligned} \frac{\partial(S_l \rho_l u_l A + S_v \rho_v u_v A)}{\partial t} + \frac{\partial(AS_l \rho_l u_l^2 + AS_v \rho_v u_v^2)}{\partial s} + A \frac{\partial P}{\partial s} = \\ - F_{fwall,l} - F_{fwall,v} - F_{f,v} - F_{f,l} \\ + (S_l \rho_l + S_v \rho_v) A \mathbf{g} \cdot \hat{\mathbf{n}}_{axis} \quad (\text{A.21}) \end{aligned}$$

Berry et al. (2014) defines the interface friction term,  $F_{f,k'}$ , as:

$$F_{f,k'} = \frac{\rho_{mix} A_{int} A}{8} \left[ C_D |u_k - u_{k'}| + \frac{12\nu}{r_0} \right] (u_{k'} - u_k) \quad (\text{A.22})$$

where  $k = l, v$  and  $k' = v, l$ ,  $r_0$  is the effective radius of a droplet/bubble,  $C_D = 0.5$  and the mixture kinematic viscosity is  $\nu = S_l \nu_l + S_v \nu_v$ . The interface frictional forces,  $F_{f,v}$  and  $F_{f,l}$ , as defined in (A.22), are equal and opposite and therefore cancel in (A.21).

Finally, we assume the wall friction terms for each phase can be modelled with a single empirical relationship, represented in this work by  $C\tau$ , where  $C$  is the circumference of the well. We also assume constant area with time. These assumptions result in:

$$\begin{aligned} \frac{\partial(S_l \rho_l u_l + S_v \rho_v u_v)}{\partial t} + \frac{1}{A} \frac{\partial(AS_l \rho_l u_l^2 + AS_v \rho_v u_v^2)}{\partial s} + \frac{\partial P}{\partial s} = \\ - \frac{C}{A} \tau + (S_l \rho_l + S_v \rho_v) \mathbf{g} \cdot \hat{\mathbf{n}}_{axis} \quad (\text{A.23}) \end{aligned}$$



Noting that  $C/A = 2/r$  and that  $\mathbf{g} \cdot \hat{\mathbf{n}}_{axis} = -g \cos \theta = -gdz/ds$ , where  $dz$  and  $ds$  are the height and hypotenuse of an elemental triangle, we are left with:

$$\begin{aligned} \frac{\partial(S_l \rho_l u_l + S_v \rho_v u_v)}{\partial t} + \frac{1}{A} \frac{\partial(AS_l \rho_l u_l^2 + AS_v \rho_v u_v^2)}{\partial s} + \frac{\partial P}{\partial s} = \\ -\frac{2}{r} \tau - (S_l \rho_l + S_v \rho_v) g \frac{dz}{ds} \end{aligned} \quad (\text{A.24})$$

which is the same as the mixture momentum conservation equation used in our simulator (note the momentum source term included in 2.43 has not been included in A.24).

### A.2.1 Momentum conservation in terms of mixture variables

A slip model is required to write the momentum conservation equation in terms of mixture variables. In Section A.2.1.1, we present the derivation of this equation using the drift-flux model. This follows the derivation given by Pan, Oldenburg, Wu and Pruess (2011), which we reproduce here for completeness. Then, in Section A.2.1.2, we derive the relationship between the relative velocity and the drift velocity and use this to derive the mixture momentum equation written in terms of the relative velocity.

#### A.2.1.1 Drift-flux formulation

Starting from the mixture momentum equation:

$$\begin{aligned} \frac{\partial(S_l \rho_l u_l + S_v \rho_v u_v)}{\partial t} + \frac{1}{A} \frac{\partial(AS_l \rho_l u_l^2 + AS_v \rho_v u_v^2)}{\partial s} + \frac{\partial P}{\partial s} = \\ -\frac{2}{r} \tau - (S_l \rho_l + S_v \rho_v) g \frac{\partial z}{\partial s} \end{aligned} \quad (\text{A.25})$$

We first use the definition of the mass flux (A.15) to write the time derivative in terms of mixture variables:

$$\frac{\partial(\rho_{mix} u_{mix})}{\partial t} + \frac{1}{A} \frac{\partial(AS_l \rho_l u_l^2 + AS_v \rho_v u_v^2)}{\partial s} + \frac{\partial P}{\partial s} = -\frac{2}{r} \tau - \rho_{mix} g \frac{\partial z}{\partial s} \quad (\text{A.26})$$

Next, the momentum flux derivative:

$$\frac{1}{A} \frac{\partial}{\partial s} [A (S_l \rho_l u_l^2 + S_v \rho_v u_v^2)] \quad (\text{A.27})$$

must be written in terms of mixture variables. For simplicity, we only work on the terms within the round brackets in (A.27) in the derivation given below.

First, we note the phase velocities can be written in terms of mixture variables (Pan, Oldenburg, Wu and Pruess, 2011). The vapour velocity is:

$$u_v = C_0 \frac{\rho_{mix}}{\rho_{mix}^*} u_{mix} + \frac{\rho_l}{\rho_{mix}^*} u_d, \quad (\text{A.28})$$

and the liquid velocity is:

$$u_l = \frac{1 - S_v C_0}{1 - S_v} \frac{\rho_{mix}}{\rho_{mix}^*} u_{mix} - \frac{S_v}{1 - S_v} \frac{\rho_v}{\rho_{mix}^*} u_d. \quad (\text{A.29})$$

Substituting these definitions into the momentum flux term results in:

$$\begin{aligned} S_l \rho_l u_l^2 + A S_v \rho_v u_v^2 = \rho_l S_l \left( \frac{1 - S_v C_0}{1 - S_v} \frac{\rho_{mix}}{\rho_{mix}^*} u_{mix} - \frac{S_v}{1 - S_v} \frac{\rho_v}{\rho_{mix}^*} u_d \right)^2 \\ + \rho_v S_v \left( C_0 \frac{\rho_{mix}}{\rho_{mix}^*} u_{mix} + \frac{\rho_l}{\rho_{mix}^*} u_d \right)^2 \end{aligned} \quad (\text{A.30})$$

Expanding out the brackets results in:

$$\begin{aligned} S_l \rho_l u_l^2 + A S_v \rho_v u_v^2 = \\ \rho_l S_l \left[ \left( \frac{1 - S_v C_0}{1 - S_v} \frac{\rho_{mix}}{\rho_{mix}^*} u_{mix} \right)^2 - 2 \frac{(1 - S_v C_0) S_v \rho_v \rho_{mix}}{(1 - S_v)^2 (\rho_{mix}^*)^2} u_{mix} u_d - \left( \frac{S_v}{1 - S_v} \frac{\rho_v}{\rho_{mix}^*} u_d \right)^2 \right] \\ + \rho_v S_v \left[ \left( C_0 \frac{\rho_{mix}}{\rho_{mix}^*} u_{mix} \right)^2 + 2 C_0 \frac{\rho_{mix} \rho_l}{(\rho_{mix}^*)^2} u_{mix} u_d + \left( \frac{\rho_l}{\rho_{mix}^*} u_d \right)^2 \right] \end{aligned} \quad (\text{A.31})$$

Expanding further, and then factorising out  $u_{mix}^2$ ,  $2u_{mix}u_d$  and  $u_d$  results in:

$$\begin{aligned} S_l \rho_l u_l^2 + A S_v \rho_v u_v^2 = u_{mix}^2 \left[ \frac{S_v \rho_v C_0^2 \rho_{mix}^2}{(\rho_{mix}^*)^2} + \frac{\rho_l \rho_{mix}^2 (1 - S_v C_0)^2}{(1 - S_v)(\rho_{mix}^*)^2} \right] \\ + 2u_{mix}u_d \left[ \frac{S_v \rho_v \rho_l \rho_{mix} C_0}{(\rho_{mix}^*)^2} - \frac{S_v \rho_v \rho_l \rho_{mix} (1 - S_v C_0)}{(1 - S_v)(\rho_{mix}^*)^2} \right] \\ + u_d^2 \left[ \frac{S_v \rho_v \rho_l^2}{(\rho_{mix}^*)^2} + \frac{\rho_l S_v^2 \rho_v^2}{(1 - S_v)(\rho_{mix}^*)^2} \right] \end{aligned} \quad (\text{A.32})$$

We will now work on terms 1, 2 and 3 on the right-hand side of A.32 individually.

In the drift-flux formulation of the momentum conservation equation, we wish to end up with the term  $\rho_{mix}u_{mix}^2$  in the momentum flux derivative. The easiest way to achieve this is to add  $\rho_{mix}u_{mix}^2 - \rho_{mix}u_{mix}^2$  to term 1 in (A.32). Term 1 becomes:

$$\begin{aligned} & \rho_{mix}u_{mix}^2 - \rho_{mix}u_{mix}^2 + u_{mix}^2 \left[ \frac{S_v \rho_v C_0^2 \rho_{mix}^2}{(\rho_{mix}^*)^2} + \frac{\rho_l \rho_{mix}^2 (1 - S_v C_0)^2}{(1 - S_v)(\rho_{mix}^*)^2} \right] = \\ & \rho_{mix}u_{mix}^2 + \frac{\rho_{mix}u_{mix}^2}{(1 - S_v)(\rho_{mix}^*)^2} [S_v \rho_v (1 - S_v) \rho_{mix} C_0^2 + \rho_l \rho_{mix} (1 - S_v C_0)^2 - (1 - S_v)(\rho_{mix}^*)^2] \end{aligned} \quad (\text{A.33})$$

Noting that:

$$S_v \rho_v (1 - S_v) \rho_{mix} C_0^2 = (1 - S_v)(S_v \rho_v C_0)^2 + S_v \rho_v \rho_l (1 - S_v)^2 C_0^2, \quad (\text{A.34})$$

$$\rho_l \rho_{mix} (1 - S_v C_0)^2 = S_v \rho_l \rho_v (1 - S_v C_0)^2 + \rho_l^2 (1 - S_v)(1 - S_v C_0)^2, \quad (\text{A.35})$$

and

$$\begin{aligned} (1 - S_v)(\rho_{mix}^*)^2 &= (1 - S_v)(S_v \rho_v C_0)^2 \\ &+ (1 - S_v)(2S_v \rho_v \rho_l C_0(1 - S_v C_0)) + (1 - S_v)\rho_l^2(1 - S_v C_0)^2. \end{aligned} \quad (\text{A.36})$$

Substituting (A.34) – (A.36) back into (A.33) and simplifying gives:

$$\begin{aligned} & \rho_{mix}u_{mix}^2 + \\ & \frac{\rho_{mix}u_{mix}^2}{(1 - S_v)(\rho_{mix}^*)^2} [S_v \rho_v \rho_l ((1 - S_v)^2 C_0^2 - 2(1 - S_v)(1 - S_v C_0)C_0 + (1 - S_v C_0)^2)] \end{aligned} \quad (\text{A.37})$$

Noting that:

$$\begin{aligned} (1 - S_v)^2 C_0^2 - 2(1 - S_v)(1 - S_v C_0)C_0 + (1 - S_v C_0)^2 &= \\ ((1 - S_v)C_0 - (1 - S_v C_0))^2 &= (C_0 - 1)^2 \end{aligned} \quad (\text{A.38})$$

Substituting (A.38) back into (A.37) gives the final simplified form of the  $u_{mix}^2$  term from (A.32):

$$u_{mix}^2 \left[ \frac{S_v \rho_v C_0^2 \rho_{mix}^2}{(\rho_{mix}^*)^2} + \frac{\rho_l \rho_{mix}^2 (1 - S_v C_0)^2}{(1 - S_v)(\rho_{mix}^*)^2} \right] = \rho_{mix} u_{mix}^2 + \frac{S_v \rho_v \rho_l \rho_{mix} u_{mix}^2}{(1 - S_v)(\rho_{mix}^*)^2} (C_0 - 1)^2 \quad (\text{A.39})$$

Similarly, the  $2u_{mix}u_d$  term in (A.32) simplifies to:

$$2u_{mix}u_d \left[ \frac{S_v \rho_v \rho_l \rho_{mix} C_0}{(\rho_{mix}^*)^2} - \frac{S_v \rho_v \rho_l \rho_{mix} (1 - S_v C_0)}{(1 - S_v)(\rho_{mix}^*)^2} \right] \quad (\text{A.40})$$

$$= \frac{2u_{mix}u_d S_v \rho_v \rho_l \rho_m}{(1 - S_v)(\rho_{mix}^*)^2} [(1 - S_v)C_0 - (1 - S_v C_0)] \quad (\text{A.41})$$

$$= \frac{2u_{mix}u_d S_v \rho_v \rho_l \rho_m}{(1 - S_v)(\rho_{mix}^*)^2} (C_0 - 1) \quad (\text{A.42})$$

Finally, the  $u_d^2$  term in (A.32) simplifies to:

$$u_d^2 \left[ \frac{S_v \rho_v \rho_l^2}{(\rho_{mix}^*)^2} + \frac{\rho_l S_v^2 \rho_v^2}{(1 - S_v)(\rho_{mix}^*)^2} \right] = \frac{S_v \rho_v \rho_l u_d^2}{(1 - S_v)(\rho_{mix}^*)^2} [(1 - S_v)\rho_l + S_v \rho_v] = \frac{S_v \rho_v \rho_l \rho_{mix} u_d^2}{(1 - S_v)(\rho_{mix}^*)^2} \quad (\text{A.43})$$

Substituting (A.39), (A.42) and (A.43) back into (A.32) gives:

$$S_l \rho_l u_l^2 + A S_v \rho_v u_v^2 = \rho_{mix} u_{mix}^2 + \frac{S_v \rho_v \rho_l \rho_{mix}}{(1 - S_v)(\rho_{mix}^*)^2} [u_{mix}^2 (C_0 - 1)^2 + 2u_{mix}u_d (C_0 - 1) + u_d^2] \quad (\text{A.44})$$

Simplifying this equation further gives:

$$S_l \rho_l u_l^2 + A S_v \rho_v u_v^2 = \rho_{mix} u_{mix}^2 + \frac{S_v \rho_v \rho_l \rho_{mix}}{(1 - S_v)(\rho_{mix}^*)^2} [u_{mix} (C_0 - 1) + u_d]^2 \quad (\text{A.45})$$

Substituting, (A.45) back into (A.26) gives the momentum conservation equation in terms of mixture variables and drift-flux parameters:

$$\begin{aligned} \frac{\partial}{\partial t} [\rho_{mix} u_{mix}] + \frac{1}{A} \frac{\partial}{\partial s} [A \rho_{mix} u_{mix}^2] + \\ \frac{1}{A} \frac{\partial}{\partial s} \left[ A \frac{S_v \rho_v \rho_l \rho_{mix}}{(1 - S_v)(\rho_{mix}^*)^2} [u_{mix}(C_0 - 1) + u_d]^2 \right] + \frac{\partial P}{\partial s} = -\frac{2}{r} \tau - \rho_{mix} g \frac{\partial z}{\partial s} \end{aligned} \quad (\text{A.46})$$

### A.2.1.2 Relative velocity formulation

To reach the relative velocity form of the mixture momentum equation, we first derive the formula for the relative velocity,  $u_r$ , in terms of the drift-flux empirical parameters ( $C_0$  and  $u_d$ ).

To do this, we substitute the definitions of the phase velocities given by Pan, Oldenburg, Wu and Pruess (2011) into the definition of the relative velocity:

$$u_r = u_v - u_l = C_0 \frac{\rho_{mix}}{\rho_{mix}^*} u_{mix} + \frac{\rho_l}{\rho_{mix}^*} u_d - \frac{1 - S_v C_0}{1 - S_v} \frac{\rho_{mix}}{\rho_{mix}^*} u_{mix} + \frac{S_v}{1 - S_v} \frac{\rho_v}{\rho_{mix}^*} u_d \quad (\text{A.47})$$

Factorising out common terms and simplifying gives:

$$u_r = \frac{1}{(1 - S_v) \rho_{mix}^*} [(1 - S_v) C_0 - (1 - S_v C_0)] \rho_{mix} u_{mix} + (\rho_l (1 - S_v) + S_v \rho_v) u_d \quad (\text{A.48})$$

Simplifying the terms inside the square brackets in (A.48) and factorising out  $\rho_{mix}$  gives the relationship between  $u_r$ ,  $C_0$  and  $u_d$ :

$$u_r = \frac{\rho_{mix}}{(1 - S_v) \rho_{mix}^*} ((C_0 - 1) u_{mix} + u_d) \quad (\text{A.49})$$

Rearranging (A.49) for  $u_d$  and substituting into (A.46) gives:

$$\begin{aligned} \frac{\partial}{\partial t} [\rho_{mix} u_{mix}] + \frac{1}{A} \frac{\partial}{\partial s} [\rho_{mix} u_{mix}^2] + \\ \frac{1}{A} \frac{\partial}{\partial s} \left[ \frac{S_v \rho_v \rho_l \rho_{mix}}{(1 - S_v)(\rho_{mix}^*)^2} \left[ \frac{(1 - S_v) \rho_{mix}^*}{\rho_{mix}} u_r \right]^2 \right] + \frac{\partial P}{\partial s} = -\frac{2}{r} \tau - \rho_{mix} g \frac{\partial z}{\partial s} \end{aligned} \quad (\text{A.50})$$

Simplifying this equation gives the conservation of momentum equation in terms of mixture variables and the relative velocity:

$$\begin{aligned} \frac{\partial}{\partial t}[\rho_{mix}u_{mix}] + \frac{1}{A} \frac{\partial}{\partial s} [A\rho_{mix}u_{mix}^2] \\ + \frac{1}{A} \frac{\partial}{\partial s} \left[ A \frac{S_v(1-S_v)\rho_v\rho_l}{\rho_{mix}} u_r^2 \right] + \frac{\partial P}{\partial s} = -\frac{2}{r}\tau - \rho_{mix}g \frac{\partial z}{\partial s} \end{aligned} \quad (A.51)$$

### A.2.2 Steady-state flowing mass fraction form

The steady-state momentum conservation equation is commonly written in terms of flowing mass fractions. However, as we discussed in Chapter 2, some authors have used a version of this equation that is only correct for wells with constant area. Below, we provide the derivation of the steady-state momentum conservation in terms of flowing mass fractions. We then highlight the difference between the form of the conservation of momentum conservation equation suitable for variable area wells with the form that assumes the wellbore area is constant.

The steady-state momentum conservation equation is:

$$\frac{1}{A} \frac{d}{ds} [AS_l\rho_l u_l^2 + AS_v\rho_v u_v^2] + \frac{dP}{ds} = -\frac{2}{r}\tau - (S_l\rho_l + S_v\rho_v)g \frac{dz}{ds} \quad (A.52)$$

By making use of the definition of the flowing mass fractions, the mass flux of each phase can be written as:

$$F_{mv} = S_v\rho_v u_v = F_m x_{fv} \quad (A.53)$$

and

$$F_{ml} = S_l\rho_l u_l = F_m x_{fl} \quad (A.54)$$

Substituting these definitions into the conservation of momentum equation results in:

$$\frac{1}{A} \frac{d}{ds} [AF_m (x_{fv}u_v + x_{fl}u_l)] + \frac{dP}{ds} = -\frac{2}{r}\tau - (S_l\rho_l + S_v\rho_v)g \frac{dz}{ds} \quad (A.55)$$

The steady-state mass conservation equation states that  $d(AF_m)/ds = 0$  in the absence of sources of mass. Therefore,  $AF_m = \text{constant}$  within the well and can be brought

outside the spatial derivative, resulting in:

$$F_m \frac{d}{ds} [(x_{fv} u_v + x_{fl} u_l)] + \frac{dP}{ds} = -\frac{2}{r} \tau - (S_l \rho_l + S_v \rho_v) g \frac{dz}{ds} \quad (\text{A.56})$$

Equation (A.56) correctly conserves momentum over a section of the well with changes in the cross-sectional area.

The version given in GWELL (Bjornsson, 1987) has  $F_m$  inside the derivative term. Although similar, this can only be derived by assuming that the wellbore area is constant. Making this assumption allows  $A$  to be removed from the spatial derivative, which results in:

$$\frac{d}{ds} [F_m (x_{fv} u_v + x_{fl} u_l)] + \frac{dP}{ds} = -\frac{2}{r} \tau - (S_l \rho_l + S_v \rho_v) g \frac{dz}{ds} \quad (\text{A.57})$$

While visually similar, (A.56) and (A.57) are not equivalent.

### A.3 Mixture conservation of energy equation

The conservation of total energy equation for a mixture is reached by summing the energy conservation equations of each phase ((A.5) and (A.9)). This summation results in:

$$\begin{aligned} & \frac{\partial(S_l \rho_l e_{Tl} A + S_v \rho_l e_{Tv} A)}{\partial t} + \frac{\partial(S_l u_l A (\rho_l e_{Tl} + P_l) + S_v u_v A (\rho_v e_{Tv} + P_v))}{\partial s} = \\ & P_{int} u_{int} A \frac{\partial(S_l + S_v)}{\partial s} + \Gamma A_{int} \left( \frac{P_{int}}{\rho_{int}} - h_{Tl,int} \right) A - \Gamma A_{int} \left( \frac{P_{int}}{\rho_{int}} - h_{Tv,int} \right) A \\ & - \bar{P}_{int} A \mu (P_v - P_l) - \bar{P}_{int} A \mu (P_l - P_v) + \bar{u}_{int} A \lambda (u_l - u_v) + \bar{u}_{int} A \lambda (u_v - u_l) \\ & + Q_{int,l} + Q_{int,v} + Q_{wall,l} + Q_{wall,v} \quad (\text{A.58}) \end{aligned}$$

Here, the pressure and velocity relaxation terms (terms 6 – 9 in (A.58)) are equal and opposite, and therefore cancel.

In (A.58), we note that  $S_l + S_v = 1$  and  $P = P_v = P_l = P_{int}$ , using the definition of total enthalpy in term 2, and then simplifying gives:

$$\begin{aligned} & \frac{\partial(S_l \rho_l e_{Tl} A + S_v \rho_l e_{Tv} A)}{\partial t} + \frac{\partial(S_l \rho_l u_l h_{Tl} A + S_v \rho_v u_v h_{Tv} A)}{\partial s} = \\ & + \Gamma A_{int} (h_{Tv,int} - h_{Tl,int}) A + Q_{int,l} + Q_{int,v} + Q_{wall,l} + Q_{wall,v} \quad (\text{A.59}) \end{aligned}$$

Here, the interface specific enthalpy term of a phase is  $h_{T\beta,int} = h_{\beta,int} + \frac{1}{2}u_{int}^2 + gz$ . Substituting the definition of  $h_{T\beta,int}$  into (A.59) results in:

$$\begin{aligned} & \frac{\partial S_l \rho_l e_{Tl} A + S_v \rho_l e_{Tv} A}{\partial t} + \frac{\partial S_l \rho_l u_l h_{Tl} A + S_v \rho_v u_v h_{Tv} A}{\partial s} = \\ & + \Gamma A_{int} \left( h_{v,int} + \frac{1}{2}u_{int}^2 + gz - h_{l,int} - \frac{1}{2}u_{int}^2 - gz \right) A \\ & + Q_{int,l} + Q_{int,v} + Q_{wall,l} + Q_{wall,v} \quad (\text{A.60}) \end{aligned}$$

which simplifies to give:

$$\begin{aligned} & \frac{\partial S_l \rho_l e_{Tl} A + S_v \rho_l e_{Tv} A}{\partial t} + \frac{\partial S_l \rho_l u_l h_{Tl} A + S_v \rho_v u_v h_{Tv} A}{\partial s} = \\ & + \Gamma A_{int} (h_{v,int} - h_{l,int}) A + Q_{int,l} + Q_{int,v} + Q_{wall,l} + Q_{wall,v} \quad (\text{A.61}) \end{aligned}$$



This equation is simplified further by noting the *energy jump condition* defined by Berry et al. (2014), which states:

$$\Gamma A_{int} A(h_{v,int} - h_{l,int}) + Q_{int,l} + Q_{int,v} = 0 \quad (\text{A.62})$$

Substituting (A.62) into (A.61) gives:

$$\frac{\partial S_l \rho_l e_{Tl} A + S_v \rho_l e_{Tv} A}{\partial t} + \frac{\partial S_l \rho_l u_l h_{Tl} A + S_v \rho_v u_v h_{Tv} A}{\partial s} = Q_{wall,l} + Q_{wall,v} \quad (\text{A.63})$$

We lump the phase wall heat transfer terms together, modelling the total external heat transfer to the formation analytically as described in Section 3.4. We note that Berry et al. (2014) defined the wall heat source term as positive for heat flow into the pipe. We use the opposite sign convention in our simulator (i.e., the wall heat flux term is positive for flow from the well to the formation) as this is the convention when modelling reservoir heat flux (Horne and Shinohara, 1979; Hasan and Kabir, 2010), therefore:

$$q_{heat} = -(Q_{wall,l} + Q_{wall,v}) / A \quad (\text{A.64})$$

Finally, assuming the wellbore area is constant with time and dividing through by the cross-sectional area gives:

$$\frac{\partial}{\partial t} [S_l \rho_l e_{Tl} + S_v \rho_l e_{Tv}] + \frac{1}{A} \frac{\partial}{\partial s} [A S_l \rho_l u_l h_{Tl} + A S_v \rho_v u_v h_{Tv}] + q_{heat} = 0 \quad (\text{A.65})$$

which is the same as the total energy equation given in (2.59) (without the energy source term). We model gravity as a body force, this manipulation is given below.

### A.3.1 Gravity as a body force

Equation (A.65) is formulated in terms of total energy meaning that gravity is accounted for within the derivative terms whereas we model gravity as a body force. Starting from the conservation of total energy given in (A.65), we substitute the definitions of total specific internal energy ( $e_{T\beta} = e_{\beta} + \frac{u_{\beta}^2}{2} + gz$ ) and total specific enthalpy ( $h_{T\beta} = h_{\beta} +$

$\frac{u_\beta^2}{2} + gz$ ) into the derivative terms and separate out the gravitational components:

$$\begin{aligned} & \frac{\partial}{\partial t} \left[ S_l \rho_l \left( e_l + \frac{u_l^2}{2} \right) + S_v \rho_l \left( e_v + \frac{u_v^2}{2} \right) \right] \\ & + \frac{1}{A} \frac{\partial}{\partial s} \left[ A S_l \rho_l u_l \left( h_l + \frac{u_l^2}{2} \right) + A S_v \rho_v u_v \left( h_l + \frac{u_l^2}{2} \right) \right] \\ & + \frac{\partial}{\partial t} [gz (S_l \rho_l + S_v \rho_l)] + \frac{1}{A} \frac{\partial}{\partial s} [gz A (S_l \rho_l u_l + S_v \rho_v u_v)] + q_{heat} - \hat{q}_{ener} = 0 \quad (\text{A.66}) \end{aligned}$$

Here, we have also included a source of total energy  $\hat{q}_{ener} = q_{mass}(h_{feed} + U_{feed}^2 + gz)$ .

Expanding the derivative terms that involve gravity using the product rule gives:

$$\begin{aligned} & \frac{\partial}{\partial t} \left[ S_l \rho_l \left( e_l + \frac{u_l^2}{2} \right) + S_v \rho_l \left( e_v + \frac{u_v^2}{2} \right) \right] \\ & + \frac{1}{A} \frac{\partial}{\partial s} \left[ A S_l u_l \left( h_l + \frac{u_l^2}{2} \right) + A S_v u_v \left( h_l + \frac{u_l^2}{2} \right) \right] \\ & + (S_l \rho_l + S_v \rho_l) \frac{\partial}{\partial t} [gz] + gz \frac{\partial}{\partial t} [S_l \rho_l + S_v \rho_l] \\ & + (S_l \rho_l u_l + S_v \rho_l u_v) \frac{\partial}{\partial s} [gz] + \frac{gz}{A} \frac{\partial}{\partial s} [A (S_l \rho_l u_l + S_v \rho_v u_v)] - q_{heat} - \hat{q}_{ener} = 0 \quad (\text{A.67}) \end{aligned}$$

Noting that both gravitational acceleration,  $g$ , and vertical depth,  $z$ , are constant with time (term three is zero) and subtracting  $gz \times (\text{A.12})$  results in:

$$\begin{aligned} & \frac{\partial}{\partial t} \left[ S_l \rho_l \left( e_l + \frac{u_l^2}{2} \right) + S_v \rho_l \left( e_v + \frac{u_v^2}{2} \right) \right] \\ & + \frac{1}{A} \frac{\partial}{\partial s} \left[ A S_l u_l \left( h_l + \frac{u_l^2}{2} \right) + A S_v u_v \left( h_l + \frac{u_l^2}{2} \right) \right] \\ & + (S_l \rho_l u_l + S_v \rho_l u_v) \frac{\partial gz}{\partial s} + q_{heat} - \hat{q}_{ener} + gz q_{mass} = 0 \quad (\text{A.68}) \end{aligned}$$

Assuming  $g$  is constant with  $s$  in term 3, and that the total source term is defined as  $\hat{q}_{ener} = q_{mass}(h_{feed} + U_{feed}^2 + gz)$ , we reach the conservation of energy equation used in

our simulator:

$$\begin{aligned} \frac{\partial}{\partial t} \left[ S_l \rho_l \left( e_l + \frac{u_l^2}{2} \right) + S_v \rho_l \left( e_v + \frac{u_v^2}{2} \right) \right] \\ + \frac{1}{A} \frac{\partial}{\partial s} \left[ A S_l u_l \left( h_l + \frac{u_l^2}{2} \right) + A S_v u_v \left( h_l + \frac{u_l^2}{2} \right) \right] \\ + (S_l \rho_l u_l + S_v \rho_l u_v) g \frac{\partial z}{\partial s} + q_{heat} - q_{ener} = 0 \quad (\text{A.69}) \end{aligned}$$

### A.3.2 García-Valladares et al. (2006) energy equation

Below we discuss the semi-discretised equations given in García-Valladares et al. (2006) and show how their rearranged energy equation can be manipulated to be the same as the conservation of total energy equation.

García-Valladares et al. (2006) gave the following semi-discretised conservation of mass equation (using our notation):

$$\left( \frac{\partial M}{\partial t} \right) + [Q_m]_i^{i+1} = 0 \quad (\text{A.70})$$

Here,  $M$  is the total mass of the fluid and the operator  $[\varphi]_i^{i+1}$  represents the difference between the inlet and outlet of a control volume:

$$[\varphi]_i^{i+1} = \varphi_{i+1} - \varphi_i \quad (\text{A.71})$$

In (A.70), the mass of a phase is  $m_\beta = \rho_\beta V_\beta$ , where  $V_\beta$  is the volume occupied by a phase. Dividing (A.70) through by the total volume of a block  $V = \Delta s A$  gives:

$$\frac{\partial \rho_{mix}}{\partial t} + \frac{1}{A} \frac{\Delta Q_m}{\Delta s} = 0 \quad (\text{A.72})$$

Taking the limit  $\Delta s \rightarrow 0$ , the discrete derivative becomes a continuous partial derivative, which results in the familiar conservation of mass equation:

$$\frac{\partial \rho_{mix}}{\partial t} + \frac{1}{A} \frac{\partial Q_m}{\partial s} = 0 \quad (\text{A.73})$$

The energy conservation equation given by García-Valladares et al. (2006) was given in a highly rearranged, semi-discrete non-conservative form of the total energy equation:

$$\begin{aligned} \tilde{Q}_m[h_{Tl}]_i^{i+1} + [Q_{mv}(h_{Tv} - h_{Tl})]_i^{i+1} + (\tilde{h}_{Tv} - \tilde{h}_{Tl}) \frac{\partial M_v}{\partial t} \\ + m_v \frac{\partial \tilde{h}_{Tv}}{\partial t} + m_l \frac{\partial \tilde{h}_{Tl}}{\partial t} - A\Delta s \frac{\partial P}{\partial t} + (\tilde{h}_{Tl} - \bar{h}_{Tl}) \frac{\partial M}{\partial t} = \tilde{q}\Delta s 2\pi r \end{aligned} \quad (\text{A.74})$$

Here,  $\dot{q}$  is the wall heat transfer term given by García-Valladares et al. (2006). Additionally, we note that the equation given by García-Valladares et al. (2006) used mass ( $M_v$ ) rather than the vapour mass flow rate ( $Q_{mv}$ ) (represented in their notation by  $m$  and  $\dot{m}$ , respectively) in term 2 of (A.74). We could not obtain the conservative form of the energy equation when vapour mass was used. Therefore, it is assumed this was a error in their notation, and vapour mass flow rate was used instead.

In (A.74),  $\bar{\varphi}$  is the arithmetic average over a control volume:

$$\bar{\varphi} = (\varphi_i + \varphi_{i+1})/2 \quad (\text{A.75})$$

and  $\tilde{\varphi}$  is the integral average over a control volume:

$$\tilde{\varphi} = \frac{1}{\Delta s} \int_z^{z+\Delta s} \varphi \, dz \quad (\text{A.76})$$

Noting that the mass of a phase is  $m_\beta = \rho_\beta V_\beta$ , where  $V_\beta$  is the volume occupied by a phase, and dividing through by the total volume of a block  $V = \Delta s A$ :

$$\begin{aligned} \frac{\tilde{Q}_m[h_{Tl}]_i^{i+1}}{A\Delta s} + \frac{[Q_{mv}(h_{Tv} - h_{Tl})]_i^{i+1}}{A\Delta s} + (\tilde{h}_{Tv} - \tilde{h}_{Tl}) \frac{\partial \rho_v S_v}{\partial t} \\ + \rho_v S_v \frac{\partial \tilde{h}_{Tv}}{\partial t} + \rho_l S_l \frac{\partial \tilde{h}_{Tl}}{\partial t} - \frac{\partial P}{\partial t} + (\tilde{h}_{Tl} - \bar{h}_{Tl}) \frac{\partial \rho_v S_v + \rho_l S_l}{\partial t} = \frac{2\tilde{q}}{r} \end{aligned} \quad (\text{A.77})$$

Again, we take the limit  $\Delta s \rightarrow 0$  and rewrite the discrete derivatives as continuous partial derivatives. Note that in the continuous formulation  $\tilde{\varphi} = \bar{\varphi}$ . This gives:

$$\begin{aligned} \frac{Q_m}{A} \frac{\partial h_{Tl}}{\partial s} + \frac{1}{A} \frac{\partial}{\partial s} (Q_{mv} (h_{Tv} - h_{Tl})) + (h_{Tv} - h_{Tl}) \frac{\partial \rho_v S_v}{\partial t} \\ + \rho_v S_v \frac{\partial h_{Tv}}{\partial t} + \rho_l S_l \frac{\partial h_{Tl}}{\partial t} - \frac{\partial P}{\partial t} = \frac{2}{r} \dot{q} \end{aligned} \quad (\text{A.78})$$

Expanding term 3 in (A.78):

$$\begin{aligned} \frac{Q_m}{A} \frac{\partial h_{Tl}}{\partial s} + \frac{1}{A} \frac{\partial}{\partial s} (Q_{mv} (h_{Tv} - h_{Tl})) + h_{Tv} \frac{\partial \rho_v S_v}{\partial t} - h_{Tl} \frac{\partial \rho_v S_v}{\partial t} \\ + \rho_v S_v \frac{\partial h_{Tv}}{\partial t} + \rho_l S_l \frac{\partial h_{Tl}}{\partial t} - \frac{\partial P}{\partial t} = \frac{2}{r} \dot{q} \end{aligned} \quad (\text{A.79})$$

Noting that:

$$h_{Tv} \frac{\partial (\rho_v S_v)}{\partial t} + \rho_v S_v \frac{\partial h_{Tv}}{\partial t} = \frac{\partial (\rho_v S_v h_{Tv})}{\partial t} \quad (\text{A.80})$$

and

$$\rho_l S_l \frac{\partial h_{Tl}}{\partial t} = \frac{\partial}{\partial t} (\rho_l S_l h_{Tl}) - h_{Tl} \frac{\partial (\rho_l S_l)}{\partial s} \quad (\text{A.81})$$

Substituting in these relationships for terms 3 and 6 in (A.79):

$$\begin{aligned} \frac{Q_m}{A} \frac{\partial h_{Tl}}{\partial s} + \frac{1}{A} \frac{\partial}{\partial s} (Q_{mv} (h_{Tv} - h_{Tl})) - h_{Tl} \frac{\partial \rho_v S_v}{\partial t} - h_{Tl} \frac{\partial \rho_l S_l}{\partial t} \\ + \frac{\partial}{\partial t} (\rho_v S_v h_{Tv}) + \frac{\partial}{\partial t} (\rho_l S_l h_{Tl}) - \frac{\partial P}{\partial t} = \frac{2}{r} \dot{q} \end{aligned} \quad (\text{A.82})$$

Combining terms 5, 6 and 7 in this equation results in the correct time derivative:

$$\begin{aligned} \frac{\partial}{\partial t} (\rho_v S_v h_{Tv} + \rho_l S_l h_{Tl} - P) + \frac{1}{A} \frac{\partial}{\partial s} (Q_{mv} (h_{Tv} - h_{Tl})) \\ + \frac{Q_m}{A} \frac{\partial h_{Tl}}{\partial s} - h_{Tl} \frac{\partial}{\partial t} (\rho_v S_v + \rho_l S_l) = \frac{2}{r} \dot{q} \end{aligned} \quad (\text{A.83})$$

Adding  $h_{Tl} \times ((\text{A.73}))$  to (A.83):

$$\begin{aligned} \frac{\partial}{\partial t} (\rho_v S_v h_{Tv} + \rho_l S_l h_{Tl} - P) + \frac{1}{A} \frac{\partial}{\partial s} (Q_{mv} (h_{Tv} - h_{Tl})) \\ + \frac{Q_m}{A} \frac{\partial h_{Tl}}{\partial s} - h_{Tl} \frac{\partial}{\partial t} (\rho_v S_v + \rho_l S_l) + h_{Tl} \frac{\partial \rho_{mix}}{\partial t} + \frac{h_{Tl}}{A} \frac{\partial Q_m}{\partial t} = \frac{2}{r} \dot{q} \end{aligned} \quad (\text{A.84})$$

Here, terms 4 and 5 cancel. Expanding term 2 in (A.84):

$$\begin{aligned} \frac{\partial}{\partial t}(\rho_v S_v h_{Tv} + \rho_l S_l h_{Tl} - P) + \frac{1}{A} \frac{\partial}{\partial s} (Q_{mv} h_{Tv}) - \frac{1}{A} \frac{\partial}{\partial s} (Q_{mv} h_{Tl}) \\ + \frac{Q_m}{A} \frac{\partial h_{Tl}}{\partial s} + \frac{h_{Tl}}{A} \frac{\partial Q_m}{\partial t} = \frac{2}{r} \dot{q} \end{aligned} \quad (\text{A.85})$$

Noting that:

$$\frac{Q_m}{A} \frac{\partial h_{Tl}}{\partial s} + \frac{h_{Tl}}{A} \frac{\partial Q_m}{\partial s} = \frac{1}{A} \frac{\partial Q_m h_{Tl}}{\partial s} \quad (\text{A.86})$$

and substituting in this relationship in place of terms 4 and 5 in (A.85):

$$\begin{aligned} \frac{\partial}{\partial t}(\rho_v S_v h_{Tv} + \rho_l S_l h_{Tl} - P) + \frac{1}{A} \frac{\partial}{\partial s} (Q_{mv} h_{Tv}) - \frac{1}{A} \frac{\partial}{\partial s} (Q_{mv} h_{Tl}) \\ + \frac{1}{A} \frac{\partial Q_m h_{Tl}}{\partial s} = \frac{2}{r} \dot{q} \quad (\text{A.87}) \end{aligned}$$

Substituting in the definition of total mass flow into term 4 in and combining the spatial derivatives gives:

$$\begin{aligned} \frac{\partial}{\partial t}(\rho_v S_v h_{Tv} + \rho_l S_l h_{Tl} - P) \\ + \frac{1}{A} \frac{\partial}{\partial s} (Q_{mv} h_{Tv} + Q_{ml} h_{Tl} + Q_{mv} h_{Tl} - Q_{mv} h_{Tl}) = \frac{2}{r} \dot{q} \end{aligned} \quad (\text{A.88})$$

Simplifying term 2 in this equation and substituting in the definitions of the mass flow for each phase gives:

$$\frac{\partial}{\partial t}(\rho_v S_v h_{Tv} + \rho_l S_l h_{Tl} - P) + \frac{1}{A} \frac{\partial}{\partial s} (A \rho_v S_v u_v h_{Tv} + A \rho_l S_l u_l h_{Tl}) = \frac{2}{r} \dot{q} \quad (\text{A.89})$$

García-Valladares et al. (2006) define their heat flux term  $\dot{q} \propto (T_{wall} - T_{fluid})$ , which is positive for heat flux from the wall/formation to the fluid (the opposite sign convention to what we use). Substituting in  $2\dot{q}/r = -q_{heat}$  and rearranging gives:

$$\frac{\partial}{\partial t}(\rho_v S_v h_{Tv} + \rho_l S_l h_{Tl} - P) + \frac{1}{A} \frac{\partial}{\partial s} (\rho_v S_v u_v h_{Tv} + \rho_l S_l u_l h_{Tl}) + q_{heat} = 0 \quad (\text{A.90})$$

which is the total energy conservation equation in conservative form (without an energy source term). Therefore, the non-conservative form of the energy equation given by García-Valladares et al. (2006) correctly conserves total energy.

### A.3.3 Thermal energy equation

In this section, we derive the equation describing the conservation of internal energy for a two-phase mixture. We start this derivation from the 6-equation model given by Yadigaroglu and Hewitt (2018). This model assumes well area is constant with time and the flow has equal phase pressures. Yadigaroglu and Hewitt (2018) gives the conservation of mass equation as:

$$\frac{\partial}{\partial t} [\rho_\beta S_\beta] + \frac{1}{A} \frac{\partial}{\partial s} [A \rho_\beta S_\beta u_\beta] - \Gamma_\beta = 0 \quad (\text{A.91})$$

Here,  $\Gamma_\beta$  is the volumetric mass transfer rate (units kg/m<sup>3</sup>/s) into phase  $\beta$ .

The conservation of momentum equation for a phase is given as (Yadigaroglu and Hewitt, 2018):

$$\frac{\partial}{\partial t} [\rho_\beta S_\beta u_\beta] + \frac{1}{A} \frac{\partial}{\partial s} [A \rho_\beta S_\beta u_\beta^2] + S_\beta \frac{\partial P}{\partial s} + \rho_\beta S_\beta g \frac{\partial z}{\partial s} + \frac{C_{w\beta}}{A} \tau_\beta + \frac{C_i}{A} \tau_{i\beta} - u_i \Gamma = 0 \quad (\text{A.92})$$

Here,  $u_i$  is the interface velocity,  $\tau_{i\beta}$  is the interface shear stress,  $C_{w\beta}$  is the wall perimeter wetted by phase  $\beta$  and  $C_i$  is the interface perimeter.

For this derivation, we require the non-conservative form of the momentum conservation equation. To derive this, we expand the derivative terms in the conservative momentum equation using the chain rule:

$$\begin{aligned} \rho_\beta S_\beta \frac{\partial u_\beta}{\partial t} + u_\beta \frac{\partial}{\partial t} [\rho_\beta S_\beta] + \rho_\beta S_\beta u_\beta \frac{\partial u_\beta}{\partial s} + \frac{u_\beta}{A} \frac{\partial}{\partial s} [A \rho_\beta S_\beta u_\beta] \\ + S_\beta \frac{\partial P}{\partial s} + \rho_\beta S_\beta g \frac{\partial z}{\partial s} + \frac{C_{w\beta}}{A} \tau_\beta + \frac{C_i}{A} \tau_{i\beta} - u_i \Gamma_\beta = 0 \end{aligned} \quad (\text{A.93})$$

We then subtract  $u_\beta \times (\text{A.91})$  to get a non-conservative form of the momentum equation:

$$\begin{aligned} \rho_\beta S_\beta \frac{\partial u_\beta}{\partial t} + \rho_\beta S_\beta u_\beta \frac{\partial u_\beta}{\partial s} \\ + S_\beta \frac{\partial P}{\partial s} + \rho_\beta S_\beta g \frac{\partial z}{\partial s} + \frac{C_{w\beta}}{A} \tau_\beta + \frac{C_i}{A} \tau_{i\beta} - (u_i - u_\beta) \Gamma_\beta = 0 \end{aligned} \quad (\text{A.94})$$

The conservation of energy equation given by Yadigaroglu and Hewitt (2018), manipulated so that gravitational potential energy is not in the derivative terms, is:

$$\begin{aligned} \frac{\partial}{\partial t} \left[ \rho_\beta S_\beta \left( h_\beta + \frac{u_\beta^2}{2} \right) \right] - S_\beta \frac{\partial P}{\partial t} + \frac{1}{A} \frac{\partial}{\partial s} \left[ A \rho_\beta S_\beta u_\beta \left( h_\beta + \frac{u_\beta^2}{2} \right) \right] \\ + \rho_\beta S_\beta u_\beta g \frac{\partial z}{\partial s} - \frac{C_{w\beta}}{A} Q_\beta - \frac{C_i}{A} Q_{i\beta} - \left( h_{i\beta} + \frac{u_i^2}{2} \right) \Gamma_\beta = 0 \quad (\text{A.95}) \end{aligned}$$

Here,  $Q_\beta$  is wall heat flux,  $Q_{i\beta}$  is interface heat flux and  $h_{i\beta}$  is the total enthalpy characteristic of the exchange (defined using a jump condition).

Substituting the definition of the specific enthalpy of phase  $\beta$  and separating out the derivative into the internal energy and kinetic energy components gives:

$$\begin{aligned} \frac{\partial}{\partial t} [\rho_\beta S_\beta e_\beta] + \frac{\partial}{\partial t} [S_\beta P] - S_\beta \frac{\partial P}{\partial t} + \frac{1}{A} \frac{\partial}{\partial s} [A \rho_\beta S_\beta u_\beta e_\beta] + \frac{1}{A} \frac{\partial}{\partial s} [A S_\beta u_\beta P] \\ + \frac{1}{2} \frac{\partial}{\partial t} [\rho_\beta S_\beta u_\beta^2] + \frac{1}{2A} \frac{\partial}{\partial s} [A \rho_\beta S_\beta u_\beta u_\beta^2] \\ - \rho_\beta S_\beta u_\beta g \frac{\partial z}{\partial s} - \frac{C_{w\beta}}{A} Q_\beta - \frac{C_i}{A} Q_{i\beta} - \left( h_{i\beta} + \frac{u_i^2}{2} \right) \Gamma_\beta = 0 \quad (\text{A.96}) \end{aligned}$$

Noting that:

$$P \frac{\partial}{\partial t} (S_\beta) = \frac{\partial}{\partial t} (P S_\beta) - S_\beta \frac{\partial P}{\partial t} \quad (\text{A.97})$$

where  $P \frac{\partial}{\partial t} (S_\beta)$  is the reversible work due to expansion or contraction of the phases (Yadigaroglu and Hewitt, 2018). Substituting (A.97) into (A.96) gives:

$$\begin{aligned} \frac{\partial}{\partial t} [\rho_\beta S_\beta e_\beta] + \frac{1}{A} \frac{\partial}{\partial s} [A \rho_\beta S_\beta u_\beta e_\beta] + \frac{1}{A} \frac{\partial}{\partial s} [A S_\beta u_\beta P] + P \frac{\partial S_\beta}{\partial t} \\ + \frac{1}{2} \left[ \rho_\beta S_\beta \frac{\partial}{\partial t} [u_\beta^2] + u_\beta^2 \frac{\partial}{\partial t} [\rho_\beta S_\beta] + \rho_\beta S_\beta u_\beta \frac{\partial}{\partial s} [u_\beta^2] + \frac{u_\beta^2}{A} \frac{\partial}{\partial s} [A \rho_\beta S_\beta u_\beta] \right] \\ + \rho_\beta S_\beta u_\beta g \frac{\partial z}{\partial s} - \frac{C_{w\beta}}{A} Q_\beta - \frac{C_i}{A} Q_{i\beta} - \left( h_{i\beta} + \frac{u_i^2}{2} \right) \Gamma_\beta = 0 \quad (\text{A.98}) \end{aligned}$$



Subtracting  $\frac{1}{2}u_\beta^2 \times (\text{A.91})$  and expanding the  $u_k^2$  derivatives using the product rule gives:

$$\begin{aligned} \frac{\partial}{\partial t} [\rho_\beta S_\beta e_\beta] + \frac{1}{A} \frac{\partial}{\partial s} [A \rho_\beta S_\beta u_\beta e_\beta] + \frac{1}{A} \frac{\partial}{\partial s} [A S_\beta u_\beta P] + P \frac{\partial S_\beta}{\partial t} \\ + \left[ \rho_\beta S_\beta u_\beta \frac{\partial}{\partial t} [u_\beta] + \rho_\beta S_\beta u_\beta^2 \frac{\partial}{\partial s} [u_\beta] \right] \\ + \rho_\beta S_\beta u_\beta g \frac{\partial z}{\partial s} - \frac{C_{w\beta}}{A} Q_\beta - \frac{C_i}{A} Q_{i\beta} - \left( h_{i\beta} + \frac{u_i^2}{2} \right) \Gamma_\beta + \frac{1}{2} u_\beta^2 \Gamma_\beta = 0 \quad (\text{A.99}) \end{aligned}$$

Subtracting  $u_k \times (\text{A.94})$  gives:

$$\begin{aligned} \frac{\partial}{\partial t} [\rho_\beta S_\beta e_\beta] + \frac{1}{A} \frac{\partial}{\partial s} [A \rho_\beta S_\beta u_\beta e_\beta] + \frac{1}{A} \frac{\partial}{\partial s} [A S_\beta u_\beta P] + P \frac{\partial S_\beta}{\partial t} \\ - u_\beta \left[ S_\beta \frac{\partial P}{\partial s} + \rho_\beta S_\beta g \frac{\partial z}{\partial s} + \frac{C_{w\beta}}{A} \tau_\beta + \frac{C_i}{A} \tau_{i\beta} - u_i \Gamma_\beta + u_\beta \Gamma_\beta \right] \\ + \rho_\beta S_\beta u_\beta g \frac{\partial z}{\partial s} - \frac{C_{w\beta}}{A} Q_\beta - \frac{C_i}{A} Q_{i\beta} - \left( h_{i\beta} + \frac{u_i^2}{2} \right) \Gamma_\beta + \frac{1}{2} u_\beta^2 \Gamma_\beta = 0 \quad (\text{A.100}) \end{aligned}$$

Simplifying (A.100) by noting that the gravity terms cancel and rearranging gives:

$$\begin{aligned} \frac{\partial}{\partial t} [\rho_\beta S_\beta e_\beta] + \frac{1}{A} \frac{\partial}{\partial s} [A \rho_\beta S_\beta u_\beta e_\beta] + \frac{1}{A} \frac{\partial}{\partial s} [A S_\beta u_\beta P] + P \frac{\partial S_\beta}{\partial t} \\ - u_\beta S_\beta \frac{\partial P}{\partial s} - u_\beta \left[ \frac{C_{w\beta}}{A} \tau_\beta + \frac{C_i}{A} \tau_{i\beta} - u_i \Gamma_\beta + u_\beta \Gamma_\beta \right] \\ - \frac{C_{w\beta}}{A} Q_\beta - \frac{C_i}{A} Q_{i\beta} - \left( h_{i\beta} + \frac{u_i^2}{2} \right) \Gamma_\beta + \frac{1}{2} u_\beta^2 \Gamma_\beta = 0 \quad (\text{A.101}) \end{aligned}$$

Simplifying further and combining the interface source terms:

$$\begin{aligned} \frac{\partial}{\partial t} [\rho_\beta S_\beta e_\beta] + \frac{1}{A} \frac{\partial}{\partial s} [A \rho_\beta S_\beta u_\beta e_\beta] + \frac{P}{A} \frac{\partial}{\partial s} [A S_\beta u_\beta] \\ + P \frac{\partial S_\beta}{\partial t} - u_\beta \left( \frac{C_{w\beta}}{A} \tau_\beta + \frac{C_i}{A} \tau_{i\beta} \right) \\ - \frac{C_{w\beta}}{A} Q_\beta - \frac{C_i}{A} Q_{i\beta} - \left( h_{i\beta} + \frac{u_i^2}{2} \right) \Gamma_\beta + \Gamma_\beta \left[ u_i u_\beta - \frac{1}{2} u_\beta^2 \right] = 0 \quad (\text{A.102}) \end{aligned}$$

Summing (A.102) over the liquid and vapour phases gives:

$$\begin{aligned} & \frac{\partial}{\partial t} [\rho_l S_l e_l + \rho_v S_v e_v] + \frac{1}{A} \frac{\partial}{\partial s} [A \rho_l S_l u_l e_l + A \rho_v S_v u_v e_v] + \frac{P}{A} \frac{\partial}{\partial s} [A S_l u_l + A S_v u_v] \\ & + P \frac{\partial S_v + S_l}{\partial t} - u_l \left( \frac{C_{wl}}{A} \tau_l + \frac{C_i}{A} \tau_{il} \right) - u_v \left( \frac{C_{wv}}{A} \tau_v + \frac{C_i}{A} \tau_{iv} \right) \\ & - \frac{C_{wl}}{A} Q_l - \frac{C_{wv}}{A} Q_v - \frac{C_i}{A} Q_{il} - \frac{C_i}{A} Q_{iv} \\ & - \left( h_{il} + \frac{u_i^2}{2} \right) \Gamma_l - \left( h_{iv} + \frac{u_i^2}{2} \right) \Gamma_v + \Gamma_l \left[ u_i u_l - \frac{1}{2} u_l^2 \right] + \Gamma_v \left[ u_i u_v - \frac{1}{2} u_v^2 \right] = 0 \quad (\text{A.103}) \end{aligned}$$

Here, term 4 is equal to zero because  $S_v + S_l = 1$ .

Continuity across the phase interface requires that  $\Gamma = \Gamma_v = -\Gamma_l$ . Making this substitution and collecting the source terms together gives:

$$\begin{aligned} & \frac{\partial}{\partial t} [\rho_l S_l e_l + \rho_v S_v e_v] + \frac{1}{A} \frac{\partial}{\partial s} [A \rho_l S_l u_l e_l + A \rho_v S_v u_v e_v] + \frac{P}{A} \frac{\partial}{\partial s} [A S_l u_l + A S_v u_v] \\ & - u_l \left( \frac{C_{wl}}{A} \tau_l + \frac{C_i}{A} \tau_{il} \right) - u_v \left( \frac{C_{wv}}{A} \tau_v + \frac{C_i}{A} \tau_{iv} \right) \\ & - \frac{C_{wl}}{A} Q_l - \frac{C_{wv}}{A} Q_v - \frac{C_i}{A} (Q_{il} - Q_{iv}) \\ & + \Gamma \left[ \left( h_{il} + \frac{u_i^2}{2} \right) - \left( h_{iv} + \frac{u_i^2}{2} \right) \right] + \Gamma \left[ \left( u_i u_v - \frac{u_v^2}{2} \right) - \left( u_i u_l - \frac{u_l^2}{2} \right) \right] = 0 \quad (\text{A.104}) \end{aligned}$$

Noting that the  $u_i/2$  terms cancel and the *energy jump condition* given by Yadigaroglu and Hewitt (2018) is:

$$\Gamma(h_{iv} - h_{il}) + \frac{C_i}{A} (Q_{il} + Q_{iv}) = 0 \quad (\text{A.105})$$

means that terms 8 and 9 in (A.104) sum to equal zero. Making these simplifications results in:

$$\begin{aligned} & \frac{\partial}{\partial t} [\rho_l S_l e_l + \rho_v S_v e_v] + \frac{1}{A} \frac{\partial}{\partial s} [A \rho_l S_l u_l e_l + A \rho_v S_v u_v e_v] + \frac{P}{A} \frac{\partial}{\partial s} [A S_l u_l + A S_v u_v] \\ & - u_l \left( \frac{C_{wl}}{A} \tau_l + \frac{C_i}{A} \tau_{il} \right) - u_v \left( \frac{C_{wv}}{A} \tau_v + \frac{C_i}{A} \tau_{iv} \right) \\ & - \frac{C_{wl}}{A} Q_l - \frac{C_{wv}}{A} Q_v + \Gamma \left[ (u_v - u_l) u_i - \frac{1}{2} (u_v^2 - u_l^2) \right] = 0 \quad (\text{A.106}) \end{aligned}$$

Assuming that we can model the combined effect of the wall heat flux of each phase with a suitable constitutive model (and switching the sign convention of the wall heat flux

term to align with our convention):

$$\begin{aligned} \frac{\partial}{\partial t} [\rho_l S_l e_l + \rho_v S_v e_v] + \frac{1}{A} \frac{\partial}{\partial s} [A \rho_l S_l u_l e_l + A \rho_v S_v u_v e_v] + \frac{P}{A} \frac{\partial}{\partial s} [A S_l u_l + A S_v u_v] \\ + q_{heat} - u_l \left( \frac{C_{wl}}{A} \tau_l \right) - u_v \left( \frac{C_{wv}}{A} \tau_v \right) - \frac{C_i}{A} (u_l \tau_{il} + u_v \tau_{iv}) \\ + \Gamma \left[ (u_v - u_l) u_i - \frac{1}{2} (u_v^2 - u_l^2) \right] = 0 \quad (\text{A.107}) \end{aligned}$$

Noting that the interface friction terms are equal and opposite, i.e.,  $\tau_i = \tau_{iv} = -\tau_{il}$ :

$$\begin{aligned} \frac{\partial}{\partial t} [\rho_l S_l e_l + \rho_v S_v e_v] + \frac{1}{A} \frac{\partial}{\partial s} [A \rho_l S_l u_l e_l + A \rho_v S_v u_v e_v] + \frac{P}{A} \frac{\partial}{\partial s} [A S_l u_l + A S_v u_v] \\ + q_{heat} - u_l \left( \frac{C_{wl}}{A} \tau_l \right) - u_v \left( \frac{C_{wv}}{A} \tau_v \right) - \frac{C_i \tau_i}{A} (u_v - u_l) \\ + \Gamma \left[ (u_v - u_l) u_i - \frac{1}{2} (u_v^2 - u_l^2) \right] = 0 \quad (\text{A.108}) \end{aligned}$$

Equation (A.108) differs from the internal energy equation given by Miller (1980*b*) by the last four terms. It is likely that these terms are small for moderate flow rates when compared to the thermal energy of the well.

For single phase flow, (A.108) simplifies to:

$$\frac{\partial}{\partial t} [\rho e] + \frac{1}{A} \frac{\partial}{\partial s} [A \rho u e] + \frac{P}{A} \frac{\partial}{\partial s} [A u] + q_{heat} - \frac{2}{r} u \tau = 0 \quad (\text{A.109})$$

We note that the friction term remains in the single-phase version of the internal energy equation.

## Appendix B

# Derivation of analytical heat transfer term

An analytical model for the formation heat transfer is used in our simulator. This model accounts for the heat transfer in the structure of the well and approximates the transient reservoir heat flux. This model was originally given by Ramey (1962) and was later presented for geothermal applications by Horne and Shinohara (1979). However, the version of this equation given in the recent publication by Vasini et al. (2018) is incorrect. Therefore, for completeness, we present the derivation of the model that we use for representing heat flux to the formation in our simulator.

The heat flux per unit length through the wellbore structure is (Ramey, 1962):

$$\frac{dQ_{heat}}{ds} = 2\pi r_{wb} U (T_{wb} - T_{cem}). \quad (B.1)$$

where  $r_{wb}$  is the wellbore radius,  $U$  is the overall heat transfer coefficient,  $T_{wb}$  is the temperature of the wellbore fluid, and  $T_{cem}$  is the temperature of the cement.

The seminal work by Ramey (1962) approximated the transient heat transfer in the reservoir using:

$$\frac{dQ_{heat}}{ds} = \frac{2\pi k_{res}(T_{cem} - T_{res})}{f(t)} \quad (B.2)$$

where  $T_{res}$  is the far-field reservoir temperature and  $f(t)$  is a non-dimensional function that approximates how the heat transfer in the reservoir changes with time. We use the model for  $f(t)$  given by Chiu and Thakur (1991).

To derive the equation describing the heat flux through both the well and the formation, we first rearrange (B.1) for  $T_{cem}$ :

$$T_{cem} = T_{wb} - \frac{1}{2\pi r_{wb} U} \frac{dq}{dz} \quad (B.3)$$

Substituting (B.3) into (B.2) and rearranging for  $dQ_{heat}/ds$  gives:

$$\begin{aligned} \frac{dQ_{heat}}{ds} &= \frac{2\pi k_{res}}{f(t)} \left( T_{wb} - \frac{1}{2\pi r_{wb} U} \frac{dq}{dz} \right) - \frac{2\pi k_{res}}{f(t)} T_{res} \\ \frac{dQ_{heat}}{ds} &= -\frac{2\pi k_{res}}{2\pi r_{wb} U f(t)} \frac{dQ_{heat}}{ds} + \frac{2\pi k_{res}(T_{wb} - T_{res})}{f(t)} \\ \frac{dQ_{heat}}{ds} + \frac{k_{res}}{r_{wb} U f(t)} \frac{dQ_{heat}}{ds} &= \frac{2\pi k_{res}(T_{wb} - T_{res})}{f(t)} \\ \left( 1 + \frac{k_{res}}{r_{wb} U f(t)} \right) \frac{dQ_{heat}}{ds} &= \frac{2\pi k_{res}(T_{wb} - T_{res})}{f(t)} \\ \frac{dQ_{heat}}{ds} &= \frac{2\pi k_{res}(T_{wb} - T_{res})}{f(t) \left( 1 + \frac{k_{res}}{r_{wb} U f(t)} \right)} \\ \frac{dQ_{heat}}{ds} &= \frac{2\pi k_{res}(T_{wb} - T_{res})}{f(t) + \frac{k_{res}}{r_{wb} U}} \end{aligned}$$

Further manipulation results in:

$$\frac{dQ_{heat}}{ds} = \frac{2\pi k_{res} r_{wb} U (T_{wb} - T_{res})}{k_{res} + r_{wb} U f(t)} \quad (B.4)$$

Equation (B.4) is given by Horne and Shinohara (1979) and models the heat flux between the well and reservoir per unit length. Dividing (B.4) by the wellbore area gives the heat flux per unit volume of the well:

$$q_{heat} = \frac{1}{A} \frac{dQ_{heat}}{ds} = \frac{2}{r} \frac{k_{res} U (T_{wb} - T_{res})}{k_{res} + r U f(t)} \quad (B.5)$$

which is suitable for use in our equation. In (B.5), the heat flux is positive when  $T_{wb} > T_{res}$ , i.e., for transfer from the well to the formation.

## Appendix C

### Additional test cases

The test cases presented in this section were used to test specific flow scenarios that do not occur in the cases discussed in Chapter 5. We have included these test cases in the appendices because they verify that our simulator can model these flow scenarios, however, they are not central to the discussions presented elsewhere in the thesis.

Test Case 13, discussed in Section C.1, models vapour down-flow into a two-phase block. Similarly, Test Case 14, discussed in Section C.2, models liquid down-flow into a two-phase block. Finally, Test Case 15, discussed in Section C.3, models liquid down-flow from a two-phase block into a liquid block.

#### **C.1 Test Case 13: vapour down-flow into a two-phase block**

Test Case 13 simulates the injection of high-enthalpy fluid at the wellhead. A two-phase feed located halfway up the well is used to condense the vapour flow to two-phase conditions. This simple test case was developed to ensure that our simulator could model vapour down-flow into a two-phase block. This flow scenario is shown in Figure C.1.

Test Case 13 simulates flow in a 100 m test well with a diameter of 0.2 m (the same well that was used for Test Cases 9 and 10). The wellbore parameters are given in Table C.1. Flow is initialised as a vapour column flowing at -3 kg/s (i.e., down-flow). These initial conditions are given in Figure C.2.

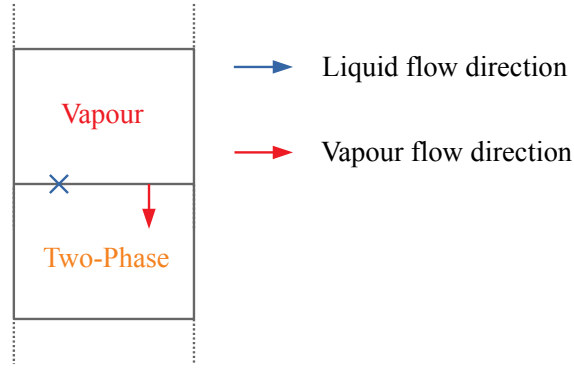


FIGURE C.1: Flow scenario showing water vapour flowing down into a two-phase block.

TABLE C.1: Simulation and wellbore parameters for Test Case 13.

Wellhead elevation	0 mRL
Inclination angle	0 °
Length	100 m
wellbore diameter	0.2 m
Pipe roughness	4.5E-05 m
Bottomhole flow condition	Closed
Reservoir heat transfer	None
Discretisation	Uniform, 100 blocks
Source term model	Lumped parameter model given in (3.78)
Feed parameter	Table C.2
Wellhead mass flow	-3 kg/s
Wellhead flowing enthalpy	2900 kJ/kg
Initial conditions	Figure C.2

TABLE C.2: Feed-zone properties and locations for Test Case 13.

Name	Elevation [mRL]	Time [sec]	$\alpha$ [kg/s/Pa]	$P$ [bar]	$h_{fix}$ [kJ/kg]	$Q_m$
Middle feed	-50 to -55	0	-	-	2000	0
		100	-	-	2000	0
		200	-	-	2000	1
Bottom feed	-99 to -100	All times	5E-6	15	2920	-

Fluid exits the well via the feed on deliverability at the bottom of the well. The properties of this feed correspond to vapour at 15 bara and are given in Table C.2. Additionally, a two-phase feed with transient parameters is located between -50 and -55 mRL. This feed does not produce any fluid to the well for the first 100 seconds. After this time, the mass flow rate from the feed increases linearly from 0 to 1 kg/s over a period of 100 seconds. The enthalpy of the feed is 2000 kJ/kg. The conditions are given in Table C.2.

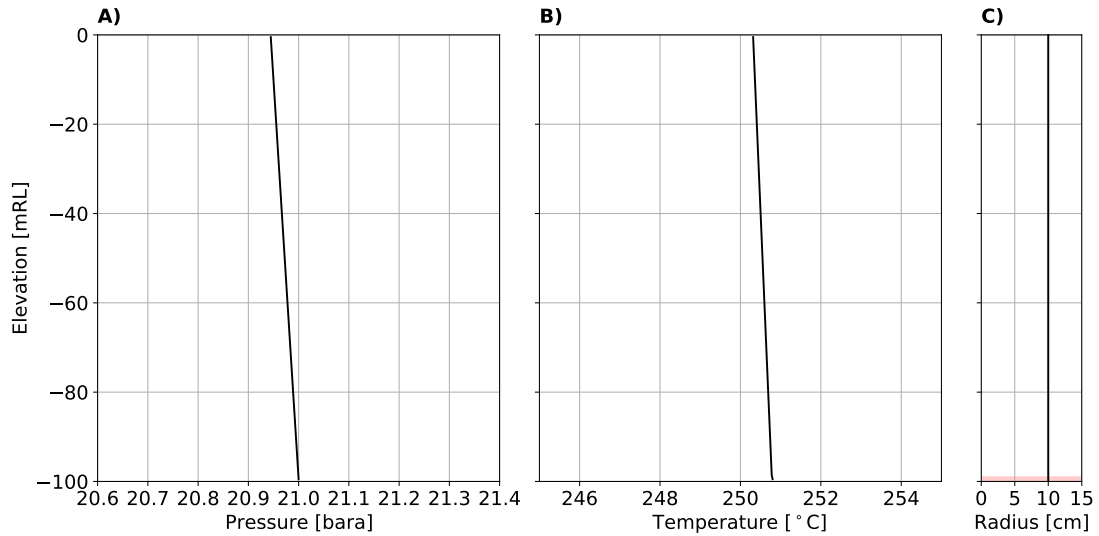


FIGURE C.2: Initial conditions for Test Case 13 showing A) pressure and B) temperature. The wellbore radius and feed location are shown in plot C).

The results in C.3 C) show the influx of fluid between -50 and -55 mRL increasing the mass flow rate in the bottom half of the well with time. The injection of lower-enthalpy fluid at this elevation causes the large drop in temperature shown in Figure C.3 B). The influx of two-phase fluid causes the bottom half of the well to condense from vapour to high-saturation two-phase fluid. This process is shown by the plot of static vapour mass fraction in Figure C.3 D). This demonstrates that our simulator can model vapour down-flow into a two-phase block.



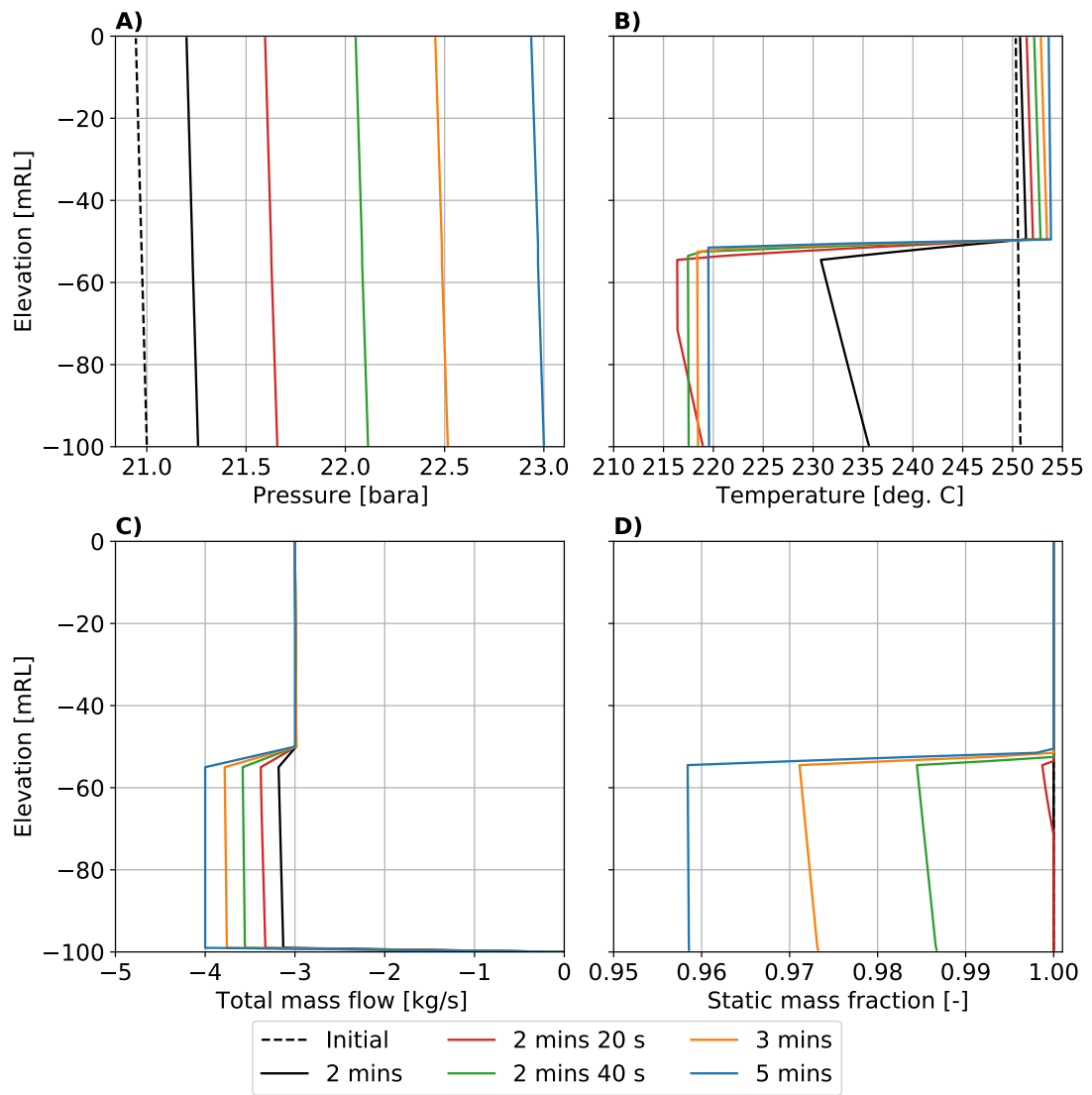


FIGURE C.3: Plots of A) pressure B) temperature C) total mass flow rate and D) static vapour mass fraction at various times for Test Case 13.

## C.2 Test Case 14: liquid down-flow into a two-phase block

Test Case 14 was developed specifically to verify that our simulator could model liquid down-flow into a two-phase block. This flow scenario is shown diagrammatically in Figure C.4.

Test Case 14 simulates flow in the same 100 m test well as was used in Test Case 9, 10 and 13. The wellbore parameters are given in Table C.4. The well is initialised as a static liquid column at 30 °C. These conditions are given in Figures C.5.

For this case, the well remains closed for the first 100 seconds of the simulation. Then, over the next 200 seconds, the mass flow rate of the liquid injected at the wellhead is increased linearly from 0 to 10 kg/s. The enthalpy of the injected fluid is 300 kJ/kg. These wellhead conditions are given in Table C.3.

We use a high-enthalpy feed-zone located between -50 and -55 mRL to transition the flow from liquid to two-phase conditions. Initially, there is no influx from this feed. At 600 seconds, we begin increasing the mass flow rate linearly from 0 to 7.5 kg/s, after which the inflow remains constant. The inflowing fluid has an enthalpy of 2500 kJ/kg. Flow exits the well via the feed at the bottom of the well. The feed-zone properties are summarised in Table C.5.

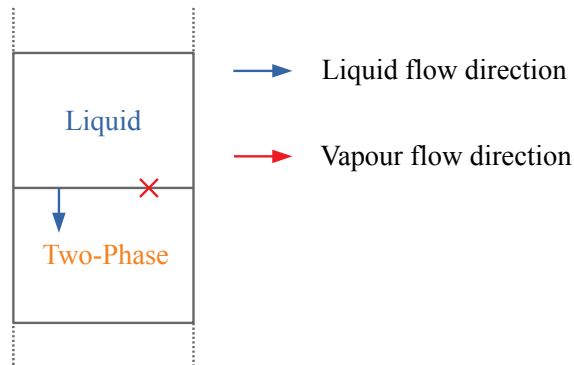


FIGURE C.4: Flow scenario showing liquid water flowing down into a two-phase block.

TABLE C.3: Mass flow and flowing enthalpy boundary conditions prescribed at the wellhead for Test Case 14.

Time [s]	0	100	300
Flowing enthalpy [kJ/kg]	300	300	300
Mass flow rate [kg/s]	0	0	-10

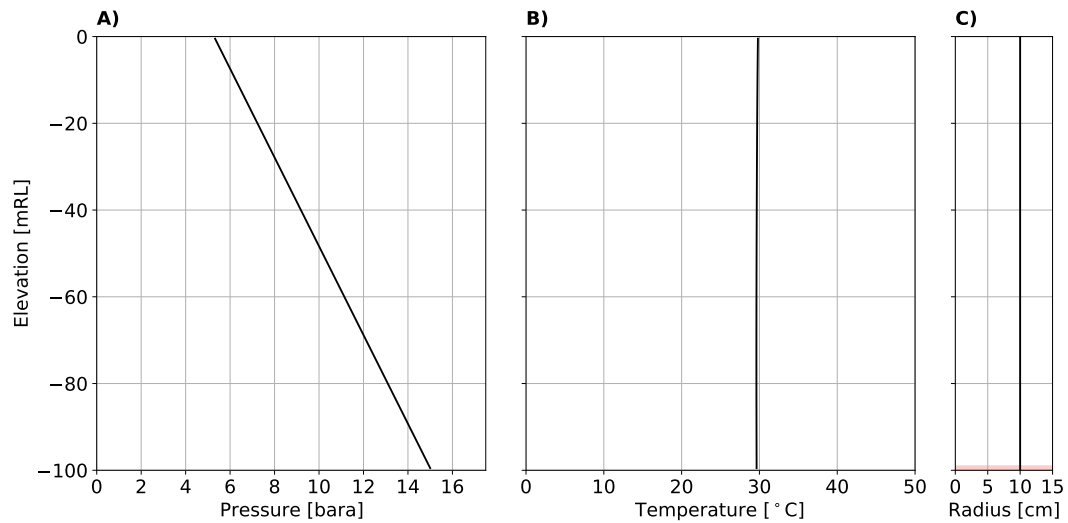


FIGURE C.5: Initial conditions for Test Case 14 showing A) pressure and B) temperature. The wellbore radius and feed location are shown in plot C).

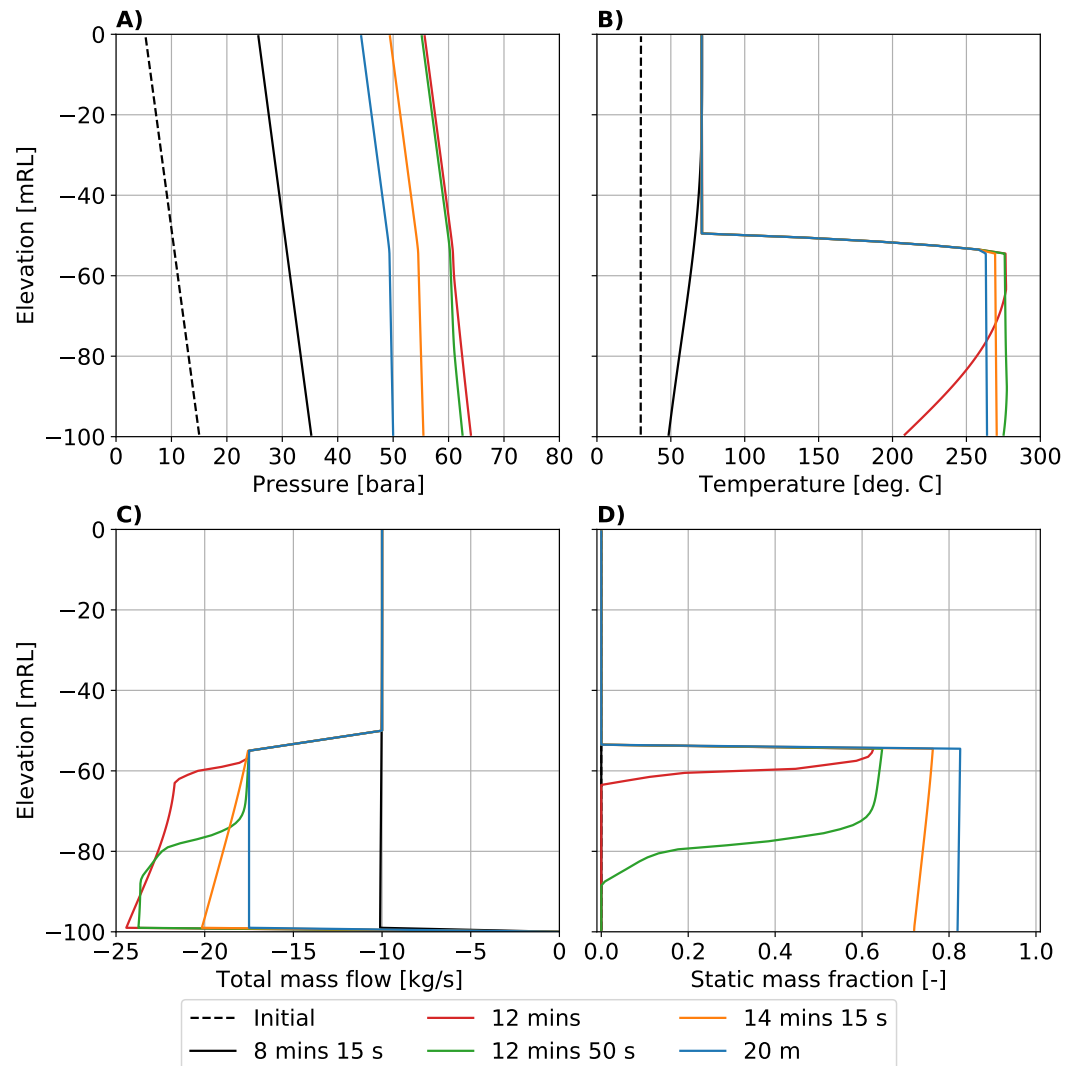


FIGURE C.6: Plots of A) pressure B) temperature C) total mass flow rate and D) static vapour mass fraction at various times for Test Case 14.

TABLE C.4: Simulation and wellbore parameters for Test Case 14.

Wellhead elevation	0 mRL
Inclination angle	0 °
Length	100 m
discretisation	100 block uniform grid
wellbore diameter	0.20 m
Pipe roughness	4.5E-05 m
Wellhead mass flow	Table C.3
Wellhead flowing enthalpy	Table C.3
Bottomhole flow condition	Closed ( $u_v = F_{VI} = 0$ )
Reservoir heat transfer	not modelled
Feed-zones	Table C.5
Friction factor model	Moody (Equation (3.58))

TABLE C.5: Feed-zone properties and locations for Test Case 14.

Name	Elevation [mRL]	Time [sec]	$\alpha$ [kg/s/Pa]	$P$ [bar]	$h_{f_{mix}}$ [kJ/kg]	$Q_m$
Middle feed	-50 to -55	0	-	-	2500	0
		600	-	-	2500	0
		700	-	-	2500	7.5
Bottom feed	-99 to -100	All times	5E-6	15	630	-

The results for Test Case 14 are shown in Figure C.6. Figure C.6 D) shows that the high-enthalpy influx causes boiling to occur below the feed-zone. This demonstrates that our simulator can model liquid down-flow into a two-phase block. In this simulation, we have used a relatively high injection mass flow rate at both the wellhead and the feed-zone. This is because vapour may flow up from the feed-zone if the injection flow rate is insufficient to drag the vapour phase down the well. If this were to occur, it would result in a counter-flow scenario rather than the flow scenario shown in Figure C.4.

### C.3 Test Case 15: liquid down-flow from a two-phase block

Test Case 15 was developed to test the flow scenario illustrated in Figure C.7. Here, liquid is flowing down from a two-phase block into a liquid block, while the vapour phase does not flow through the interface. Test Case 15 simulates flow in a 1000 m vertical well with a constant diameter of 0.2 m. Heat flux is not modelled for this case.

To achieve the flow scenario shown in Figure C.7, we use two liquid feed-zones, the properties of which are given in Table C.7. Here, the properties of the middle feed remain constant throughout the simulation. The feed located at the bottom of the well is cooled and then depressurised during the simulation. We note that these transient

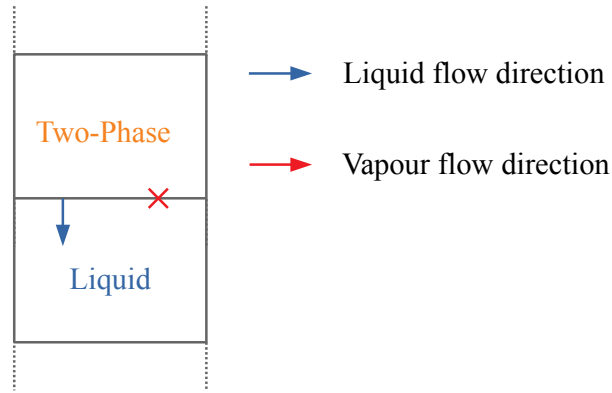


FIGURE C.7: Flow scenario showing liquid down-flow from a two-phase block into a liquid block.

TABLE C.6: Simulation and wellbore parameters for Test Case 15.

Wellhead elevation	0 mRL
Inclination angle	0 °
Length	1000 m
discretisation	200 block uniform grid
wellbore diameter	0.2 m
Pipe roughness	4.5E-05 m
Wellhead pressure condition	5.5 bara
Bottomhole flow condition	Closed ( $u_v = F_{Vl} = 0$ )
Reservoir heat transfer	None
Friction factor model	Moody (Equation (3.58))

TABLE C.7: Feed-zone properties and locations for Test Case 15.

Name	Elevation [mRL]	PI [m <sup>3</sup> ]	Time [days]	P [bara]	T °C	$S_v$ [-]
Middle feed	-750 to -800	1.0E-13	all times	70	275	0.0
Bottom feed	-950 to -1000	1.0E-13	1	100	300	0.0
			10	100	190	0.0
			20	20	190	0.0

conditions are not intended to represent physically realistic reservoir processes. Instead, the properties of this feed were varied until the desired flow scenario was achieved.

Test Case 15 begins from the flowing two-phase conditions given in Figures C.8 and C.9. These correspond to the wells flowing state with a wellhead pressure of 5.5 bara. This wellhead pressure remains constant throughout the simulation.

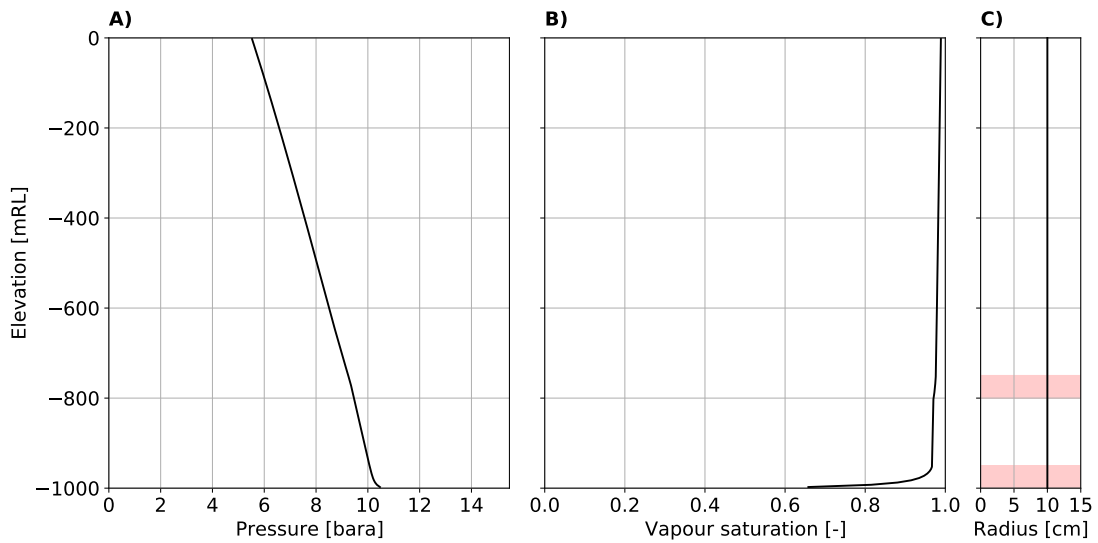


FIGURE C.8: Initial conditions for A) pressure and B) vapour saturation for Test Case 15. Plot C) shows the feed locations and the wellbore structure.

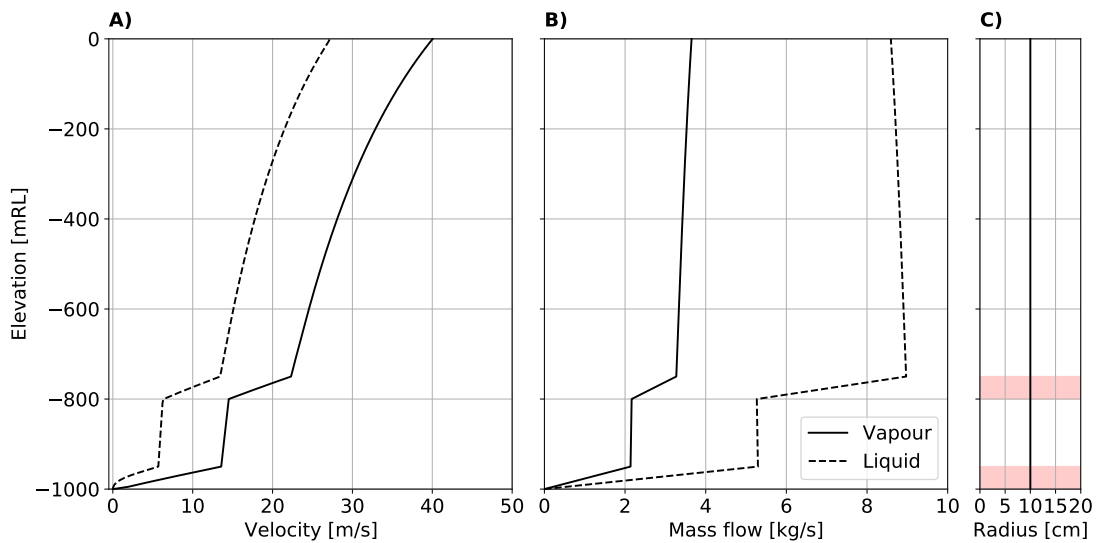


FIGURE C.9: Initial conditions for A) phase velocities and B) phase mass flow rates for Test Case 15. Plot C) shows the feed locations and the wellbore structure.

The results of this simulation are given in Figure C.10. The temperature of the deep feed is reduced over the 9 day period between 1 and 10 days. The effects of this cooling are shown by the wellbore profiles at 6 and 9 days. The decreasing enthalpy of the fluid from the deep feed causes the vapour saturation in the well to decrease over this time period, especially in the bottom 200 m of the well. This is shown in Figure C.10 D). After 9 days, the bottom 100 m of the well has condensed to liquid conditions. This decrease in vapour saturation causes an increase in the averaged density of the fluid below the feed located at -800 mRL. This causes the large increase in pressure in the bottom 200 m of the well that is shown in Figure C.10 A). As the bottomhole pressure increases, the influx from the deep feed decreases. After 10 days, the temperature of the deep feed has cooled to 190 °C.

After decreasing the temperature, the pressure of the deep feed was reduced from 100 bara to 20 bara over a 10 day period. The final pressure of the feed was chosen to be lower than the bottomhole pressure after the feed had been cooled (which was approximately 27.5 bara). This allowed outflow to the deep feed to occur. Figure C.10 C) and D) show that after 25 days, liquid flows down from the feed beginning at -800 mRL and exits the well via the deep feed. This demonstrates that our simulator can model the flow scenario in which liquid water flows down from a two-phase block.

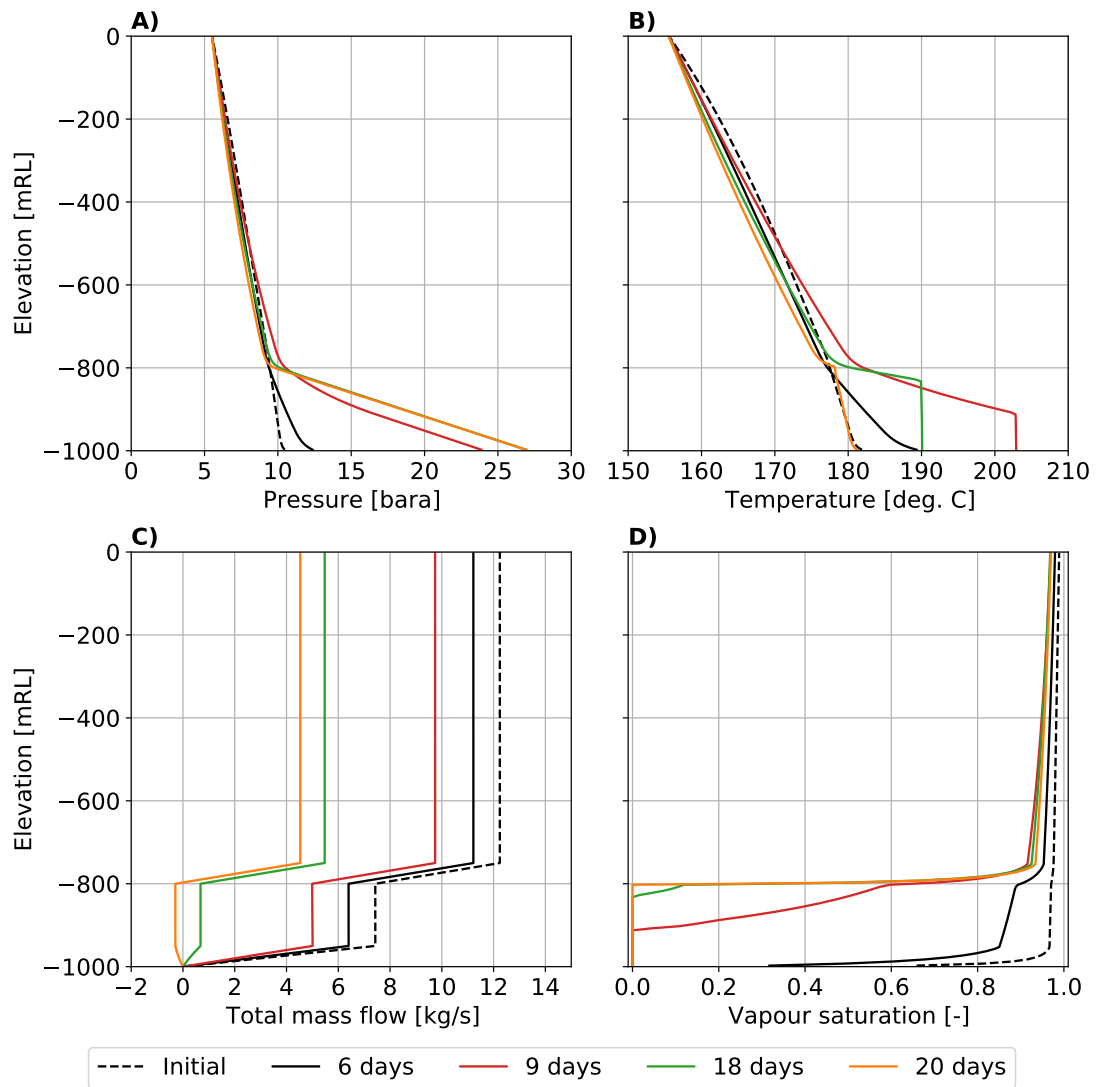


FIGURE C.10: Plots of A) pressure B) temperature C) total mass flow rate and D) vapour saturation at various times for Test Case 15.



## Appendix D

# Viscosity of an air-water vapour mixture

In this section, we present the equations used in our simulator to calculate the viscosity of a mixture of air and water vapour. This formulation, originally presented by Hirschfelder et al. (1954), is used in a modified form in TOUGH2 (EOS3) and Waiwera. We have implemented the method used in Waiwera.

The viscosity of the air-water vapour mixture is defined by Hirschfelder et al. (1954) as:

$$\mu_v = 0.1 \frac{1 + Z}{X + Y}. \quad (\text{D.1})$$

Here, we have adjusted the units of the equation originally given by Hirschfelder et al. (1954) from g/cm/s to kg/m/s (Pa s).

In D.1:

$$X = \frac{(m_v^a)^2}{\mu^a} + \frac{2m_v^a m_v^w}{\mu^{aw}} + \frac{(m_v^w)^2}{\mu^w} \quad (\text{D.2})$$

$$Y = \frac{3}{5} A_{aw}^* \left\{ \frac{(m_v^a)^2}{\mu^a} \left( \frac{MW^a}{MW^w} \right) + \frac{2m_v^a m_v^w}{\mu^{aw}} \left( \frac{(MW^a + MW^w)^2}{4MW^a MW^w} \right) \left( \frac{(\mu^{aw})^2}{\mu^a \mu^w} \right) + \frac{(m_v^w)^2}{\mu^w} \left( \frac{MW^w}{MW^a} \right) \right\} \quad (\text{D.3})$$

$$Z = \frac{3}{5} A_{aw}^* \left\{ (m_v^a)^2 \frac{MW^a}{MW^w} + 2m_v^a m_v^w \left[ \left( \frac{(MW^a + MW^w)^2}{4MW^a MW^w} \right) \left( \frac{\mu^{aw}}{\mu^a} + \frac{\mu^{aw}}{\mu^w} \right) - 1 \right] + (m_v^w)^2 \frac{MW^w}{MW^a} \right\} \quad (D.4)$$

Here,  $m_v^\kappa$  and  $MW^\kappa$  are the mole fraction and molecular weight of component  $\kappa$ , respectively. The viscosity of pure air and water vapour are given by  $\mu^a$  and  $\mu^w$ , respectively. The empirical parameter  $A_{aw}^*$  is defined in (D.12) below.

In (E.2) – (E.4), the viscosity of pure air,  $\mu^a$  (in g/cm/s) is calculated from (Hirschfelder et al., 1954):

$$\mu_v^a = 266.93 \times 10^{-7} \frac{\sqrt{MW^a T}}{(\sigma^a)^2 \Omega^a T^{a*}} \quad (D.5)$$

where  $\sigma^a$  is the collision diameter (given in Table D.1),  $T$  is the temperature (in °K) and the reduced temperature,  $T^{a*}$ , is calculated as:

$$T^{a*} = \frac{T}{f^a}, \quad (D.6)$$

where the potential parameter  $f^a$  is given in Table D.1.

In (D.5), the parameter  $\Omega^a$  is calculated as:

$$\Omega^a = \frac{1.188 - 0.051 T^{a*}}{T^{a*}}. \quad (D.7)$$

Hirschfelder et al. (1954) suggested the viscosity of water vapour be calculated in the same way as described above for air. However, we implement the method used in TOUGH2 and Waiwera. Both reservoir simulators use an empirical correlation for vapour viscosity instead. We use the viscosity of water vapour from the IAPWS-08 formulation for the viscosity of ordinary water (Huber et al., 2009).

The parameter  $\mu^{aw}$  in (E.2) – (E.4) is defined by Hirschfelder et al. (1954) as:

$$\mu_v^{aw} = 266.93 \times 10^{-7} \frac{\sqrt{2MW^a MW^w T / (MW^a + MW^w)}}{(\sigma^{aw})^2 \Omega^{aw} T^{aw*}} \quad (D.8)$$

Here,

$$T^{aw*} = \frac{T}{\sqrt{f^a + f^w}}, \quad (D.9)$$

where the potential parameters  $f^a$  and  $f^w$  are given in Table D.1.

In (D.8),  $\Omega^{aw}$  is calculated as:

$$\Omega^{aw} = \frac{1.48 - 0.412 \ln(T^{aw*})}{T^{aw*}}, \quad (\text{D.10})$$

and

$$\sigma^{aw} = \frac{\sigma^a + \sigma^w}{2}, \quad (\text{D.11})$$

where  $\sigma^a$  and  $\sigma^w$  are given in Table D.1.

Finally,  $A^{aw*}$ , which is used in (E.3) and (E.4) above, is defined as:

$$A_{aw}^* = \frac{1.095}{T^{aw*}}. \quad (\text{D.12})$$

TABLE D.1: Constants used in the calculation of the viscosity of a mixture of air and water vapour.

$\sigma^a$ [Å]	$\sigma^w$ [Å]	$f^a$ [°K]	$f^w$ [°K]	$MW^a$ [g/mol]	$MW^w$ [g/mol]
3.617	2.655	97	363	28.96	18.01582

# Bibliography

- Akbar, S., Fathianpour, N. and Al-Khoury, R. (2016), ‘A Finite Element Model for High Enthalpy Two-Phase Flow in Geothermal Wellbores’, *Renewable Energy* **94**, 223–236.
- Alvarez Del Castillo, A., Santoyo, E. and García-Valladares, O. (2012), ‘A New Void Fraction Correlation Inferred from Artificial Neural Networks for Modelling Two-Phase Flows in Geothermal Wells’, *Computers and Geosciences* **41**, 25–39.
- Alvarez, R. and Cinco, F. (2011), ‘Use of Wellbore Simulation as a Tool to Evaluate Well Issues in Mature Geothermal Fields’, *Geothermal Resources Council Transactions* **35**, 1383–1388.
- Anderson, J. D. J. (1995), *Computational Fluid Dynamics: The Basics with Applications*, McGraw-Hill Book Company.
- Armand, A. A. (1945), ‘Resistance to Two Phase Flow in Horizontal Tubes (in Russian)’, *Izv. VTI* **15**(1).
- Armenta, M. F., Montes, M. R. and Alcala, L. M. (2015), ‘Wellbore Modeling of Production Well H-1D using WellSim, Los Humeros Geothermal Field, México’, in: *Proceedings of the World Geothermal Congress 2015*, Melbourne, Australia.
- Aster, R., Borchers, B. and Thurber, C. (2013), *Parameter Estimation and Inverse Problems*, 2nd edn, Academic Press, New York.
- Aunzo, Z. P., Bjornsson, G. and Bodvarsson, G. S. (1991), Wellbore Models GWELL, GWNACL, and HOLA User’s Guide, Technical report, Lawrence Berkeley Laboratory, California.

- Axelsson, G. (2012), The Physics of Geothermal Energy, *in* Ali Sayigh, ed., ‘Comprehensive Renewable Energy’, Vol. 7, Elsevier Ltd., chapter 2, pp. 3–50.
- Ayala, M. A. R. (2010), Coupled geothermal reservoir-wellbore simulation with a case study for the Námafjall field, N-Iceland, Master’s thesis, University of Iceland.
- Barelli, A., Corsi, R., Del Pizzo, G. and Scali, C. (1982), ‘A Two-Phase Flow Model for Geothermal Wells in the Presence of Non-condensable Gas’, *Geothermics* **11**(3), 175–191.
- Baroczy, C. J. (1966), ‘A Systematic Correlation for Two-Phase Pressure Drop’, *Chemical Engineering Progress Symposium Series* **62**, 232–249.
- Battistelli, A., Finsterle, S., Marcolini, M. and Pan, L. (2020), ‘Modeling of Coupled Wellbore-Reservoir Flow in Steam-Like Supercritical Geothermal Systems’, *Geothermics* **86**.
- Battistelli, A., Rivera, J. R., Celati, R. and Mohamed, A. (1990), ‘Study of the Effect of Several Wellbore Conditions on the Output Characteristic of Wells at the Asal Field, Republic of Djibouti’, in: *Proceedings of the 15th Workshop on Geothermal Reservoir Engineering*, Stanford, California.
- Battistelli, A., Rivera, J. R. and Ferragina, C. (1992), ‘The Modelling of Flow in Geothermal Wells Applied to the Reservoir Engineering Study of the Asal field: Republic of Djibouti’, presented at: *The PNOC-EDC Geothermal Conference*, Manila, Philippines.
- Beattie, D. (1973), ‘A Note on the Calculation of Two-Phase Pressure Losses’, *Nuclear Engineering and Design* **25**, 395–402.
- Bendiksen, K. H., Maines, D., Moe, R. and Nuland, S. (1991), ‘The Dynamic Two-Fluid Model OLGA: Theory and Application’, *SPE Production Engineering* **6**(02), 171–180.
- Berry, R. A., Peterson, J. W., Zhang, H., Martineau, C., Zhao, H., Zou, L. and Andrs, D. (2014), RELAP-7 Theory Manual, Technical report, Idaho National Laboratory.
- Bhagwat, S. M. and Ghajar, A. J. (2012), ‘Similarities and Differences in the Flow Patterns and Void Fraction in Vertical Upward and Downward Two Phase Flow’, *Experimental Thermal and Fluid Science* **39**, 213–227.

- Bhat, A., Swenson, D. and Gosavi, S. (2005), 'Coupling the HOLA Wellbore Simulator with TOUGH2', in: *Proceedings of the 30th Workshop on Geothermal Reservoir Engineering*, Stanford, California.
- Bilicki, Z., Kestin, J. and Michaelides, E. E. (1981), Flow in Geothermal Wells: Part III. Calculation Model for Self-Flowing Well, Technical report, Brown University, United States.
- Bjornsson, G. (1987), A Multi-Feedzone Geothermal Wellbore Simulator, Master's thesis, University of California, Berkeley.
- Bjornsson, G. and Bodvarsson, G. S. (1987), 'A Multi-Feedzone Wellbore Simulator', *Geothermal Resource Council Transactions* **11**, 503–507.
- Bodvarsson, G. S. and Benson, S. M. (1984), 'The Krafla Geothermal Field, Iceland 1. Analysis of Well Test Data', *Water Resources Research* **20**(11), 1515–1530.
- Boure, J. A. and Delhay, J. M. (1982), General Equations and Two-Phase Flow Modeling, in G. Hetsroni, ed., 'Handbook of Multiphase Systems', McGraw-Hill.
- Brown, G. (2018), 'The History of the Darcy-Weisbach Equation for Pipe Flow Resistance', in: *Proceedings of the Environmental and Water Resources History Sessions at ASCE Civil Engineering Conference and Exposition*, Washington, D.C., 34–43.
- Butterworth, D. (1975), 'A Comparison of Some Void-Fraction Relationships for Co-Current Gas-Liquid Flow', *International Journal of Multiphase Flow* **1**(6), 845–850.
- Chadha, P. K., Malin, M. R. and Palacio-Perez, A. (1993), 'Modelling of Two-Phase Flow Inside Geothermal Wells', *Applied Mathematical Modelling* **17**, 263–245.
- Chen, J. J. (1986), 'A Further Examination of Void Fraction in Annular Two-Phase Flow', *International Journal of Heat and Mass Transfer* **29**(11), 1760–1763.
- Chierici, G., Giannone, G., Schlocchi, G. and Terzi, L. (1981), 'A Wellbore Model for Two-Phase Flow in Geothermal Reservoirs', presented at: *56th Annual Fall Technical Conference and Exhibition of the Society of Petroleum Engineers of AIME*, San Antonio, Texas.

- Chisholm, D. (1973), 'Pressure Gradients Due to Friction During the Flow of Evaporating Two-Phase Mixtures in Smooth Tubes and Channels', *International Journal of Heat and Mass Transfer* **16**(2), 347–358.
- Chisholm, D. (1983), *Two-phase Flow in Pipelines and Heat Exchangers*, Pittman Press Ltd, Bath, England.
- Chiu, K. and Thakur, S. C. (1991), 'Modeling of Wellbore Heat Losses in Directional Wells Under Changing Injection Conditions.', presented at: *SPE Annual Technical Conference and Exhibition*, Dallas, Texas.
- Cinar, M. and Onur, M. (2015), 'A Wellbore Model for Geothermal Wells Containing Considerable Amount of CO<sub>2</sub>', in: *Proceedings of the World Geothermal Congress 2015*, Melbourne, Australia.
- Cinar, M., Onur, M. and Satman, A. (2006), 'Development of a Multi-Feed P-T Wellbore Model for Geothermal Wells', in: *Proceedings of the 31st Workshop on Geothermal Reservoir Engineering*, Stanford, California.
- Colebrook, C. F. (1939), 'Turbulent Flow in Pipes, with Particular Reference to the Transition Region Between the Smooth and Rough Pipe Laws', *Journal of the Institution of Civil Engineers* **11**(4), 133–156.
- Croucher, A. (2020), Waiwera User Guide, Technical report, The University of Auckland, Auckland, New Zealand.
- Croucher, A., O'Sullivan, J., Yeh, A. and O'Sullivan, M. (2018), 'Benchmarking and Experiments with Waiwera, a New Geothermal Simulator', in: *Proceedings of the 43rd Workshop on Geothermal Reservoir Engineering*, Stanford, California.
- Degrez, G. (2009), Implicit Time-Dependent Methods for Inviscid and Viscous Compressible Flows, with a Discussion of the Concept of Numerical Dissipation, in J. F. Wendt, ed., 'Computational Fluid Dynamics: An Introduction', 3rd edn, Springer, chapter 9, pp. 204–226.
- Diener, R. and Friedel, L. (1998), 'Reproductive Accuracy of Selected Void Fraction Correlations for Horizontal and Vertical Upflow', *Forschung im Ingenieurwesen* **64**(4-5), 87–97.

- Dispenza, C. F. C. (1987), ‘The Entrainment Approach in Modelling Two-Phase Flow in Geothermal Wells’, in: *Proceedings of the Second Int. Symp. on Two-Phase Gas-Liquid Flow in Pipes*, Morelos, Mexico.
- Dittman, G. L. (1977), Wellflow for Geothermal Wells - Description of a Computer Program Including Effects of Brine Composition, Technical report, Lawrence Livermore Laboratory.
- Dittmann, A. (2000), ‘IAPWS Industrial Formulation 1997 for the Thermodynamic Properties of Water and Steam’, *International Steam Tables* **122**, 7–150.
- Dix, G. E. (1971), Vapor Void Fractions for Forced Convection with Subcooled Boiling at Low Flow Rate, PhD thesis, University of California, USA.
- Doran, H. R., Renaud, T., Falcone, G., Pan, L. and Verdin, P. G. (2021), ‘Modelling an Unconventional Closed-Loop Deep Borehole Heat Exchanger (DBHE): Sensitivity Analysis on the Newberry Volcanic Setting’, *Geothermal Energy* **9**(4).
- Duns, H. and Ros, N. C. J. (1963), ‘Vertical Flow of Gas and Liquid Mixtures in Wells’, in: *Proceedings of the 6th World Petroleum Congress*, Frankfurt, Germany, 451–465.
- Elliot, D. G. (1975), Comparison of Brine Production Methods and Conversion Processes for Geothermal Electric Power Generation, Technical report, Environmental Quality Laboratory California Institute of Technology, Pasadena, California.
- Farouq Ali, S. M. (1981), ‘A Comprehensive Wellbore Steam/Water Flow Model for Steam Injection and Geothermal Applications’, *Society of Petroleum Engineers of AIME* **21**(05), 527–534.
- Finger, J. and Blankenship, D. (2010), Handbook of Best Practices for Geothermal Drilling, Technical report, Sandia National Laboratories, Livermore, California.
- Finsterle, S. (2011), iTOUGH2 Universal Optimization Using the PEST Protocol, Technical report, Lawrence Berkeley National Laboratory, Berkeley.
- Franz, P. (2015), ‘Paiwera – a Robust Wellbore Simulator for Geothermal Applications’, in: *Proceedings of the 37th New Zealand Geothermal Workshop*, Taupo, New Zealand.



- Franz, P. and Clearwater, J. (2021), Volsung User Manual, Technical report, Flow State Solutions, New Zealand.
- Freeston, D. H. and Gunn, C. (1993), 'Wellbore Simulation - Case Studies', in: *Proceedings of the 18th Workshop on Geothermal Reservoir Engineering*, Stanford, California.
- Freeston, D. H. and Hadgu, T. (1987), 'Modelling of Geothermal Wells with Multiple Feed Points: A Preliminary Study', in: *Proceedings of the 9th New Zealand Geothermal Workshop*, 59–64.
- Friedel, J. (1979), 'Improved Friction Pressure Drop Correlations for Horizontal and Vertical Two- Phase Pipe Flow', presented at: *The European Two-Phase Flow Group Meeting*, Ispra, Italy.
- Gando, A., Gando, Y., Ichimura, K., Ikeda, H., Inoue, K., Kibe, Y., Kishimoto, Y., Koga, M., Minekawa, Y., Mitsui, T., Morikawa, T., Nagai, N., Nakajima, K., Nakamura, K., Narita, K., Shimizu, I., Shimizu, Y., Shirai, J., Suekane, F., Suzuki, A., Takahashi, H., Takahashi, N., Takemoto, Y., Tamae, K., Watanabe, H., Xu, B. D., Yabumoto, H., Yoshida, H., Yoshida, S., Enomoto, S., Kozlov, A., Murayama, H., Grant, C., Keefer, G., Piepke, A., Banks, T. I., Bloxham, T., Detwiler, J. A., Freedman, S. J., Fujikawa, B. K., Han, K., Kadel, R., O'Donnell, T., Steiner, H. M., Dwyer, D. A., McKeown, R. D., Zhang, C., Berger, B. E., Lane, C. E., Maricic, J., Miletic, T., Batygov, M., Learned, J. G., Matsuno, S., Sakai, M., Horton-Smith, G. A., Downum, K. E., Gratta, G., Tolich, K., Efremenko, Y., Perevozchikov, O., Karwowski, H. J., Markoff, D. M., Tornow, W., Heeger, K. M. and Decowski, M. P. (2011), 'Partial radiogenic heat model for Earth revealed by geoneutrino measurements', *Nature Geoscience* **4**(9), 647–651.
- García, A., Ascencio, F., Espinosa, G., Santoyo, E., Gutiérrez, H. and Arellano, V. (1999), 'Numerical Modeling of High-Temperature Deep Wells in the Cerro Prieto Geothermal Field, Mexico', *Geofísica Internacional* **38**(4), 251–260.
- García, A., Espinosa-Paredes, G. and Barragán, R. M. (2002), 'Effect of Non-Condensable Gases on the Flow of Water and Steam in Geothermal Wells', *Geofísica Internacional* **41**(4), 377–383.

- Garcia-Gutierrez, A., Espinosa-Paredes, G. and Hernandez-Ramirez, I. (2002), 'Study on the Flow Production Characteristics of Deep Geothermal Wells', *Geothermics* **31**(2), 141–167.
- García-Valladares, O., Sánchez-Upton, P. and Santoyo, E. (2006), 'Numerical Modeling of Flow Processes Inside Geothermal Wells: An Approach for Predicting Production Characteristics with Uncertainties', *Energy Conversion and Management* **47**, 1621–1643.
- Garg, S. K., Pritchett, J. W. and Alexander, J. H. (2004), 'A New Liquid Hold-Up Correlation for Geothermal Wells', *Geothermics* **33**(6), 795–817.
- Geffraye, G., Antoni, O., Farvacque, M., Kadri, D., Lavialle, G., Rameau, B. and Ruby, A. (2011), 'CATHARE 2 V2.5-2: A Single Version for Various Applications', *Nuclear Engineering and Design* **241**(11), 4456–4463.
- Godbole, P. V., Tang, C. C. and Ghajar, A. J. (2011), 'Comparison of Void Fraction Correlations for Different Flow Patterns in Upward Vertical Two-Phase Flow', *Heat Transfer Engineering* **32**(10), 843–860.
- Gould, T. L. (1974), 'Vertical Two-Phase Steam-Water Flow in Geothermal Wells', *Journal of Petroleum Technology* **26**(08), 833–842.
- Goyal, K. P., Miller, C. W. and Lippmann, M. J. (1980), 'Effect of Measured Wellhead Parameters and Well Scaling on the Computed Downhole Conditions in Cerro Prieto Wells', in: *Proceedings of the 6th Workshop on Geothermal Reservoir Engineering*, Stanford, California, 130–138.
- Grant, M. A. (1977), 'Permeability Reduction Factors at Wairakei', presented at: *AIChE-ASME Heat Transfer Conference*, Salt Lake City, Utah.
- Grant, M. A. and Bixley, P. F. (2011), *Geothermal Reservoir Engineering*, 2nd edn, Academic Press.
- Gudmundsdottir, H. (2012), A coupled wellbore-reservoir simulator utilizing measured wellhead conditions, Magister scientiarum, University of Iceland.

- Gudmundsdottir, H. and Jonsson, M. T. (2015), ‘The Wellbore Simulator FloWell – Model Enhancement and Verification’, in: *Proceedings of the World Geothermal Congress 2015*, Melbourne, Australia.
- Gudmundsdottir, H., Jonsson, M. T. and Palsson, H. (2013*a*), ‘A Coupled Wellbore-Reservoir Simulator utilizing Measured Wellhead Conditions’, in: *Proceedings of the 38th Workshop on Geothermal Reservoir Engineering*, Stanford, California.
- Gudmundsdottir, H., Jonsson, M. T. and Palsson, H. (2013*b*), ‘The Wellbore Simulator FloWell’, in: *Proceedings of the 38th Workshop on Geothermal Reservoir Engineering*, Stanford, California.
- Gunawan, F., Hastriansyah, G., Prabowo, T. and Zuhro, A. A. (2015), ‘Remedial Work in a Geothermal Well Case Study: Sendangan-3, Tompaso Project’, in: *Proceedings of the World Geothermal Congress 2015*, Melbourne, Australia.
- Gunn, C. (1992), Aspects of Geothermal Wellbore Simulation, Master’s thesis, The University of Auckland, Auckland, New Zealand.
- Hadgu, T. (1989), Vertical Two-phase Flow Studies and Modelling of Flow in Geothermal Wells, PhD thesis, The University of Auckland, Auckland, New Zealand.
- Hadgu, T. and Freeston, D. H. (1990), ‘A Multipurpose Wellbore Simulator’, *Geothermal Resources Council Transactions* **14**, 1279–1286.
- Hagedorn, A. and Brown, K. (1965), ‘Experimental Study of Pressure Gradients Occurring During Continuous Two-Phase Flow in Small-Diameter Vertical Conduits’, *Journal of Petroleum Technology* **17**, 475–484.
- Harmathy, T. Z. (1960), ‘Velocity of Large Drops and Bubbles in Media of Infinite or Restricted Extent’, *AIChE Journal* **6**(2), 281–288.
- Harrison, R. (1975), Method for the Analysis of Geothermal Two-Phase Flow, Master’s thesis, University of Auckland, Auckland, New Zealand.
- Hasan, A. R. and Kabir, C. S. (2010), ‘Modeling Two-Phase Fluid and Heat Flows in Geothermal Wells’, *Journal of Petroleum Science and Engineering* **71**, 77–86.

- Hastriansyah, G., Yuniar, D. M. and Silaban, M. S. P. (2015), 'Well Remedial Evaluation and Prediction of Post Remedial Condition of a Suspected Multiple Feedzone Well Using Wellbore Simulation, Case Study: Well Sendangan-4', in: *Proceedings of the World Geothermal Congress 2015*, Melbourne, Australia.
- Hirschfelder, J. O., Curtiss, C. F. and Bird, R. B. (1954), *Molecular Theory of Gases and Liquids*, John Wiley and Sons, New York, chapter 8, pp. 528–530.
- Hole, H. (2008), 'Geothermal Well Design - Casing and Wellhead', presented at: *Petroleum Engineering Summer School*, Dubrovnik, Croatia.
- Horne, R. and Shinohara, K. (1979), 'Wellbore Heat Loss in Production and Injection Wells', *Journal of Petroleum Technology* **31**(1), 116–118.
- Huber, M. L., Perkins, R. A., Laesecke, A., Friend, D. G., Sengers, J. V., Assael, M. J., Metaxa, I. N., Vogel, E., Mareš, R. and Miyagawa, K. (2009), 'New International Formulation for the Viscosity of H<sub>2</sub>O', *Journal of Physical and Chemical Reference Data* **38**(2), 101–125.
- IAPWS (2014), Revised Release on the Surface Tension of Ordinary Water Substance, Technical report, The International Association for the Properties of Water and Steam, Moscow, Russia.
- Irvine, T. F. and Liley, P. E. (1984), Thermodynamic Property Equations for Air, in 'Steam and Gas Tables with Computer Equations', Academic Press, chapter V, pp. 97–98.
- Ishii, M. and Hibiki, T. (2011), *Thermo-Fluid Dynamics of Two-Phase Flow*, 2nd edn, Springer Science+Business Media, New York.
- Itoi, R., Inagaki, H., Tanaka, T. and Iwasaki, T. (2014), 'Effects of Low Temperature Water Inflow into Wellbore at Shallow Feedzone of Production Well on Steam-Water Two-Phase Flow in Well', in: *Proceedings of the 36th New Zealand Geothermal Workshop*, Auckland, New Zealand.
- Itoi, R., Kakihara, Y., Fukuda, M. and Koga, A. (1988), 'Numerical Simulation of Well Characteristics Coupled with Steady Radial Flow in a Geothermal Reservoir', in: *Proceedings of the International Symposium on Geothermal Energy*, Kumamoto, Japan.

- Itoi, R., Katayama, Y., Tanaka, T., Kumagai, N. and Iwasaki, T. (2013), 'Numerical Simulation of Instability of Geothermal Production Well', *Geothermal Resource Council Transactions* **37**, 837–842.
- Kato, M., Okabe, T., Ujyo, S. and Kunzman, R. (2015), 'Development of Wellbore Simulator and High Temperature PTS+FLUID Sampler Logging System for a Highly Deviated Well', in: *Proceedings of the World Geothermal Congress 2015*, Melbourne, Australia.
- Khasani, Deendarlianto and Ryuichi, I. (2021), 'Numerical Study of the Effects of CO<sub>2</sub> Gas in Geothermal Water on the Fluid-Flow Characteristics in Production Wells', *Engineering Applications of Computational Fluid Mechanics* **15**(1), 111–129.
- Khasani, Jalilinasrabady, S., Fujii, H. and Itoi, R. (2017), 'Numerical Study on the Effects of Wellhead Restriction Modes on the Transient Behaviours of a Geothermal Well Deliverability Applicable for a Short Period of Measurement', *Geothermics* **69**(2), 34–44.
- Kim, C. and Roy, R. P. (1981), 'Two-Phase Flow Dynamics by a Five-Equation Drift-Flux Model', *Letters in Heat and Mass Transfer* **8**, 57–68.
- King, T. R., Freeston, D. H. and Winmill, R. L. (1995), 'A Case Study of Wide Diameter Casing for Geothermal Systems', in: *Proceedings of the 17th New Zealand Geothermal Workshop*, 241–244.
- Kocamustafaogullari, G. (1971), Thermo-Fluid Dynamics of Separated Two-Phase Flow, PhD thesis, Georgia Institute of Technology.
- Lee, J., Facchini, A. and Joo, H. G. (2019), 'Development of a Drift-Flux Model Based Core Thermal-Hydraulics Code for Efficient High-Fidelity Multiphysics Calculation', *Nuclear Engineering and Technology* **51**(6), 1487–1503.
- Liles, D. R. (1979), 'The Three-Dimensional Two-Fluid Numerical Treatment of Reactor Vessels in TRAC', presented at: *The American Nuclear Society National Topical Meeting on Computational Methods in Nuclear Engineering*, Williamsburg, Virginia.

- Lockhart, R. and Martinelli, R. (1949), ‘Proposed Correlation of Data for Isothermal Two-Phase, Two-Component Flow in Pipes’, *Chemical Engineering Progress* **45**(1), 39–48.
- Lu, X., Watson, A., Gorin, A. V. and Deans, J. (2006), ‘Experimental Investigation and Numerical Modelling of Transient Two-Phase Flow in a Geysering Geothermal Well’, *Geothermics* **35**(4), 409–427.
- Marquez, S. L., Sazon, T. A. S. and Omagbon, J. B. (2015), ‘SIMGWEL: EDC’s New Geothermal Wellbore Modeling Software’, in: *Proceedings of the World Geothermal Congress 2015*, Melbourne, Australia.
- McGuinness, M. J. (2013), ‘The Impact of Varying Wellbore Area on Flow Simulation’, in: *Proceedings of the 38th Workshop on Geothermal Reservoir Engineering*, Stanford, California.
- McGuinness, M. J. (2014), ‘Feedpoint viscosity in geothermal wellbore simulation’, *Geothermics* **50**, 24–29.
- McGuinness, M. J. (2015), SwelFlo User Manual, Technical report, Marsan Consulting Ltd, Wellington, New Zealand.
- Michaelides, E. E. (1980), Models for Geothermal Wells, PhD thesis, Brown University.
- Miller, C. W. (1979), Numerical model of transient two-phase flow in a wellbore, Technical report, Lawrence Berkeley National Laboratory, Berkeley, California.
- Miller, C. W. (1980a), ‘Wellbore Storage Effects in Geothermal Wells’, *Society of Petroleum Engineers Journal* **20**(06), 555–566.
- Miller, C. W. (1980b), Wellbore User’s Manual, Technical report, Lawrence Berkeley Laboratory, Berkeley, California.
- Miller, C. W., Benson, S. M., O’Sullivan, M. J. and Pruess, K. (1982), ‘Wellbore Effects in the Analysis of Two-Phase Geothermal Well Tests’, *Society of Petroleum Engineers Journal* **22**(03), 309–320.
- Molina, P. O., Malate, R. C. M., Buning, B. C., Yglapaz, D. M., Austria, J. J. C. and Lacanilio, A. M. (1998), ‘Productivity Analysis and Optimisation of Well SK-2D

- Mindanao I Geothermal Project, Philippines', in: *Proceedings of the 23rd Workshop on Geothermal Reservoir Engineering*, Stanford, California.
- Mubarok, M. H. and Zarrouk, S. J. (2017), 'Discharge Stimulation of Geothermal Wells: Overview and Analysis', *Geothermics* **70**, 17–37.
- Murray, L. and Gunn, C. (1993), 'Toward Integrating Geothermal Reservoir and Wellbore Simulation: Tetrad and Wellsim', in: *Proceedings of the 15th New Zealand Geothermal Workshop*, New Zealand.
- Nandanwar, M. S. and Anderson, B. J. (2014), 'Coupled Reservoir, Wellbore and Surface Plant Simulations for Enhanced Geothermal Systems', in: *Proceedings of the 39th Workshop on Geothermal Reservoir Engineering*, Stanford, California.
- Nathenson, M. (1974), 'Flashing flow in Hot Water Geothermal Wells', *Journal of Research of the U.S. Geological Survey* **2**(6), 743–751.
- Oddie, G., Shi, H., Durlofsky, L. J., Aziz, K., Pfeffer, B. and Holmes, J. A. (2003), 'Experimental Study of Two and Three Phase Flows in Large Diameter Inclined Pipes', *International Journal of Multiphase Flow* **29**(4), 527–558.
- Orkiszewski, J. (1967), 'Predicting Two-Phase Pressure Drops in Vertical Pipe', *Journal of Petroleum Technology* **19**(6), 829–838.
- Ortiz-Ramirez, J. (1983), Two-Phase Flow in Geothermal Wells: Development and Uses of a Computer Code, Technical report, Stanford University, United States.
- Pan, L., Freifeld, B., Doughty, C., Zakem, S., Sheu, M., Cutright, B. and Terrall, T. (2015), 'Fully Coupled Wellbore-Reservoir Modeling of Geothermal Heat Extraction Using CO<sub>2</sub> as the Working Fluid', *Geothermics* **53**, 100–113.
- Pan, L. and Oldenburg, C. M. (2012), 'T2-WELL An Integrated Wellbore-Reservoir Simulator', in: *Proceedings, TOUGH Symposium 2012*, Berkeley, California.
- Pan, L. and Oldenburg, C. M. (2014), 'T2Well - An Integrated Wellbore-Reservoir Simulator', *Computers and Geosciences* **65**, 46–55.

- Pan, L., Oldenburg, C. M., Freifeld, B. M. and Jordan, P. D. (2018), ‘Modeling the Aliso Canyon Underground Gas Storage Well Blowout and Kill Operations Using the Coupled Well-Reservoir Simulator T2Well’, *Journal of Petroleum Science and Engineering* **161**, 158–174.
- Pan, L., Oldenburg, C. M., Pruess, K. and Wu, Y.-S. (2011), ‘Transient CO<sub>2</sub> Leakage and Injection in Wellbore-Reservoir Systems for Geologic Carbon Sequestration’, *Greenhouse Gases: Science and Technology* **1**(4), 335–350.
- Pan, L., Oldenburg, C. M., Wu, Y.-S. and Pruess, K. (2011), T2Well/ECO2N Version 1.0: Multiphase and Non-Isothermal Model for Coupled Wellbore-Reservoir Flow of Carbon Dioxide and Variable Salinity Water, Technical report, Lawrence Berkeley National Laboratory, Berkeley, California.
- Pan, L., Webb, S. W. and Oldenburg, C. M. (2011), ‘Analytical Solution for Two-Phase Flow in a Wellbore Using the Drift-Flux Model’, *Advances in Water Resources* **34**, 1656–1665.
- Parlaktuna, M. (1985), Two-Phase Wellbore Simulator and Analysis of Reinjection Data from Svartsengi, Iceland, Technical report, National Energy Authority, Reykjavik.
- Pereira, V. E. and Fowler, A. C. (2020), ‘Exsolving Two-Phase Flow in Oil Wells’, *Geophysical and Astrophysical Fluid Dynamics* **114**(3).
- Poettman, F. H. and Carpenter, P. G. (1952), ‘The Multiphase Flow of Gas, Oil, and Water Through Vertical Flow Strings with Application to the Design of Gas-lift Installations’, presented at: *Drilling and Production Practice*, New York, New York.
- Premoli, A., Francesco, D. and Prima, A. (1970), ‘An Empirical Correlation for Evaluating Two-phase Mixture Density Under Adiabatic Conditions’, in: *Proceedings of the European Two-Phase Flow Group Meeting*, Milan, Italy.
- Pruess, K., Oldenburg, C. M. and Moridis, G. (2012), TOUGH2 User’s Guide, Version 2, Technical report, Lawrence Berkeley National Laboratory, Berkeley, California.
- Ramey, H. J. (1962), ‘Wellbore Heat Transmission’, *Journal of Petroleum Technology* **14**(04), 427–435.



- Ribeiro, J. X., Liao, R., Aliyu, A. M., Baba, Y. D., Archibong-Eso, A., Ehinmowo, A. and Zilong, L. (2020), ‘An Assessment of Gas Void Fraction Prediction Models in Highly Viscous Liquid and Gas Two-phase Vertical Flows’, *Journal of Natural Gas Science and Engineering* **76**(111).
- Richter, H. J. (1981), ‘Flooding in Tubes and Annuli’, *International Journal of Multiphase Flow* **7**(6), 647–658.
- Rouhani, S. Z. and Axelsson, E. (1970), ‘Calculation of Void Volume Fraction in the Subcooled and Quality Boiling Regions’, *International Journal of Heat and Mass Transfer* **13**(2), 383–393.
- Rutqvist, J., Pan, L., Hu, M., Zhou, Q. and Dobson, P. (2018), ‘Modeling of Coupled Flow, Heat and Mechanical Well Integrity during Variable Geothermal Production’, in: *Proceedings of the 43rd Workshop on Geothermal Reservoir Engineering*, Stanford, California.
- Rutqvist, J., Pan, L., Spycher, N., Dobson, P., Zhou, Q. and Hu, M. (2020), ‘Coupled Processes Analysis of Flexible Geothermal Production from Steam-and Liquid-Dominated Systems: Impact on Wells’, in: *Proceedings of the 45th Workshop on Geothermal Reservoir Engineering*, Stanford, California.
- Sánchez-Upton, P. (1995), ‘The Wellbore Simulator SIMU93’, in: *Proceedings of the World Geothermal Congress 1995*, Florence, Italy.
- Sánchez-Upton, P. (2000), ‘The Wellbore Simulator SIMU2000’, in: *Proceedings of the World Geothermal Congress 2000*, Tohoku, Japan, 2851–2856.
- Sanyal, S. K., Brown, S., Fandriana, L. and Juprasert, S. (1979), ‘Sensitivity Study of Variables Affecting Fluid Flow in Geothermal Wells’, in: *Proceedings of the Stanford Geothermal Workshop*, Stanford, California.
- Satman, A., Ugur, Z. and Onur, M. (1999), ‘The Effect of Calcite Deposition on Geothermal Well Inflow Performance’, *Geothermics* **28**(3), 425–444.
- Shi, H., Holmes, J. A., Durlofsky, L. J., Aziz, K., Diaz, L. R., Alkaya, B. and Oddie, G. (2005), ‘Drift-Flux Modeling of Two-Phase Flow in Wellbores’, *SPE Journal* **10**(01), 24–33.

- Shirdel, M. and Sepehrnoori, K. (2012), 'Development of a Transient Mechanistic Two-Phase Flow Model for Wellbores', *SPE Journal* **17**(03), 942–955.
- Smith, S. L. (1969), 'Void Fractions in Two-phase Flow: a Correlation Based Upon an Equal Velocity Head Model', *Proc. of the Institution of Mechanical Engineers* **184**, 647–664.
- Spalding, D. B. (1972), 'A Novel Finite difference Formulation for Differential Expressions involving both First and Second Derivatives', *International Journal for Numerical Methods in Engineering* **4**, 551–559.
- Tachimori, M. (1982), 'A Numerical Simulation Model for Vertical Flow in Geothermal Wells', in: *Proceedings of the 8th Workshop on Geothermal Reservoir Engineering*, Stanford, California.
- Taitel, Y., Bornea, D. and Dukler, A. E. (1980), 'Modelling Flow Pattern Transitions for Steady Upward Gas-Liquid Flow in Vertical Tubes', *AIChE Journal* **26**(3), 345–354.
- Takahashi, M. (1988), 'A Wellbore Flow Model in the Presence of CO<sub>2</sub> Gas', in: *Proceedings of the 13th Workshop on Geothermal Reservoir Engineering*, Stanford, California.
- Thome, J. R. (2006), Void Fractions in Two-Phase Flows, in 'Engineering Data Book III', Wolverine Tube, Inc., chapter 17.
- Tian, S. and Finger, J. T. (2000), 'Advanced Geothermal Wellbore Hydraulics Model', *Journal of Energy Resources Technology* **122**, 142–146.
- Tokita, H. and Itoi, R. (2004), 'Development of the MULFEWS Multi-Feed Wellbore Simulator', in: *Proceedings of the 29th Workshop on Geothermal Reservoir Engineering*, Stanford, California.
- Upadhyay, R. N., Hartz, J. D., Tomkoria, B. N. and Gulati, A. S. (1977), 'Comparison of Calculated and Observed Pressure Drops in Geothermal Wells Producing Steam-Water Mixtures', Presented at: *52nd Annual Fall Technical Conference and Exhibition of the Society of Petroleum Engineers*, Denver, Colorado.

- Vasini, E. M., Battistelli, A., Berry, P., Bonduà, S., Bortolotti, V., Cormio, C. and Pan, L. (2018), 'Interpretation of Production Tests in Geothermal Wells with T2Well-EWASG', *Geothermics* **73**, 158–167.
- Vijayan, P. K., Patil, A. P., Pilkhwal, D. S., Saha, D. and Venkat Raj, V. (2000), 'Assessment of Pressure Drop and Void Fraction Correlations with Data from Two-phase Natural Circulation Loops', *Heat and Mass Transfer* **36**(6), 541–548.
- Webb, S. W. and Rowe, D. S. (1986), Modelling Techniques for Dispersed Multiphase Flows, in N. Cheremisinoff, ed., 'Encyclopedia of fluid mechanics', Vol. 3: Gas-Liquid Flows, Gulf Publ. Co, chapter 31, pp. 908–962.
- Willhite, G. (1967), 'Over-all Heat Transfer Coefficients in Steam And Hot Water Injection Wells', *Journal of Petroleum Technology* **19**(05), 607–615.
- Woldesemayat, M. A. and Ghajar, A. J. (2007), 'Comparison of Void Fraction Correlations for Different Flow Patterns in Horizontal and Upward Inclined Pipes', *International Journal of Multiphase Flow* **33**(4), 347–370.
- Yadigaroglu, G. and Hewitt, G. F., eds (2018), *Introduction to Multiphase Flow*, Springer.
- Yamamura, K., Itoi, R., Tanaka, T. and Iwasaki, T. (2016), 'Numerical Model of Transient Steam-Water Two-Phase Flow in Geothermal Production Wells', in: *Proceedings of the 38th New Zealand Geothermal Workshop*, Auckland, New Zealand.
- Yamamura, K., Itoi, R., Tanaka, T. and Iwasaki, T. (2017), 'Numerical Analysis of Transient Steam-Water Two-Phase Flow in Geothermal Production Wells with Multiple Feed Zones', in: *Proceedings of the 42nd Workshop on Geothermal Reservoir Engineering*, Stanford, California.
- Zarrouk, S. J. and McLean, K. (2019), *Geothermal Well Test Analysis: Fundamentals, Applications and Advanced Techniques*, 1st edn, Academic Press.
- Zivi, S. M. (1964), 'Estimation of Steady-State Steam Void-Fraction by Means of the Principle of Minimum Entropy Production', *Journal of Heat Transfer* **86**(2), 247–251.
- Zolfagharroshan, M. and Khomehchi, E. (2020), 'A Rigorous Approach to Scale Formation and Deposition Modelling in Geothermal Wellbores', *Geothermics* **87**.

- Zou, L., Zhao, H. and Zhang, H. (2015), ‘Numerical Implementation, Verification and Validation of Two-Phase Flow Four-Equation Drift Flux Model with Jacobian-free Newton-Krylov Method’, *Annals of Nuclear Energy* **87**, 707–719.
- Zuber, N. and Findlay, J. A. (1965), ‘Average Volumetric Concentration in Two-Phase Flow Systems’, *Journal of Heat Transfer* **87**(4), 453–468.